

Università degli Studi "G. d'Annunzio" Chieti-Pescara
Scuola Superiore "G. d'Annunzio"

PhD in Engineering Earth and Planetary Sciences
XXXVII cycle

Building of 3D models and estimation of the site spectral response

PhD Candidate
Primofiore Ilaria

Supervisor
Prof. Vessia Giovanna

Co-Supervisor
Dr. Laurenzano Giovanna

Doctoral Years 2021/2024








Università degli Studi "G. d'Annunzio" Chieti-Pescara
Scuola Superiore "G. d'Annunzio"
Istituto Nazionale di Oceanografia e Geofisica Sperimentale - Trieste

PhD in Engineering Earth and Planetary Sciences
XXXVII cycle

Building of 3D models and estimation of the site spectral response

PhD Candidate
Primofiore Ilaria
Università degli Studi "G. d'Annunzio" di Chieti-Pescara
INGEO Department
SSD GEOS-03/B

Supervisor
Associate Prof. Vessia Giovanna
Università degli Studi "G. d'Annunzio" di Chieti-Pescara

Co-Supervisor
Dr. Laurenzano Giovanna
Istituto Nazionale di Oceanografia e Geofisica Sperimentale - Trieste

PhD Coordinator
Full Prof. Berardi Luigi
Università degli Studi "G. d'Annunzio" di Chieti-Pescara

Doctoral Years 2021/2024

SUMMARY

ABSTRACT ..... *IV*

GLOSSARY ..... *VI*

Chapter 1 INTRODUCTION *1*

1.1. Local Seismic Response **1**

1.2. Content overview **2**

Chapter 2 LITERATURE REVIEW *1*

2.1. Observed local seismic effects **1**
2.1.1. Mono-dimensional effects 2
2.1.2. Bi-dimensional effects 5
2.1.2.1. Valley effects 5
2.1.2.2. Topographic effects 6
2.1.3. Three-dimensional effects 10

2.2. Numerical simulation methods review **13**
2.2.1. Discretization methods 13
2.2.2. Seismic source modelling 17
2.2.3. Constitutive material laws 17
2.2.3.1. Elastic linear behaviour 18
2.2.3.2. Viscoelastic behaviour 18
2.2.3.3. Elastic nonlinear behaviour 20

Chapter 3 GROUND MOTION PARAMETERS *1*

3.1. Fourier spectrum **1**
3.2. Transfer and amplification functions **2**
3.3. Response spectrum **6**
3.4. Predominant period **7**
3.5. Fundamental resonance frequency **7**
3.6. Duration **8**
3.7. PGA, PGV and PGD **8**
3.8. Amplification factors **9**
3.9. Housner intensity **10**
3.10. Housner factors **10**
3.11. Torsional motion **10**

Chapter 4 METHODOLOGY *12*

4.1 Build a 3D model **12**
4.1.1. Geophysical investigation methods 13
4.1.1.1. Seismic reflection 13
4.1.1.2. Vertical seismic profile 13
4.1.1.3. Multichannel Analysis of Surface Waves 14
4.1.1.4. Refraction Microtremor 14
4.1.1.5. Horizontal-to-Vertical Spectral Ratio 15
4.1.1.6. Generalised Inversion Technique 16
4.1.2. Integrate experimental data to build a model 17
4.1.3. Geomodeller 20

4.2. Numerical simulations 21
4.2.1. Definition of a seismic input 21
4.2.2. 1D simulations 22
4.2.3. 2D simulations 23
4.2.4. 3D simulations 24
4.2.4.1. SPECFEM3D 24
4.2.4.2. FLAC3D 25

Chapter 5 CASE STUDY SITES 1

5.1. Sarca Valley 1
5.1.1. Geological-structural settings 3
5.1.2. Seismological settings 7
5.1.3. Geophysical data collection 9
5.1.3.1. Boreholes 9
5.1.3.2. Seismic reflection sections 13
5.1.3.3. Vertical seismic profile 14
5.1.3.4. Multichannel Analysis of Surface Waves 15
5.1.3.5. Refraction Microtremor 18
5.1.3.6. Horizontal to Vertical Spectral Ratio 22
5.1.3.7. Generalized Inversion Technique 23

5.2. Arquata del Tronto ridge 24
5.2.1. Geological-structural settings 25
5.2.2. Seismological settings 28
5.2.3. Geophysical settings 32

Chapter 6 RESULTS AND DISCUSSIONS 1

6.1. Sarca Valley 1
6.1.1. Building a 3D model 2
6.1.1.1. Surveys integration 2
6.1.1.2. 3D model creation 18
6.1.2. Local Seismic Response analyses 24
6.1.2.1. Model validation through numerical simulations 24
6.1.2.2. 1D Seismic Numerical Simulations 26
6.1.2.3. 2D Seismic Numerical Simulations 30
6.1.2.4. 3D simulations 34

6.2. Arquata del Tronto 40
6.2.1. Comparisons between linear and non-linear simulations 44
6.2.2. Directional effects 47
6.2.3. Torsional motions 49

CONCLUSIONS 53

APPENDIX 57

REFERENCES 124

ACKNOWLEDGMENT 145

ABSTRACT

The severity of earthquake-induced shaking is strongly influenced by local site features, which emphasises the crucial role of applied geology in the assessment of seismic evaluations. This study aims to contribute to both scientific progress and territorial prevention by providing tools for urban planning and civil protection, in particular by identifying areas of increased seismic shaking using 3D models of two geomorphological configurations known to generate site effects: a deep valley and an irregular relief. Furthermore, this study aims to deepen the understanding of three-dimensional seismic site effects, which are often neglected in conventional analyses.

The research focusses on two complex study areas: the Sarca Valley in northern Italy and the Arquata del Tronto ridge in central Italy.

The Sarca Valley, on the shores of Garda Lake, is a sedimentary basin up to 400 m deep, which predisposes it to significant seismic amplification in a low- medium seismic territory. The Autonomous Province of Trento (PAT), to which the Sarca Valley belongs, has prioritised territorial safety and recognised the need to address seismic risk in an area prone to amplification effects, as previous microzonation studies had shown. The study area is of great importance from a touristic, commercial and industrial point of view, which makes a comprehensive understanding of its seismic behaviour essential.

The Arquata del Tronto hill, on the other hand, is located in an area of high seismic reference hazard in the heart of the Apennines and was devastated by the 2016 seismic sequence. Its geology consists of an asymmetrical ridge, alternating folded and fractured layers and a small closed valley known as the Borgo area. The assessment of 3D directional and rotational effects is a key aspect of this study area; however, the research goes beyond this aspect and offers important contributions for planning and reconstruction. A detailed understanding of site-specific seismic behaviour, including three-dimensional effects, provides comprehensive insights for engineering practise and improves the development of effective risk mitigation strategies.

To assess ground motion modifications, simulations of seismic wave propagation were carried out using accurate three-dimensional digital models of the subsurface. These models take into account the lithological variations and group the materials based on their seismic properties. Model validation is performed by analysing experimental seismic recordings at both sites, followed by detailed 1D, 2D and 3D response analysis simulations.

The results confirm significant seismic amplification in both study areas, with resonance frequencies varying in different zones. The analyses implemented the equivalent linear behaviour of soils. The results from the Sarca Valley showed a shift of the amplification peaks to lower frequencies compared to linear viscoelastic assumptions. Surface waves generated at the valley margins prolonged the seismic shaking. The simulations of the Arquata del Tronto ridge pointed out a directional polarisation of the seismic oscillations, which was due to the asymmetric geometry of the ridge and the lithological properties.

Three-dimensional simulations showed that out-of-plane vibrations and torsional motions are amplified by factors such as low shear wave velocities and topographic slopes.

Finally, it was observed that each component recorded at the surface is influenced by the other two perpendicular input components. These conversions from one component to another are called cross-coupling effects and are due to lateral heterogeneities in the buried morphologies. All these results are collected in maps that illustrate the spatial distribution of ground motion parameters (such as amplification, frequency content, angular velocities, rotational angles) that need to be considered in building design and territorial planning in urban areas.

GLOSSARY

Accelerogram	Sequence of acceleration values in the time domain.
Amplification factor (FA)	It is the ratio between the average values of the output and input elastic acceleration **response spectra** of a specific study site, over the period ranges: ΔT_1 =0.1-0.5 s; ΔT_2= 0.4-0.8 s; ΔT_3= 0.7-1.1 s, according to the Italian guidelines for Seismic Microzonation (SM Working Group, 2015)
Amplification function	Variation of the seismic amplitude, due to the filtering action of the soil deposits starting from the bedrock up to the surface (related to the physical-mechanical and geometrical properties of the system itself). The amplification function is defined as the ratio between the output **Fourier amplitude spectrum** and the input **Fourier amplitude spectrum**.
Anisotropy	Lack of isotropy, i.e. the physical and mechanical properties of a material have different values in the different directions considered.
Attenuation	Reduction in the amplitude of the seismic signal as it moves away from the source. Attenuation is caused by the geometric dissipation of seismic wave energy (i.e. the decrease in energy density as the size of the wavefront increases) and by **damping** (i.e. the inelastic properties of materials).
Bedrock	In general, this is a compact, rigid, unaltered rock. In seismic response analysis, seismic bedrock is defined as a lithostratigraphic layer characterised by a shear

	wave velocity Vs of 800 m/s or more (according to the Italian building code NTC18).
Boundary condition	Prescription of a constraint or controlled condition along a model boundary (e.g., fixed displacement or force for mechanical problems, impermeable boundary for groundwater flow problems, boundary for heat transfer, etc.).
Constitutive model	Stress and strain behaviour of each lithotype. Several constitutive models to assimilate different types of behaviour are available. Constitutive models and material properties can be assigned individually.
Convolution	Mathematical operator in the frequency domain that corresponds to the **Fourier transform** of the product of two functions in the time domain. It consists of integrating the product between the first and second functions, which are translated by a given value.
Damping	The damping ratio is defined as the ratio between the damping coefficient (c) and the critical damping coefficient (c0): D=c/c0. The critical damping is the value of the damping at which the free movement is stopped. It expresses the ability of a material or structure to dissipate the energy that passes through it. If the stress has an oscillatory character, it is expressed as the ratio between the amount of energy ΔW dissipated by the system in a single oscillation and the maximum elastic energy W associated with the same oscillation: D= ΔW/4πW.
Empirical Amplification Function (EAF)	Referring to real-world recorded ground motion signals, it is defined as the ratio between the **Fourier amplitude spectrum** recorded at the outcrop of the study site and the **Fourier amplitude spectrum**

	recorded at the outcrop of the reference site, considering only the two horizontal components.
Fourier amplitude spectrum	The modulus of the **Fourier transform**. Together with the phase spectrum, it uniquely describes the temporal signature of a signal. It shows how the amplitude of the motion is distributed with the frequency.
Fourier phase spectrum	Together with the amplitude spectrum, it uniquely describes the temporal signature of a signal. It shows how the phase angles are distributed about the frequency.
Fourier transform	Mathematical operator with which a time function can be expressed as a complex frequency function. It decomposes a time signal into harmonics and assigns an amplitude and a phase to each of them.
Fundamental resonance frequency	The lowest frequency of a periodic waveform. In the field of seismic response, the frequency corresponds to the peak of the H/V curve.
Housner factors (FH)	Ratio between the **Housner intensity** calculated for the study site and the **Housner intensity** calculated for the reference site.
Housner intensity (SI)	The integral of the pseudo-velocity **response spectrum** over the period range ΔT=0.1-2.5 s. It is measured in terms of displacement (cm). The SI summarises the amplitude and frequency content of the seismic response of a site (or a structure) in the period range most relevant to engineering behaviour.
Local amplification	See **Local Seismic Response**.
Local effects	Effects resulting from the behaviour of the ground for a seismic event and due to the presence of lithostratigraphic and morphological conditions that

	determine **local amplifications** and phenomena of ground instability (slope instability, liquefaction, fault ruptures, subsidence, etc.).
Local Seismic Response (LSR)	Changes of seismic motion in amplitude, frequency and duration due to the specific lithostratigraphic and morphological conditions of a site. It can be quantified by the **amplification function**.
Peak Ground Acceleration (PGA)	The geometric mean of the highest absolute value of the acceleration of the two horizontal components recorded on the topographic surface.
Peak Ground Displacement (PGD)	The geometric mean of the highest absolute value of the displacement of the two horizontal components recorded on the topographic surface.
Peak Ground Rotation (PGR)	The highest absolute value of the angular velocity around the x-axes recorded on the topographic surface.
Peak Ground Velocity (PGV)	The geometric mean of the highest absolute value of the velocity of the two horizontal components recorded on the topographic surface.
Predominant period	Period corresponding to the maximum value of the smoothed **Fourier amplitude spectrum.**
Response function	Referring to numerical simulations of seismic wave propagation, it is defined as the ratio between the **Fourier transform** (considering both amplitude and phase spectra) recorded at the outcrop of the numerical model of the study site and the **Fourier transform** (considering both amplitude and phase spectra) recorded at the outcrop of the numerical model of the reference site.

Response spectrum	The maximum response of a single-degree-of-freedom system to a given input motion. It describes the maximum amplitude with which oscillators with different periods and a **damping** ξ of 5% respond to a certain seismic action. The classic representation of the response spectrum is in terms of pseudo-acceleration.
Site effects	See **local effects**.
Synthetic amplification function	Referring to numerical simulations of seismic wave propagation, it is defined as the ratio between the **Fourier amplitude spectrum** recorded at the outcrop of the numerical model of the study site and the **Fourier amplitude spectrum** recorded at the outcrop of the numerical model of the reference site.
Transfer Function (TF)	Variation of the seismic signal, generated by the ground system (related to the physical-mechanical and geometrical properties of the system itself). The TF is defined as the ratio between the output **Fourier transform** (considering both amplitude and phase spectra) and the input **Fourier transform** (considering both amplitude and phase spectra).

CHAPTER 1

INTRODUCTION

The amplitude of the ground shaking at the site and the destruction caused by earthquakes are greatly influenced by local subsoil conditions (i.e., geology, topography, etc.), as renowned for a long time. Mallet (1862), in his report on the 1857 Naples earthquake, noted that local geological conditions were responsible for the damages. Wood (1908) demonstrated that local soil and geological conditions were related to the intensity of the ground shaking in the 1906 San Francisco earthquake. MacMurdo (1824) after the 1819 earthquake in Cutch, India, pointed out that buildings founded on the rock were not as badly damaged as those built on the soil. Gutenberg (1927) proposed site-dependent amplification factors based on microseismic recordings under various geological conditions.

Only in the last 100 years, the availability of recording instruments has made it possible to quantitatively measure the effects on the local site (Housner, 1952; Trifunac and Brady, 1975; Reiter, 1990). However, the need to predict the local seismic effects in many complex geomorphological conditions has boosted the development of numerical codes for simulating the surface amplification/deamplification effects of the seismic wave propagation under different soil/rock response models. This work aims to analyse through three-dimensional numerical simulations the surface effects induced by the seismic wave propagation in two geological complex study areas: the Arquata del Tronto ridge (central Italy) and the Sarca valley (northern Italy).

1.1. Local Seismic Response

The Local Seismic Response (LSR) is defined as the changes of seismic motion in amplitude, frequency and duration due to the specific lithostratigraphic, morphological conditions, and underground settings of the soil/rock formations of a site.

In the frequency domain, the seismic motion U(f) suffered at a site during an earthquake can be described as the product of three terms:

$$U(f) = S(f) \cdot P(f) \cdot R(f) \quad \text{(Eq. 1.1)}$$

where S(f) describes the motion at the source, P(f) describes the propagation through the Earth's crust from the source to the site, and R(f) describes the site term (Figure 1.1).

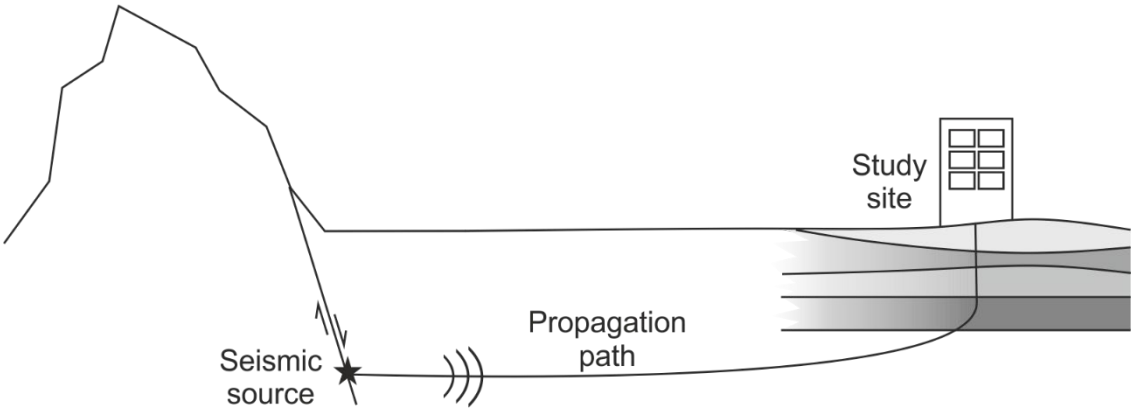


Figure 1.1. Schematic representation of the phenomena that determine the seismic motion at the surface.

The site term refers to many factors that can alter the characteristics of the incoming seismic motion from the bedrock to the surface due to the underlying geological formations. These factors are related to the mechanical properties, subsoil setting of the soil deposits and rock formations, and the morphological features.

The LSR is therefore described by the term R(f), which can be rewritten as follows:

$$R(f) = \frac{U(f)}{S(f) \cdot P(f)} \quad \text{(Eq. 1.2)}$$

that is the ratio between the seismic motion at site U(f) and the seismic motion just due to the source and the propagation path were considered.

This frequency function R(f) which describes the variations in the amplitude spectrum due to site effects, is called the amplification function.

1.2. Content overview

This section provides an overview of the structure and organisation of the work. It outlines the content to guide the reader through the course of the research and its results.

The chapter "Literature review" provides an overview of the relevant literature and identifies the main theories, concepts, and previous research on which this study is based. In this chapter, the methods of numerical simulations of seismic wave propagation commonly used to analyse seismic response are explained in detail.

The chapter “Methodology” describes the research design and the methods of analysis used in the study. First, the main parameters used to represent the seismic response are presented. Then I explain the whole research process, starting with the collection of engineering geological information, the construction of a 3D model, the simulation of wave propagation in 3D and finally the analysis of the results.

The chapter “Case study sites” presents the two sites where the method is applied and provides detailed information on their geographical, geological, tectonic and seismological characteristics. Finally, this chapter also reports on the geophysical and geognostic datasets collected for the definition of the three-dimensional model.

The chapter “Results and discussions” present the outcomes, including the creation of the 3D models, the description of the results of the seismic numerical simulation and the interpretation of the data obtained. The implications of the results of the research questions and the existing literature are discussed. Finally, the main findings, the limitations of the study and suggestions for future research are summarised.

CHAPTER 2

LITERATURE REVIEW

This chapter summarises some research work and provides an overview of the current state of knowledge in the scientific literature on local seismic effects. It is divided into two main parts: the first paragraph explains the observed seismic effects, which are categorised according to different types, while the second illustrates the different numerical simulation techniques of seismic wave propagation and thus the numerically reproduced seismic effects.

2.1. Observed local seismic effects

Ground motion due to an earthquake can be described mainly through three characteristics, i.e. the amplitude, the frequency content and the duration. Changes in these characteristics of seismic motion have been observed due to LRS. This section collects the most important works in the literature that have analysed and quantified the LSR. They are divided into three main categories: 1D, 2D and 3D effects.

1D or stratigraphic effects describe how seismic waves propagate through the vertical stratification and are thus altered. 2D effects include changes in ground motion due to non-horizontal and non-plane-parallel stratigraphic geometries, such as valley geometries and topographic morphologies. A three-dimensional geological reconstruction includes all complex structures that do not show plane symmetry, such as asymmetric morphologies, valley shapes, topographic features, faults or geologic discontinuities, anisotropy and faults. Considering these factors is essential for an accurate estimation of the LSR (Huang et al., 2021; Liviani et al., 2022). The concept of "three-dimensional seismic effects" refers to the variations in seismic motion that lead to deformations that occur on planes perpendicular to

the input stress plane. These deformations can only be accurately identified if all three spatial directions are simulated and taken into account.

2.1.1. Mono-dimensional effects

Stratigraphic or 1D effects refer to a series of changes that occur due to seismic motion near a location with a free horizontal surface and plane-parallel surface stratification with negligible lateral material and horizontal heterogeneity.

This phenomenon occurs when seismic waves interact with geologic structures, resulting in an increasing amplitude of the ground motion. The ancient city of Jericho, built on alluvial soils, suffered increased damage during the 1927 earthquake due to such ground conditions (Feldman & Shapira, 1994).

Consider a two-layer sedimentation sequence: The underlying layer B has a higher seismic S-wave velocity than the overlying layer A. The waves incident at the base of the surface formation propagate through it and strike the free surface, which reflects them completely, only to arrive back at the bedrock interface, where they are partially reflected and partially refracted (Figure 2.1).

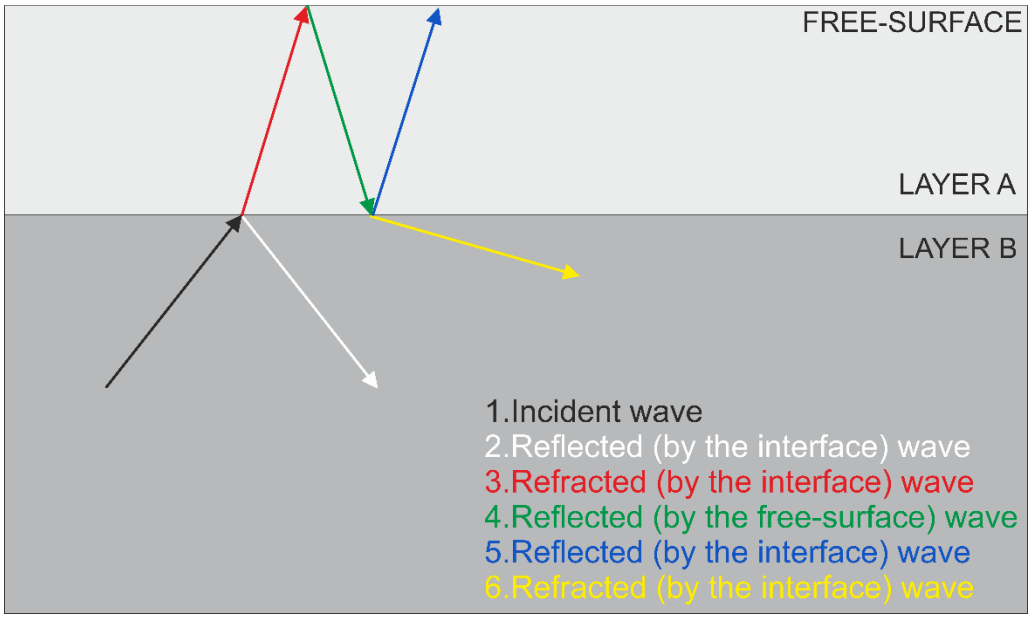


Figure 2.1 Schematic representation of the phenomenon of stratigraphic amplification. The model consists of two layers, with Vs increasing with depth. The figure illustrates the process by which incident seismic waves are reflected and refracted by the two layers.

The higher the impedance contrast between surface layer A and layer B, the greater the amount of reflected energy that remains "trapped" in the deposit (layer A). The seismic impedance contrast I is defined as

$$I = \frac{\rho_B \cdot V_{S,B}}{\rho_A \cdot V_{S,A}} \qquad \text{(Eq. 2.1)}$$

where ρ_A and ρ_B are the densities of layer A and layer B and $V_{S,A}$ and $V_{S,B}$ are the propagation velocities of the shear waves in layers A and B respectively.

With linear elastic behaviour, the confinement of the waves leads to constructive interference and thus to an amplification of the signal (peak of the amplification function) at the natural frequencies

$$f_n = \frac{V_S}{4H(2n+1)} \qquad \text{(Eq. 2.2)}$$

where H is the thickness of the surface layer and n is an integer greater than or equal to zero. Of particular interest is the first natural frequency (with index n=0), the so-called fundamental frequency of the soil (Dobry et al., 1976)

$$f_0 = \frac{V_S}{4H} \qquad \text{(Eq. 2.3)}$$

which normally varies between 0.2 Hz (for very thick or very soft deposits) and 10 Hz (for very thin deposits or fractured and weathered rock). However, this range of values can only be significant if we consider a horizontal topography and no other kind of amplification effect than the stratigraphic one.

This phenomenon is called resonance (Bard & Bouchon, 1985; Bard & Gariel, 1986). The amplification of selected frequencies by the ground creates a double resonance effect that causes different damage to the buildings depending on the natural frequency of the buildings: the closer the amplified ground frequency is to the building the greater the damage.

In the more general case of the non-linear behaviour of the soil, the two cases of a non-deformable or a deformable rocky substrate can be distinguished (Figure 2.2). When the rocky substrate is non-deformable, the natural frequencies of the site remain unchanged compared to the linear case and the amplification function has finite maximum values that decrease with increasing frequency (attenuation phenomena at high frequencies) and are inversely proportional to the damping of the soil.

When the rocky subsurface is deformable and the shear deformation caused by the seismic motion increases, the peaks of the amplification function are reduced and shifted to lower frequencies (Lanzo & Silvestri, 1999).

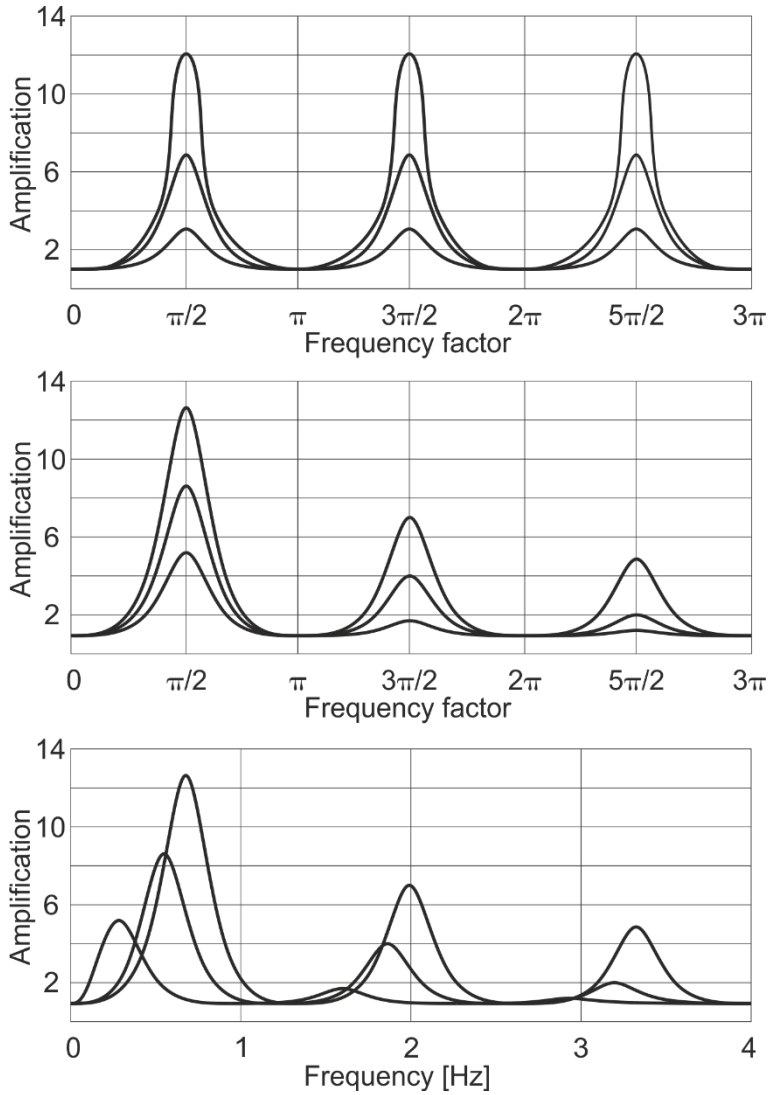


Figure 2.2. Upper panel: Amplification functions in the case of a flat horizontal surface layer with elastic behaviour for three cases of impedance contrast with a non-deformable subsoil. Middle panel: Amplification function in the case of soil with non-elastic behaviour and non-deformable subsoil. Lower panel: Amplification function in the case of a soil with non-elastic behaviour and deformable subsoil.

2.1.2. Bi-dimensional effects

2.1.2.1. Valley effects

In alluvial valleys and tectonic valleys, where the shape of the rock shows a pronounced concavity, the effects of focussing of the waves and the formation of surface waves in the areas near the valley edge are added to the stratigraphic effects.

The phenomenon occurred in some cases where the earthquake damage was localized along the edges of alluvial valleys (Pitarka et al., 1996). Conversely, surface waves that originate at the valley margins and propagate in a horizontal direction (Aki & Larner, 1970; Pitarka et al., 1996; Raptakis et al., 2000) are generated in sediments with relatively low propagation velocities and natural periods between 0.5 and 5 s, leading to an increase in the duration of seismic motion.

The extension of the duration of seismic motion has been observed, often due to trapped waves that are reflected many times within the deposits in the sedimentary basin and interact with each other in a complex way. In the 2011 Tohoku earthquake, the sediment-filled basin beneath the Kanto Plain caused a long-lasting shaking in Tokyo, significantly amplifying the effects of the earthquake (Ghofrani & Atkinson, 2015).

A valley's seismic response, which is filled with alluvial sediments, is strongly influenced by its buried geometry. The shape ratio SR is a parameter defined as the ratio between the maximum depth h of the valley and half of the width l. When the ratio h/l is lower than 0.25 the valley is called shallow, and the predominant seismic amplification is due to the stratigraphic effect described above (Bard & Bouchon, 1985). If the study of the seismic response is carried out in an area far enough from the valley margins, it is possible to analyse it with simple 1D models. For values of SR higher than 0.25, the valley is called deep, and its dynamic response is definitively more complex than 1D case (Bard & Bouchon, 1985; Bard & Gariel, 1986). Deep alluvial valleys are characterised by the interaction among volume and surface waves that are much more complex than those of superficial valleys, as shown in a study by Bard and Gariel (1986). In this study, the results of one- and two-dimensional numerical simulations were compared with simplified geometric models of two alluvial valleys with identical geotechnical properties, one

with a shape factor of 0.1 (shallow valley) and the other with a shape factor of 0.4 (deep valley). In the case of a shallow valley, the 1D model provides results that are in good agreement with those of the 2D model in the centre of the valley, while the differences become more pronounced towards the edges where the interference phenomena between vertical waves and refracted surface waves are pronounced. In the case of a deep valley, the 1D and 2D models give significantly different results in terms of the shape and amplitude of the amplification function both in the centre and at the edges of the valley. Therefore, for large shape factors, it is necessary to use 2D for LSR analyses with numerical simulations. Note that the shape ratio is not an exhaustive parameter, since in the real world, valley edge effects can also occur in contexts where the SR is less than 1. Some researchers (Paolucci, 1999b; Vessia et al., 2011; Faccioli & Vanini, 2003) have proposed to consider the 2D effect for simplified studies through a geometric coefficient for valleys with high SR. From the study, it appears that the SR is one of the most important factors, followed by the seismic input signals and the impedance contrast between rock and soil. It is therefore proposed to consider the downstream effect with a "geometric coefficient" S_G, similar to the "topographic coefficient" S_T already foreseen in the Italian building code.

Moving from 1D analysis to multidimensional analysis of site response, the aggravation factor is the key point that highlights all the differences. According to the statistical analysis of Zhu et al. (2018), in deep basins, the 1D seismic ground motion is aggravated across the entire width of the basin, especially within the spectral period 0.1 s to the 1D fundamental frequency in the centre of the basin and the aggravation factor between 1.3 and 1.8.

2.1.2.2. Topographic effects

Local effects due to the influence of topography have been observed in numerous events, including three major earthquakes in Italy: that is, the 1976 Friuli earthquake (Brambati et al, 1980), the 1980 Irpinia earthquake (Sirovich, 1982), and the 1997 Umbria-Marche earthquake (Sirovich, 1982). These effects have been observed worldwide leading to remarkable amplification of seismic motion, as in the case of the 1964 Alaska earthquake (Idriss & Seed, 1968) and the 1994 Northridge earthquake (Celebi, 1996; Spudich et al, 1996).

The effects of topography on seismic motion vary depending on the type of morphology. Broadly speaking, we can distinguish three categories of morphology: isolated relief, ranges and highland (Stewart et al., 2002).

The causes of variations in seismic motion associated with isolated relief are attributed to two main phenomena (Bard, 1982): the focussing of waves near the relief crest (Figure 2.3) and the interaction and interference of direct waves reflected and refracted by the topography shape.

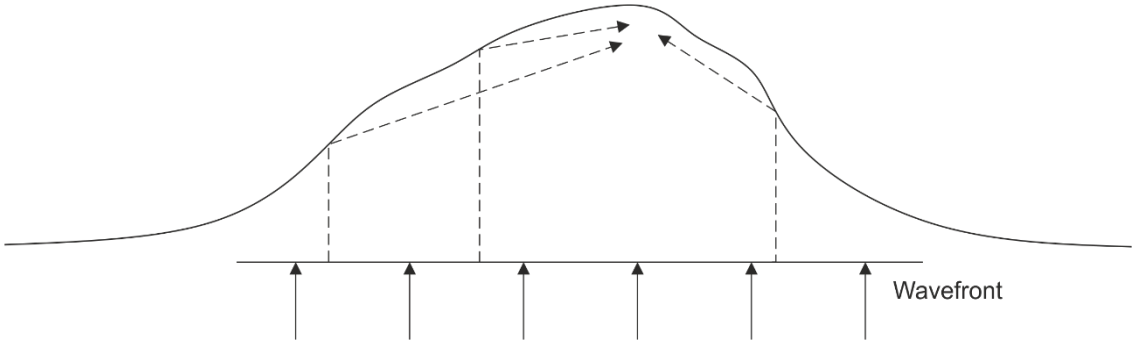


Figure 2.3. Schematic representation of the phenomenon of wave focussing.

The simplest model to quantify the phenomenon was presented by Aki (1988) who sketches the topographical irregularity by an undefined wedge with an apex angle ϕ in the hypothesis of an elastic, homogeneous and isotropic medium. The wedge is subjected to an SH wave that is vertically incident and polarised parallel to the axis of the wedge. The amplification factor A, defined as the ratio between the amplitude of the displacement at the vertex (v) and that of the same point in the case of a flat and horizontal surface (v0), goes back to Sanchez-Sesma (1990) expression:

$$A = \frac{v}{v_0} = \frac{2\pi}{\phi} \qquad \text{(Eq. 2.4)}$$

Figure 2.4 shows that the topographic effect always means an amplification of the seismic motion at the crest. It can also be relevant for relatively mild topographies (for example: for ϕ=2π/3=120° an amplification A=3 results).

A more realistic model was analysed by Geli et al. (1988). By numerically modelling the propagation phenomenon of vertically incident SH waves, the authors obtained the amplification function A corresponding to some points on the crest, sides and base of the relief as a function of the normalised frequency η:

$$\eta = \frac{2L}{\lambda} \qquad \text{(Eq. 2.5)}$$

where L is the half-width of the relief at the base and λ is the wavelength of the incident wave. They find that for a wide frequency band, there is a clear amplification effect at the apex; in particular, the amplification reaches its maximum value when the length of the incident wave λ is equal to half the width L. The phenomenon of amplification (or de-amplification) is frequency-dependent and only limited to a range of frequency values. As shown by numerical modelling and in good agreement with experimental observations, the maximum topographic amplification effects concern a frequency band corresponding to a band of wavelengths comparable to the horizontal dimension of the relief base (Geli et al., 1988; Sanchez-Sesma, 1990; Baron et al., 2022). Wang et al. (2018) state that the amplification factor is correlated to the curvature, which is smoothed over a characteristic length equal to half the wavelength in the rock. The amplification of high-frequency waves correlates with small-scale features, and the amplification of long-period waves correlates with large-scale features in the horizontal dimension.

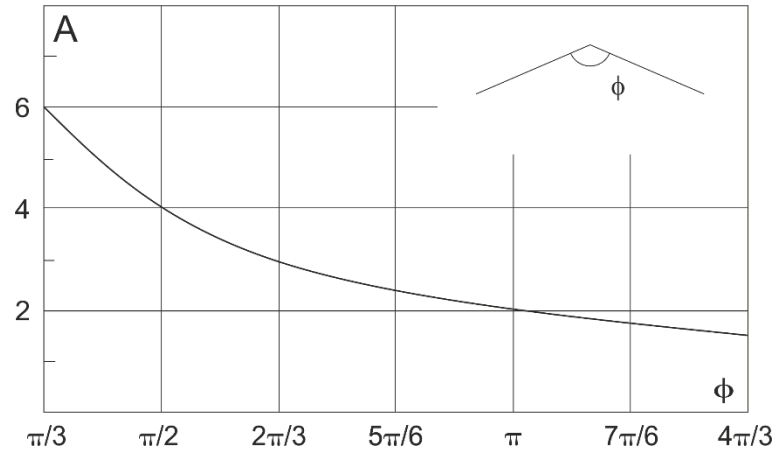


Figure 2.4. Variation of amplification as a function of the apex angle ϕ (Sanchez-Sesma, 1990).

According to the study by Jiang et al. (2023), elevations can be positively correlated with amplification factors if the wavelengths of the incident waves are significantly longer than the dimensions of the local topography. They found that elevation, slope, aspect and frequency are the most important parameters influencing topographic amplification factors. At the sides and base of the relief, the amplification function exhibits a fluctuating trend due to the constructive and destructive interference between incident and refracted waves. The amplification

increases as a function of the H/L shape factor, thus topographic amplification tends to increase as the steepness of the relief increases. The mechanisms of topographic amplification also depend on the angle of incidence (Kawase and Aki, 1990). Especially for SV waves, there may be cases where the presence of topography causes the critical incidence angle to be reached when the parallel component to the surface gets a peak amplitude. The study by Geli et al. (1988) even emphasises that the amplification of the two horizontal components (corresponding to the motion caused by the S-waves) is commonly larger than the vertical component (mainly caused by the P-wave). Moreover, for wave crests that exhibit a 2D shape, the amplification of the motion in the perpendicular direction to the axis of the wave crest is often larger.

Another way to describe the phenomenon is to attribute the amplification of the seismic motion to the resonance of the entire relief. This is, for example, the approach of Paolucci et al. (2002), who studied the case of a two-dimensional profile with an asymmetric triangular shape consisting of a material with elastic, homogeneous and isotropic behaviour with SH and SV incident waves.

The fundamental frequency of the f_{2D} survey is as follows:

$$f_{2D} = f \frac{V_S}{L_1+L_2} \qquad \text{(Eq. 2.6)}$$

where f is a coefficient that depends on the type of incident wave, the Poisson's ratio of the material and the geometric properties of the relief. For the most common values of the shape coefficient H/L, for SH waves, the fundamental frequency of the oscillation can be found with a coefficient f of about 0.7, while for SV waves the frequency is about 30% higher than for SH waves and the coefficient f therefore takes values between 0.7 and 1. Maufroy et al. (2014) present a method in which the curvature of the Earth's surface is used to estimate the amplification due to the topographic effect. It is defined as the second spatial derivative of elevation above mean sea level. To obtain the amplification values at a given frequency, they consider the curvature smoothed over a characteristic length corresponding to half the wavelength of the S-wave (i.e., the frequency-scaled curvature [FSC]), based on the assumption of a correlation between seismic amplification and curvature. FSC estimates of topographic amplification are robust and can be easily obtained from DEM and S-wave velocity values in the area of interest. Lee et al. (2009a) show that large-scale topography can influence the propagation of seismic waves

in nearby areas: for a shallow earthquake, the ridge will significantly scatter the surface waves and reduce the amplitude of motion in the nearby basin. However, as the hypocentre moves deeper, the topography scatters the body waves, which subsequently propagate into the basin as surface waves. These waves continue to interact with the basin and surrounding mountains, eventually leading to complex amplification patterns. Finally, the review article by Zhou et al. (2018), summarises some of the most important assessments of topographic effects on seismic ground motion.

2.1.3. Three-dimensional effects

The most complete approach to evaluating seismic behaviour is to create a three-dimensional model that can take all complex features of both the subsoil setting and the surface shape into account. Thanks to three-dimensional simulations of seismic wave propagation three-dimensional seismic effects can be assessed. These 3D effects occur when the ground motion changes not only in the same but also in a different plane to the input stress. Hence, it is crucial to understand the effects of converting the input from one component to another. As early as 1998, Tumarkin (1998) suggested that a 3D response function, which takes into account the cross-coupling effect between the three components of motion, can provide a better understanding of propagation effects in complex 3D geological structures. Over time, other authors have also dealt with this topic (e.g. Paolucci et al., 1999a) and more recently, Parolai et al. (2023) have used seismic noise recordings to suggest that the effects of cross-coupling play a significant role in site response.
But in general, this transition from one direction to another influences the seismic response in many ways and causes three-dimensional effects.
Primofiore et al. (2020) used numerical 3D simulations to show that the perpendicular direction to the crest has the highest peak values. This behaviour could be related to the amplified vibration of the ridge in the direction perpendicular to its length, as observed by He et al. (2020) and Pischiutta et al. (2010). Massa et al. (2014) not only confirmed that topographic amplification is more pronounced in the component perpendicular to the direction of the prevalent relief extension, but also noted that the direction from the source to the site plays an important role in determining the extent of topographic amplification and that topographic effects in

combination with subsurface heterogeneities can lead to atypical topographic effects. The importance of seismic motion polarisation in identifying site effects was also highlighted by Burjanek et al. (2014), who however also emphasised how topographic effects are related to those due to heterogeneities in the physical properties of the relief-forming materials, which calls into question the feasibility of estimating site effects based only on topography. Pischiutta et al. (2014) analysed the polarisation of the wave fields interpreted as the result of the fractures associated with faults, polarised orthogonally to their dominant direction. Panzera et al. (2017) also found a predominant direction of amplification with an almost perpendicular relationship to the mapped faults and fracture fields. The shear wave splitting results showed that the polarisation of the wave field and the directions of the fast S-waves tend to be orthogonal, i.e. strongly dependent on the anisotropy of the medium. At the same time, when analysing the ambient seismic noise, Pischiutta et al. (2017) found a predominant amplification roughly perpendicular to the central axis of the fault network associated with the Vado di Corno fault (central Apennine - Italy). To verify this, they ruled out the role of topography in controlling the polarisation and amplitude of the waves through numerical simulations. Knowing this behaviour, they propose to use the method to estimate the predominant orientation of fracture networks in subsurface zones within fault zones. Using the same recording method, Pischiutta et al. (2022) investigated the effects of directional amplification of ground motion using three different techniques. They arrived at coherent results highlighting the occurrence of directional amplification and polarisation effects. They found that the polarisation is parallel to the faulting of the active fault system, showing a strong correlation with co-seismic ruptures and active faults. This was interpreted as fault-guided waves, and/or as the intense fluid circulation in the hydrothermal system probably plays a role in the polarization at 90°.

Deformations that occur in planes other than the input stress plane also lead to induced rotations. The torsional component of strong motions is gaining increasing attention (Guidotti et al., 2018) as it is becoming apparent that it can contribute significantly to the overall response of structures to earthquake motions.

The motions produced by earthquakes can be fully described by three translational and three rotational components. In practice, the rotational components are usually neglected and only the three orthogonal components of the translational motion

are considered (Lee et al., 2009b). However, the rotation of objects during seismic events is a phenomenon that has been observed for centuries. For example, Boschi et al. (1995) reported a rotational sign on the Column of Marcus Aurelius in Rome; during the 1783 Calabria earthquake, the rotation of two ornamental obelisks was noted (Ferrari, 2006); during the 2009 L'Aquila earthquake, photographs of rotated tombs were collected (Stewart & Di Capua, 2009); and in Greece, after the 2014 Kefalonia earthquake, many tombstones were found rotated (Papazachos et al., 2014); in Norcia, after the August 2016 earthquake, a church pinnacle was found to have rotated (Penna et al., 2019). These are just a few examples of reports where there is photographic evidence of the rotations.

In addition, numerically averaged rotations can be calculated from pairs of parallel transducers. Some examples show rotations in the range of 10^{-6} to 10^{-3} rad and angular accelerations of 10^{-4} to 10^{-1} rad/sec^2 (Trifunac, 2009).

Today, the phenomenon is interpreted to mean that seismic waves can cause rotational motion due to the asymmetric distribution of forces acting on the objects. Before the advent of seismographs that could record vertical ground motion, the role of ground rotation was extensively debated in the late nineteenth century (see Milne (1893) who examined the limitations of early seismographic instruments). Still torsional motions are often neglected in studies of seismic site effects because these deformations are difficult to measure (Lee et al., 2009a). However, engineers have recognised the importance of rotational ground motions (Castellani et al., 2012) and Lee and Trifunac (1985) have already reproduced synthetic torsional accelerograms. Stupazzini et al. (2009) analysed seismically- induced rotational motions, concentrating on the near-field regions. The authors used 3D numerical simulations to analyse a Mw=6.0 event with a lateral slip mechanism in the Grenoble valley, taking into account the local site characteristics. The analysis showed that the rotational motions strongly depend on the local conditions and topographic features, with a variability of up to one order of magnitude. Maximum ground rotation values of about 1 mrad and rotation rates of 10 mrad/s were predicted. It was also found that phenomena such as the directivity of the source and non-linear ground behaviour significantly influence the rotation amplitudes. Using a similar method, Baron et al. (2022) also evaluated the seismically induced peak rotation rate around the vertical axis in a three-dimensional simulation. The magnitude of the induced torsional motions (~ 0.1 mrad/s) is compatible with those

observed or predicted in corresponding cases in the literature (e.g. Spudich and Fletcher, 2008). Furthermore, they introduce a parameter describing the scaling factor between the site-induced angular velocity around the horizontal axis (i.e. the torsional motion) and the translational acceleration of the vertically incident plane wave and even analyse the motion changes in different frequency bands. In agreement with Baron et al. (2022), Ghayamghamian and Motosaka (2003) also found a relationship between amplification and torsional movement. Due to the torsional behaviour and the coupling of the horizontal motion, the peaks are divided into their resonant frequencies with low amplification values. Taking into account the torsion and the coupling of the horizontal motion in the wave equation, the effects are analysed numerically.

2.2. Numerical simulation methods review

Poursatip et al. (2020) have investigated the essential components required for a realistic simulation of earthquake-induced seismic waves over extensive regions. Building on this work, the following sections review the existing literature on wave discretisation methods, seismic source modelling, material damping laws and domain truncation methods.

2.2.1. Discretization methods

Several methods have been used for the simulation of seismic events, including analytical and semi-analytical methods, numerical methods, and hybrid methods. Analytical methods are limited to simple domains and homogeneous geology, while numerical methods are more versatile but require significant computational power. Hybrid methods combine the strengths of both approaches.

The Finite Difference Method (FDM) is the main discretisation technique used in seismology due to its low computational cost. However, modelling complex surface features or heterogeneous areas with a structured finite difference mesh is not trivial. To obtain sufficient resolution over the entire model, the grid spacing must be adapted to the slowest wave velocity. This small grid spacing must then be used for the entire model, which requires considerable computational effort and high

storage capacity. Newer octree-based FDM techniques (Wang & Petersson, 2019), which rely on a practical change in grid spacing, have attempted to address this shortcoming. Early seismic studies using FDM mostly focussed on two-dimensional models. The simulation of the 1989 Loma Prieta earthquake in the Santa Clara Valley by Frankel and Vidale (1992) is one of the first three-dimensional finite-difference studies. Yomogida and Etgen (1993) developed a three-dimensional approach with staggered grids and a high-order method to reduce numerical scattering and simulated the 1987 Whittier-Narrows earthquake in the Los Angeles basin with a point source model. Aoi and Fujiwara (1999) used discontinuous grids to reduce the computational cost of heterogeneous three-dimensional simulations.

The Finite Element Method (FEM) offers greater flexibility in simulating complex geometric domains, making it a valuable tool for seismic simulations, especially in large basins characterised by heterogeneity and significant topographic features (Poursatip et al, 2020). The non-diagonal nature of the consistent mass matrices in FEM requires an implicit time step, but techniques such as mass lumping or other mass diagonalisation methods are often used to avoid this (Bao et al., 1998; Basu, 2009). For even higher accuracy, the spectral element method can be used, which we will discuss later. One of the earliest applications of the finite element method in wave simulation was the work of Lysmer and Darke (1971), who investigated Love waves in a non-horizontally stratified half-plane resembling an alluvial valley. Archuleta and Frazier (1978) later presented a method to simulate a finite fault in a three-dimensional half-space, while Hisada et alii (1998) used an unstructured mesh in the Osaka basin model to study long-period strong motions during the Kobe earthquake.

The Spectral Element Method (SEM) combines the geometric flexibility of the FEM with the precision of the pseudo-spectral approach. This technique goes back to the work of Orszag (1980) and Patera (1984) in fluid dynamics and was later applied to elastodynamic problems by Gazdag (1981) and Kosloff and Baysal (1982). The main advantage of SEM over FEM is its ability to diagonalise the mass matrix, which allows efficient parallelisation when using explicit solvers. Many researchers have used SEM for the calculation of elastic wave motion, including

Faccioli et al. (1997), Komatitsch and Tromp (1999) (among others). Komatitsch and Vilotte (1998) introduced spectral elements in seismology, while Komatitsch et al. (2001) used unstructured triangular and quadrilateral spectral elements for two-dimensional wave simulations. Komatitsch and Tromp (1999) applied the spectral element method to simulate seismic waves from a moment tensor source in a three-dimensional layer cake model, verifying their results with Bouchon (1981). Furumura and Koketsu (2000) used a parallel 3D pseudo-spectral approach to model the 1995 Kobe earthquake, and Seriani (1997) proposed a powerful iterative solver for the spectral element method in seismic wave modelling. The use of spectral elements in seismology has been extensively researched. Komatitsch et al. (2001) have developed a new approach in which Fekete points are introduced for triangular elements that correspond to quadrature points in quadrilateral elements. This integration allows the creation of a seamless mesh that combines both quadrilateral and triangular elements within a discretized domain. In addition, Casadei et al. (2002) introduced a hybrid finite element/spectral element technique for seismic simulations in complicated geological environments.

The main feature of the discontinuous Galerkin (dG) approach to solving partial differential equations is that the variables do not have to be continuous across element boundaries. In addition, dG methods offer straightforward matrix construction, easy mesh refinement and fitting, simple discretisation of complex domains, localised and highly scalable parallel algorithms and non-uniform high-order local approximations, although this comes with a larger total number of degrees of freedom compared to the finite element method. dG discretisations are known to be more costly but also very accurate. Compared to other discretisation methods, dG methods have lower numerical dispersion, making them well suited for accurate simulation of waves over large areas. Kaser and Dumbser (2006) implemented a dG method for wave simulation in a two-dimensional domain using triangular elements and achieved high accuracy in both space and time. Wilcox et al. (2010) developed a high-order dG method for coupled elastic-acoustic media using an octree-based mesh to adapt the mesh resolution to the local wave velocity.

In the Boundary Element Method (BEM), the radiation boundary condition can be considered exactly if Green's function in closed form is available for the problem under consideration. BEM solutions are often restricted to linear homogeneous domains for which the Green's function is available. BEM approaches can be divided into direct (DBEM) and indirect (IBEM). The DBEM uses a generalised integration by parts to reduce the spatial dimensionality of the problem; the unknowns are displacements and tractions. In contrast, IBEM does not retain the primary variables as unknowns in the integral equation (Poursatip et al., 2020). Some examples of the application of DBEM in seismology are the works of Fishman and Ahmad (1995), Reinoso et al. (1997) (among others). Beskos (1987) reviewed the use of DBEM in elastodynamics for frequency and time domain problems. He presented the integral formulation of two- and three-dimensional problems and also discussed the consideration of various material properties, such as inhomogeneity, anisotropy, viscoelasticity and poroelasticity. Manolis and Beskos (1988) provided the formulation and numerical implementation of the BEM for elastic, time-dependent problems, such as two- and three-dimensional solids, cracked solids, foundations and buried structures.

"Hybrid method" is a vague term that refers to the combination of several techniques to utilise their advantages and develop a more efficient method. Commonly used hybrid methods model the unbounded extent of the medium with an analytical or a specialised numerical technique and use a general numerical method for the finite region of the domain. FDM can be coupled with FEM to take advantage of the speed and simplicity that FDM offers in most parts of the simulation domain, as well as the ease of handling a traction-free boundary condition on irregular surfaces that FEM offers. For example, Moczo et al. (1997) combined FEM for modelling topographic features with FDM for the rest of the domain and investigated the propagation of P and SV waves in a viscoelastic heterogeneous half-space, including topography. Semblat et al. (2005) used a FEM-BEM approach to investigate how different soil layers affect the seismic response at a site. Romero et al (2013) focused on the nonlinear behaviour of structures using a FEM-BEM model in the time domain.

2.2.2. Seismic source modelling

The introduction of the seismic source into the numerical modelling is one of the greatest challenges in the simulation of seismic wave motions. The difficulty is twofold: (i) sometimes the rupture mechanism of the fault is not fully understood and (ii) often no commonly accepted and adopted kinematic seismic source model is available.

Overall, two main approaches can be considered: the seismic source is located outside or inside the computational domain.

-The seismic source is included in the computational domain. This model provides a realistic approach for the simulation of seismic motion due to earthquakes. However, this approach requires a large computational domain as the source is often far away from the area of interest. In this approach, at least two types of source models are possible: (a) a point source, which can be used for the simulation of weak earthquakes (e.g. aftershocks) or faults of negligible size compared to the dimension of the seismic zone, and (b) an extended source model, which is used for the simulation of strong earthquakes (e.g. mainshocks) or faults of considerable size covering a relatively large part of the area of interest.

-The seismic source is located outside the model. In this case, the seismic loading is introduced into the model in the form of effective forces acting either on the truncated boundary of the domain or on another artificial boundary within the domain of interest. Simulations of this type usually cover smaller areas and can be useful for analysing the local effects of earthquakes.

2.2.3. Constitutive material laws

The amplitude of the seismic wave appears to be influenced by the effects of geometric attenuation and anelastic damping. Geometric divergence means a reduction in amplitude due to the distribution of wave energy in larger and larger volumes of rock as the wave propagates away from the source. Inelastic damping, on the other hand, is due to the attenuation caused by frictional forces that convert the energy of the waves into heat. The research field of soil dynamics analyses how a lithology reacts to energy dissipation through inelastic damping and therefore describes the deformation behaviour of a lithology under dynamic and/or

cyclic actions, i.e. which change over time (dynamic) and this variation is periodic (cyclic) (Crespellani & Facciorusso, 2010. Silvestri, 2005).

To obtain a comprehensive overview of the different classifications of material models, it is essential to consider all categories, even those that are not directly relevant to our specific focus. The models used in seismic simulations can be categorised according to three different aspects:

1. Materials are classified into two groups based on the dependence of stress on strain rate: (i) rate-independent models, where stress is only a function of strain but not strain rate, and (ii) rate-dependent models (viscous materials), where stress depends on strain rate.
2. Depending on the relationship between stress and strain, the material models are either (i) linear or (ii) non-linear.
3. In terms of the residual permanent strain after unloading, materials are either: (i) elastic, where they fully recover their original state after unloading, or (ii) plastic, where a permanent strain remains in the material after unloading.

These classifications are then combined: In general, three types of behaviour are obtained that characterise the lithologies, which we will examine below.

2.2.3.1. Elastic linear behaviour

The simplest model to represent soil is the linear elastic model, i.e. a Hooke's spring. This behaviour refers to a material that undergoes a deformation under stress that is proportional to the stress itself. The deformation is completely reversible. This model lacks any damping or energy dissipation mechanism.

2.2.3.2. Viscoelastic behaviour

The widely used model of elastic material is not able to adequately account for the loss of wave energy. Neglecting the gradual loss of wave energy during propagation, known as seismic attenuation, can lead to an overestimation of motion, especially in regions with a high capacity for energy dissipation, such as sediments with soft soils. The attenuation of seismic waves is caused by three phenomena:

-Geometric propagation refers to the reduction in the density of wave energy as it expands in an elastic medium and moves away from the source. This spreads the

total energy over a larger surface in space. If there is no other damping mechanism, the volumetric integral of the kinetic energy and the strain energy remain constant over the entire domain.

-Scattering attenuation is the redistribution of wave energy within the domain due to the reflection and refraction of waves at the material interfaces of heterogeneous media.

-Intrinsic attenuation is the conversion of kinematic energy into heat due to internal friction at grain boundaries and microscopic cracks in the domain particles. In contrast to the other types, this damping therefore reduces the total energy within the domain.

The first two types of attenuation are commonly taken into account in the mathematical wave model. In contrast, it is difficult to include intrinsic attenuation in a model due to the complicated nature of the internal friction of the ground.

The classical approach to simulate intrinsic damping is to use viscoelastic material models. The quality factor Q has received the most attention among all the parameters used to measure the intrinsic damping. This is dimensionless and indicates the proportion of energy loss per cycle:

$$Q = \frac{2\pi W}{\Delta W} \qquad \text{(Eq. 2.7)}$$

where W is the peak elastic energy and ΔW is the hysteresis area, i.e. the amount of energy lost in one loading cycle. The greater the Q the lower the damping.

Mathematically, energy loss occurs when stress and strain are out of phase, which means that the modulus of elasticity and phase velocity are frequency-dependent. Consequently, damping is related to velocity dispersion, and each frequency experiences a different amount of damping.

The high-frequency components of a wavelet move faster in a viscoelastic or dispersive region and experience higher attenuation as they cycle more. Laboratory tests show that the energy loss per cycle is frequency-independent for the frequency range of interest to seismology (Kjartansson, 1979; Assimaki et al., 2012). Thus, the quality factor Q must be frequency-independent.

Bielak et al. (2011) also optimised the viscoelastic simulation by introducing a displacement-based model of internal friction, in contrast to previous studies, which were all based on stress and strain. Their method is memory efficient and is also well suited for the finite element method. Savage et al. (2010) integrated a 3D

damping model with constant Q into their spectral element method for simulating seismic wave motion.

2.2.3.3. Elastic nonlinear behaviour

In the past, the nonlinear behaviour of soil materials was generally neglected in seismic simulations, perhaps because of the considerable complexity that a nonlinear model would entail. Moreover, linear models usually provide satisfactory results (Seylabi et al., 2018). It was also assumed that large deformations and nonlinear behaviour can only occur in regions close to the seismic source. However, observations of strong earthquakes, especially in sediment-filled basins, as noted by Aki (2003), confirm the non-linear behaviour of soil. Hardin and Drnevich (1982) have shown in experiments that the shear modulus of the soil decreases with increasing stress. This in turn leads to a lower shear wave velocity and a higher damping of the soil, which results in a lower amplification of the movement. An example of studying the seismic response with non-linear behaviour of the soil was proposed by Xu et al. (2003). They developed a numerical method using unstructured finite element triangulations, whose applications showed that the inelastic behaviour of the soil causes a reduction in the amplitude of the accelerations, but only a small shift at the low frequencies. Subsequently, Taborda and Bielak (2009) also investigated nonlinear soil conditions and showed that they significantly affect the spatial variability of ground motions. The study by Liu et al. (2022) investigates the seismic response of 3D basins using a nonlinear constitutive model and shows that the amplification effects of ground motions are more pronounced in deeper soil layers. They also indicate that the presence of a soft interlayer increases the short-period component of the response spectrum and shortens the predominant period of the basin. In their recent study, Wang et al. (2023) discuss the importance of considering nonlinearity when implementing a new model for a 3D sedimentary basin. The study shows that the acceleration peaks at the surface can be larger in a nonlinear basin than in a linear basin. In addition, the resonance period of the nonlinear basin becomes larger and the amplification factor of the peak acceleration decreases with increasing intensity of the ground motion. A detailed literature review on soil nonlinearity can be found in Xu et al. (2003).

CHAPTER 3

GROUND MOTION PARAMETERS

The ground motion parameters such as the amplitude, frequency content, and duration of strong ground motions are described by different types of factors; some may represent two or three of these characteristics, while others may describe only one. It is assumed that due to the complexity of ground shaking, it is impossible to find a single parameter that fully captures all the important characteristics of ground motion.

To observe and describe all properties of the seismic signals, fixed parameters must be determined and defined, which will be introduced hereinafter.

3.1. Fourier spectrum

Earthquakes generate complicated loads with motion components that cover a large frequency range. The distribution of the amplitude of the ground motion over different frequencies is described by the frequency content. The motion of an earthquake cannot be fully characterised without considering its frequency content, as this content has a significant influence on the effects of the motion. To decompose a time recording and obtain information about the spectral content of a signal, the mathematical tool called Fourier Transform is used.

According to Fourier's theorem, a general periodic function x(t) with period T can be decomposed into an infinite number of harmonics, the summation of which gives the periodic output function:

$$x(t) = a_0 + \sum_{n=1}^{\infty}[a_n \ cos\ (\omega_n t) + b_n\ sin(\omega_n t)] \qquad \text{(Eq. 3.1)}$$

in which ω_n is the pulsation of the nth harmonic and the constants a_0, a_n and b_n represent the amplitudes of the harmonics, and which can also be written as follows:

$x(t) = a_0 + \sum_{n=1}^{\infty} c_n \ sin\,(\omega_n t + \varphi_n)$ (Eq. 3.2)

Each n[th] harmonic is then associated with a pulsation ω_n, an amplitude c_n and a phase φ_n can be derived.

The accelerogram is represented by a discrete function with a finite number N of frequencies and thus we have the discrete Fourier transform. The Fourier series provides a complete description of the ground motion, as the motion can be fully recovered from the inverse Fourier transform.

The Fourier transform is the operator by which a function of time $x(t)$, with certain properties, can be expressed as a complex function of frequency $X(t)$, defined as:

$X(f) = F[x(t)] = \int_{-\infty}^{+\infty} x(t) \cdot e^{-i2\pi f t} dt$ (Eq. 3.3)

The signal $x(t)$ can again be described as an inverse Fourier transformation of:

$x(t) = F^{-1}[X(f)] = \int_{-\infty}^{+\infty} X(f) \cdot e^{i2\pi f t} df$ (Eq. 3.4)

The signal is decomposed into harmonics and each of them is associated with an amplitude and a phase. The graphical representation of the amplitudes, with the frequency of the harmonics, is known as the Fourier amplitude spectrum. The representation of the phase angles with the frequency is called a Fourier phase spectrum.

The Fourier amplitude spectrum consists of the modulus of the Fourier transform. It expresses the frequency content of a movement very clearly. The frequency corresponding to the largest amplitude is called the fundamental frequency (or period). The diagram with the phase versus frequency shows the Fourier phase spectrum. Since the phase angles are the points in time at which the peaks of the harmonic motions occur, the Fourier phase spectrum influences the change in ground motion over time.

3.2. Transfer and amplification functions

The Fourier transform is used in many scientific fields as it is a fundamental tool for simplifying temporal signals. In the field of seismic analysis, one of the most common applications is the development of the convolution process. The theorem for the convolution of two time signals $x(t)$ and $y(t)$ allows the convolution to be expressed by multiplying the respective Fourier transforms in the frequency domain:

$$F[x(t) * y(t)] = F[x(t)] \cdot F[y(t)] \quad \text{(Eq. 3.5)}$$

This theorem finds application in the treatment of linear time-invariant systems (or LTI systems). By 'system' we mean a physical process that assigns an output signal $x_{out}(t)$ to an input signal $x_{in}(t)$

$$x_{in}(t) \rightarrow [system] \rightarrow x_{out}(t) \quad \text{(Eq. 3.6)}$$

LTI systems form a particular group of systems that possess the properties of linearity and time invariance and can be characterised by their impulsive response, i.e. by the output signal $h(t)$ corresponding to an input signal in the form of the 'Dirac delta' $\delta(t)$ (an impulse of infinitesimal duration and uniform average amplitude)

$$\delta(t) \rightarrow [\text{LTI system}] \rightarrow h(t) \quad \text{(Eq. 3.7)}$$

The output signal of a given LTI system for any input signal $x_{in}(t)$ can be expressed by convolving the latter with the impulse response

$$x_{out}(t) = h(t) * x_{in}(t) \quad \text{(Eq. 3.8)}$$

i.e. using the convolution theorem by multiplying the Fourier spectrum of the input signal by the Fourier spectrum of the impulse response, also called the Transfer Function $H(f)$

$$X_{out}(f) = H(f) \cdot X_{in}(f) \quad \text{(Eq. 3.9)}$$

We denote the quantities in the time domain with lower case letters and the Fourier transform of the corresponding quantities with upper case letters.

In a three-dimensional case study, the function consists of a 3x3 matrix: the time series $h_{ij}(x, t)$ describes the ith spatial component of the time series observed at site x when it is hit by an incident impulsive plane wave that is vertically polarised in the jth direction, with unit amplitude.

We can express the modified ground motion:

$$y(x, t) = [y_1(x, t), y_2(x, t), y_3(x, t)] \quad \text{(Eq. 3.10)}$$

at site x for any vertically incident seismic input:

$$u(t) = [u_1(t), u_2(t), u_3(t)] \quad \text{(Eq. 3.11)}$$

as

$$y_i(x, t) = \Sigma_j h_{ij}(x, t) * u_j(t) \quad \text{(Eq. 3.12)}$$

where * denotes the convolution in time.

The expression is commonly evaluated in the frequency domain by replacing the convolution by multiplication with the convolution theorem:

$$Y_i(x, f) = \Sigma_j H_{ij}(x, f) U_j(f) \quad \text{(Eq. 3.13)}$$

where upper case letters denote the Fourier transforms of the corresponding time series, which are labelled with lower case letters.

In a seismic response study, the transfer function (TF from now on) defines the variation of the seismic signal generated by the ground system and can therefore be directly related to the physical-mechanical and geometrical properties of the system itself. The TF is defined as the ratio between the output Fourier spectrum and the input Fourier spectrum (later it will be better explained how this calculation is carried out). As this is a complex function, we define the TF by considering both the Fourier amplitude spectrum and the Fourier phase spectrum. Therefore, we obtain the resulting quantities as complex numbers. However, if we refer only to the modulus, the Amplification Function $|H(x, f)|$ is defined as

$$|H_{ij}(x, f)| = \frac{|Y_i(x,f)|}{|U_j(f)|} \quad \text{(Eq. 3.14)}$$

Transfer and amplification functions can be calculated based on real ground motion records or by numerical simulations of seismic wave propagation.

For empirical seismic recordings, in order to calculate the so-called Empirical Amplification Function, the spectral ratio between the recordings in the study site and the recordings in the reference site is determined (Diagourtas et al., 2002). Normally, only the Fourier amplitude spectrum and only the horizontal components of the motion are considered, but this depends on the method used. Further information can be found in section 3.1 where the experimental LSR methods are described.

In numerical methods, however, the quantification of the input motion can be solved with two methods: (1) with the original input signal of the simulation or (2) with the signal recorded at the surface of a numerical reference site.

The seismic input ratio entails the problem of doubling at the surface, because the amplitudes of the incident waves are increased by a fixed factor of exactly two when reflections and conversions occur (Sun & McMechan, 2008). Known as free-surface effect, in a half-space model, the spectral ratio between a wave observed at the surface and a wave travelling towards the surface is twice the amplitude, as

there is a superposition of the incident and reflected waves that doubles the amplitude at the surface. In order to correct this inconsistency, the spectral ratios between the surface recordings and the basal input motion must be divided by two.

Another method that avoids these problems is the reference site method. It requires the creation of a numerical reference model and the simulation of a seismic wave propagation analogue to the simulation of the study site model. This method attempts to reproduce the experimentally observed amplifications as faithfully as possible. A reference site must be characterised by a homogeneous, isotropic, unfractured or unweathered rock (with the same properties of the study site bedrock) and a flat surface topography.

As a result of all these distinctions, we thus obtain different types of functions, depending on which method we use and which quantity we place in the denominator of the spectral ratio.
In numerical LRS methods, using the reference site method, we denote the solutions in the frequency domain in both the reference and studied site by $Y_{ij\ ref}$ and Y_{ij} respectively (where i stands for the spatial component of the solution and j for the polarisation of the excited plane wave), so we can express the components of the Response Function of the studied model as the ratios:

$$\begin{aligned} H_{11} &= \frac{Y_{11}}{Y_{11\ ref}} \quad H_{12} = \frac{Y_{12}}{Y_{12\ ref}} \quad H_{13} = \frac{Y_{13}}{Y_{13\ ref}} \\ H_{21} &= \frac{Y_{21}}{Y_{21\ ref}} \quad H_{22} = \frac{Y_{22}}{Y_{22\ ref}} \quad H_{23} = \frac{Y_{23}}{Y_{23\ ref}} \\ H_{31} &= \frac{Y_{31}}{Y_{31\ ref}} \quad H_{32} = \frac{Y_{32}}{Y_{32\ ref}} \quad H_{33} = \frac{Y_{33}}{Y_{33\ ref}} \end{aligned} \qquad \text{(Eq. 3.15)}$$

and, if we denote the solutions using only the Fourier amplitude spectra in the reference and studied site by $|Y_{ij\ ref}|$ and $|Y_{ij}|$ respectively, we can express the components of the Synthetic Amplification Function of the studied model as the ratios:

$$\begin{aligned} |H_{11}| &= \frac{|Y_{11}|}{|Y_{11\ ref}|} \quad |H_{12}| = \frac{|Y_{12}|}{|Y_{12\ ref}|} \quad |H_{13}| = \frac{|Y_{13}|}{|Y_{13\ ref}|} \\ |H_{21}| &= \frac{|Y_{21}|}{|Y_{21\ ref}|} \quad |H_{22}| = \frac{|Y_{22}|}{|Y_{22\ ref}|} \quad |H_{23}| = \frac{|Y_{23}|}{|Y_{23\ ref}|} \\ |H_{31}| &= \frac{|Y_{31}|}{|Y_{31\ ref}|} \quad |H_{32}| = \frac{|Y_{32}|}{|Y_{32\ ref}|} \quad |H_{33}| = \frac{|Y_{33}|}{|Y_{33\ ref}|} \end{aligned} \qquad \text{(Eq. 3.16)}$$

In numerical LRS methods, using the input motion for the spectral ratio, we obtain the “source-dependent response function”:

$$H_{ij}(x,f) = \frac{Y_{ij}(x,f)}{U(f)} \quad \text{(Eq. 3.17)}$$

where Yij (x,f) is the solution in the frequency domain at the study site surface and U(f) is the input motion. For a simulation with the same seismic input in the three spatial components, but recording three different oscillation components at the surface, we obtain

$$\begin{aligned} H_{11} &= \frac{Y_{11}}{U} \quad H_{12} = \frac{Y_{12}}{U} \quad H_{13} = \frac{Y_{13}}{U} \\ H_{21} &= \frac{Y_{21}}{U} \quad H_{22} = \frac{Y_{22}}{U} \quad H_{23} = \frac{Y_{23}}{U} \\ H_{31} &= \frac{Y_{31}}{U} \quad H_{32} = \frac{Y_{32}}{U} \quad H_{33} = \frac{Y_{33}}{U} \end{aligned} \quad \text{(Eq. 3.18)}$$

In the same fashion, we have the “source-dependent amplification function” when we consider only the Fourier amplitude spectra

$$|H_{ij}(x,f)| = \frac{|Y_{ij}(x,f)|}{|U(f)|} \quad \text{(Eq. 3.19)}$$

that, in three-dimensional solutions, becomes:

$$\begin{aligned} |H_{11}| &= \frac{|Y_{11}|}{|U|} \quad |H_{12}| = \frac{|Y_{12}|}{|U|} \quad |H_{13}| = \frac{|Y_{13}|}{|U|} \\ |H_{21}| &= \frac{|Y_{21}|}{|U|} \quad |H_{22}| = \frac{|Y_{22}|}{|U|} \quad |H_{23}| = \frac{|Y_{23}|}{|U|} \\ |H_{31}| &= \frac{|Y_{31}|}{|U|} \quad |H_{32}| = \frac{|Y_{32}|}{|U|} \quad |H_{33}| = \frac{|Y_{33}|}{|U|} \end{aligned} \quad \text{(Eq. 3.20)}$$

3.3. Response spectrum

A type of spectrum frequently used in earthquake practice is the response spectrum, which describes the maximum response of a single- degree- of- freedom (SDOF) system to a given input motion as a function of the natural frequency and the damping ratio of the SDOF system. The values of the response spectrum describe the maximum amplitudes of N oscillators with different periods T_1, T_2, […], T_N, and a damping ξ = 5% which respond to a certain seismic action y(t). The classical representation of the response spectrum is the pseudo-acceleration as a function of the period. The calculation of the response spectrum, expressed in terms of displacement, $S_d(T)[y(t)]$, is based on the simple oscillator equation:

$$\ddot{x} + 2\xi\frac{2\pi}{T}\dot{x} + \frac{4\pi^2}{T^2}x = -\ddot{y} \quad \text{(Eq. 3.21)}$$

which is solved for a series of values T_1, T_2, […], T_N to which we assign the maximum absolute amplitude:

$$S_d(T)[y(t)] = |x(t)| \quad \text{(Eq. 3.22)}$$

The following approximations apply to the response spectra in terms of velocity and acceleration:

$$S_v(T)[y(t)] \approx \frac{2\pi}{T} S_d(T)[y(t)] \quad \text{(Eq. 3.23)}$$

$$S_a(T)[y(t)] \approx \frac{4\pi^2}{T^2} S_d(T)[y(t)] \quad \text{(Eq. 3.24)}$$

The amplitude, the frequency content, and (to a lesser extent) the duration of the input motion influence the spectral values.

The response of structures is of great importance in earthquake engineering and the response spectrum has proven to be an important and useful tool for characterising strong ground motions.

As defined by the Italian "Centro per la Microzonazione Sismica e le sue Applicazioni", the response spectra to be used for the estimation of the seismic response in a base hazard scenario are estimated by convolving the response functions (see previous paragraph) with a compatible seismic input with the Uniform Hazard Spectrum (UHS) calculated for an exceedance probability of 10 in 50 years, as defined in the Italian Seismic Code NTC18 (further details in section 4.3 "Definition of a seismic input").

3.4. Predominant period

One parameter that provides a general representation of the frequency content of a ground motion is the predominant period T_p. It is defined as the period corresponding to the maximum value of the Fourier amplitude spectrum. To avoid the excessive influence of individual peaks in the Fourier amplitude spectrum, the T_p is often determined from a smoothed spectrum.

3.5. Fundamental resonance frequency

The fundamental resonance frequency of a site (f_0) is commonly defined as the lowest frequency of a periodic waveform. In the field of seismic response, Horizontal-to-Vertical spectral ratio (HVSR), both from earthquake records (EHV)

and from seismic noise records (NHV), the fundamental frequency is calculated as the frequency corresponding to the peak of the H/V curve. The f_0 can be well estimated according to the method of Puglia et al. (2011): when a peak is detected, the procedure identifies the corresponding f_0 with greater precision at high frequency (1 decimal digit for frequencies<1 Hz and 2 decimal digits for f>1 Hz). Although the H/V curve can provide an accurate estimate of the f_0, it is not an instrument that can be used to evaluate the amplification value (Parolai, 2012).

3.6. Duration

An earthquake accelerogram usually includes all accelerations from the beginning of the earthquake to the point at which the motion has returned to the level of ambient noise. For engineering purposes, only the part of the accelerogram is of interest.

Over time, there have been various approaches to defining the actual evaluation of the duration of strong motion in an accelerogram. The bracketed duration (Bolt, 1969) is defined as the time between the first and last exceedance of a threshold acceleration (usually 0.05 g). Another definition of duration (Trifunac and Brady, 1975) is based on the time interval between the points at which 5% and 95% of the total energy was recorded. The methods used by other authors to refine the calculation of the exact duration have been investigated but regardless of the approach used, the results generally converge to a very similar outcome (Kramer, 1996).

The duration of the shaking can have a strong influence on the damage caused by earthquakes. Many physical processes, such as the degradation of the stiffness and strength of structures and the build-up of pore water pressure in saturated sands, are sensitive to the number of load or stress reversals that occur during an earthquake.

3.7. PGA, PGV and PGD

The most commonly used measure of the amplitude of an earthquake is the peak ground acceleration (PGA), i.e. the peak horizontal acceleration. More specifically,

it is defined as the geometric mean of the highest absolute value of the acceleration of the two horizontal components.

The largest dynamic forces that occur in certain types of structures (e.g. very stiff structures) are closely related to the PGA. Vertical accelerations are less considered in earthquake engineering, mainly because the safety margins against gravity-induced static vertical forces in structures usually provide sufficient resistance.

Peak ground velocity (PGV) is another useful parameter for characterising the amplitude of ground motion. It is the geometric mean of the highest absolute value of the velocity of the two horizontal components recorded on the topographic surface. As velocity is less sensitive to the higher frequency components of ground motion, PGV describes the amplitude of ground motion at intermediate frequencies more accurately than PGA.

Peak ground displacements (PGD) are generally associated with the low-frequency components of earthquake ground motion. However, they are often difficult to determine accurately due to signal processing errors in the filtering and integration of accelerograms and long-period noise. For this reason, the PGD is less common.

3.8. Amplification factors

The spectral amplification factors (FA) are calculated from the site-specific response spectra (see previous paragraph) for three period bands, according to the Italian guidelines for Seismic Microzonation (SM Working Group, 2015) as the ratio between the average values of the output and input response spectra, over the period band, using:

$$FA = \frac{SA_{out}}{SA_{in}} \qquad \text{(Eq. 3.25)}$$

$$SA = \frac{1}{\Delta T}\int_{T0}^{Tf} RS(T)\, dT \qquad \text{(Eq. 3.26)}$$

where RS is the elastic acceleration response spectrum.

The FAs are calculated for the following three-period intervals: ΔT_1 =0.1-0.5 s; ΔT_2= 0.4-0.8 s; ΔT_3= 0.7-1.1 s, covering the classical period of interest for the

buildings. The 3 amplification factors FA1, FA2 and FA3 are named accordingly. The result of the calculation will always be dimensionless.

3.9. Housner intensity

The Housner Intensity or Response Spectrum Intensity (SI) is a measure introduced by Housner (1959) to capture the potential seismic response of structures, with fundamental periods between 0.1 and 2.5 s. This parameter for the severity of seismic motion is related to the potential damage induced by the shaking since most structures have a fundamental period ranging between 0.1 and 2.5 s. Mathematically, the response spectrum intensity SI(ξ) is defined as the integral of the pseudo-velocity response spectrum (PSV) over the period range. The formal expression is given by:

$$SI(\xi) = \int_{0.1}^{2.5} PSV(\xi, T)\, dT \qquad \text{(Eq. 3.27)}$$

where ξ stands for the structural damping ratio and PSV(ξ,T) denotes the pseudo-velocity response spectrum as a function of the damping ratio ξ and the period T. This integral provides a single parameter that summarises the amplitude and frequency content of the seismic response in the range that is most relevant to the structural behaviour. In dimensional terms, the Housner intensity is a displacement (cm).

3.10. Housner factors

The Housner factor (FH) is calculated by normalising the Housner intensity calculated for the site over the Housner intensity of the reference site:

$$FH = \frac{SI}{SI_0} \qquad \text{(Eq. 3.28)}$$

The result of the calculation will always be dimensionless.

3.11. Torsional motion

The propagation of a vertically incident seismic wave can cause an excitation at the surface that not only oscillates in the horizontal plane but also torsionally, i.e. can cause a rotation around the vertical axis. In this work, we follow the notation proposed by Evans and the International Working Group on Rotational Seismology

(2009) which describe the rotation around the vertical axis (torsional motion) using the rotational rate:

$$\dot{\theta}_z(t) = \frac{1}{2}\left(\frac{dv_y}{dx_x} - \frac{dv_x}{dx_y}\right) \qquad \text{(Eq. 3.29)}$$

In the case of a plane wave, we can derive a proportionality between the rotational motion and the time derivative of the translational displacement (Newmark 1969). If we denote with $\dot{\theta}_z(t)$ the Fourier spectrum of the rotation rate around the vertical axis and with $\ddot{U}(f)$ the acceleration spectrum of the transversely polarised horizontal wave motion (SH waves and Love waves), we can write also:

$$\left|\dot{\theta}_z(t)\right| = \frac{s(f)}{2}\left|\ddot{U}(f)\right| \qquad \text{(Eq. 3.30)}$$

where s(f) denotes the horizontal slowness, that is the inverse of the frequency-dependent apparent horizontal phase velocity of the propagating wave. The scaling factor between the rotational rate and the translational acceleration changes slowly and monotonically with frequency (e.g. Trifunac and Todorovska, 2001).

One parameter that has been used (Smerzini et al., 2009) to describe the torsional motion is the Peak Ground Rotation PGR, which is determined as the highest value of the rotational velocity ($\dot{\theta}_z(t)$) during the time history of the seismic waves.

CHAPTER 4

METHODOLOGY

This chapter outlines the research methodology used in this study and describes the research design and workflow in detail. The methodology applied is described by different phases: 1) the acquisition of geophysical and geognostic data, 2) the integration and organisation of these data to ensure consistent results from different sources, 3) the synthesis of the data to create a unified three-dimensional geophysical model, and 4) the execution of numerical simulations (1D, 2D and 3D) to validate the model and 5) analyse their seismic responses. The aim is to provide an overview of the methodological choices made to ensure the reproducibility and validity of the study.

4.1 Build a 3D model

To perform numerical 3D simulations of seismic waves and to evaluate the LSR, it is necessary to reconstruct a realistic model of the subsurface of the study area. For this purpose, at first, we collected geological-physical data; we then managed and interpreted the information using the Geomodeller software to create a model that was as accurate as possible.

The model is reconstructed by three-dimensional interpolation of the collected data to ensure consistency and continuity in the representation of the subsurface properties. The model is validated through an iterative process in which numerical simulations are compared with experimental recordings to verify the accuracy of the reconstructed subsurface properties. Discrepancies between simulations and observations are analysed to iteratively refine the model and ensure that it accurately and consistently reflects subsurface conditions. This comprehensive approach ensures robust and transparent integration of different data sets, minimises uncertainties and maximises the value of the information gained.

4.1.1. Geophysical investigation methods

The geophysical exploration methods which are used to reconstruct the 3D model, are briefly explained below.

4.1.1.1. Seismic reflection

The seismic reflection method is a technique that is performed on the surface and is used to study the subsurface by analysing the reflection of seismic waves. The main equipment consists of a seismic source, e.g. explosives, mechanical vibrators or air guns in marine areas, and a series of geophones.

The seismic source generates vibrations at the surface that propagate through the ground to depth. When they hit a boundary between layers with different seismic impedances, part of the energy is reflected at the surface, while the other part propagates downward. The reflected signals are recorded by a series of receivers set alongside a measurement line (seismic profile). The source and receiver system are systematically moved along a profile and the test is repeated at several locations to collect a complete set of reflections from the subsurface formations. The collected data is processed to remove noise, correct the travel time of the waves (to compensate for depth variations) and improve the signal-to-noise ratio by overlaying multiple recorded traces (stacking). Finally, the migration corrects all distortions caused by non-vertical wave paths and thus enables the correct reconstruction of the position of the reflectors. The measurements can be performed in 2D, 3D and even 4D configurations (including the time factor for monitoring studies). Seismic reflection provides high-resolution images of subsurface structures at great depths and is widely used in subsurface exploration. Its ability to cover large areas makes it a valuable tool for 3D modelling.

4.1.1.2. Vertical seismic profile

The Vertical Seismic Profile (VSP) method is a technique for investigating the properties of the subsurface by analysing the propagation of seismic waves recorded in a borehole. The main equipment consists of a mechanical seismic vibrator and a single geophone connected to a synchronised trigger. The seismic source is placed at different locations - at the wellhead (zero offset), close to the borehole (near offset) and further away (far offset) along specific directions - to

generate vibrations. A single geophone, which is moved incrementally upwards from the bottom of the borehole, detects both the direct (downward) seismic energy and the reflected (upward) waves from the subsurface formations. The test is repeated at each depth and at each source position, with each vibration lasting approximately 20 seconds. The acquired data is filtered to remove noise and then processed to analyse waveforms, determine propagation velocities and identify tectonic or lithological discontinuities. VSP offers a higher resolution than surface seismic methods as the waves only pass through the subsurface layers once and attenuation is minimised. This method enables the creation of detailed models of subsurface formations and is particularly effective for the characterisation of deep structures.

4.1.1.3. Multichannel Analysis of Surface Waves

The method called Multichannel Analysis of Surface Waves (MASW) is a geophysical technique for studying the properties of the subsurface by analysing the propagation of surface waves, that are Rayleigh waves. The main equipment consists of an array of geophones placed along the surface to detect surface wave signals generated by a seismic source, such as a hammer blow, a mechanical vibrator or an explosive. The seismic source generates surface waves that propagate through the ground. These waves are recorded by several geophones set in array at different positions. By measuring the arrival times and amplitudes of the surface waves at different distances from the source, the data is processed to analyse the wave propagation and separate the different frequency components based on their velocity. From this, the shear wave velocity profile of the subsurface can be derived. MASW is a non-invasive method that provides high-resolution images of near-surface structures. It is particularly effective for site characterisation.

4.1.1.4. Refraction Microtremor

The Refraction Microtremor (ReMi) method is a geophysical technique used to estimate the velocity profile of subsurface shear waves by analysing the propagation of ambient seismic noise, which consists mainly of surface waves such as Rayleigh waves. This passive seismic method is non-invasive and efficient,

making it ideal for urban areas. The setup usually includes an array of geophones (6 to 48 geophones or more), a seismograph and optionally a controlled seismic source. The geophones are set linearly on the surface to detect surface waves generated by ambient noise such as traffic, wind or distant machinery and/or active sources such as hammer blows. The ambient noise is recorded over periods of 15 to 60 seconds or more. The recorded waveforms are used to determine the phase velocities of Rayleigh waves at different frequencies. As Rayleigh waves are dispersive, their velocity varies with frequency and reflects the properties of the subsurface at different depths. The recorded signals are analysed to create a dispersion curve that represents the relationship between wave velocity and frequency. This curve is then used in an inversion procedure to model the shear wave velocity profile of the subsurface. The method provides 1D profiles that can be combined to create 2D images for larger areas.

4.1.1.5. Horizontal-to-Vertical Spectral Ratio

The HVSR (Horizontal-to-Vertical Spectral Ratio) method is a passive seismic technique used to estimate the resonance frequency of the subsurface. It is particularly effective in areas where the bedrock is overlain by unconsolidated sediments with a high seismic impedance contrast. This non-invasive method is cost-effective, efficient and well suited for various applications. The HVSR method uses a single, broadband, three-component seismometer to record seismic environmental noise generated by natural sources (e.g. wind, ocean waves) or human activity (e.g. traffic, industrial vibrations). The seismometer records vibrations along three axes: one vertical and two horizontal (north-south and east-west). As a rule, the measurements are taken over a period of 20 to 30 minutes at a single location. The technique is based on the calculation of the spectral ratio between the horizontal and vertical components of the ambient seismic noise. A clear and well-defined peak (equal or higher than 2) in the HVSR curve indicates a significant seismic impedance contrast.

The method was originally introduced by Yutaka Nakamura (1989). Since then, it has been refined and the SESAME guidelines (SESAME Working Group, 2004) became the internationally recognised standard for its application and interpretation. To ensure the accuracy of the results, these guidelines prescribe the following key criteria:

- Data quality criteria: the ambient seismic noise must be stable and representative of the on site conditions. Measurements should avoid transient signals or noise dominated by local sources (e.g. machinery) that could distort the H/V ratio.
- Criteria for spectral peak values: the HVSR curve must have a clear, well-defined peak value in order to reliably determine the fundamental resonance frequency.
- Stationarity of the signal: The recorded noise must be stationary over the entire measurement period (normally 20–30 minutes). Stationarity is assessed by dividing the recording into smaller time windows and ensuring that the spectral characteristics are consistent across these windows.
- Noise directivity criteria: The ambient noise must be diffuse and isotropic and must not have significant directional distortions that could distort the H/V ratio.
- Validation of the results: The results should be reproducible through multiple measurements at the same location. The consistency of the HVSR curves across different recordings is crucial for the validation of the identified resonance frequency.

4.1.1.6. Generalised Inversion Technique

The Generalised Inversion Technique (GIT) is a geophysical method widely used in seismology to characterise ground motion and estimate subsurface properties. The technique is based on the analysis of seismic waves and ambient noise recorded in a network of seismic stations (from days to years). GIT uses a mathematical inversion to separately estimate the contributions of the seismic source, propagation path and local site effects. This method assumes that the observed spectral amplitude of ground motion at a seismic station can be expressed as a combination of these three terms. The inversion is performed using a system of linear equations derived from the logarithmic spectral amplitudes of multiple events at multiple stations. The inversion can even be performed in two steps following the procedure of Castro et al. (1990): in the first stage, source and attenuation effects are separated without introducing a parametric model for the attenuation, while in the second stage, the site and source functions are refined

using the attenuation-corrected data. This two-stage process helps to resolve the trade-off between source and attenuation parameters.

The technique involves pre-processing the signals to correct for instrument response, remove trends and isolate specific time windows that contain S or P waves. These signal windows are then transformed into the frequency domain using the FFT method and the resulting amplitude spectra are smoothed with running time windows to minimise numerical instabilities. A crucial prerequisite for reliable results is to ensure a sufficient signal-to-noise ratio (SNR), which is usually defined as a ratio of more than 3 for the analysed frequencies.

To avoid ambiguities in connection with the inversion, the amplification at a reference station is usually set to one for all frequencies. If there is no reference station, the average amplification in the entire network can also be set to zero. This normalisation ensures consistent results while preserving the relative relationships between the source, path and location contributions.

The results of the inversion include source spectra, path attenuation curves and site amplification functions for each station. The absolute value of the site functions may be affected by the lack of a perfect reference station, but this limitation does not affect the reliability of the source estimates. An important advantage of GIT is its flexibility in areas where ideal reference stations are not available, as it does not depend on the assumption of a perfect reference site. However, it requires a robust data set with records from multiple events and stations to achieve effective separation of source, path and site contributions.

4.1.2. Integrate experimental data to build a model

In the first phase, the available geological and geophysical data were collected from various sources. The data were selected on the basis of spatial coverage and resolution to ensure a complete representation of the subsurface conditions. The integration of this data required harmonisation work and, where necessary, the resolution of conflicts between overlapping datasets.

An important limitation of this method is the lack of direct data, such as wells and deep boreholes in many locations in the area, which could lead to uncertainties in these zones.

To integrate the results of the geophysical and geognostic investigations into a comprehensive model, a structured methodological approach with critical analysis and data synthesis is required. The data is converted into common units, in particular the Vs parameter. The results are then compared to identify matches and discrepancies, focussing on areas where the data naturally correlate. For matched data, a weighted average criterion is applied: higher weight is given to methods that are considered more reliable due to their resolution, coverage and repeatability. For discordant data, the causes of the discrepancies are analysed, taking into account whether they are due to methodological limitations, different scales of investigation or intrinsic heterogeneities of the subsurface. If significant discrepancies are identified, data that do not fit the comprehensive model are documented and excluded, and these decisions are justified.

In this study, particular emphasis was given to the direct data from boreholes, as they offer the highest reliability. The confidence of the other methods (indirect ones) and the accuracy of their results were then assessed in descending order: seismic reflection sections, vertical seismic profile data, MASW analysis, ReMi analysis, GIT analysis and HVSR analysis. This hierarchy reflects the decreasing degree of resolution, sensitivity to subsurface heterogeneity and robustness of each technique. Although HVSR surveys alone cannot be considered completely reliable in areas with complex geological structures (non-1D), their value increases considerably when combined with data obtained using more robust and proven surveying methods. However, this method is based on the assumption that the seismic effect is 1D and is not able to capture effects related to 2D morphologies, such as valley edge effects. Nevertheless, the combined use of HVSR measurements with in-depth data increases their reliability and enabled HVSR to be used with confidence.

A useful approach is to correlate the peaks of the H/V curves with the depth data: the peak of the resonance frequency is well correlated with the thickness of the sediment z, according to the relationship given by Ibs-von Seht and Wohlenberg (1999):

$$z = a\, f_0^{\,b} \qquad \text{(Eq. 4.1)}$$

where the parameters *a* and *b* are determined empirically by regressing the values of f_0 and *z* at a certain number of sites at a known depth *z*.

The application of these methods requires knowledge of the bedrock depth (or the interface where impedance contrast is present and generates the peak of the noise curve) at a certain number of points for an appropriate sampling range. Several authors have determined the values of the parameters *a* and *b* by regressing the f_0 data obtained from the seismic noise curves and the depth of the subsurface. See for example: Parolai et al. (2002), D'Amico et al. (2008), Delgado et al. (2000), Hinzen et al. (2004), Garcia-Jerez et al. (2006), Motamed et al. (2007), Gosar and Lenart (2010), Luzi et al. (2011), Fairchild et al. (2013), Johnson and Lane (2016), Tün et al. (2016), Bignardi (2017), Molnar et al. (2018), Thabet (2019) and Panzera et al. (2022).

Information on the depth of the subsurface is relatively fragmentary. Reliable data can be obtained from boreholes and certain geophysical surveys able to provide vertical profiles that intersect the bedrock. When HVSR surveys are carried out under suitable conditions (e.g. conforming to Nakamura rules), they can be correlated with depth data from nearby sites.

To test the reliability of the interpolation, the R^2 coefficient is calculated. This is a statistical measure to assess how well the linear interpolation line can explain the variability of the observed data. It is calculated as follows:

$$R^2 = 1 - \frac{SSR}{SST} \quad \text{(Eq. 4.2)}$$

where:

- SSR (Sum of Squares of Residuals) measures the error of the model compared to the observed data.

$$SSR = \sum_{i=1}^{n}(y_i - \hat{y}_i)^2 \quad \text{(Eq. 4.3)}$$

- SST (Total Sum of Squares): measures the total variability of the data compared to its mean value.

$$SST = \sum_{i=1}^{n}(y_i - \bar{y})^2 \quad \text{(Eq. 4.4)}$$

where y_i is the observed values, $\hat{y}_i$ is the values estimated by the model and $\bar{y}$ is the mean of the observed values.

By applying a linear regression to these datasets, the average depth values can be estimated based on the peak values f_0 of the HVSR measurements.

4.1.3. Geomodeller

The creation of 3D geological models of the subsurface is essential for carrying out 3D numerical simulations of seismic wave propagation. Therefore, it is necessary to develop a 3D digital geological model of the study area that integrates the previously collected surface and subsurface data. This process requires the use of advanced automated tools. For this purpose, we chose GeoModeller (Calcagno et al., 2008; Guillen et al., 2004), a software developed by Intrepid Geophysics (https://www.intrepid-geophysics.com/products/geomodeller/, last accessed November 2024) specifically designed to create complex 3D models from numerous different information/data from above and below the ground surface. Although the software is primarily intended for the oil and gas and mining sectors, it is also used in the fields of geothermal energy, hydrogeology, engineering and scientific research. The system is based on classical geological stratigraphic rules constrained by primary geological data such as exposed lithological contacts, dip data and boreholes. It has various interpolation methods and a 3D mesh calculator. It offers options for importing data of various types and exporting the final model or individual data in many different formats.

The geological 3D model for the study area must first be defined in terms of size, location and reference system. In order to constrain the geometry of the various lithofacies, their interfaces and fault traces must be manually implemented. In GeoModeller, the 3D model is built step by step, gradually integrating the available data. At each stage, the implicit surfaces of the lithofacies boundaries are calculated and the intermediate results are checked before further elements are integrated.

In the following sections we describe the process of model validation, in which the morphologies of the lithological boundaries within the GeoModeller software are adjusted through several iterations. This iterative process is continued until the simulated ground motions match the recorded experimental data and a satisfactory agreement between the experimental and numerical curves is achieved. After validation, the 3D model was used as input for numerical simulations to evaluate the local seismic response of the study area.

4.2. Numerical simulations

This chapter presents the numerical methods used in this thesis to simulate the propagation of seismic waves. However, before discussing the procedure, it is important to give an overview of the parameters used in the analysis and the specific settings chosen for the simulations.

4.2.1. Definition of a seismic input

In seismic simulations, the input motion is represented by an impulsive wave, which is characterised by unitary amplitude. The considered frequency range is 0.1 - 20 Hz, which is relevant for engineering applications. The dynamic input (shown in Figure 4.1) is used uniformly in all numerical simulations to ensure a standardised framework for the analysis and comparison of results. The wave is applied as a vertically incident motion in three different directions: as shear stress components along the x- and y-axis (corresponding to the spatial directions NS and EW, respectively) and as normal stress along the z-axis.

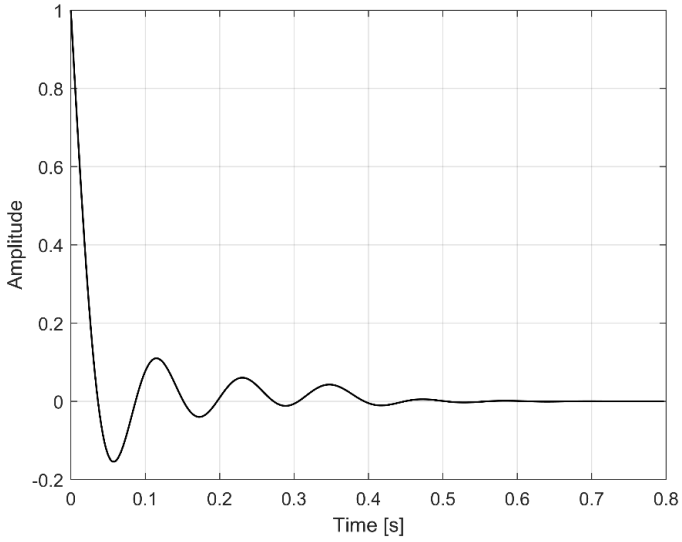


Figure 4.1. Time history of the impulse wave used as seismic input in the numerical simulations.

In this study, we estimate the site-averaged amplification considering a set of earthquake records as seismic input. According to the Italian Building Code (NTC2018), based on the National seismic hazard map (MPS Working Group, 2004, approved with OPCM 3519/2006), the input motion applied to the numerical model on rigid soils (with Vseq > 800 m/s; Cat. A) consists of a set of seven

accelerograms spectral compatible with the target acceleration spectrum of the Italian building code NTC18 (Ministero delle Infrastrutture e dei Trasporti, 2018) in the period range 0.1-1.1 s. A horizontal acceleration is assumed with a probability of more than 10% in 50 years, i.e. for a return period of 475 years. For this purpose, seven acceleration curves were selected using the REXELweb application (Sgobba et al., 2019) according to the seismic hazard of the area.

The seven accelerograms and the corresponding spectra for the municipality of Arquata del Tronto were selected by Luzi et al. (2019) as part of the third-level microzonation study conducted in central Italy (ISPRA, 2017).

For the Sarca Valley study area, conversely, the third level of Macrozonation Studies is not available. Then, according to the MPS04-S1 hazard model, the region is associated with three different computational nodes of the grid (ID 10508, ID 1059 and ID 10731) and has a peak ground acceleration (PGA) between 0.10 g and 0.15 g. The disaggregation analysis resulting for node 10508 (Riva del Garda) identifies magnitudes between 4.0 and 6.5 and distances below 40 km as the most important factors for the seismic hazard of the site named “Disaggregation Pair”. Similar results are also observed for the other nodes (Arco and Nago-Torbole). Some events with slightly larger epicentre distances (up to 60 km) were also considered in the selection to extend the data set. Taking into account the historical seismicity and the seismogenic characteristics of the study area, only events with reverse faulting or strike were considered. In addition, only recordings obtained on seismic bedrock (with Vs > 800 m/s; category A) were considered. The recordings obtained for the Riva del Garda site were not scaled. However, in order to use the same waveforms throughout the study area and to take into account the low variability of the reference hazard, a scaling factor of 0.95 was applied to the seven recordings for the Arco zone and 1.075 for Nago-Torbole.

4.2.2. 1D simulations

Numerical analyses in one dimension (1D) were performed with the commercial code LSR2D by STACEC (https://www.stacec.com/risposta-sismica-locale-lsr-2d_pp92.aspx last accessed November 2024).

Although the software was originally developed for two-dimensional seismic response analyses, it also includes an option for one-dimensional calculations. The

method is based on the finite element approach and allows the evaluation of stresses and strains caused by the propagation of shear waves. The seismic input (as described in the previous chapter) is applied to the subsurface at the base of the model and propagates through the entire spatial domain, which is discretised into square elements of 1 m, arranged vertically in a single column.
The behaviour of soils and rocks is represented using the equivalent linear model, based on shear modulus (G) and damping ratio (D) updated at each time step of the analysis, according to the strain level induced by the seismic input (See Chapter 2.2.3 for more information). The results are calculated in the time domain and output in the form of acceleration over time.

4.2.3. 2D simulations

Two-dimensional (2D) numerical analyses were also carried out using the commercial software LSR2D developed by STACEC. The method is based on the finite element approach, where the seismic input is applied at the base of the subsurface model. All settings are kept consistent with those of the one-dimensional studies. The seismic waves propagate through the two-dimensional spatial domain which is represented by a cross-section vertical plane of the ground discretised into triangular elements adapting to the geometries of the layer boundaries. The maximum element size is 5 m, then it is progressively refined to 2 m in those areas where the layers are thinner and the Vs are lower. This refinement maximises the numerical stability of the solution and avoids unwanted numerical effects associated with the maximum propagation frequency f_{max} of 20 Hz. To avoid numerical aliasing, the following rule for the maximum element size h_{max} is adopted:

$$h_{max} = \frac{Vs_{min}}{6 \div 8\ f_{max}} \qquad \text{(Eq. 4.5)}$$

To represent realistic boundary conditions at the edges, the wave absorption is implemented with "free-field" attenuation conditions. The results are calculated in time domain and visualised as time-dependent accelerations.

4.2.4. 3D simulations

Physics-based numerical modelling of seismic wave propagation in 3D heterogeneous damped media represents a demanding computational task. Several accurate and computationally efficient numerical methods for modelling the earthquake ground motion in 3D heterogeneous media has been developed so far (e.g. Moczo et al., 2014).

The methods used here are of two types (the spectral element method (SEM) and the finite difference method (FDM), see chapter 2.2.1 for more information), as the three-dimensional analyses were carried out with two different software applications. The spatial computational domain consists in both cases of an unstructured hexahedral mesh corresponding to the geometry of the 3D model. Each element is characterised by the mechanical properties of the unit that occupies its position in the 3D geological model. Then, considering the values of the mechanical properties and the dimensions of the elements, the time step stability criterion leads to an accurate solution of the seismic waves up to a specific frequency. In the Results chapter, the maximum observable frequency value is given for each individual case. The finite size of the spatial domain limits the validity of the modelling results for frequencies below 1 Hz.

4.2.4.1. SPECFEM3D

The method used is the spectral element method (SEM), which was first introduced by Seriani and Priolo (1994) for the study of acoustic and elastic waves. In this study, the SEM method is applied to SPECFEM3D Cartesian (https://geodynamics.org/resources/specfem3dcartesian, last accessed November 2024). This implementation involves the discretisation of the spatial domain into hexahedral elements and the expansion of the wave field with Legendre polynomials (Komatitsch and Tromp, 1999). The code implements a viscoelastic damping behaviour that is modelled as a linear, time-invariant and velocity-proportional phenomenon (see chapter 2.2.3 for more information). The quality factor Q quantifies the energy loss per cycle for both shear and bulk loads (leading to the quality factors Qs and Qk, respectively). The damping process is controlled by a series of standard linear Zener solids (Komatitsch and Tromp,

2002). The programme avoids the artefacts of boundary reflection thanks to the use of Perfectly Matched Layers (Xie et al., 2014).

To apply the dynamic input, a point seismic source is simulated. This represents an explosive uniform source that generates isotropic spherical waves. To configure this type of source, the coordinates of the source must be defined and a specific time function assigned (the type of seismic input is described in the previous section 4.2.1). The sources in the simulated models are all located at a depth of more than 10 km. Since the waves propagate radially, the numerical model must have a considerable depth. In particular, the model domain must be sufficiently extended so that the wavefront becomes planar when it reaches the surface. This ensures that the wavefront hits all points of the study area simultaneously. The mesh is optimised depending on the dominant frequency of the input signal. For the deeper layers, which consist entirely of bedrock of Vs=2500m/s, elements with a size of 50 m are used. With increasing proximity to the surface, the mesh becomes finer and finer in order to capture the higher frequency component of the seismic waves.

A set of three numerical analyses are performed with the same model but three different polarisations of the seismic source (NS, EW and vertical oscillation). The data are recorded in a regular network of receivers/stations at the surface. The spacing of the recording points is defined as every two elements of the grid. As the resolution of the surface mesh varies between models, the station spacing varies accordingly. Finally, the code is configured so that the three components of the oscillations are recorded on this grid for each simulation.

4.2.4.2. FLAC3D

This study also uses FLAC3D (https://www.itascacg.com/software/flac3d, last accessed November 2024) with the implementation of the finite difference method (FDM). The code implements both viscous and equivalent linear damping to account for energy loss during wave propagation. Rayleigh damping is used to represent viscoelastic behaviour, while hysteretic damping is used to simulate non-linear behaviour. For Rayleigh damping, both the damping ratio and the natural frequency must be determined for each lithological unit. The damping values are calibrated to match the viscoelastic parameters used in SPECFEM3D, allowing a

comparison of the results between the two codes. In particular, the Qk factor from SPECFEM3D is converted to a damping ratio using the relationship from Siebert (1986):

$$D = 1/2Q \quad \text{(Eq. 4.6)}$$

The natural frequency of the system can be determined by a preliminary dynamic simulation which provides the dominant frequencies of the free oscillations after an initial perturbation.

For the hysteretic damping, the shear modulus reduction curves and the damping ratio are determined. This frequency-independent approach provides a more realistic representation of the non-linear behaviour and avoids the reduction of the time step often associated with viscous damping. The calibration of the hysteretic damping curves, as described by Cundall (2006), is performed using experimental data.

A sigmoidal curve (sig4), hereinafter, was chosen to reproduce the experimental modulus reduction curve, with the parameters detailed in the results.

The grid resolution is optimised based on the dominant wavelength of the seismic waves. Boundary reflection artefacts are minimised using the viscous boundary method developed by Lysmer and Kuhlemeyer (1969), in which independent dashpots in normal and shear directions are used to fully absorb the outgoing waves.

To apply the dynamic input, a planar seismic source was simulated. In contrast with the SPECFEM3D configuration, this latter does not require a deep model domain as the source is applied directly at the base of the model. The input motion was transferred to a compliant (non-rigid) base, which is treated as a continuation of the lithological domain. The compliant base uses quiet (absorbing) boundaries where the velocity time history is converted to the time history of the stress using the following equations:

$$\sigma_n = 2\left(\rho\, C_p\right) v_n \quad \text{(Eq. 4.7)}$$

and

$$\sigma_s = 2\,(\rho\, C_s)\, v_s \quad \text{(Eq. 4.8)}$$

Here, σ_n and σ_s are the normal and shear stresses, ρ is the density, C_p and C_s are the P- and S-wave velocities, and v_n and v_s are the time histories of the normal

and shear velocities used as input. As described in section 4.2.1, an impulsive plane wave was used as input motion.

The dynamic input direction was changed three times in separate simulations: as shear stress in the x and y directions (corresponding to NS and EW polarisation) and as normal stress in the z direction. The data were recorded at surface nodes arranged in a regular grid. The simulation results include the three components of ground motion recorded at these nodes and provide a comprehensive characterisation of the site response for each polarisation.

CHAPTER 5

CASE STUDY SITES

This chapter provides a comprehensive overview of the study area and describes its geological features, tectonic setting and seismological context. In addition, this section provides a comprehensive collection of all available geophysical surveys that have been conducted in the region to provide a comprehensive understanding of subsurface conditions. This part is essential for the further interpretation and analysis of this study.

5.1. Sarca Valley

The study area is located in the lower Sarca Valley in the Provincia Autonoma di Trento, in the Trentino region (northern Italy). This area corresponds to the NNE-SSW orientated section of the Sarca Valley, which extends from the Ceniga Gorge in the north (between the villages of Ceniga and Massone) to Garda Lake in the south. The valley plain in this section has a length of about 5–6 kilometres and a width of about 3–4 kilometres. The sedimentary plain is surrounded by a complex orography in which steep slopes alternate with minor slopes interrupted by smaller valleys and depressions. The most important of these valleys are the Tenno Valley, which enters from the right side of the main basin in a NNW-SSE direction, and the Loppio Valley, which enters from the opposite side in a roughly E-W direction and connects the Sarca Valley with the Adige Valley. Both valleys, the second even more pronounced, are suspended valleys, a legacy of the action of ancient glacial tongues that covered and shaped a large part of the area (Castellarin et al., 2005). In addition, the ridge of Brione mount adds to the complexity of the orographic framework, which extends along the length of the lake for about 2–2.5 km to the NNE, dividing the main valley into two sections of different widths. The most densely populated areas are located near the lake and on the right side of the valley. The municipalities in the valley plain where fluvial sediments are present

include Arco, Riva del Garda and Nago-Torbole. However, if we also include the neighbouring areas in the analysis, the municipalities of Tenno, Ledro and Mori are also part of the study area.



Figure 5.1. Extract from digital orthophotos. Provided by the Italian National Geoportal and acquired by the Agency for Agricultural Supply with a digital camera with 50-centimetre pixels. Resolution 1:10,000. Published in 2012, acquired in 2011.

5.1.1. Geological-structural settings

This valley has a structure characterised by steep rocky slopes dominated by Mesozoic to Cenozoic lithologies (Castellarin et al., 2005) (Fig. 5.2). A clear difference between the western and eastern parts of the area can be seen in the Lower and Middle Jurassic rock units (Castellarin et al., 2005; 2006). West of Riva del Garda, the platform units (Corna Limestone) and the basin deposits (Tofino Formation) belong to the so-called Bacino Lombardo. To the east of Riva del Garda, the grey limestone rocks of the Piattaforma Veneta were deposited during the Lower Jurassic. At the southern end of the Sarca Valley, between Arco and Riva del Garda, younger rock units can be found. These are mainly micritic limestones from the Cretaceous (Maiolica and Scaglia Rossa) and carbonates from the Eocene (Malcesine and Nago limestones) (Castellarin et al., 2005). The most recent rock units are sandstones from the late Oligocene and lower Miocene (Monte Brione formation), which form the summit of Brione mount.

Structurally, the study area is located in the central sector of the Southern Alps, at the intersection of the Giudicarie thrust system, which is orientated NNE-SSW, and the Schio-Vicenza thrust system, which is orientated NW-SE (Castellarin and Cantelli, 2000; Venzo et al., 1977). The described rock sequence was controlled by compressional tectonic events, caused by the above-mentioned tectonic structures, which determined the pelagic deep-sea area of the Bacino Lombardo in the west to overlap with the ancient sublittoral margin of the Piattaforma Veneta in the east.

The tectonic lineament where these two areas meet and overlap lies exactly on the western edge of the lower Sarca Valley and is known as the Ballino-Garda Line. It runs north-south to Ballino, then turns towards Riva del Garda and continues in a NNE-SSW direction along the Brescia shore (Simoni et al., 2001). In addition to the Ballino-Garda Line, the Composite Seismogenic Source of the Giudicarie (ITHACA Working Group, 2019) comprises several related faults, of which the Mount Lomasone Fault and the Sarca Line are particularly noteworthy. All three tectonic lineaments exhibit reverse kinematics and are no longer active. Subsequently, strike-slip faults developed, including one of the most important structures in the valley: the Cima Nanzone Fault, which shows a leftward displacement.

These examples represent only some of the tectonic lineaments in this area, as numerous smaller faults are also associated with this system (Fig. 5.3).

The regional structural conditions have a considerable influence on the morphology of the valley bedrock, which is highly asymmetrical. The Giudicarie fault system has acted as a regional transfer zone since the Late Cretaceous, creating a well-developed NNE-SSW oriented fold and thrust belt with distinct morphological features (Picotti et al., 1995; Castellarin et al., 2006). In the study area, this is particularly evident in the orientation of the valley (NNE-SSW), the gently dipping strata on the eastern side of the valley and the asymmetrical shape of the buried valley floor (Fig. 5.2; Felber et al., 1998). In addition to the surface geology, velocity anomalies in the upper crust have been identified and correlated with these main fault systems in terms of shape, orientation and thickness (Viganò et al., 2013). The formation of the valley is therefore closely linked to Alpine tectonics, with neotectonic uplift and post-collisional compression having deepened this depression, which became the natural basin for the subsequent sedimentation processes. During the Messinian salinity crisis, the Mediterranean Sea dried up due to the closure of the Strait of Gibraltar. This phenomenon led to a lowering of the sea level, which caused the pre-alpine rivers to dig deep river canyons to reach the new ground level. This contributed to the formation of a steep, deeply incised valley, a precursor of today's morphology. During the Pleistocene, glaciations played a decisive role in shaping the valley: during the last glaciation (Würm), the glaciers occupied the Sarca Valley and advanced into the area where Garda Lake is located today. The Garda glacier extended over a length of more than 60 kilometres with an ice tongue that cut deep into the valley, widening it and leaving behind a deeply incised bedrock and heterogeneous glacial sediments. As the glacier retreated, lakes formed, enclosed by the moraines left behind by the retreating ice. When the late-glacial lake dried up, the Sarca River became the most important geomorphological factor. It meandered through the valley and transported large amounts of sedimentary material from the surrounding slopes and the higher areas upstream. During that time, the river flowed through the western part of Brione mount. The eastern part remained largely unaffected by the erosion and sedimentation processes described above. Only in the Holocene did the river change its course, probably due to tectonic causes, so that the eastern part was only affected by the more recent geomorphological events. The

abundance of sediments was increased by landslides (e.g. the Marocche of Dro), in which large accumulations of debris blocked the course of the river and formed temporary lake basins, and by erosion, which was accentuated by Neolithic deforestation and other human interventions in more recent times.

The sedimentary valley of the lower Sarca thus has a complex evolutionary history, and the entire sedimentary fill of the valley, from bedrock to surface, consists of a combined sequence of glacial, lacustrine, fluvial and colluvial deposits. Starting from the deepest layer (Brogiolo, 2013), the sequence includes:

- Glacial deposits: Sedimentary material (gravels and sands) that accumulated on the valley floor during the movement of the glacier. They represent the valley floor during the last glacial maximum and have a thickness of around 40 metres.
- Late glacial lacustrine deposits: A layer of silt and clay rich in plant remains, indicating a lake formed during the retreat of the glacier. The thickness of this layer often exceeds 50 metres.
- Fluvial deposits: River gravels and sands that indicate the erosion and depositional activity of the Sarca River. The thickness exceeds 100 metres, indicating long periods of fluvial deposition alternating with erosion phases.
- Younger deposits: The uppermost layers consist of mixed sediments of fluvial, lacustrine and colluvial origin, derived from both natural and anthropogenic activities during the Holocene.

These data indicate that the overall thickness results from complex layering and tells a dynamic geological story. The considerable thickness reflects intense transport and sedimentation activities associated with paleoenvironmental and climatic changes.

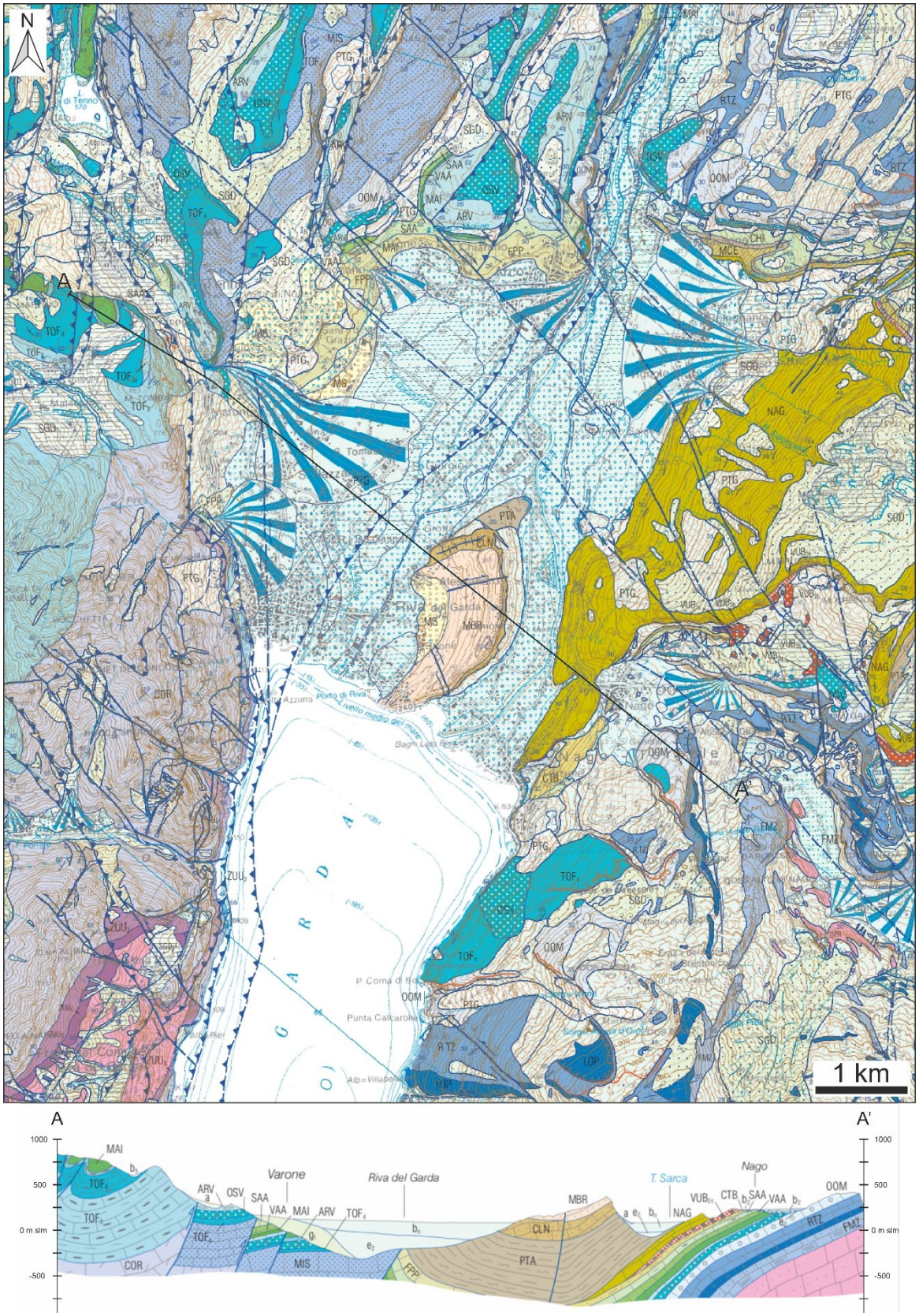


Figure 5.2. Extract from the Geological Map of Italy, sheet 080 “Riva del Garda”, produced at a scale of 1:50,000 by the Geological Survey of the Provincia Autonoma di Trento, with the original geological section attached.

5.1.2. Seismological settings

As far as seismicity is concerned, southern Trentino is seismically active (Fig. 5.3). A comprehensive overview of historical and instrumental seismicity can be found in Guidoboni et al. (2018) and Viganò et al. (2015). This is due to the current deformation of the upper crust in the Giudicarie seismotectonic area (hypocenters at 0–15 km depth), where compression is still active today and moderate earthquakes occur (Viganò et al., 2008; 2015). The Giudicarie fault zone, located between the Po Valley and the inner Alpine chain, is seismically active only along its southern part (Garda Lake area), and is part of the Southern Alpine Giudicarie thrust system. This front is a S-SE verging external arc, a ramp of the southernmost compressional fault system in the Alps.

The seismicity is intermediate: historical and instrumental catalogues (Boschi et al., 2000; Rovida et al., 2016; Pondrelli et al., 2006; Guidoboni et al., 2018) show a scattered but significant distribution of seismicity along the strike in the central sector of this region. A destructive earthquake occurred south-east of this source on 3 January 1117 (Mw 6.6, Veronese) (Magri and Molin, 1986; Guidoboni and Comastri, 2005). A key earthquake occurred on 30 October 1901 (Mw 5.7, Salò), which was followed about a century later by another event on 24 November 2004 (Mw 5.2) in practically the same area.

A moderate earthquake documented in the Italian macroseismic database (Locati et al., 2022) affected Riva del Garda and its surroundings (13 December 1976, ML 4.3, Ledro) and caused macroseismic effects with an intensity of up to VII on the Mercalli scale in the municipalities of the study area. Using a new localisation approach proposed by Viganò et al. (2021), this seismic event could be linked to the same source responsible for a seismic swarm in 2015 (maximum ML 4.1). Based on the most recent records of seismic events from the instrumental monitoring networks of the Provincia Autonoma di Trento (Garbin et al., 2018), the area from Garda Lake to the Lessini Mountains is one of the most seismically active regions in the central Southern Alps, confirming the information on seismic hazard (Figure 5.3).

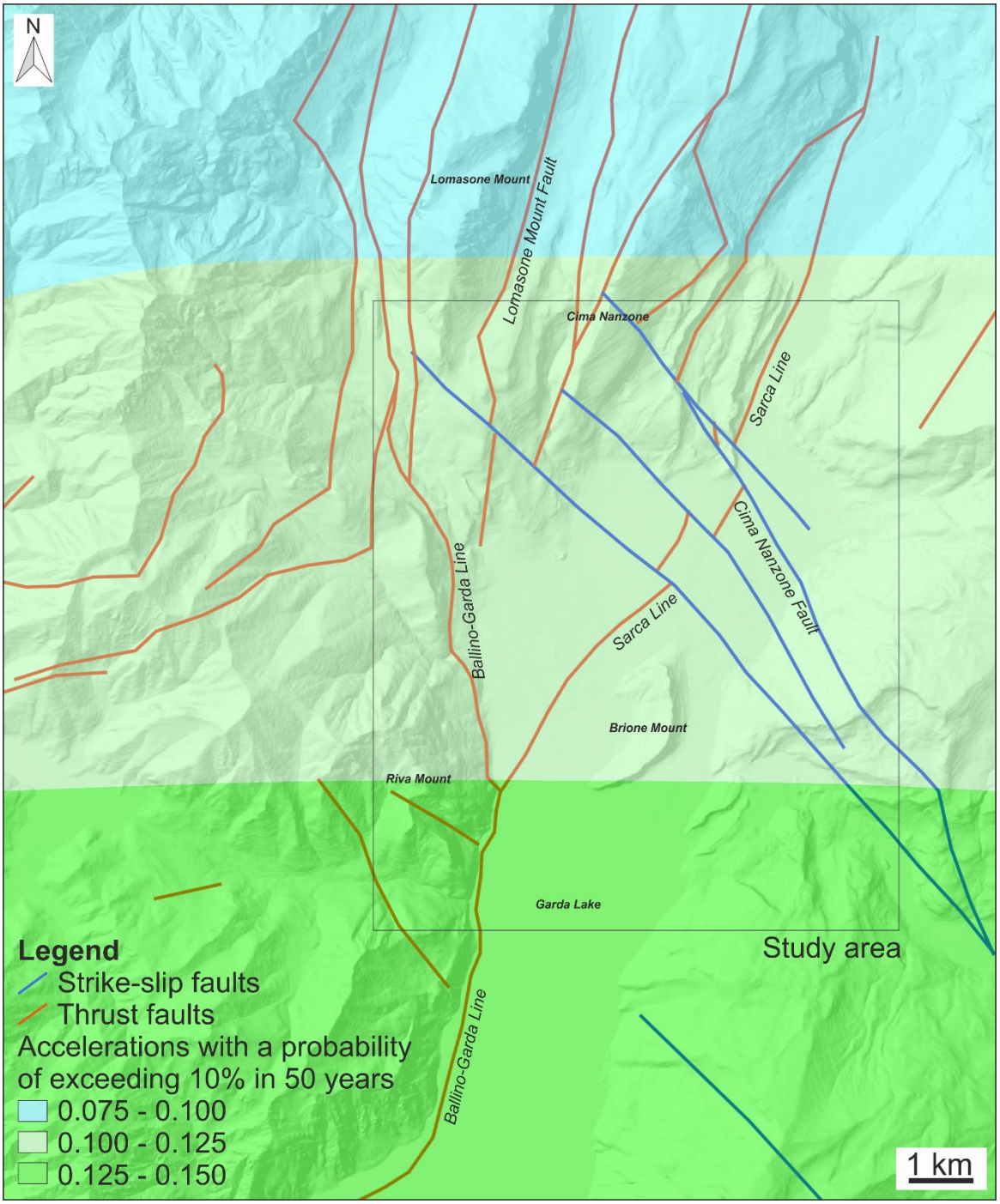


Figure 5.3. Seismo-tectonic features of the area. Data from different sources were combined. The faults are provided by the Database of Individual Seismogenic Sources (DISS Working Group, 2021) and the Catalogue of "ITaly HAzard from CApable faulting" (ITHACA Working Group, 2019). The shaded background colours are provided from the Italian Seismic Hazard Map (Meletti et al., 2006) and indicate the PGA shaking value (expressed in g) to be expected with a probability of exceedance of 10 % in 50 years on rigid (Vseq > 800 m/s) and flat ground.

5.1.3. Geophysical data collection

A comprehensive series of geological and geophysical investigations were carried out in the Valle del Sarca study area. These investigations (including borehole data, seismic surveys, gravimetric measurements and others) allowed a detailed characterisation of the subsurface conditions.

5.1.3.1. Boreholes

The study area is characterised by the presence of numerous boreholes and drillings, which provide a unique opportunity to obtain direct observations of the subsurface geological formations. Boreholes are drilled for various purposes, e.g. as water wells, geotechnical survey boreholes, hydrocarbon exploration drillings, and others. In general, they are vertical or sub-vertical excavations that penetrate the ground and allow the extraction of cores and the study of the lithologies and structures of the subsoil in order to obtain direct data on the morphology of the strata and other important geological features.

Among the boreholes available in the study area, two are particularly noteworthy due to their great depth (Figs. 5.4 and 5.5). However, due to their close proximity, their usefulness for regional subsurface characterisation is limited to a single data point. In addition, there are two other boreholes with sufficient depth to penetrate the deeper geological bedrock (Figs. 5.4 and 5.5).

Two geognostic boreholes were drilled by the Geological Survey of the PAT. The first, a destructive borehole drilled in 1996 (borehole B in Figure 5.4), reached bedrock at a depth of approximately 223 metres. The second borehole was drilled shortly afterwards: This was a water extraction well (borehole A in Figure 5.4) drilled in 1997. It is located close to the first borehole and indicates a bedrock depth of 272.5 metres. The information on well C was kindly provided to us by a private citizen who had built the well for the purpose of collecting water. Well D was realised by Fuganti (2008) for a study on the origin of the natural mineral water spring of Linfano. This last well is located directly at the foot of the rocky slope of Brione mount and is therefore affected by debris and gravitational deposits.

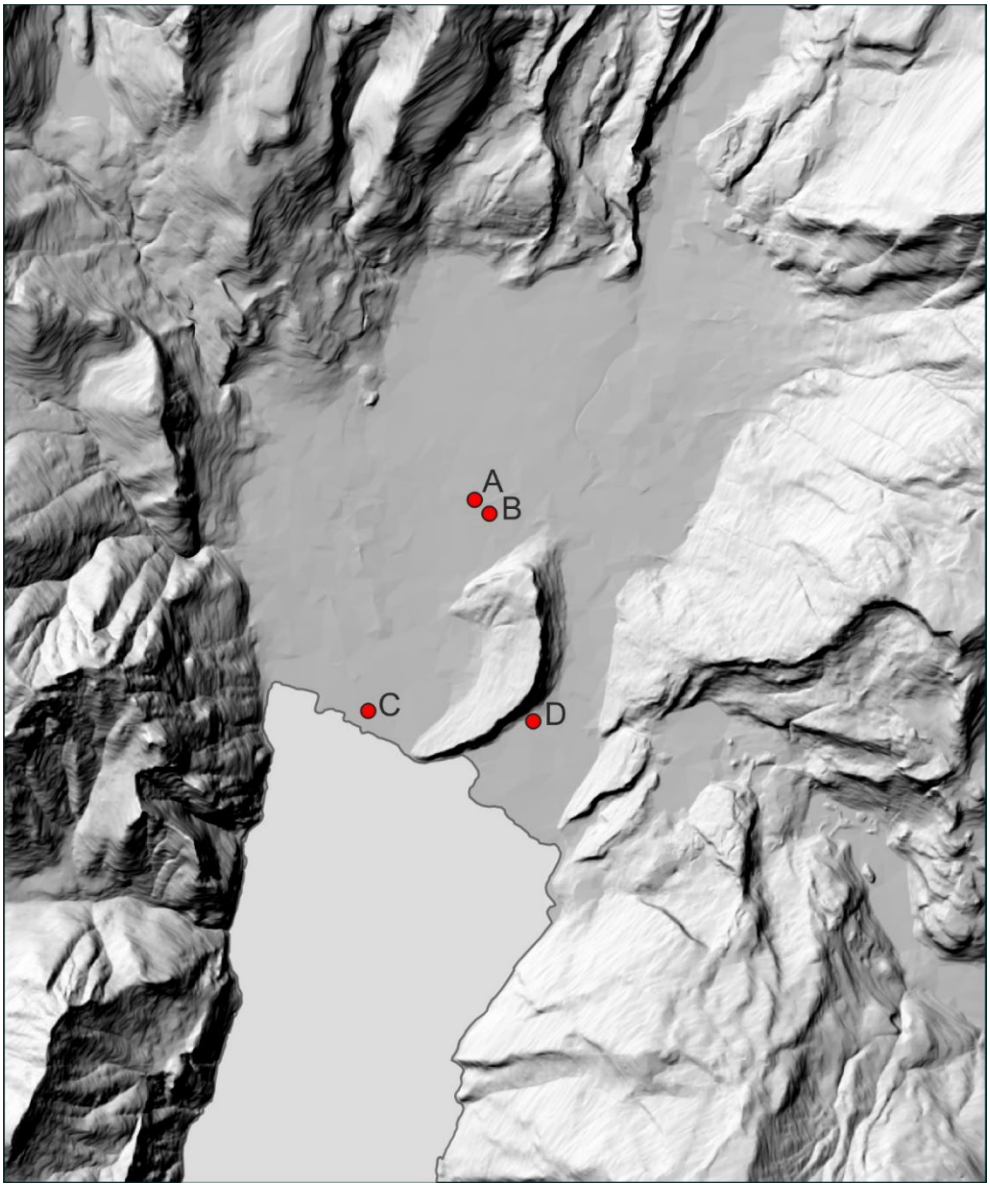


Figure 5.4. Location map of the 4 deepest boreholes of the valley.

In addition, since 1993, the PAT Geological Survey has codified and computerised the data from drillings carried out on behalf of the PAT, both its own and those of external companies and private citizens. They were carried out by private citizens, companies or by the public administration, for various reasons, e.g. for preventive investigations for a construction project or to extract water from the aquifer. The drilling catalogue documents around 190 boreholes of varying depths, from a few metres to a maximum depth of around 100 m. Although not all of these boreholes reach the bedrock, they provide valuable information on the shallower stratigraphic intervals and thus contribute to a more comprehensive understanding of the near-surface geology.

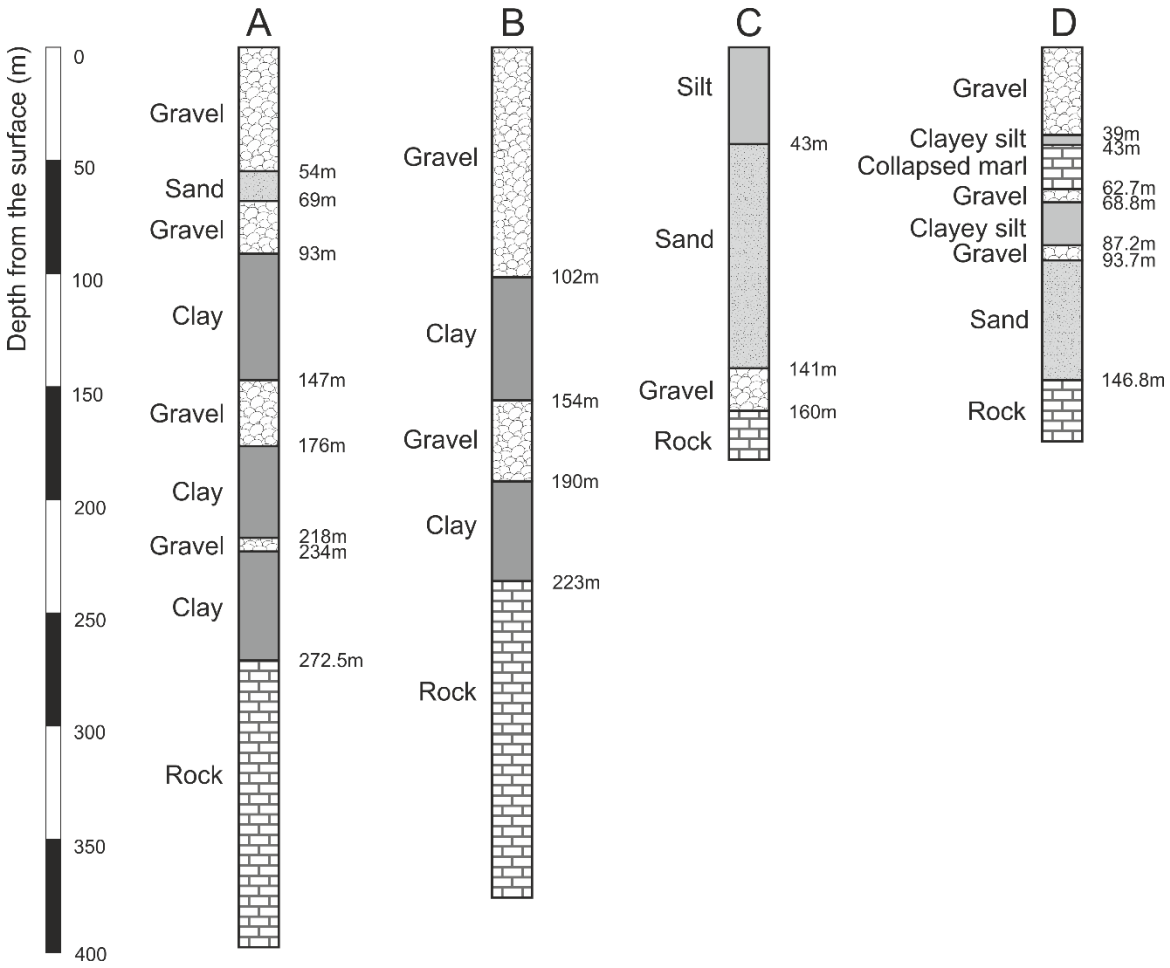


Figure 5.5. Synthetic schematic representation of the stratigraphy found in the four deep boreholes in the study area.

The data can be inspected and downloaded from the Portale Geocartografico Trentino at the site https://webgis.provincia.tn.it/. The spatial distribution of these boreholes is shown in Figure 5.6 and a detailed summary of the associated data can be found in Appendix.

However, even if boreholes provide indisputable and concrete evidence of the geological features at the point of penetration, their main limitation is that they provide a localised, point-by-point representation of the subsurface. This means that the lateral continuity of the observed stratigraphic sequences and the stability of layer thicknesses and properties in the surrounding area cannot be fully guaranteed. Consequently, the information obtained from a single borehole cannot always be extrapolated to a larger area without introducing a degree of uncertainty.

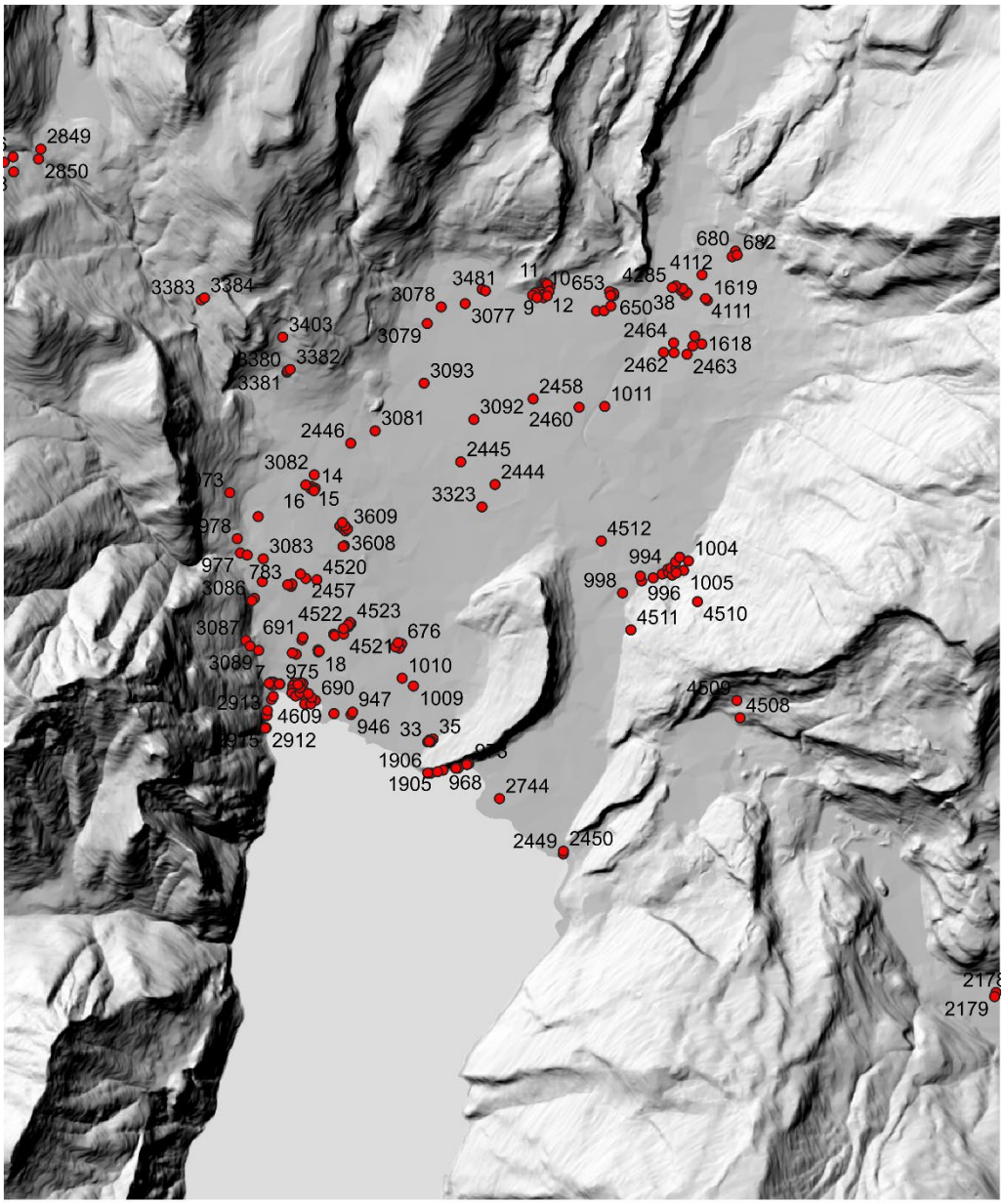


Figure 5.6. Spatial distribution of the wells collected by PAT Geological Survey.

This limitation emphasises the need to integrate borehole data with other direct and indirect investigations in order to develop a reliable and comprehensive model of the subsurface. Although boreholes primarily define geological features rather than seismic stratigraphic properties, they are essential for constraining nearby geophysical surveys. They provide a robust framework for correlating physical and geophysical properties and greatly improve the reliability and resolution of geophysical models. Consequently, boreholes serve as crucial calibration points that allow the integration of indirect geophysical data with concrete geological evidence.

5.1.3.2. Seismic reflection sections

The seismic profile (Figure 5.7), which is oriented approximately perpendicular to the valley axis NW-SE, was realised in 1996 in two parts with a total length of 2280 m (Felber et al., 1998).

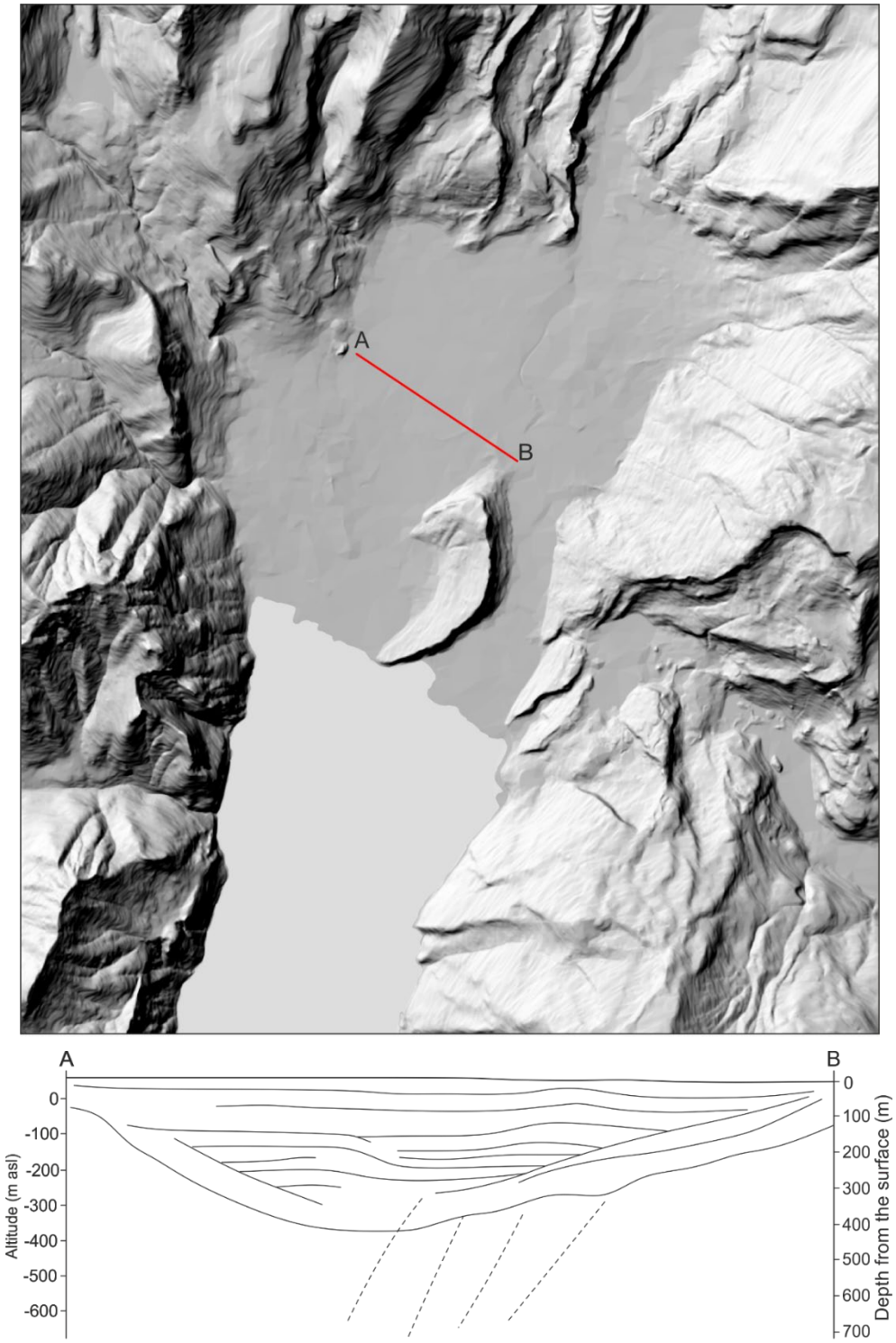


Figure 5.7. Above: seismic section trace. Below: synthetic representation of the interfaces identified by seismic reflection investigation. From Felber et al. (1998).

In the section, the author points out the discontinuity between the rock substrate and the sediment fill at a depth of about 380-420 m from the surface, at the deepest point of the valley. The discontinuity is not clearly marked, but rather represents a band zone. Another important discontinuity was found at a depth of about 280 m from the surface, measured at the deepest point of the valley.

5.1.3.3. Vertical seismic profile

A vertical seismic profile survey (VSP) was carried out on behalf of the PAT (Corubolo et al., 2013). The survey was carried out in the aforementioned 'Arco borehole' (site A in Figure 5.4), whose strategic location allowed a better interpretation of the data obtained, as it is located in an area with extensive existing stratigraphic and geophysical information from neighbouring surveys. This context facilitated stratigraphic and geophysical correlations, which improved the quality of the subsurface characterisation.

The results of the VSP survey provided a detailed seismic description of the subsurface (Figure 5.8).

In particular, several seismic units were identified: (i) a near-surface layer with a thickness of about 150 m, characterised by relatively low velocities (VP of 1900 m/s on average) and indicative of poorly consolidated deposits; (ii) an intermediate layer with a thickness of about 120 m and higher velocities (VP of 2500 m/s on average) corresponding to very dense sediments that fulfil the criteria typically associated with seismic bedrock; and (iii) a bedrock with even higher seismic velocities attributable to lithified rock formations such as marls or limestones. These results certainly come from the seismic survey, but the advantage is that they can be assigned to the borehole stratigraphy and also to the seismic reflection section A-B shown in the previous paragraph.

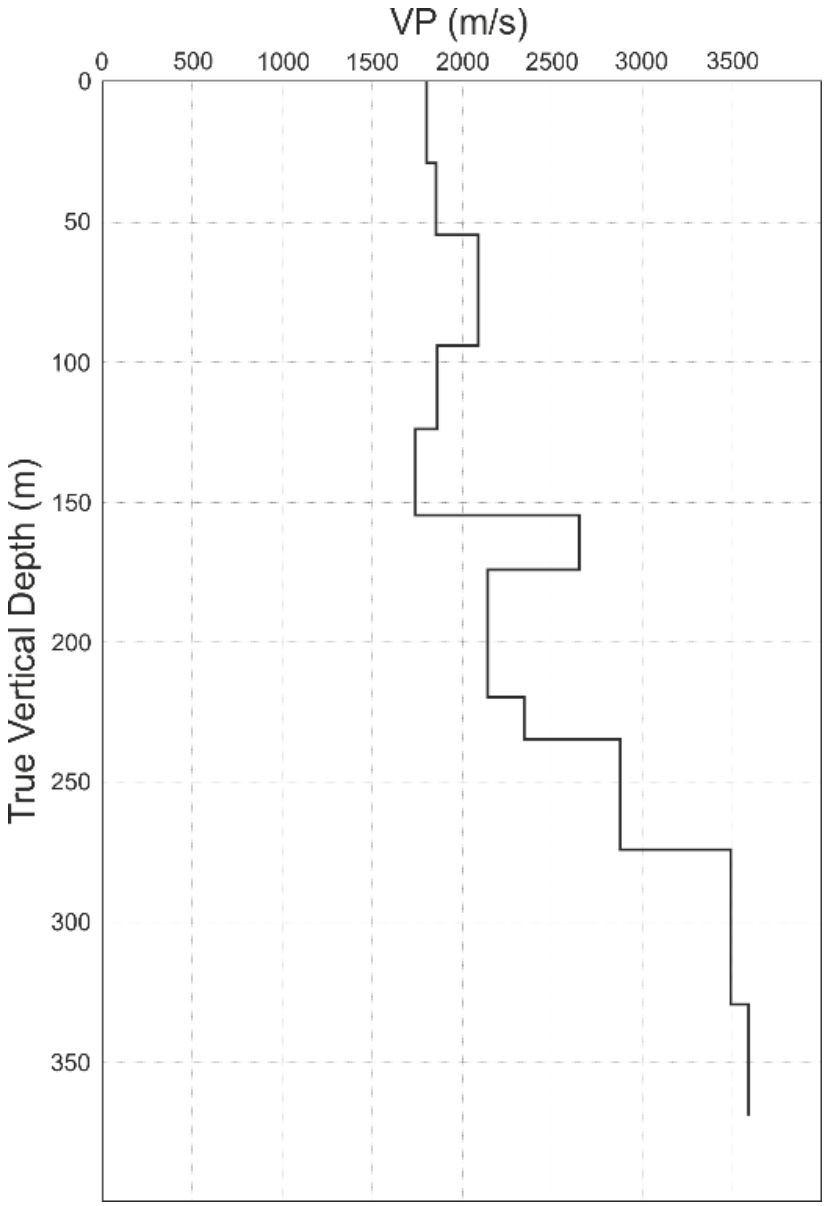


Figure 5.8. Vp profile on the vertical of the Arco borehole.

5.1.3.4. Multichannel Analysis of Surface Waves

The Geological Survey of the PAT carried out ReMi, MASW and HVSR investigations to obtain information on the seismic properties of the subsurface. The results of these investigations are entered into a special database that is constantly updated following the investigations, which are carried out gradually. The data can be inspected and downloaded on the website www.arcgis.com/home/item.html?id=dc41feadffba4cc5abd298aa74b723b1. In addition to these surveys, further MASW measurements were carried out by OGS as part of the studies conducted under the PAT-OGS project agreement. The survey points labelled "TN" in Figure 5.9 correspond to these measurements. In

addition, four further MASW measurements (labelled ST, CV, VG and PC) were carried out by a professional geologist who provided the resulting data for this study. The figure 5.10 summarizes all the Vs profiles obtained from the investigations.

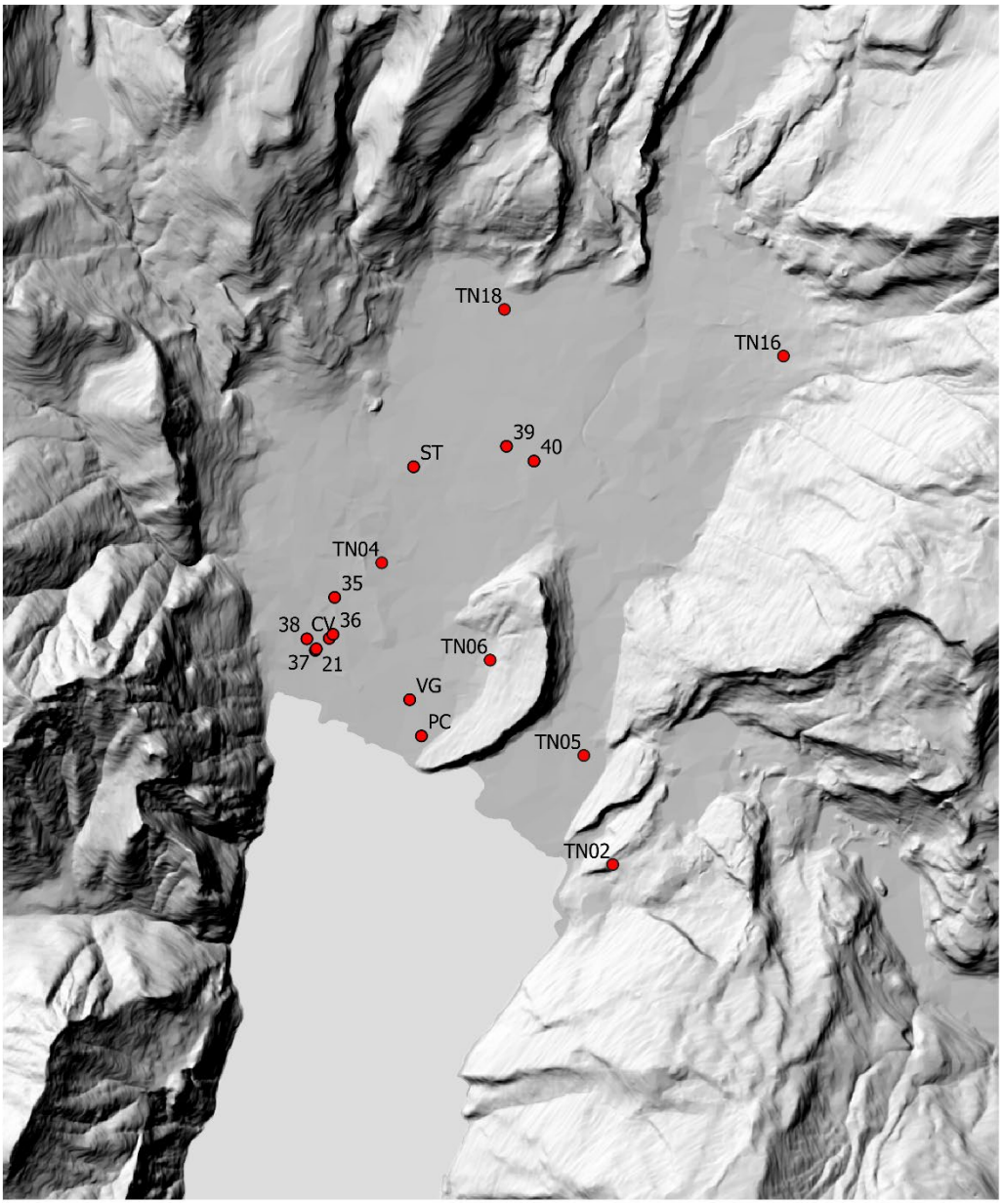


Figure 5.9. Spatial distribution of the locations where MASW surveys were conducted.

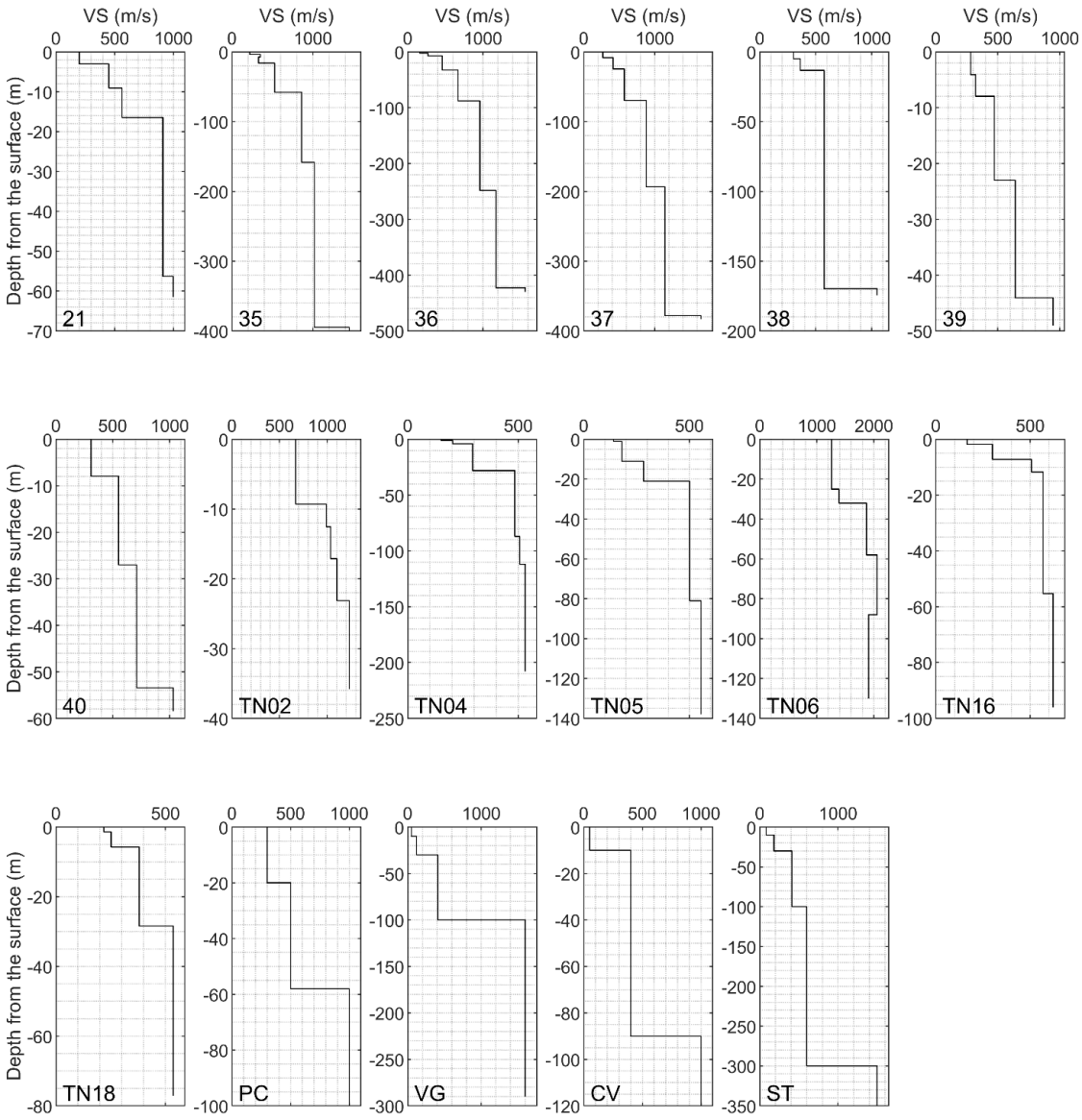


Figure 5.10. Vs profiles obtained from MASW surveys.

5.1.3.5. Refraction Microtremor

Since 2002, the Geological Survey of PAT has embarked on an experimental phase of the ReMi technique to obtain information on subsurface structures, even in environments normally considered 'hostile' to geophysical methods, such as urban areas. The results of these surveys are stored in a special database that is constantly updated as new surveys are carried out. The data can be inspected and downloaded on the website www.arcgis.com/home/item.html?id=dc41feadffba4cc5abd298aa74b723b1.

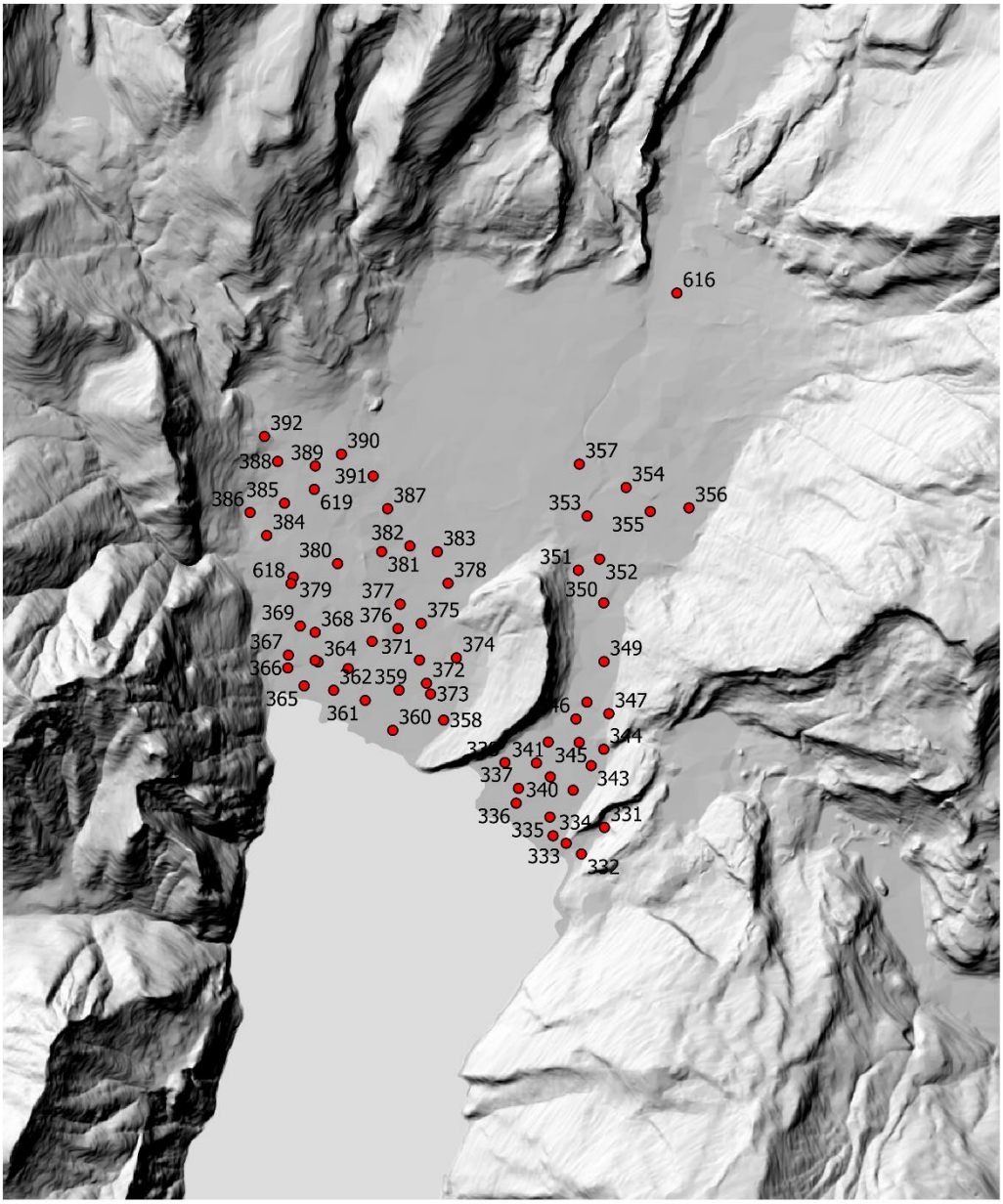


Figure 5.11. Spatial distribution of the locations where ReMi surveys were conducted.

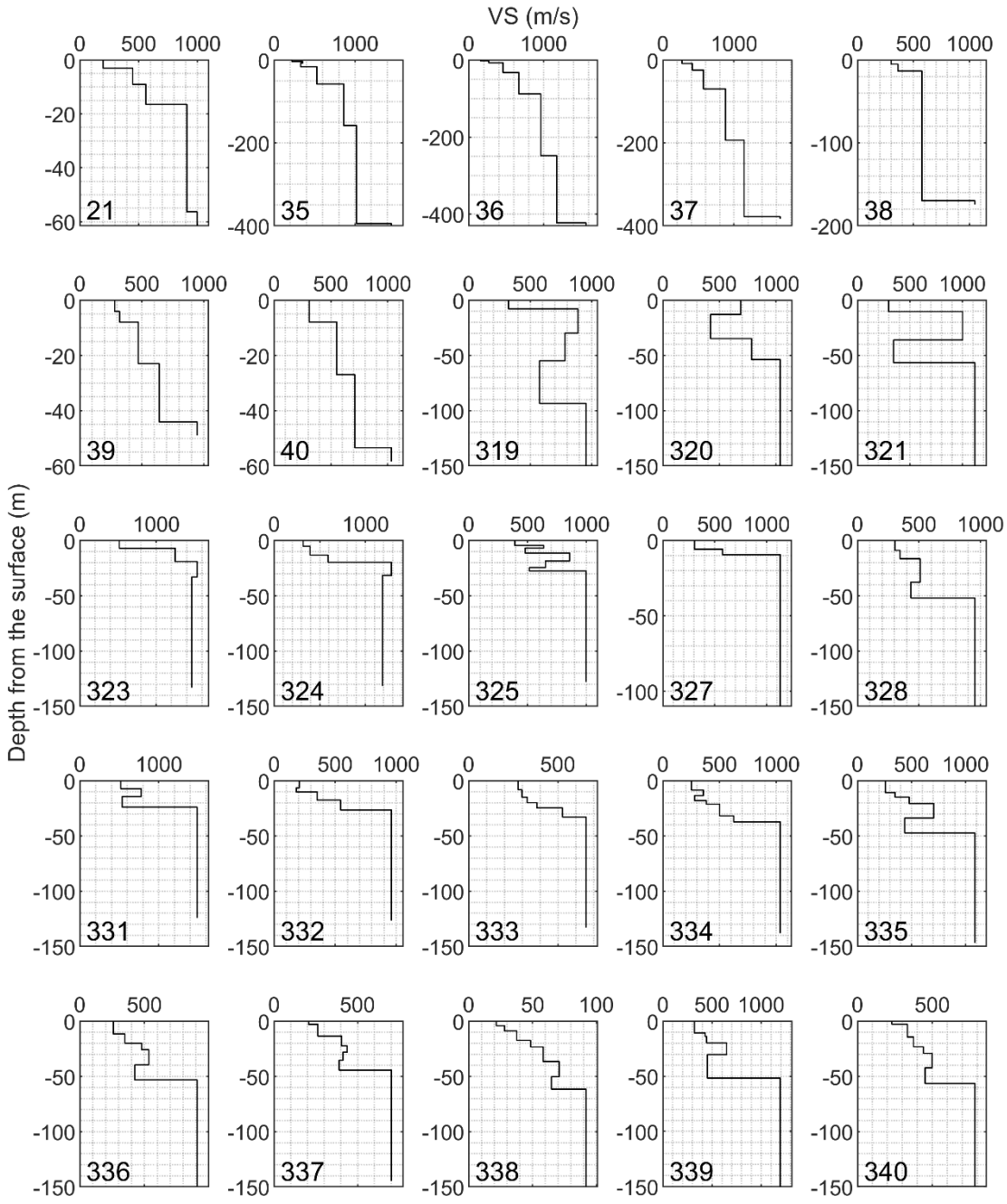


Figure. 5.12. Vs profiles obtained from ReMi surveys.

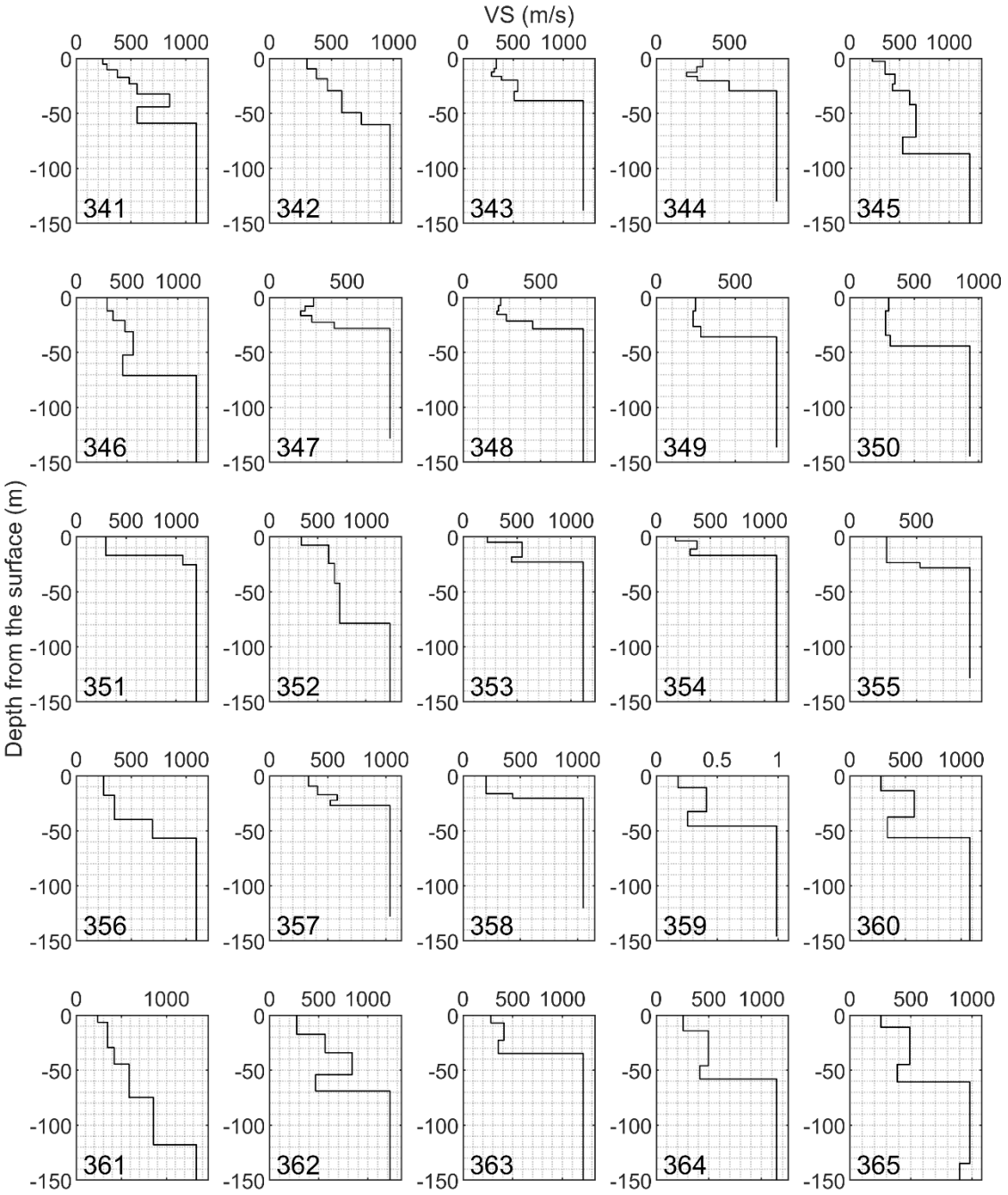


Figure 5.12. (continued).

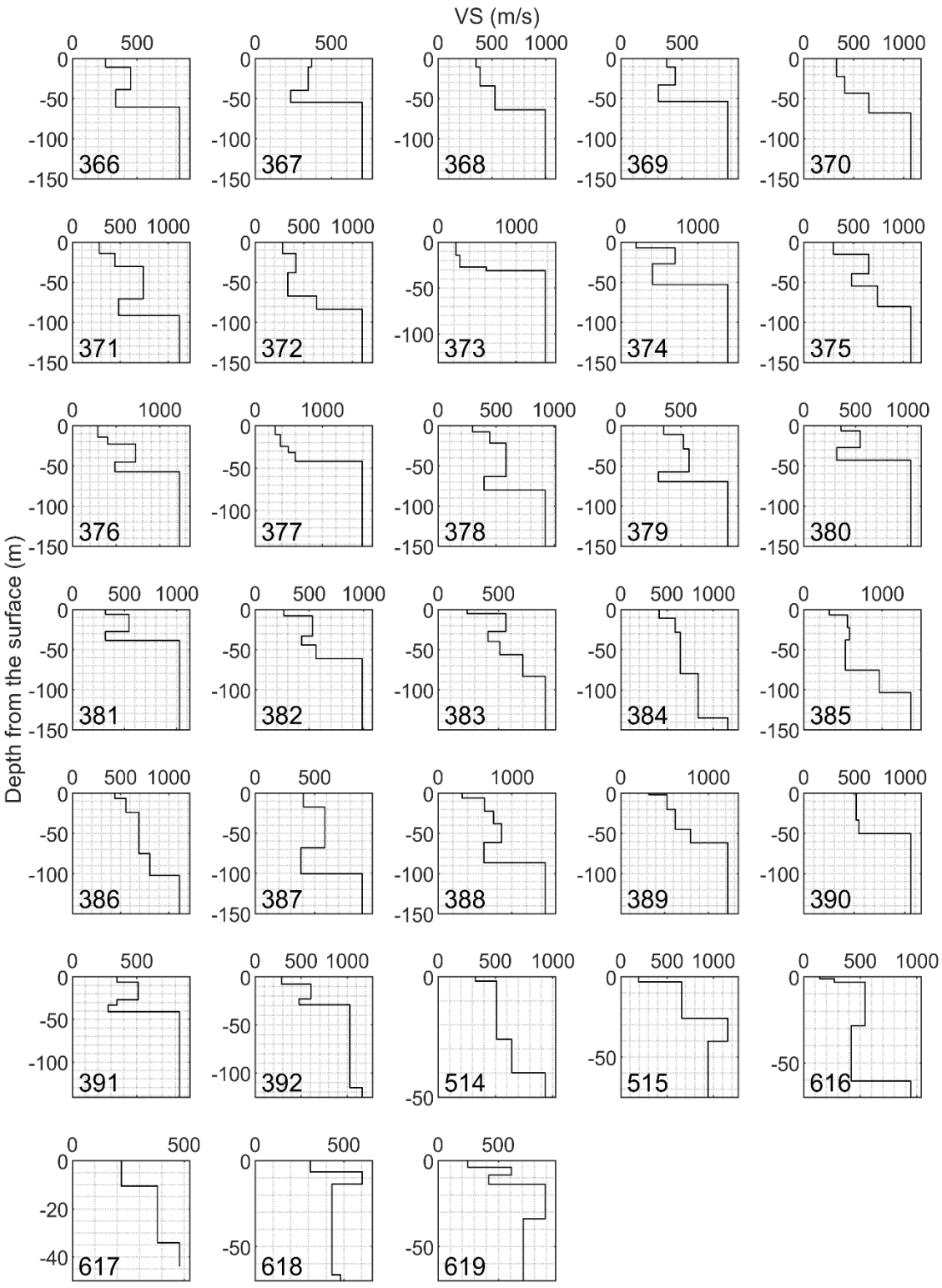


Figure 5.12. (continued).

5.1.3.6. Horizontal to Vertical Spectral Ratio

A total of 119 recordings of seismic environmental noise were made as part of the OGS-PAT project. The horizontal and vertical spectral ratio curves (H/V) were derived from these recordings. Figure 5.13 shows the spatial distribution of the recording points, while the Appendix contains the plots of the corresponding H/V curves.

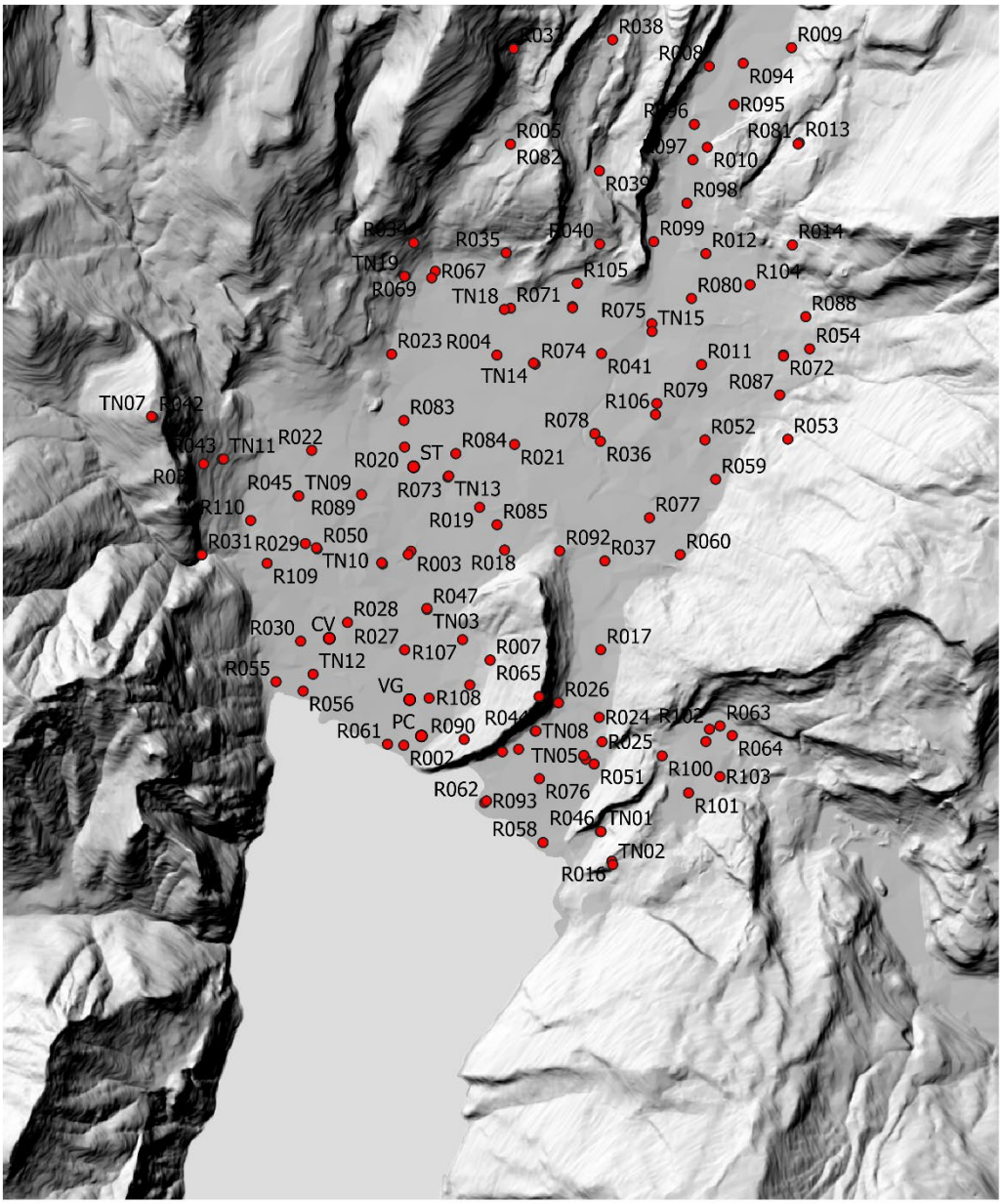


Figure 5.13. Spatial distribution of the locations where HVSR surveys were conducted.

In this study, the peaks of the H/V curves were determined according to the criteria proposed by Nakamura (1989), who interpreted these peaks as indicators of the

resonance frequency. However, not all detected peaks were included in the final analysis, as some did not meet the necessary requirements for a reliable geological interpretation.

In addition to these surveys, four HVSR surveys were carried out at the same locations as the MASW surveys (points labelled ST, CV, VG and PC) by the same professional geologist.

5.1.3.7. Generalized Inversion Technique

As part of the OGS-PAT project, 19 temporary seismic stations were also set up to record earthquakes and seismic noise (Figure 5.14), which were operated for around 16 months. The spectral conditions were calculated with respect to a reference site (GIT) in order to determine the amplifications of the study sites with respect to the reference site and the resonance frequencies.

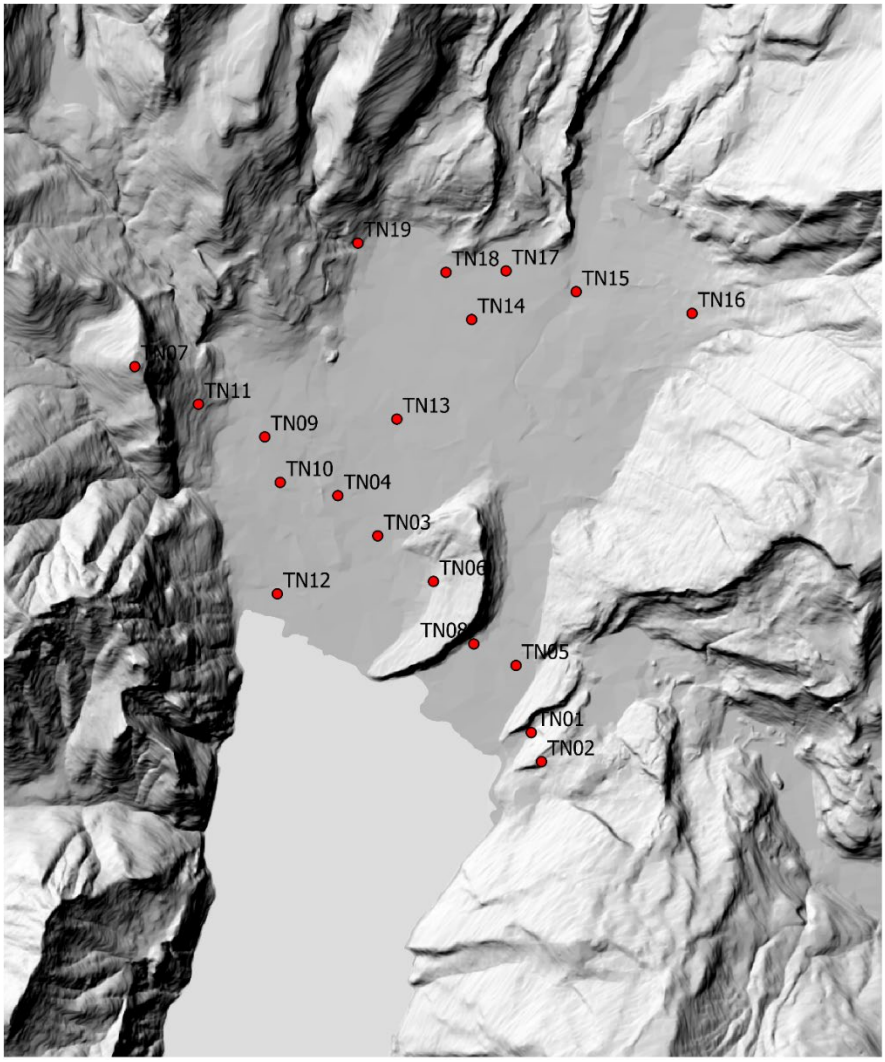


Figure 5.14. Spatial distribution of the locations where GIT surveys were conducted.

5.2. Arquata del Tronto ridge

Arquata del Tronto is a municipality in the province of Ascoli Piceno, in the Marche region. The area is located in central Italy and is part of the protected areas of both Monti Sibillini National Park and Gran Sasso-Monti della Laga National Park. It is a sparsely populated municipality: it consists of a small historic centre, strategically located on a rocky promontory (Figure 5.15), and 13 hamlets, including Borgo, which is less than 1 km from the centre and was built on a small plain. The entire relief has the shape of a triangle, develops in an east-west direction and lies between the course of the Tronto River and a narrow ditch. The outermost part, i.e. the top of the relief, on which most of the buildings stand, has an orthogonal orientation (roughly N-S) and is connected to the rest of the hill by a narrow corridor.



Figure 5.15. Extract from digital orthophotos. Provided by the Italian National Geoportal and acquired by the Agency for Agricultural Supply with a digital camera with 50-centimetre pixels. Resolution 1:10,000. Published in 2012, acquired in 2011.

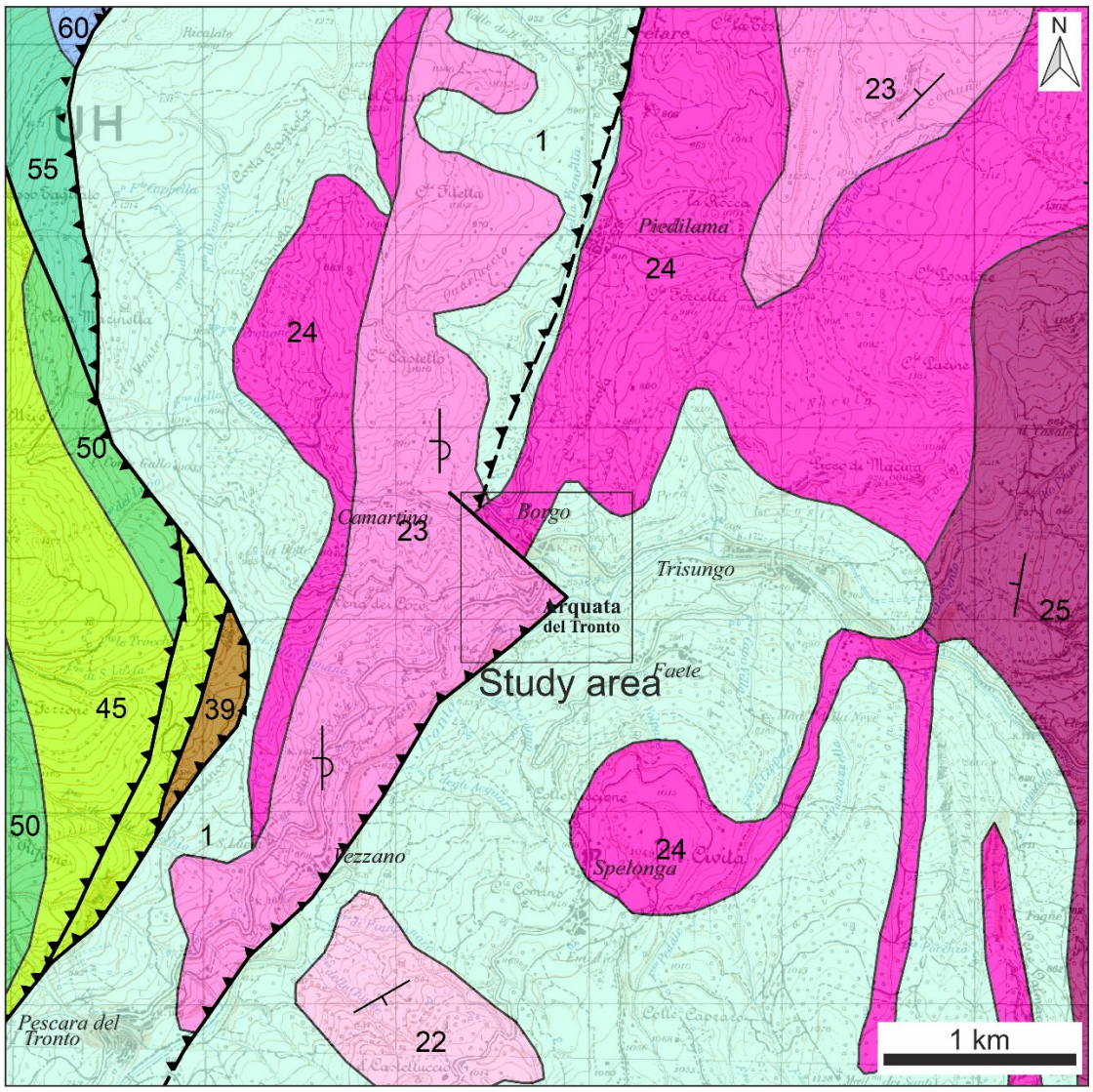
5.2.1. Geological-structural settings

Arquata del Tronto lies on the outer edge of the Apennines at the base of a section of the Sibillini Thrust, which in the Pliocene superimposed the basal carbonate sequence of Umbria-Marche with an ENE movement over the Laga Formation. The layers are west-dipped and have a steep dip angle. They were classified as layers with a reverse flank. It has therefore been hypothesised that they are part of a larger anticline at the top of an overthrust, a geological reconstruction proposed by Primofiore et al. (2020).

The compression regime that led to the Apennine orogeny, which began in the Oligocene and continued in the Pliocene (and still continues today in the Calabrian Apennines and in the coastal area and off the coast of the Marche and Romagna), is linked to the anti-clockwise rotation of the Sardinian-Corsican block and the Adriatic plate. From the Miocene onwards, the central Apennines are involved in the orogeny and develop fold and thrust tectonics, which mainly affect the carbonate sequences deposited on the continental margin of the Adriatic Sea. In the Upper Miocene, the orogenic phase caused the front of the chain to move eastwards, leading to the formation of a deep foredeep in which thick sequences of turbiditic sandstones were deposited: this is the sequence of the Laga Formation that characterises the study area (Figure 5.16).

For detailed analysis, we refer to the 1:5,000-scale geological maps produced by ISPRA's Geological Survey of Italy as part of Level III microzonation studies (Figure 5.17).

The geological formations in the territory of the municipality of Arquata del Tronto all belong to the Umbria-Marche sequence and to the turbiditic formation of the Monti della Laga. The local substrate is represented by the Laga Formation with a total thickness of about 3000 metres; a continuous and repetitive sequence of different lithofacies, each divided into four main units based on the ratio of sandstone and pelite and named with different letters from b to e.



Legend

- 1 Quaternary continental deposits

Laga Formation - Pre-evaporitic member

- 22 Pelitic-arenaceous association I
- 23 Pelitic-arenaceous association II
- 24 Arenaceous-pelitic association
- 25 Arenaceous association

Pre-turbidite deposits

- 39 Scaglia cinerea
- 45 Scaglia bianca - Scaglia rossa
- 50 Marne a fucoidi
- 55 Maiolica
- 60 Limestones a posidonia
- Attitude (Dip direction)
- Thrust fault
- Fault

Figure 5.16. Extract from the Geological map of the Laga and Cellino basins and surrounding carbonate reliefs (Southern Marche, North-Eastern Lazio, Northern Abruzzo), produced by Centamore et al. (1991), at a scale of 1:100,000.

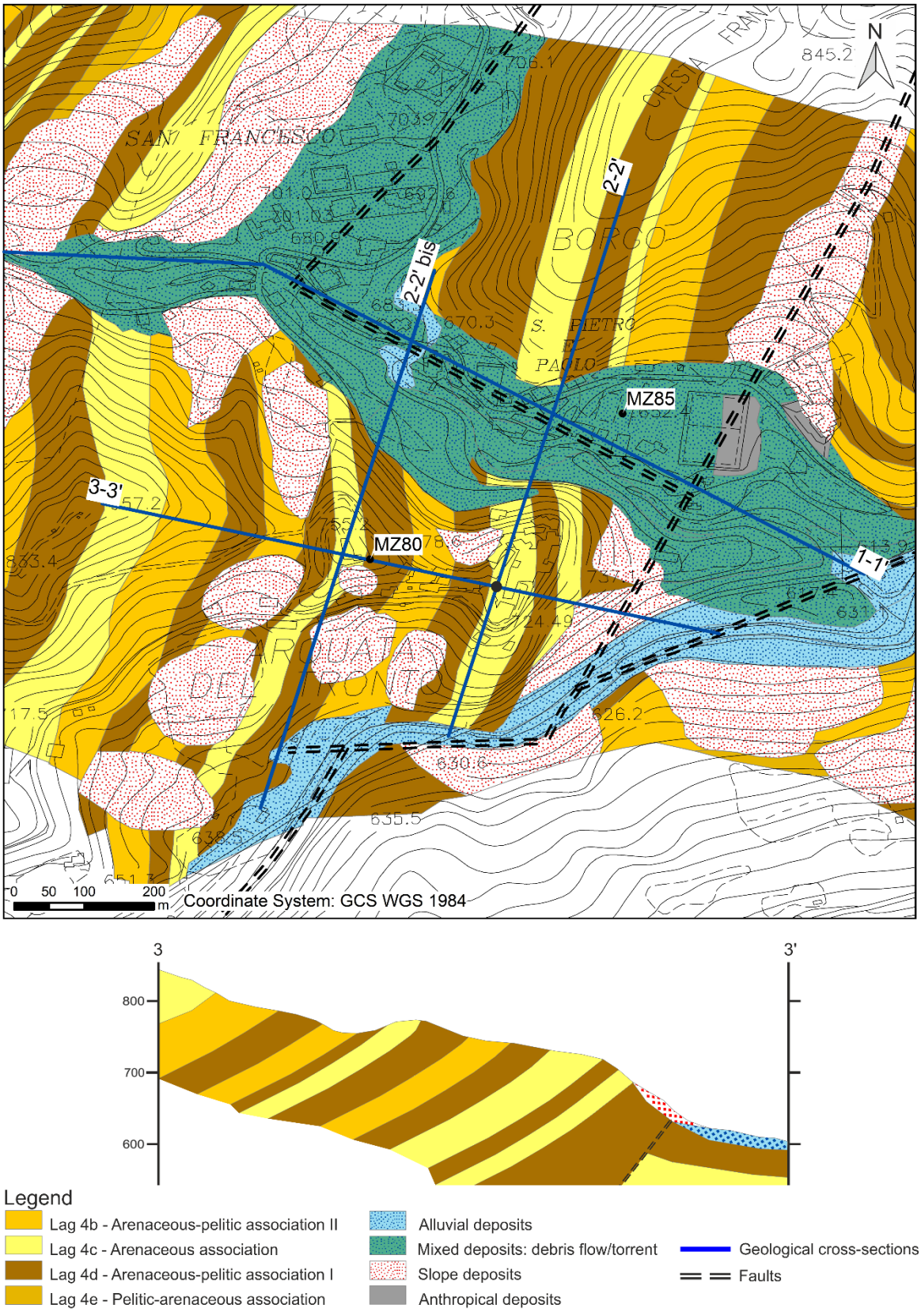


Figure 5.17. Simplified extract from the geological and geomorphological map used for the level 3 Seismic Microzonation studies of the Macroarea 1 Arquata del Tronto and Montegallo (AP), with the associated cross-section 3-3' (from Primofiore et al., 2020).

They are mostly covered by a depositional layer consisting of calcareous slope debris mixed with arenaceous debris in a sandy-silty matrix, or by fluvial deposits from the Quaternary and recent past, the thickness of which varies according to the origin of the deposit and the morphology of the accumulation area.

The Arenaceous-Pelitic Association II (LAG4b) consists of medium and thick tabular layers, a complete Bouma sequence (facies C and subordinate D1 and D2), A/P ratio between 1 and 3.

The Arenaceous Association (LAG4c) consists of thick to very thick Arenaceous layers that are fused together or separated by thin pelitic intercalations. The bodies have largely tabular and lenticular geometries. Predominant facies A1, A2, B1, B2, C1 and C2. At various levels there are arenitic-pelitic horizons and subordinate pelitic-arenitic horizons that cannot be mapped. The sequence can be attributed to channelled deposits of an internal fan.

The Arenaceus-Pelite Association I (LAG4d) consists of a sequence of Arenaceus horizons in very thick layers in facies A1, B1 and C1 and Arenaceus-Pelite horizons in facies C2, C1 and D1. The A/P ratio is between 3 and 10. The exposed unit has at least three fissure systems and is sometimes altered at the surface.

The pelitic-arenitic association (LAG4e) consists of thin pelitic-arenitic layers in facies D2 and D3 with interbedded arenitic-pelitic horizons of varying heights, consisting of interbeds, in the predominant facies C2, C1, B1 and D1. The sequence can be attributed to unchannelled deposits of an external fan.

5.2.2. Seismological settings

On 24 August 2016 at 01:36 (UTC), a magnitude 6.0 earthquake struck central Italy, affecting thousands of people and causing significant casualties and damage in the region. The event had a purely normal focal mechanism with a NNW/SSE direction (azimuth ≈ 156°), which is consistent with the current tectonic regime of the central Apennines.

On 26 October at 17:10 and 19:18 UTC, two events of magnitude ML 5.4 and 5.9 respectively occurred in the area directly north of the previously affected area. The epicentres, which are only a few kilometres apart, are located in the municipalities of Castelsantangelo sul Nera and Ussita in the province of Macerata.

On 30 October at 06:40 UTC, a new strong earthquake with a magnitude of Mw 6.5 occurred in the area on the border between Marche and Umbria, 5.5 km from Norcia. The damage and collapses have increased significantly.

On 18 January 2017, the provinces of L'Aquila (Montereale, Pizzoli, Capitignano and Campotosto) and Rieti (Amatrice) were hit by 4 further events with a magnitude greater than 5.0 within a few hours: at 09:25 UTC, Mw 5.1; at 10:14 UTC, Mw 5.5; at 10:25 UTC, Mw 5.4) and at 13:33 UTC Mw 5.0. The epicentre of these events was located between the epicentre of the 2009 L'Aquila earthquake in the south and the southern part of the seismic sequence that began in the north in August.

In total, the series of earthquakes in central Italy affected an area about 50 kilometres long, stretching from Pizzoli (in the south) to Visso (in the north). A total of around 50,000 tremors were recorded, of which around 60 had a magnitude between 4 and 5 and nine events had a magnitude ≥ 5.

Arquata was completely levelled by this seismic sequence and the hamlet of Borgo also suffered severe damage.

Numerous studies have aimed to analyse the local effects of the site on soil movement and to evaluate the amplification phenomena that have affected the structures both in the town of Arquata del Tronto and in the surrounding areas. Among many, we can mention the works of Galli et al. (2016), Sextos et al. (2018), Costanzo and Caserta (2019), Graziani et al. (2019), Lanzo et al. (2019), Laurenzano et al. (2019), Amanti et al. (2020), Primofiore et al. (2020) and others.

Central Italy is seismically very active (Figure 5.18). A comprehensive overview of historical and instrumental seismicity can be found in Guidoboni et al. (2018).

In Table 5.1, the earthquakes that generated a macroseismic intensity greater than or equal to VI on the Mercalli-Cancani-Sieberg MCS scale in Arquata del Tronto were selected. This threshold was chosen because VI on the MCS scale is the first objective intensity level associated with structural damage.

These 10 events are symbolic of the intense seismic activity in central Italy. However, there are many other earthquakes that are of lower intensity than Arquata or for which there are no historical reports, so this information has been lost.

Table 5.1. Earthquakes with MCS intensity greater than or equal to VI in Arquata del Tronto.

Date	Epicentral location	Epicentral intensity	Mw
1730 05 12	Valnerina	9	6,0
1916 07 04	Monti Sibillini	6-7	4,8
1972 11 26	South Marche	8	5,5
1950 09 05	Gran Sasso	8	5,7
1930 04 07	Monti Sibillini	5-6	4,5
1943 01 29	Monti Sibillini	6-7	4,9
1941 12 19	Monti Sibillini	7	5,0
1943 10 03	Ascolano	8	5,7
1979 09 19	Valnerina	8-9	5,8

Figure 5.18 summarises the most important errors taken from various sources. From the catalogue "ITaly HAzard from CApable faulting" (ITHACA Working Group, 2019), the Monte Vettore and Monte Bove faults are clearly visible in addition to the Vettoretto, Piano Grande and Castelluccio faults.

Two important tectonic lines are highlighted in the Database of Individual Seismogenic Sources (DISS Working Group, 2021): Accumoli-Amatrice, representing the northern segment of the Monti della Laga - Gorzano (MLG) fault system, which was activated during the 2016-17 sequence; Muccia-Castelluccio di Norcia, representing the outer frontal and lateral ramp of the Olevano-Antrodoco-Sibillini (OAS) thrust system, which was inverted during the 2016-17 sequence and reactivated in the current extensional regime.

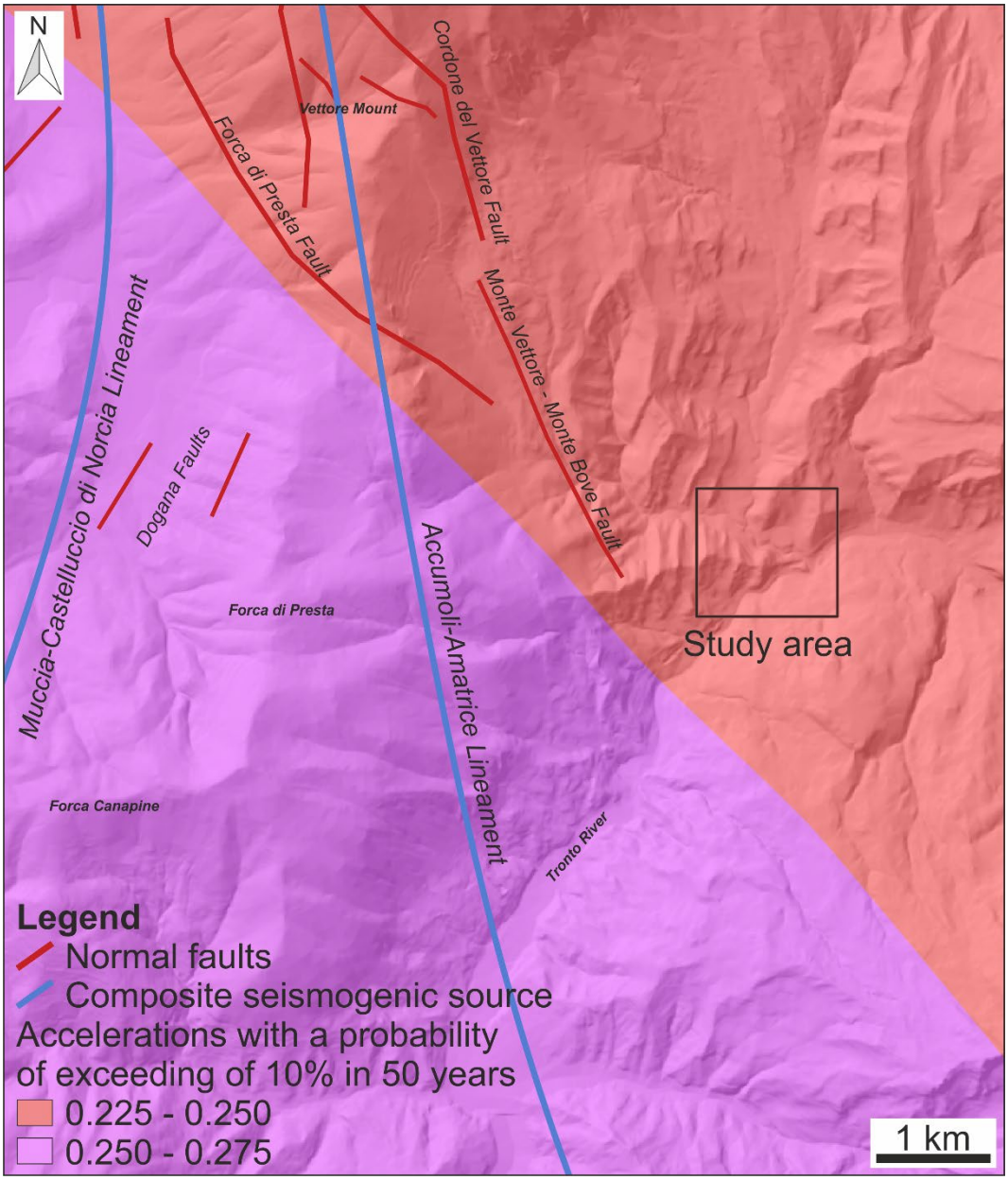


Figure 5.18. Seismo-tectonic features of the surroundings of the study area. Data from different sources were combined. The faults are provided by the Database of Individual Seismogenic Sources (DISS Working Group, 2021) and the Catalogue of "ITaly HAzard from CApable faulting" (ITHACA Working Group, 2019). The shaded background colours are provided from the Italian Seismic Hazard Map (Meletti et al., 2006) and indicate the PGA shaking value (expressed in g) to be expected with a probability of exceedance of 10 % in 50 years on rigid (Vseq > 800 m/s) and flat ground.

5.2.3. Geophysical settings

The entire data collection phase has already been completed at this site, as has the data integration phase to determine a subsurface model and associated parameters. Specific details on the formation of the model can be found in Primofiore et al. (2020).

Numerous investigations were conducted during the III level of microzonation studies. From there, the geophysical properties of each lithological unit were defined. The soils were then grouped according to their physical-mechanical properties (Table 5.2).

Table 5.2. Geophysical and geotechnical parameters used for the numerical model.

Lithology	Vs [m/s]	Vp [m/s]	Qs	Q_K	ρ [kg/m^3]
Arenaceous association	1000	2500	100	350	2200
Pelitic association	900	2250	90	315	2100
Weathered layer	700	1700	70	245	2000
Recent deposits	450	1100	45	160	1800

For the purposes of numerical simulations, we determine the values of five physical properties: the velocity of propagation of compressional waves (Vp), the shear wave velocity (Vs), the mass density ρ and the elastic quality factors for the shear deformation Qs and for the volumetric deformation Qk.

The different geological layers of the Laga Formation were grouped into two lithotypes: a predominantly pelitic layer (Lag 4e and 4b) and a predominantly arenaceous layer (Lag 4c and 4d). In addition, the deposits of different origin were combined into a single lithotype. Finally, a layer with fractures and a superficial alteration of the overlying rock was observed, so that a new lithotype of weathered layer was defined.

In the Results chapter, the graphical representation of the three-dimensional model obtained and the morphologies of the lithotypes are shown.

CHAPTER 6

RESULTS AND DISCUSSIONS

The results presented in this chapter aim to provide a comprehensive understanding of the seismic response of the two study areas and insights into the influence of subsurface conditions on ground motion propagation. Through the use of geophysical surveys and advanced numerical simulations, the study evaluates the interplay between geological structures and seismic wave behaviour under different conditions, highlighting key features specific to each site.

This chapter demonstrates the importance of using advanced modelling techniques for each site to ultimately contribute to the development of targeted mitigation strategies.

6.1. Sarca Valley

For the Sarca Valley, the work begins with the systematic integration of the various data sets presented in the previous chapter (see subchapter 5.1).

The initial phase is crucial for the development of a robust and consistent 3D model that can accurately represent the complex lithostratigraphic composition of the area.

The considerable width of the valley (about 400m in the deepest zone) leads to a shape ratio Sr of 0.2, which is calculated as the ratio between the maximum depth of and half of the width (Bard & Bouchon, 1985). According to the different classifications in the literature (see chapter 2.1.2 for more information), the valley is always defined as shallow. These characteristics reduce the dominance of 2D-3D effects compared to what would be expected in a deeper valley. However, as the morphology of the valley is very complex, 2D-3D effects are still present, especially near the edges of the valley and in the connecting zones between different areas where the resonance frequencies can be influenced.

For this reason, each lithostratigraphic unit must be carefully digitally reproduced with regard to its geometric configuration and its physical-mechanical properties. The resulting model is then validated by seismic numerical simulations. The synthetic seismograms generated by these simulations are compared with experimental data to validate the model.
Then, in order to evaluate the presence of three-dimensional effects on the seismic response, 1D and 2D simulations were performed in addition to the 3D ones, keeping the same properties, settings and seismic inputs.

6.1.1. Building a 3D model

This chapter describes the process that led to the reconstruction of the 3D model. It began with the integration and harmonisation of the available geognostic and geophysical investigations, followed by the three-dimensional reconstruction of the model by spatial 3D interpolation of the data through Geomodeller software (https://www.intrepid-geophysics.com/products/geomodeller/, last accessed November 2024), a commercial software developed by Intrepid Geophysics to create three-dimensional models from a variety of datasets.

6.1.1.1. Surveys integration

Before illustrating the procedure for determining the depth of the lithological interfaces, it is important to reconstruct the shape variation of the bedrock within the valley. As described in section 5.1.1, the geological evolution of this area suggests that the glacier eroded the western part of the valley. The results of the seismic noise analysis showed clear differences in fundamental frequency between the two areas located to the west and east of Monte Brione, suggesting a corresponding variation of bedrock depths. In particular, in the small valley to the east of Monte Brione, H/V curves showed higher resonance frequencies and the absence of a second H/V peak, suggesting that the bedrock is in direct contact with superficial deposits. This is consistent with the geological history of the area. The second H/V peak is otherwise observed in the western area and may indicate the presence of an additional interface within the deposits. Based on this observation, a spatial subdivision of the area into two zones was done (Figure 6.1). The western area, shaded purple, represents a zone where the bedrock underlies layers of

deposits at great depths; the yellow area corresponds to a narrow valley to the east of Monte Brione, where the youngest superficial deposits are in direct contact with the bedrock.

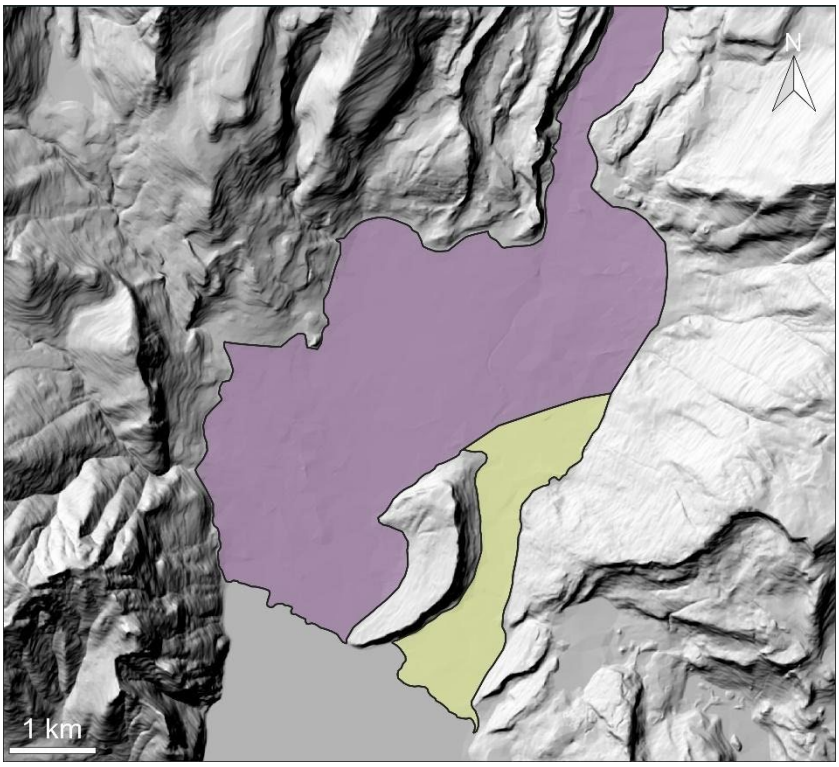


Figure 6.1. Maps showing the division of the area into two zones based on the HVSR peak analysis.

The two primary lithological units are distinguished in bedrock and sedimentary fill of the Sarca valley. The “Riva” seismic reflection profile (A-B section in Fig. 5.7) shows a 50 m wide band as the boundary between the deposits and the bedrock unit. A more accurate estimate of the bedrock depth can be obtained by interpolating the seismic reflection profile with the "Riva" borehole (Fig. 5.4, Location B), where the drilling stratigraphy shows that the geological bedrock is located at a depth of 223 m. When the borehole is projected along the section, it intersects the bedrock contact as shown in Fig. 6.2. Similarly, the "Arco" borehole (Fig. 5.4, Location A) encountered bedrock at a 272m depth, as confirmed by the vertical seismic profile survey. The projection of this borehole along the section shows that the boundary is closer to the upper boundary suggested by the seismic section. Based on these comparisons, the upper limit (red dashed line in Figure 6.2) can ultimately be defined as the sediment-bedrock boundary.

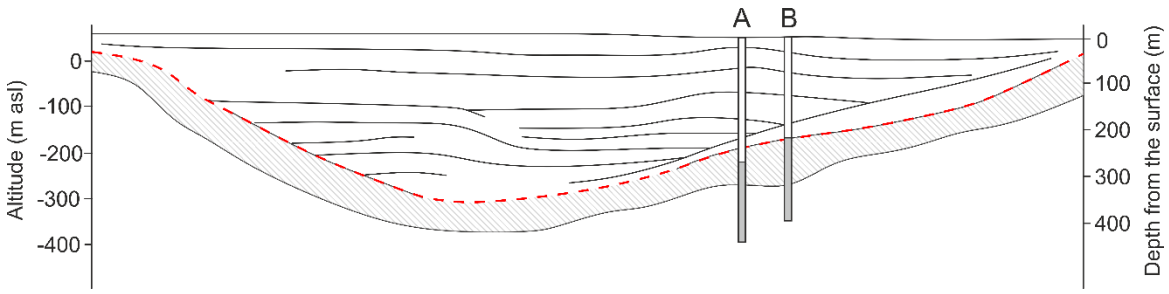


Figure 6.2. Cross-section illustrating the subsurface structure interpreted from the seismic reflection profile and the position of two boreholes (marked A and B). The hatched zone represents the band of the bedrock limit. Boreholes A and B penetrate this boundary at different depths. The red dashed line marks the boundary we determined between the sedimentary fill and the underlying bedrock.

If a Poisson's ratio of 0.2 is assumed for unweathered limestone, according to the relation by Mavko et al. (2020):

$$\frac{V_P}{V_S} = \sqrt{\frac{2-2\nu}{1-2\nu}} \qquad \text{(Eq. 6.1)}$$

a Vp/Vs ratio of about 1.6 can be estimated. Consequently, taking into account the Vp values estimated from the vertical seismic profile (Fig. 5.8), we obtain a Vs of about 2500 m/s for the bedrock. This value was used as a reference parameter for evaluating the morphology of the bedrock surface and for comparisons with other geophysical surveys.

The available MASW profiles in the western part of the valley do not reach the bedrock (Fig. 6.3), as the Vs values never exceed 1700 m/s. This is due to the limited resolved depth of surface waves in MASW techniques. Although the MASW survey is not able to directly detect the bedrock, this method still provides an indirect estimate of the minimum depth of the bedrock, indicating that it is certainly below the depth reached by the geophysical surveys.

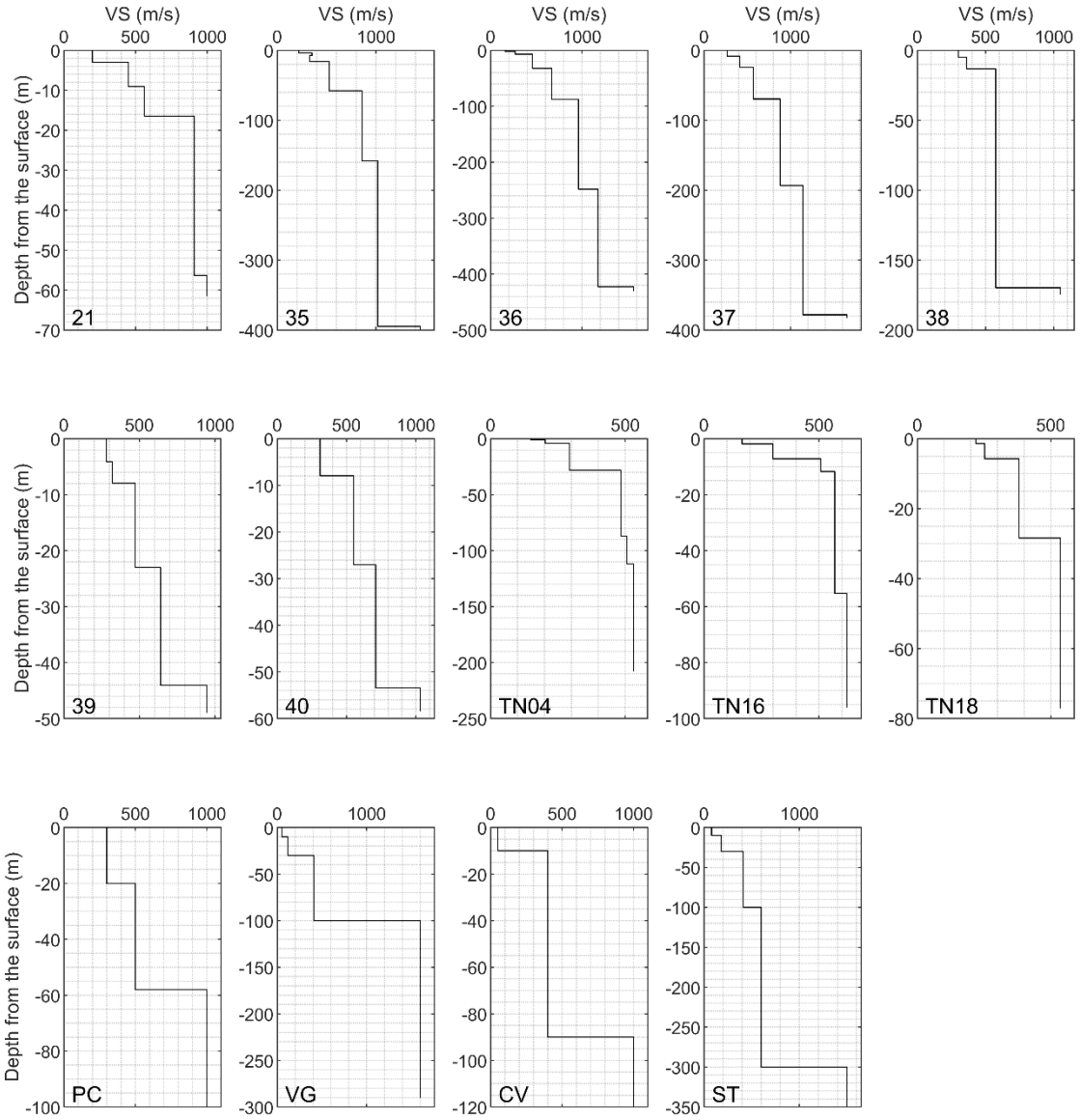


Figure 6.3. MASW surveys available in the western area of the valley

Additional information about the subsurface characters is provided by the HVSR investigations. However, its validity can be limited as it is particularly sensitive to valley edge effects or topographic morphology. Nevertheless, HVSR surveys can be considered a useful tool, especially when the collected data are carefully compared and correlated with other geophysical surveys and stratigraphic data.

In the present study, the results of the HVSR surveys are taken into account in order to improve their validity through calibration.

A useful approach is to correlate the peaks of the H/V curves with the depth data. Namely, the peak of the resonance frequency is well correlated with the thickness of the sediment z (see Chapter 4.1 for more details).

Given the extensive study area, 1D geophysical methods proved to be the most practical approach to gather sufficient information about the subsurface across the region. However, the inherent uncertainties of 1D surveys had to be carefully considered. In particular, the marginal areas of the valley offered additional complexity in addition to the stratigraphic effects. To reduce these uncertainties, the 1D results were systematically validated with complementary data sources such as 2D geophysical techniques and exploratory drilling. This integrated approach enabled the quantification of potential errors and facilitated the derivation of a calibrated estimate.

In the case of this study area, thanks to the extensive seismic noise measurement campaign, it was possible to create a complete map of the resonance frequencies (Laurenzano et al, 2023), which clearly shows a central area of the valley with very low f_0 values (below 1 Hz), an eastern area with f_0 values between 1 and 5 Hz, while areas on the edges of the valley or on a slope tend to have high resonance frequencies, even up to 10 Hz, or in some cases a flat curve, indicating a thinner or absent sediment cover.

As for data on bedrock depth, the information is rather fragmentary. We can count on three boreholes and some other geophysical surveys that intersect the bedrock and provide an estimate of its depth, such as MASW, ReMi, and seismic reflections.

Therefore, some HVSR measurements (where the peak is clear and conformed to Nakamura rules) are matched with depth data in the vicinity of the HVSR measurements.

A summary of the studies considered can be found below in Table 6.1 and a map showing their spatial distribution in Figure 6.4.

This correlation improved the robustness of the results, reduced the uncertainty associated with each method and provided a robust basis for interpretation of the data and subsequent geophysical modelling.

Table 6.1 Data used for interpolation of peak frequency values.

Depth survey	HVSR measurement	Bedrock depth (m)	Frequency peak (Hz)
“Arco” borehole	R019	272.5	0.65
“Riva” borehole	R085	223	0.85
“DuLac” borehole	R061	160	1.3
Seismic reflection section (central point)	R084	380	0.54
ReMi no.389	R022	61	2.3
ST MASW	ST HVSR	300	0.7

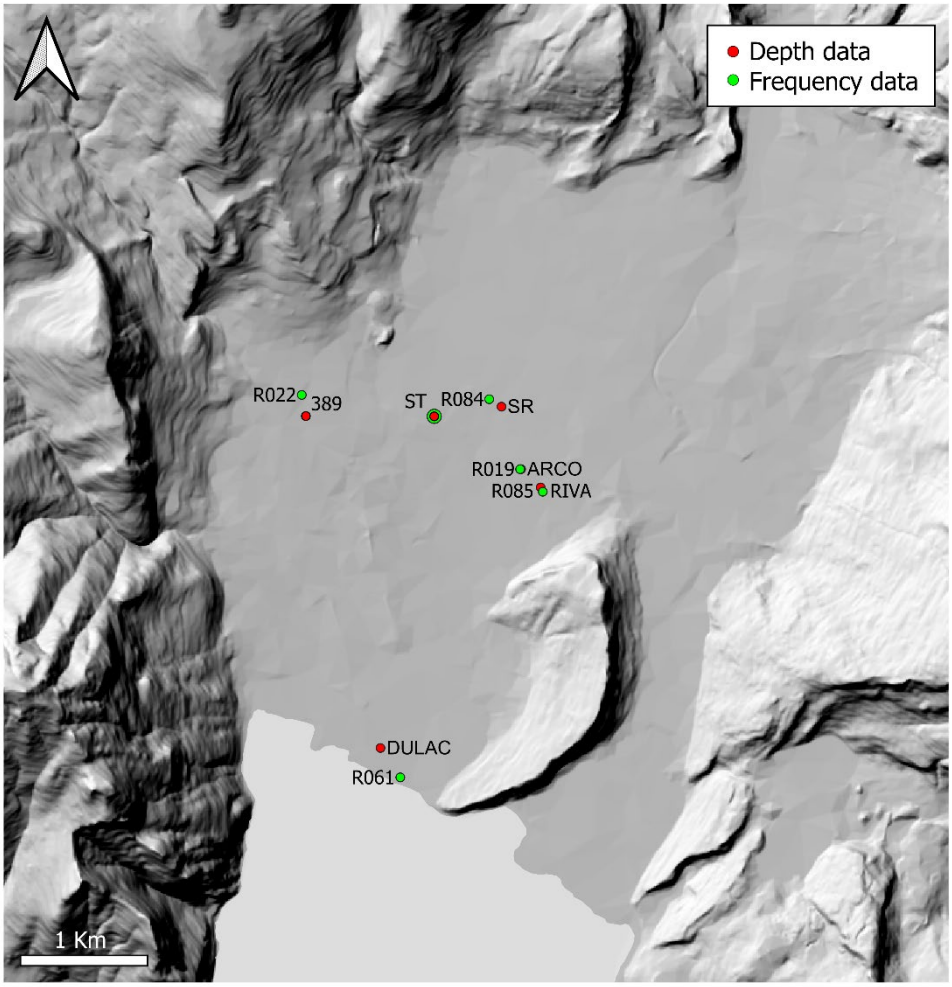


Figure 6.4. Location map of the data contained in Table 6.1.

The regression is obtained by interpolating the natural logarithm of the data yielded a mean regression line (Fig. 6.5) with coefficients a=5.21 (the y-intercept of the line) and b=−1.20 (the slope of the line). The resulting equation is therefore:

$$ln\,(z) = 5.21 - 1.2\,ln(f) \qquad \text{(Eq. 6.2)}$$

where z is the depth of the bedrock and f is the resonance frequency.

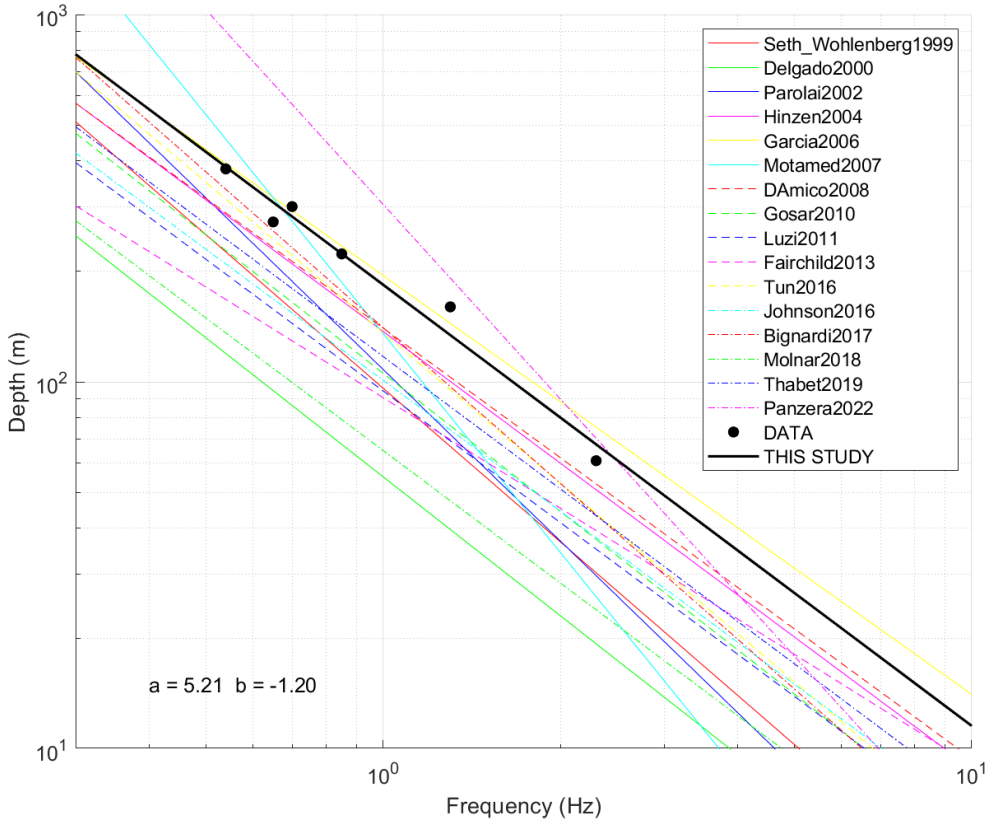


Figure 6.5. Relationship between resonance frequency and bedrock depth. Black dots represent the experimental data from Table 6.1. The solid black line was determined by a linear regression of the recorded data, with the corresponding coefficients a and b given at the bottom left of the figure. The relationships obtained in previous studies using similar methods are shown with coloured lines for comparison.

In addition to the regression derived from this study, the results of other studies using similar methods are also shown graphically in Figure 6.3. It can be observed the following: (1) the slope of our line is comparable to that one of previous studies and (2) the plotted points show a slight deviation from the interpolation line. These results indicate a good agreement between the data obtained and the general trend observed in other geological contexts.

The coefficient of determination R^2, (defined in Chapter 4.1.2) gives an estimation of the goodness of the regression line in minimising the variance of the data. It is 0.963 for this model. This value shows excellent agreement between the observed data and the linear regression used for the interpolation.

As we consider these values to be representative of the relationship between the resonance frequency and the depth of the bedrock, the average depth of the bedrock was re-calculated at each HVSR point (Figure 6.6).

In view of all these considerations, the bedrock depth provided by the HVSR surveys must be considered with caution. However, a critical evaluation of the results obtained and their integration with complementary methods will help to shed light on the subsurface features. In the final interpolation, these depth values derived from the regression were also taken into account, albeit with less relevance than the others.

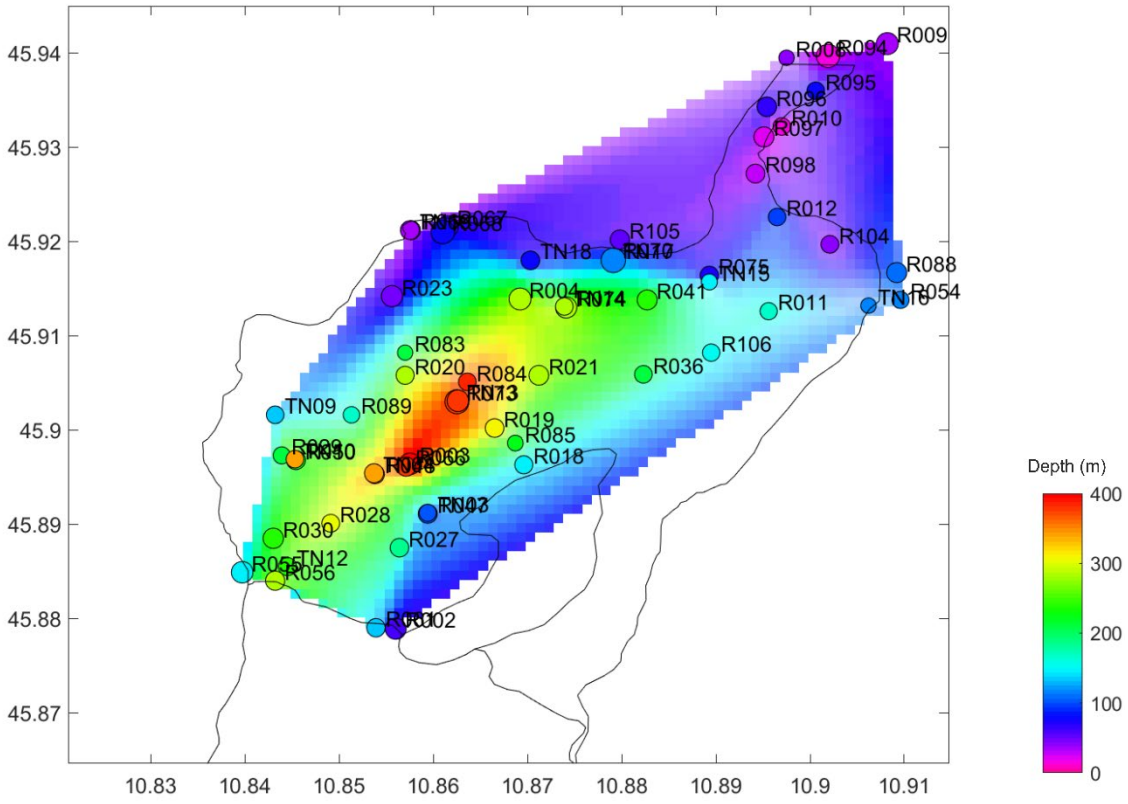


Figure 6.6. Bedrock depth obtained by the regression of resonance frequencies from HVSR. The points are interpolated and the intermediate areas were filled with a colour gradient that corresponds to the interpolation between the values of the neighbouring points.

This information on the bedrock depth is inserted into the workspace of the Geomodeller software. The following section (6.1.1.2) analyses and discusses the reconstruction of the 3D geometry of the interface.

Several investigations indicate heterogeneity within the sedimentary fill.

Although the information provided by boreholes as well as the vertical seismic profile indicate the presence of different layers of deposits within the valley, we have chosen to consider only two layers: the younger and shallower depositional layer and the stiffer and deeper deposit layer. This choice was also led by the limited resolution in the frequency band of the seismic simulations (which we will discuss in detail later).

This simplification is supported by the detection of a second resonance peak in some H/V curves in the western part of the valley, which is associated with the presence of a secondary interface.

The following sections describe the procedure used to reconstruct the morphology of this secondary interface between the two types of sedimentary deposits, which we will henceforth refer to as the "upper boundary".

Starting by analysing the four deep boreholes, different stratifications within the valley can be identified (Fig. 5.5). However, these data are of limited use, as geological strata do not correspond to geophysical layers. The vertical seismic profile (VSP), on the other hand, proves to be extremely useful in this context, but shows more than one discontinuity (Fig. 5.5). Two of these seem to be the most plausible because they agree with all other available data: the first discontinuity occurs at 54 m under the ground level and marks the boundary of an upper layer with an average Vp of 1800 m/s; the second discontinuity is observed at 155 m and defines a layer with an average Vp of 1900–2000 m/s. At this stage, it is unclear which of the two coincides with the boundary identified in the other investigations. This point will therefore be taken up again later in this chapter, as other investigations are related to this one.

The MASW measurements gave an important contribution. Despite their shallowness, in most of the cases along the Vs profiles we are able to recognise the upper boundary. Figure 6.3 shows the Vs profiles from the MASW measurements that fall within the western region. In many measurements, an interface at about Vs = 900 m/s is clearly recognisable. The Vs of the deep stiffer deposit can be fixed at this value. For some velocity profiles, the upper boundary remains undetermined. The MASW38, TN04, TN16 and TN18 profiles, for example, show Vs values of 500–600 m/s extending to great depths, even beyond 100 m (Fig. 6.3), which is not actually plausible from a geophysical point of view in

this study area. Consequently, these four investigations only provide information on the first few metres of depth and are excluded when determining the morphology of the upper boundary.

In addition, all of the ReMi surveys (Fig. 5.12) carried out in the region were taken into account when defining the upper boundary.

Finally, it is important to analyse the information provided by the HVSR survey campaign.

The same methodology used for the definition of the bedrock interface is repeated for the upper boundary. Used data are reported in Table 6.2 and a map showing their spatial distribution is shown in Figure 6.7. The regression is obtained by interpolating the natural logarithm of the data yielded a mean regression line with coefficients a=5.21 (the y-intercept of the line, on a natural logarithmic scale) and b=−1.19 (the slope of the line, on a natural logarithmic scale). The resulting equation is therefore obtained:

$$ln\ ln\ (Z)\ = 5.21\ -\ 1.19\ ln\ (f) \qquad \text{(Eq. 6.3)}$$

It can be observed that the slope of the obtained line is similar to those obtained in previous studies by other authors (Fig. 6.8).

The coefficient of determination R^2 is 0.762, which shows good agreement between the observed data and the linear regression used for the interpolation.

Also in this case, we estimated the interface depth by converting the f_0 values at the seismic noise measurement point using Eq. (6.3) and the result is shown in Figure 6.9. In the cases where the value was unclear, it was decided to exclude the data rather than misinterpreting them.

Table 6.2. Data used for interpolation of peak frequency values.

Depth survey	HVSR measurement	Interface depth (m)	Frequency peak (Hz)
ReMi no.365	R056	60	2.4
ReMi no.382	R003	61	2.3
MASW39	R021	44	3.5
MASW36	R028	90	2.1
VSP	R073	54	2.9

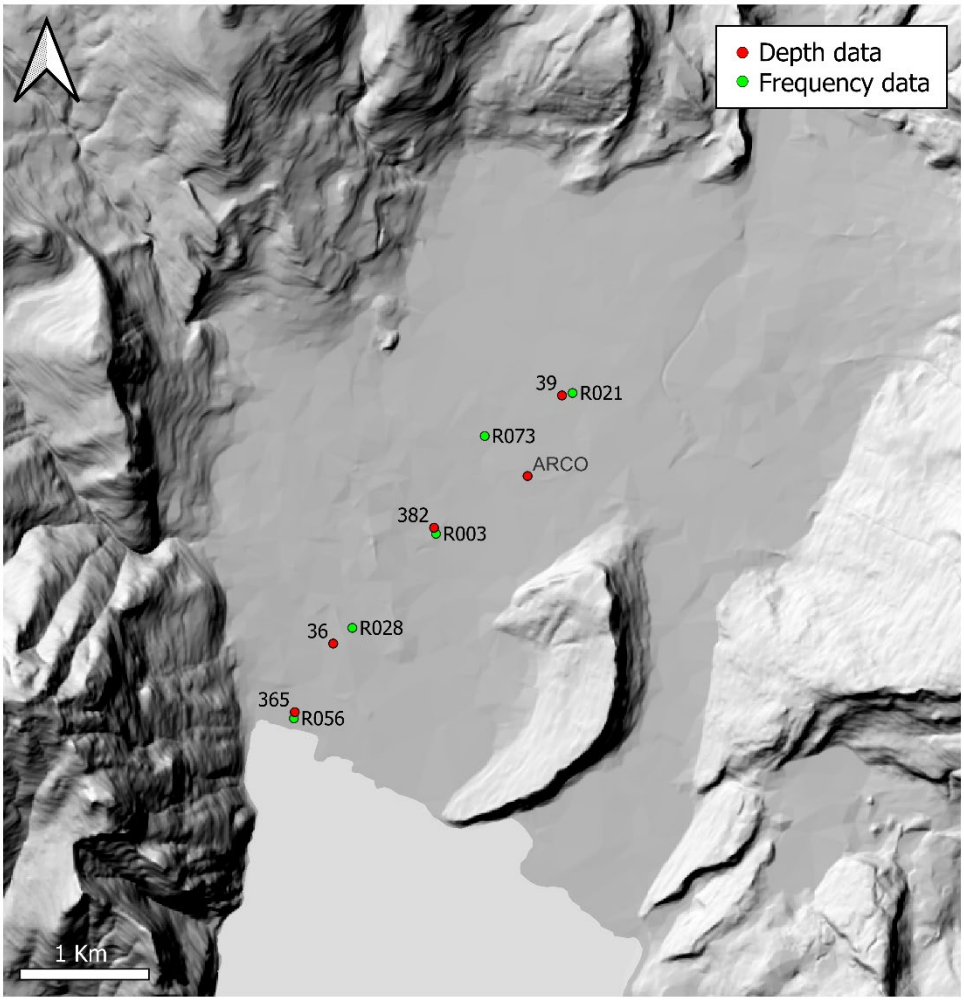


Figure 6.7. Location map of the data contained in Table 6.2.

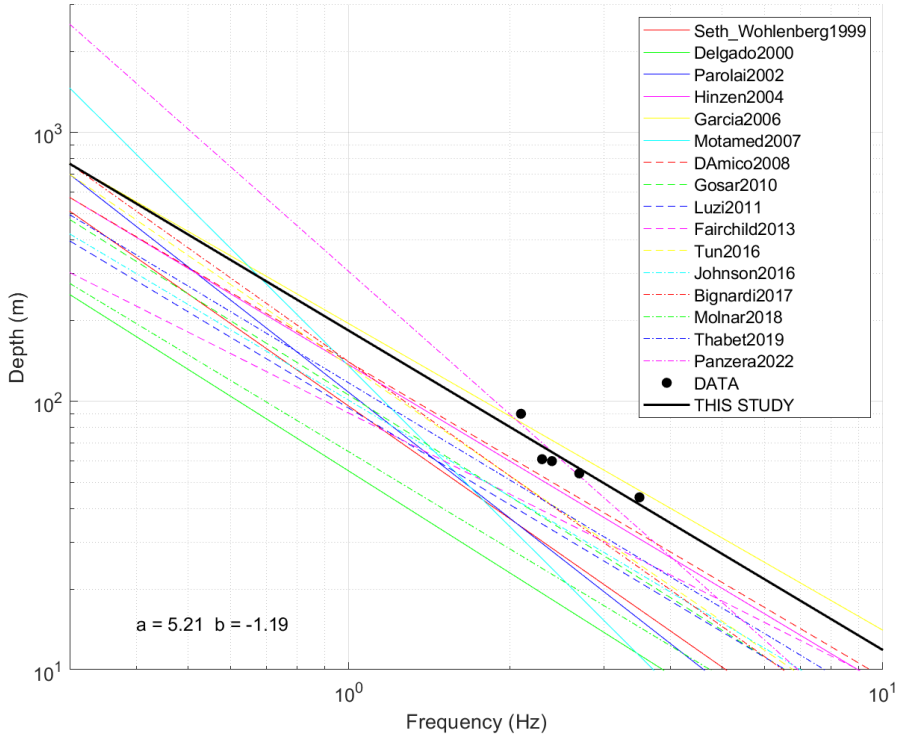


Figure 6.8. Relationship between resonance frequency and Sediment/bedrock interface depth. Black dots represent the experimental data from Table 6.2. Other detail as in Figure 6.5.

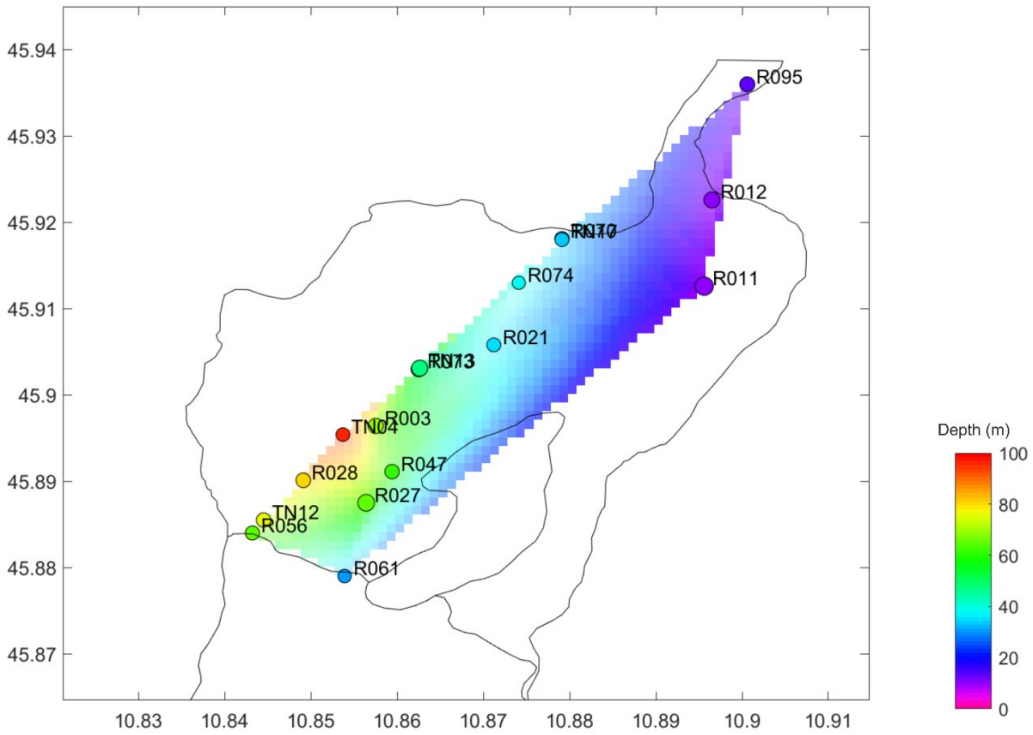


Figure 6.9. Sediment/bedrock interface depth obtained by the regression of resonance frequencies from HVSR. Other details in figure 6.6.

The discussion on the vertical seismic profile, which we left open at the beginning of the chapter, is thus clearer: the interface in good agreement with the discontinuity at about 54 m indicated in the seismic profile (Fig. 5.8), which marks the limit of an upper layer with an average V_P of 1800 m/s.

Finally, the depth of the interface between the deposits and the bedrock in the valley area to the east of Monte Brione is determined, using the same approach. The data available in this area were the following: a MASW investigation, 21 ReMi investigations, 18 HVSR analyses, 24 shallow boreholes and one deep borehole. Their location is shown in Figure 6.10.

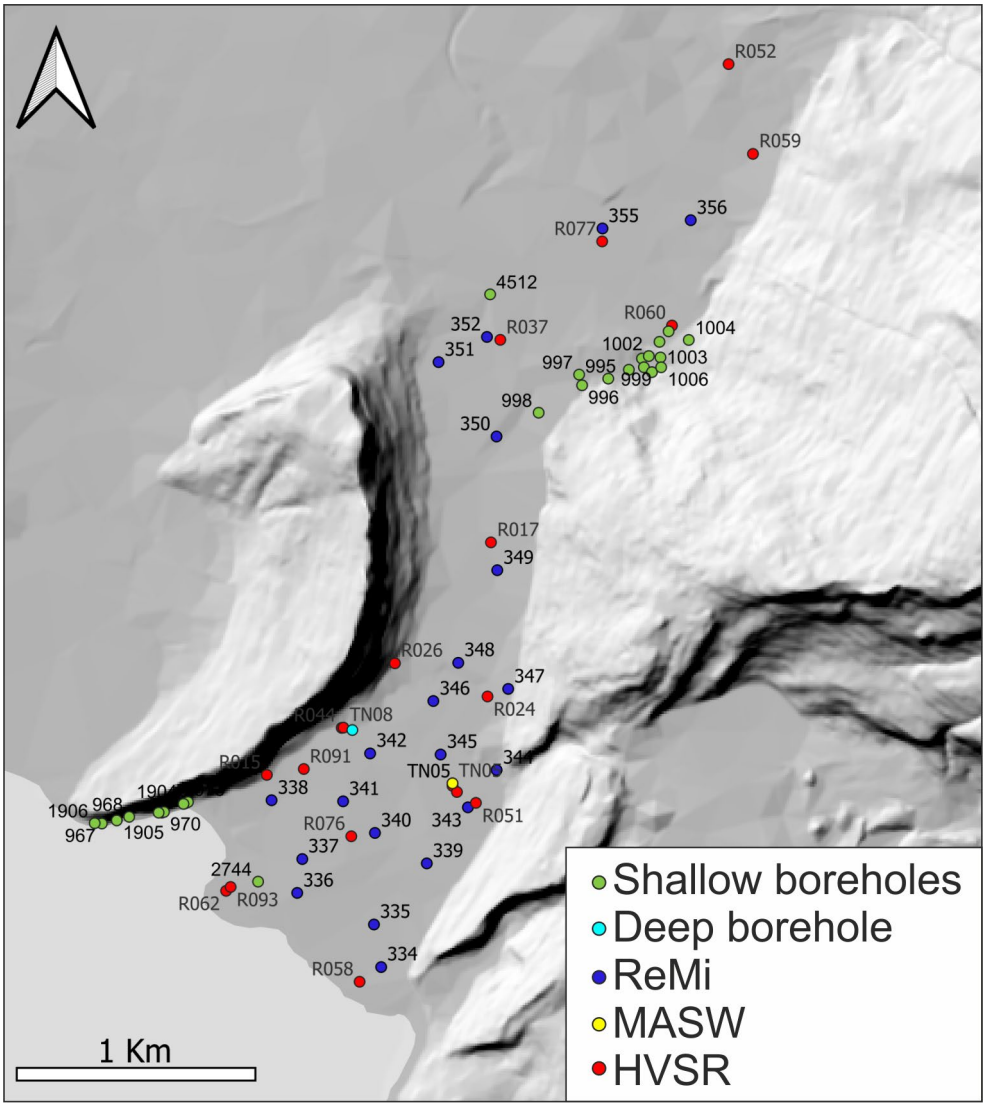


Figure 6.10. Location of the study sites in the eastern region of the valley.

The only one deep borehole is located at the edge of the valley below the slope of the Monte Brione (marked by the light blue circle in Fig. 6.10) and has been affected over time by the accumulation of rockfall material. This compromises the ability to accurately identify the stratigraphy and relate it to the rest of the valley. There are many boreholes in the area. However, many of them are too shallow to reach the bedrock (see Appendix). Nevertheless, they provide an indirect estimate of the minimum depth of the bedrock, suggesting that it is below the depth reached by the geophysical surveys. A MASW survey carried out in this area (TN05, marked by the yellow circle in Fig. 6.10) indicates an interface at a depth of 21 m (Fig. 5.10). The vertical Vs profiles obtained by the 21 ReMi surveys carried out in this area are shown in Figure 6.11. The depth values at which Vs discontinuities are clearly recognisable are taken into account in the construction of the boundary between the bedrock and the sediments.

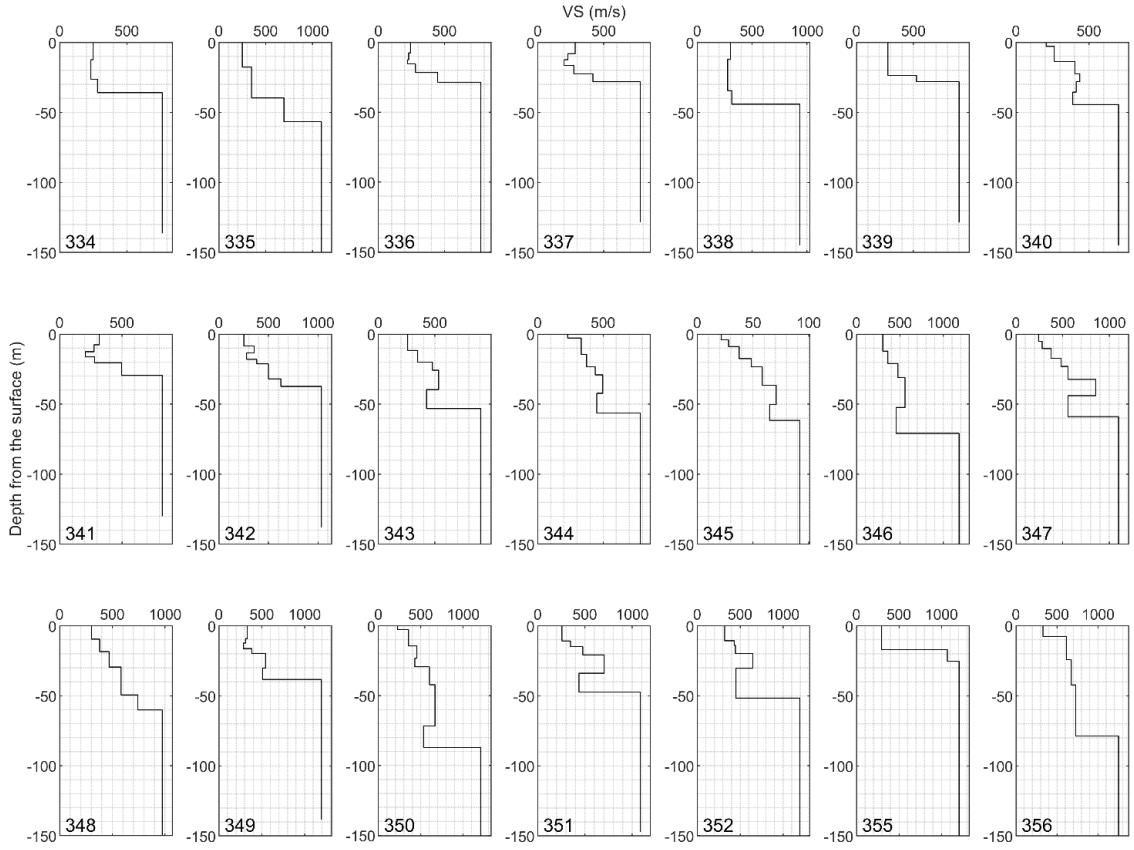


Figure 6.11. Vs profiles from the ReMi surveys carried out in the eastern area.

From 18 recordings of ambient noise, acquired in the eastern area, an equal number of H/V curves can be derived, each associated with resonance frequency peaks (all H/V curve diagrams are available in the Appendix).

Again, the same methodology used for the definition of the bedrock interface is repeated also for this area. In particular, 6 HVSR measurements are related to other measurements (in their surroundings) that provide depth values. A summary of the investigations considered can be found in Table 6.3 and a map showing their location in Figure 6.12.

Table 6.3. Data used for interpolation of peak frequency values.

Depth survey	HVSR measurement	Bedrock depth (m)	Frequency peak (Hz)
ReMi no.355	R077	28	2.0
TN05 MASW	TN05 HVSR	21	2.3
TN05 MASW	R057	21	2.6
ReMi no.349	R017	38	1.5
ReMi no.340	R076	58	1.2
ReMi no.334	R058	38	1.4

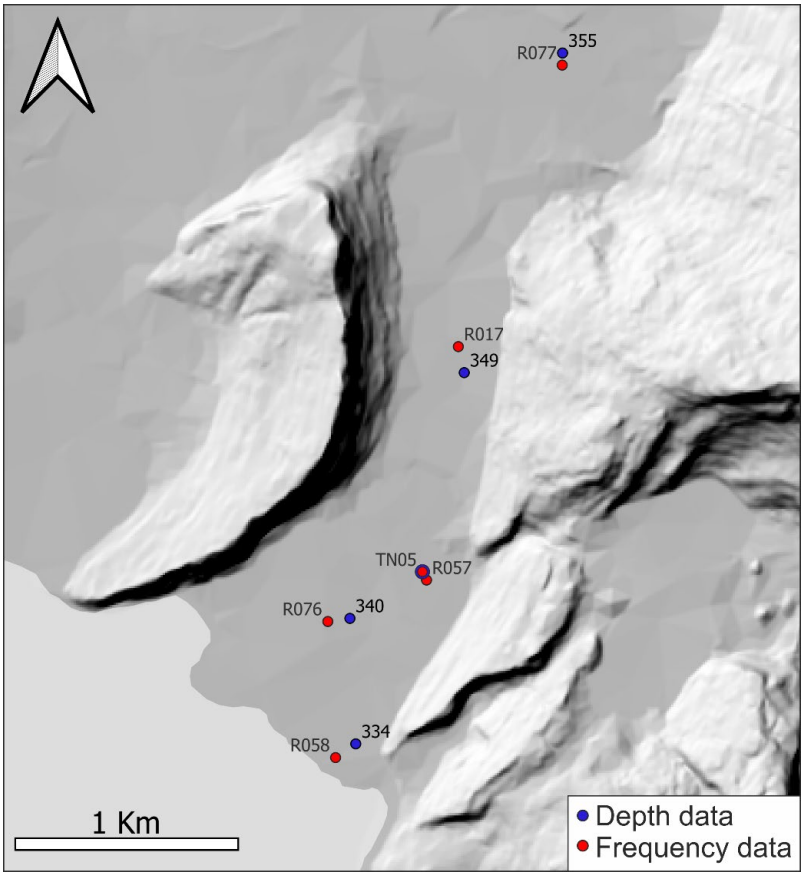


Figure 6.12. Location map of the data contained in Table 6.3.

The regression is obtained by interpolating the natural logarithm of the data yielded a mean regression line (Fig. 6.13) and the resulting equation is therefore the following:

$ln\,(z)\ = 4.18\ -\ 1.27\ ln(f)$ (Eq. 6.4)

where z is the depth of the bedrock and f is the resonance frequency. The coefficient of determination R2 is 0.932 and shows excellent agreement between the observed data and the linear regression used for the interpolation.

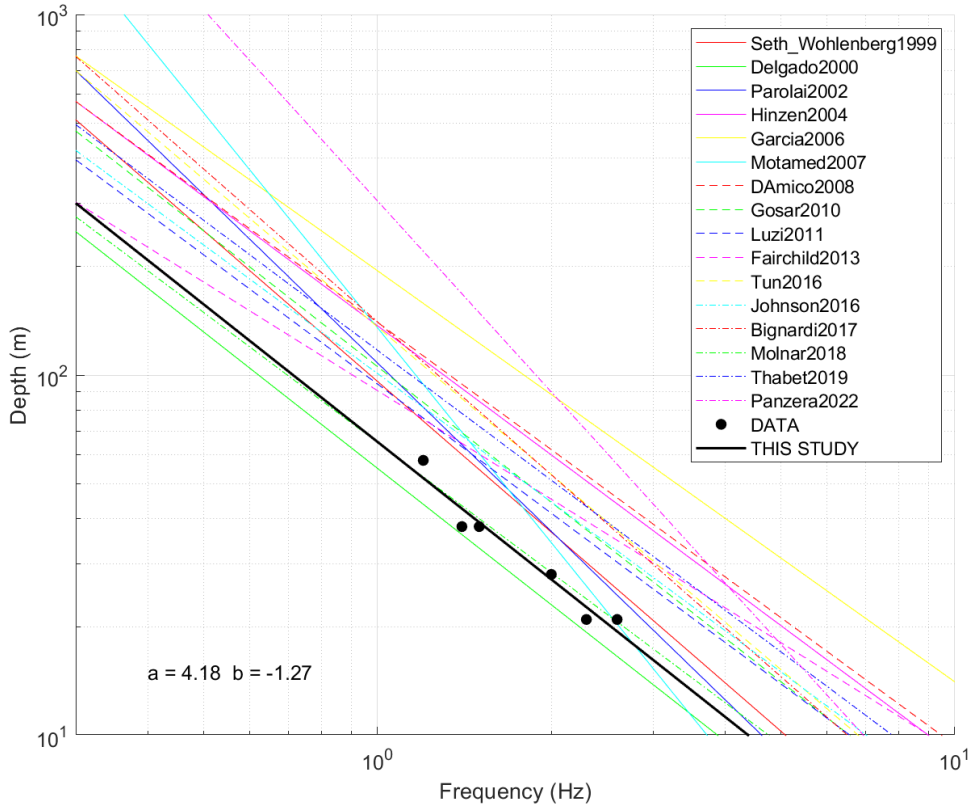


Figure 6.13. Relationship between resonance frequency and bedrock interface depth for the valley east of Mt Brione. Black dots represent the experimental data from Table 6.3. Other details as in Figure 6.5.

In this case, too, the line obtained by the regression agrees well with that of earlier studies. As we consider these values to be representative of the relationship between the resonance frequency and the depth of the bedrock, the average depth of the bedrock is recalculated at each HVSR point (Figure 6.14).

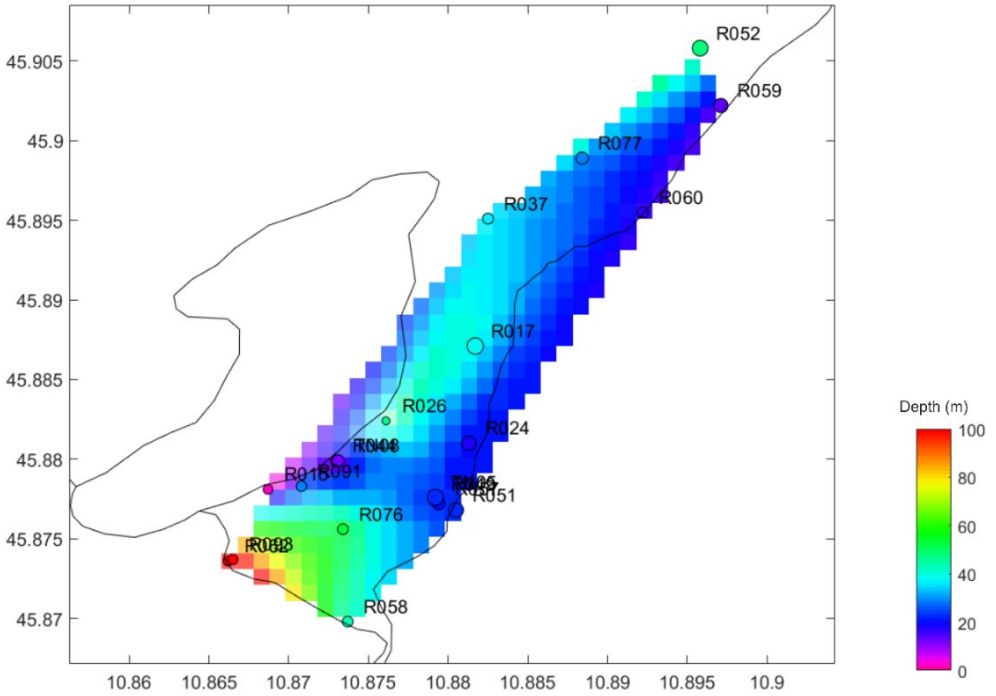


Figure 6.14. Bedrock depth obtained by the regression of resonance frequencies from HVSR for the valley east of Mt Brione. Other details in figure 6.6.

6.1.1.2. 3D model creation

At the beginning of a new project, the working volume in which the 3D geometries must be reconstructed is defined and a cartographic projection system is assigned. In this study, the chosen reference system is WGS 1984 / UTM Zone 32N, which uses plane coordinates in kilometres. The model dimensions and vertex coordinates are summarised in Table 6.4.

Table 6.4. Spatial properties of the 3D model.

X dimension	10 km
Y dimension	12 km
Z dimension	3 km
X coordinates	640000 m; 650000 m
Y coordinates	5089700 m; 5077700 m
Z coordinates	-1400 m slm; 1600 m slm

The first step was to import the Digital Terrain Model, that represents the trend of the soil surface without the anthropogenic and vegetative elements (Figure 6.15). The TINITALY/1.1 DTM with a resolution of 10 m was used for this study (Tarquini et al., 2007, http://tinitaly.pi.ingv.it/, last accessed November 2024).

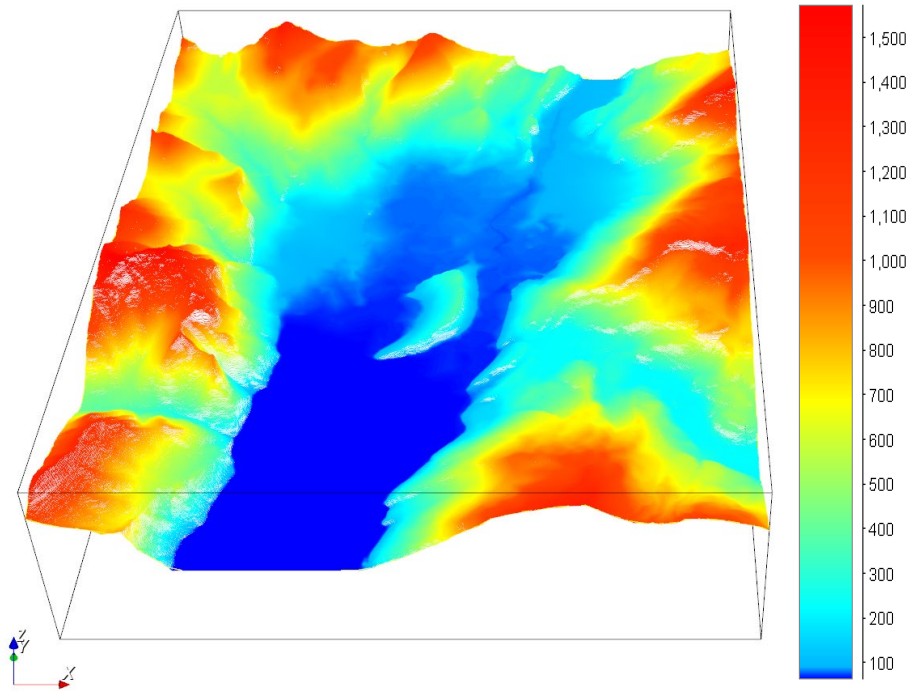


Figure 6.15. Digital elevation model, cropped to fit the study area.

The second step consists in the definition of the stratigraphic pile of geological model: lithological units are defined to reflect significantly different geological and geophysical parameters. The stratigraphic pile is shown in Table 6.5.

Table 6.5. Stratigraphic pile: list of lithological units imported into Geomodeller, in descending order of age.

LITHOLOGICAL UNIT	COLOUR
Lake	
Recent alluvial deposits	
Old heterogenic deposits	
Monte Brione sandstones	
Bedrock (Piattaforma Veneta limestones)	
Bedrock (Bacino Lombardo limestones)	

A unit representing the Garda Lake was also added. Although this is a conceptual or "fictional" layer, it must be included as if it were real, in order to accurately represent the body of water.

Table 6.5 shows two types of bedrock, represented by grey and brown colours. This distinction is maintained to emphasise the presence of a significant tectonic lineament linking the two structural domains, as described in Section 5.1.2. Although there are no significant geophysical differences between these units, both primary rock domains have been included in the model for completeness.

The investigations in the two areas, where the alluvial fans are observed, did not reveal any differences in the Vs. The HVSR investigations also did not reveal any differentiation in the frequency peaks compared to the surrounding areas. It was therefore decided to merge the alluvial fans with the recent deposits in the same unit.

At the same time, in addition to lithological discontinuities, erosive discontinuities (unconformities) and tectonic discontinuities (faults) are also regarded as essential structural features and were integrated either at the beginning or during the modelling process. In this study area, all major tectonic lineaments are taken into account, and Figure 6.16 defines the shape and the relationships between faults.

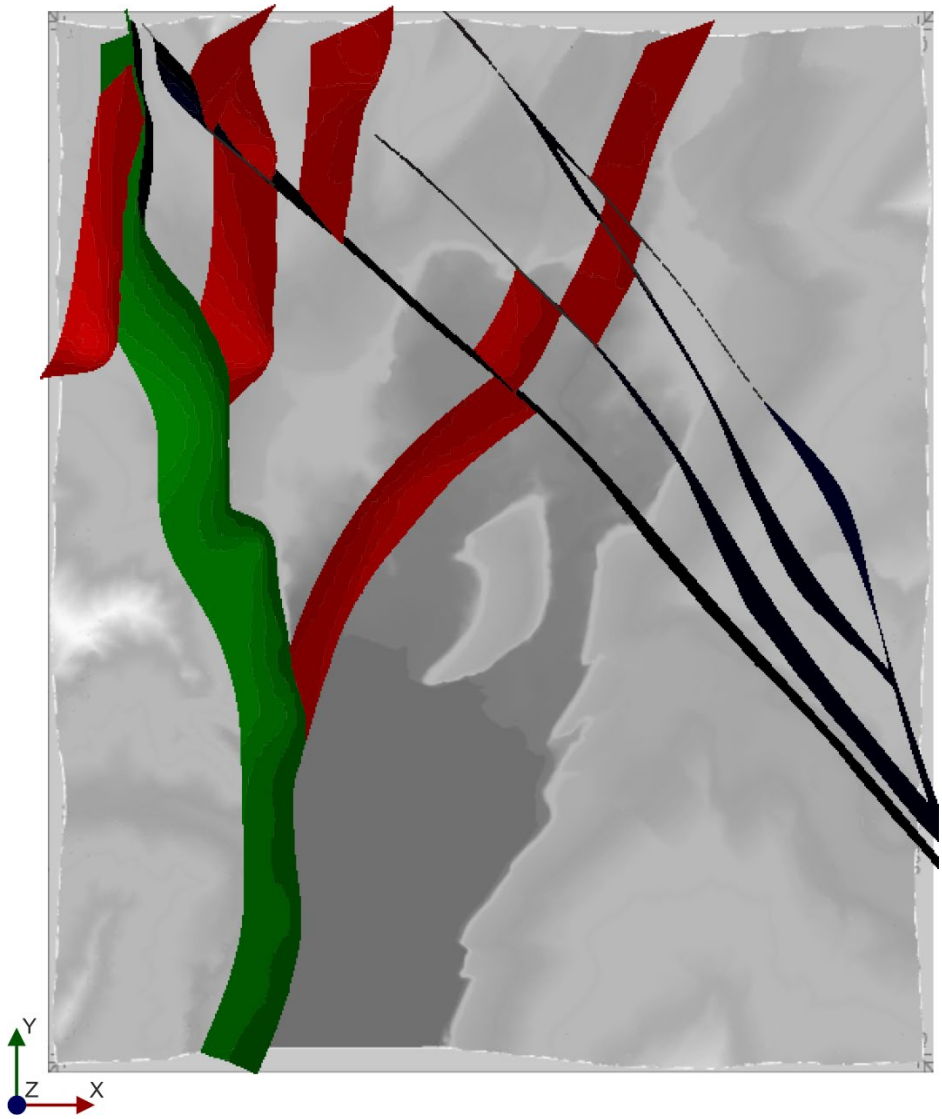


Figure 6.16. Main tectonic lineaments within the study area, selected from a large number of faults documented in the literature.

The faults are shown in three different colours. The strike faults, which are the youngest and have an approximately vertical dip, are shown in black. The thrust faults are shown in red and green: The green colour underlines the importance of the Ballino-Garda tectonic line, which is one of the main structural features in the area. The other faults, coloured red, are of lesser importance, but nevertheless belong to the same lineament, which is made up of branches divided into several sections of approximately the same geological age. All faults affect the limestones of the bedrock, but none appear to have displaced the lithological units that make up the valley fill. For this reason, they do not outcrop and are not visible when observing the model as a whole.

The data can be imported in the project work in several ways: directly on the topographic surface, via vertical profiles (representing synthetic boreholes), via sections that can be orientated vertically or in any direction, or directly via specific coordinates. Raster maps are integrated into the model by georeferencing and subsequent digitisation. Thousands of surface and depth data points, describing lithological contacts and tectonic discontinuities, have been imported to accurately represent the subsurface morphology of each unit.

Geomodeller employs a vector field interpolator to construct 3D interfaces and fault planes. The reconstructed 3D model is finally displayed in Figure 6.17. Users can export either the final model or individual datasets in a variety of formats.

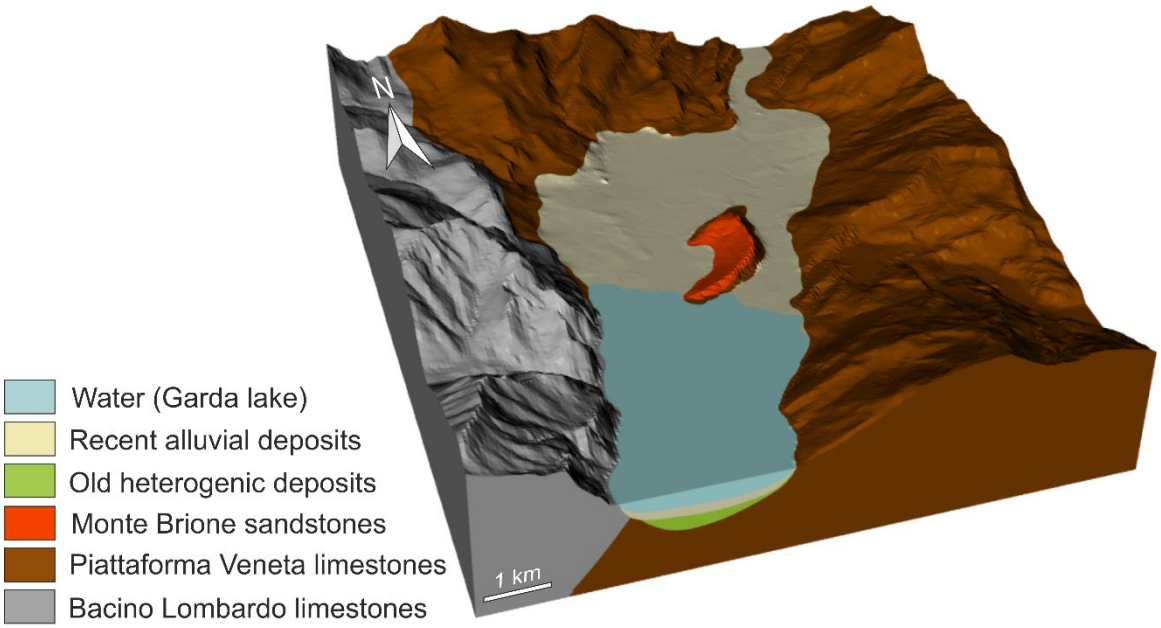


Figure 6.17. Reconstruction of the subsurface 3D model of the Sarca Valley study area.

To perform the physics-based numerical simulations of the seismic wave propagation, the geophysical parameters of each unit must be defined. In particular, we assigned to each unit the values of the following parameters:

– the velocities V_P and V_S of the compressional and the shear seismic wave, respectively;

– the mass density ρ;

– the Poisson's ratio;

– the factors Q_K and Q_S, shear and volumetric damping factors, respectively;

– the total attenuation coefficient D.

Table 6.6 lists the values of physical properties assigned to the lithological units. The addition of a superficial weathering and fractured layer can be seen in Table 6.6 although not shown in Figure 6.17.

This layer was included in the model with a variable thickness, from 25 to 30 m, to account for the weathering of the outcropped limestones. In addition, the thin sandstone layer, which occurs exclusively on Monte Brione and is accurately represented in the 3D model, is considered analogous to the weathered layer in terms of physical properties. Consequently, four different lithological-physical units are identified, to which it must be added the lake water layer.

Table 6.6. Physical and mechanical properties of the lithological units encompassing the subsurface lithotypes of the Sarca Valley. The properties listed include S-wave velocity, P-wave velocity, density, Poisson's ratio, shear damping factor, volumetric damping factor and total damping coefficient.

Properties	Lithological units				
	Recent deposits	Old deposits	Weathered layer	Bedrock	Water
Vs (m/s)	450	950	920	2500	0
Vp (m/s)	1825	2175	2100	4500	1500
ρ (Kg/m^3)	1800	2150	2000	2800	1000
υ	0.4	0.3	0.3	0.2	-
Q_K	150	300	300	750	10000
Q_S	50	100	100	250	0
D	1.1%	0.5%	0.5%	0.2%	0

6.1.2. Local Seismic Response analyses

Before numerical simulations are used to investigate the local seismic response, the model must be validated, i.e. it must be proven that the characteristics of the ground motions simulated with the 3D model are compatible with the characteristics of the ground motions actually observed at the seismic stations in the study area.

Once the reconstructed subsurface model is as realistic as possible, local seismic response analyses can be performed. In order to evaluate the presence of three-dimensional effects on the seismic response, 1D and 2D simulations were performed in addition to the 3D numerical simulations, keeping the same properties, settings and seismic inputs.

6.1.2.1. Model validation through numerical simulations

The 3D model shown in Figure 6.17 is validated by the SPECFEM3D software (Peter et al., 2011) by numerical simulation of seismic wave propagation and comparative analyses are carried out at 19 points corresponding to the locations of the temporary seismic stations installed on site (Fig. 5.14).

The seismic input used is an impulsive plane wave with uniform amplitude polarised along the three spatial components (see Chapter 4 for more details). The frequency range considered was 0.5-5 Hz and was determined based on the hexahedral mesh size used in the numerical simulations, which is 25m in the x-direction, 25m in the y-direction and about 25 m in the z-direction, since near surface the elements adapt locally to the topography.

The following parameters were used to compare empirical data with synthetic data and to verify the validity of the model created with Geomodeller:

- Amplification functions derived from the application of the Generalised Inversion Technique (GIT) to earthquake recordings from 19 seismological stations. These curves represent the spectral amplification of the site compared to a reference site (site TN02, which is located on rock without amplifications).

- Response functions calculated as the spectral ratio between the output recorded at the 19 synthetic stations and the output at the same reference station TN02, convolved with the same earthquake records used in the GIT analyses (RSSR).

In this study, a moving average was applied to numerical data. Smoothing was intentionally kept to a minimum by using a centred 3-point window to calculate the average. This approach ensures that the most important features of the data are preserved while avoiding excessive smoothing. In choosing the smoothing parameters, a balance was sought between improving the readability of the functions and preserving the integrity of the experimental results.

In order to achieve a reasonable match, iterative tests were performed that included adjustments of the morphologies within the Geomodeller project. After several iterations of the numerical simulations, a good fitting between the curves was achieved, as shown in Figure 6.18.

The comparative analysis of the curves shows that the simulation results exhibit more pronounced oscillations compared to the experimental recordings. In particular, the numerical response functions show greater local variability, while the experimental amplification functions appear smoother and follow a more regular trend.

This discrepancy could be due to frequency-dependent attenuation in the experimental data or, more likely, to noise filtering of the measurements, which would yield smoother amplification functions than the simulated ones.

Discrepancies between the experimental and numerical amplification functions are observed in the low frequency range (generally < 0.7 Hz). The lower amplification values observed in the numerical results could be due to different factors: The numerical model may not fully capture certain site-specific features, such as small-scale heterogeneities or damping properties, which may affect the response at low frequencies; or the experimental data may be affected by limitations in the measurement setup, including sensor sensitivity and background noise, especially at low frequencies.

However, it is important to highlight that low frequencies are not the focus of this study, as our analysis concentrates on the range between 0.7 Hz and 4 Hz. While the discrepancy at low frequencies is acknowledged, it does not affect the validity

of the results within the target frequency range, where the agreement between experimental and numerical data is satisfactory.

For certain stations, no optimal fit is achieved: for example, the response function of station TN11 in the numerical simulation remains consistently lower than the experimental amplification. Although the station is located on bedrock (where the theoretical amplification should be 1), it is likely that local factors, such as stronger fracturing of the outcropping rock, lead to a higher experimental amplification. However, this discrepancy does not necessarily need to be reproduced as the focus of this study is on the valley area.

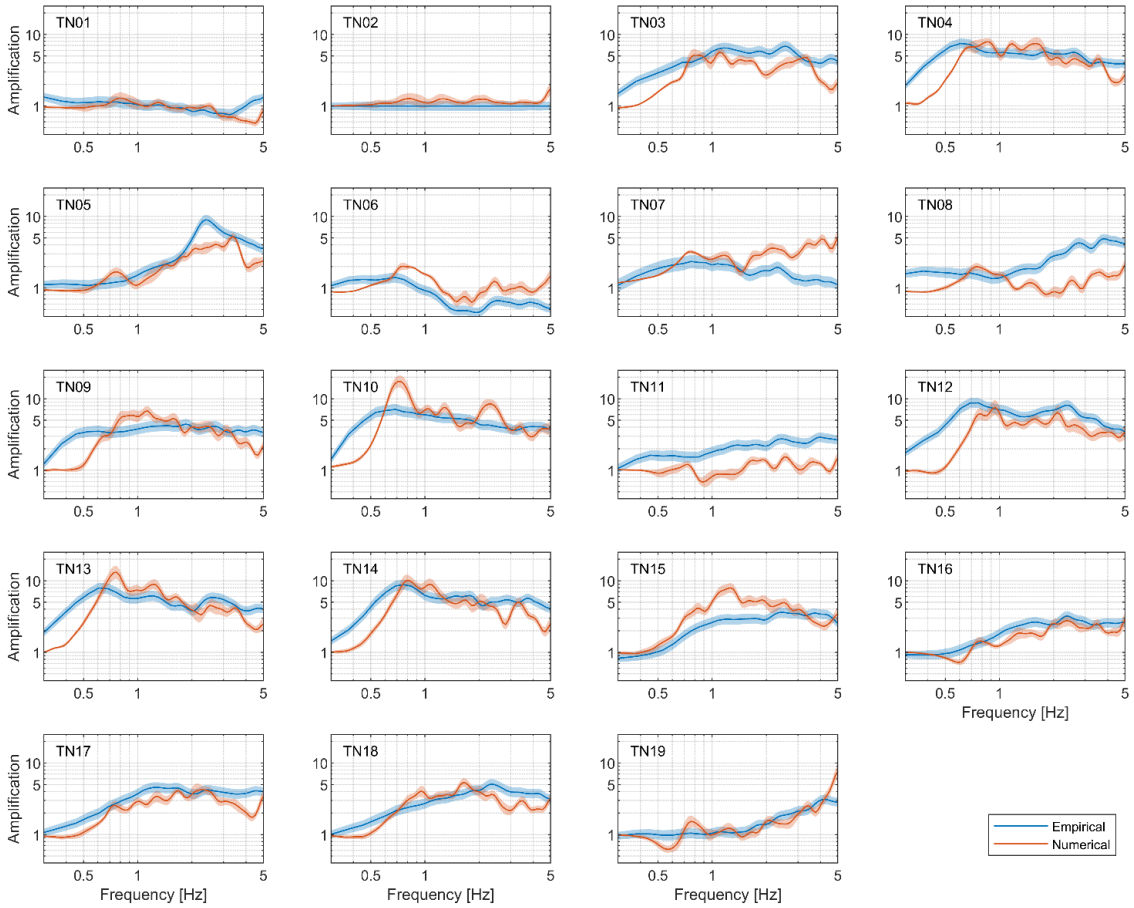


Figure 6.18. Comparison between empirical data (GIT) and numerical results from the simulation (RSSR). The shaded band shows the standard deviation.

6.1.2.2. 1D Seismic Numerical Simulations

In order to evaluate and prove the existence of three-dimensional effects on the seismic response, 1D simulations were carried out and then compared with the 2D

and 3D analyses. Mono-dimensional analyses are performed based on the assumption that the seismic wave propagates vertically through horizontal plain-parallel layers. These analyses do not take into account lateral variations either in geometries or physical properties. Therefore, they primarily capture the phenomenon of seismic amplification caused by the stratigraphic effect.

The Sarca Valley study site is not suitable for such an analysis, as additional seismic effects are to be expected here. Nevertheless, we want to carry out the analysis, examine the results and compare them to recognise the differences.

The results were extracted and compared with those of the reference site TN02 to obtain synthetic response functions for each of the 19 seismic stations selected as comparison points. Figure 6.19 shows the stratigraphic profiles extracted from the 3D model at these 19 stations, used for the 1D analyses. The analysis was carried out with the LSR2D software, which also supports a 1D mode. To ensure consistency between the 1D, 2D and 3D analyses, the same settings is used for all models: a viscoelastic model is chosen to represent the attenuation behaviour of the soil. Also the used physical properties are the same for 1D, 2D and 3D simulations and listed in Table 6.6.

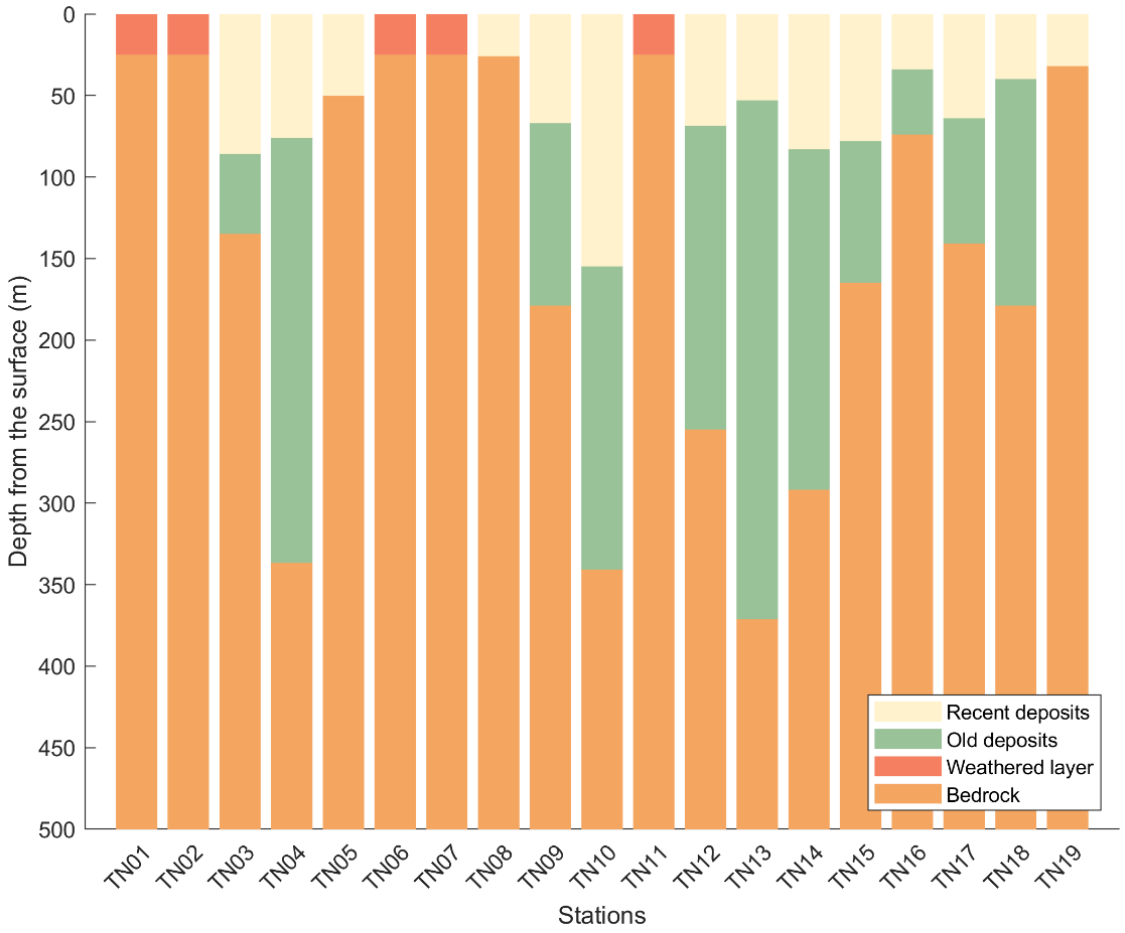


Figure 6.19. Stratigraphic columns extracted from the 3D model at the locations of the temporary stations, used as designed stratigraphy for the 1D simulations.

Since only the stratigraphic effect is taken into account, the amplifications shown in Figure 6.20 are exclusively due to the presence of deposits of different thicknesses. At stations TN01, TN02, TN06, TN07 and TN11, where the rock is outcropping, the spectral ratio calculated in relation to an identical location leads to an amplification of 1. Furthermore, the analysis of the remaining 14 plots shows the presence of similarities between the different transfer functions. In order to identify possible clusters, the general shape, position and amplitude of the peaks were considered. Based on these observations, a possible subdivision into two valley zones with different responses can be proposed: The first zone includes stations TN5, TN8, TN16 and TN19, which are characterised by curves with well-defined and prominent peaks that are free of significant minor fluctuations; the second zone includes all other stations, which have a more complex and heterogeneous shape.

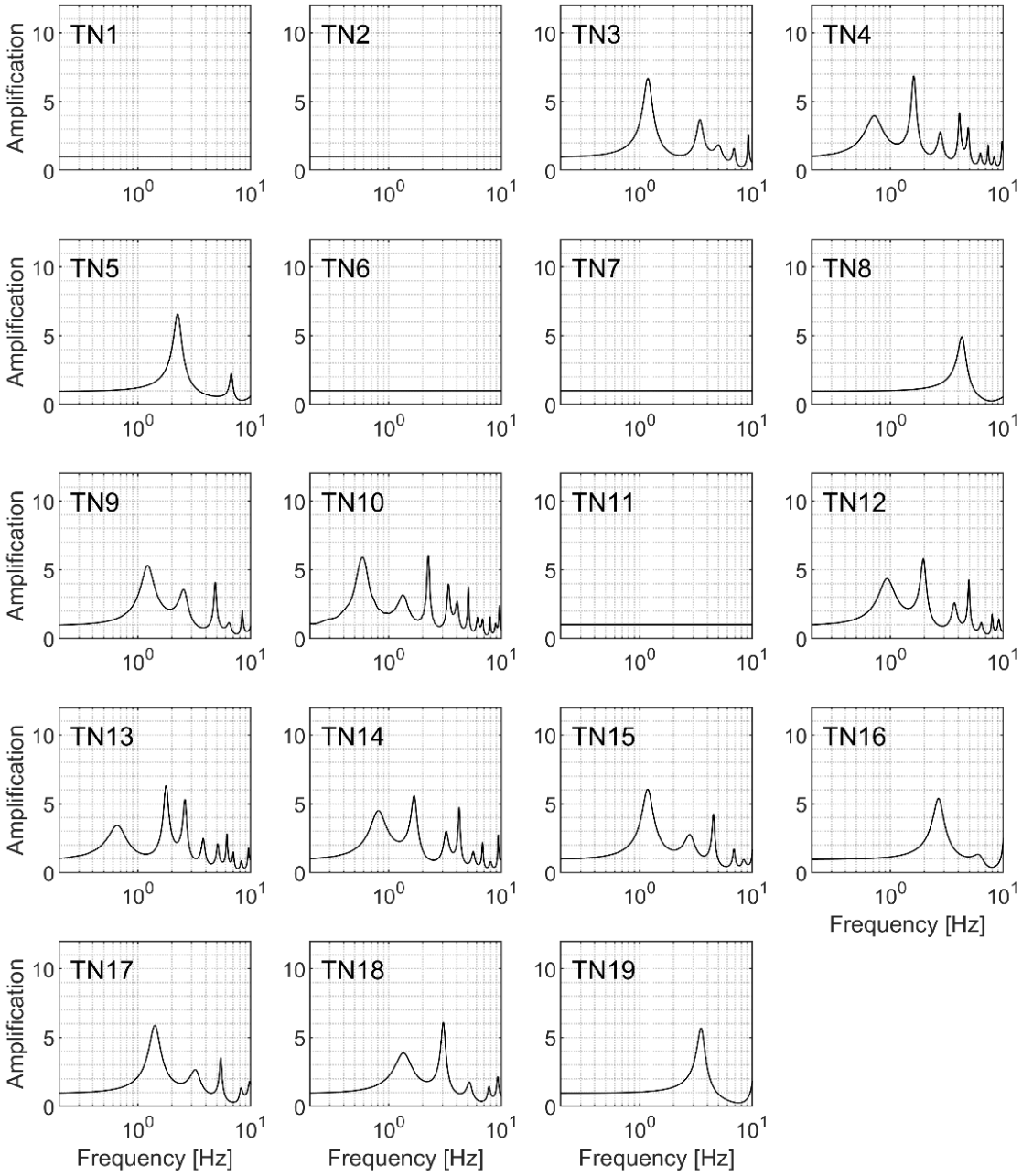


Figure 6.20. Amplification results from 1D simulations.

Figure 6.18 shows that geophysical investigations empirically demonstrate amplifications of up to 9. The results of 1D analyses indicate that the input motion is amplified by a factor of up to 7, even when only the stratigraphic effects are considered. This result clearly shows that the stratigraphic effect plays an important role in the overall seismic response.

6.1.2.3. 2D Seismic Numerical Simulations

2D analyses of seismic response take into account the spatial variation of soil properties and geometries and offer greater reliability in modelling geological conditions compared to 1D analyses. At the same time, they are associated with lower computational costs than 3D analyses, making them a common choice for many response studies.

For the Sarca valley, as the temporary stations were installed in three approximately linear transects, the 2D analyses were carried out on three sections corresponding to these transects (Fig. 6.21).

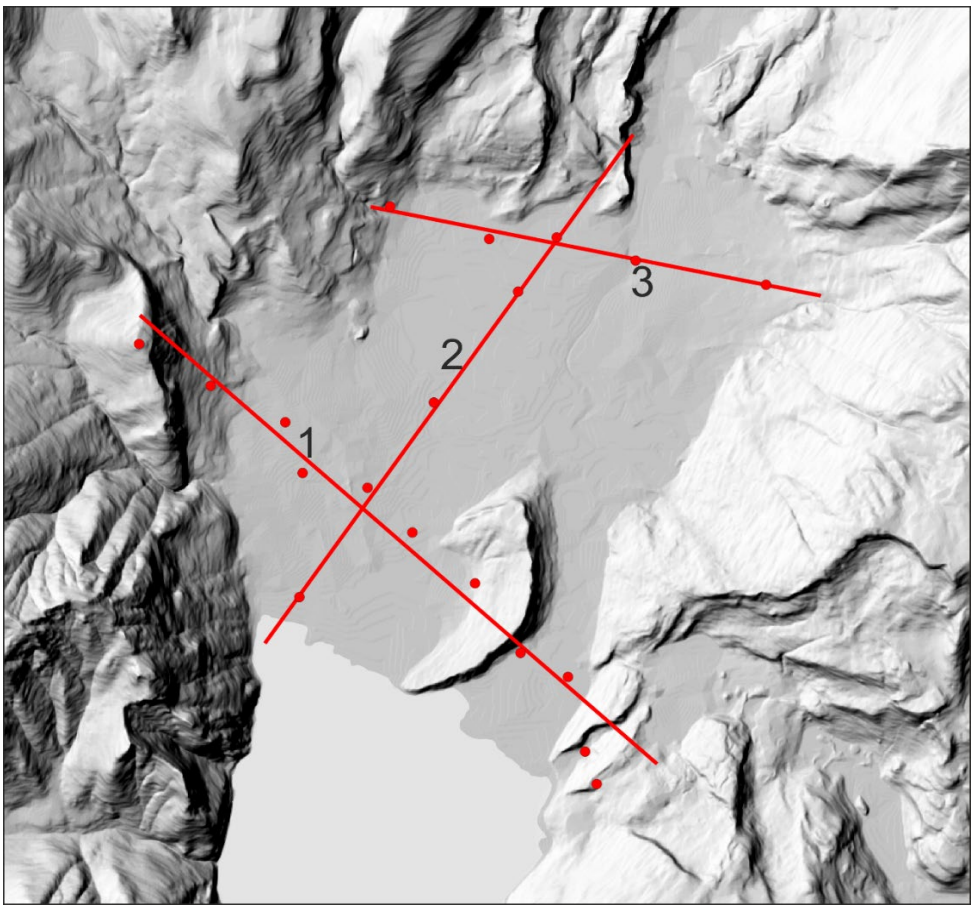


Figure 6.21. Location of the temporary seismic stations (red dots) and position of the sections (red lines) analysed using the 2D method.

The projects were created with the LSR2D software, whereby the physical and mechanical properties correspond to those of the 1D analyses and should also be applied in 3D. For this analysis, the section was discretised into triangular elements with a size of 5 m to ensure a reliable analysis of the seismic response up to frequencies of 10 Hz. Figure 6.22 shows sections of the 3D subsurface model used

for the 2D simulations. Although not visible in this figure, boundary conditions are applied at both ends of the sections (see Chapter 4 for more details).

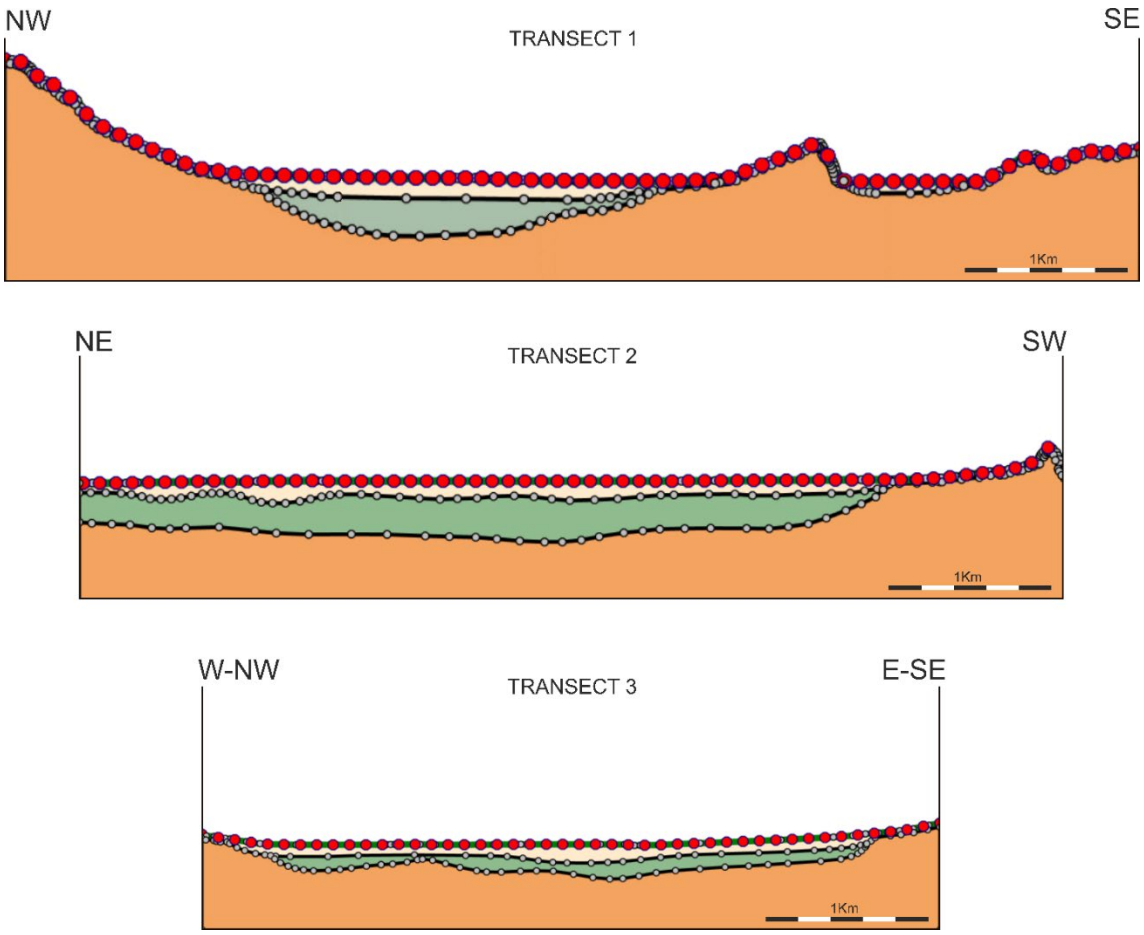


Figure 6.22. Sections extracted from the 3D subsurface model used for the 2D simulations. The scale is the same both vertically and horizontally in all three sections.

Oscillations propagating through the section were recorded at evenly spaced surface receivers, shown as red dots in Figure 6.22. Various results were derived from these seismic recordings, which are described below. As can be seen in Figure 6.21, the spatial arrangement of the seismic stations is distributed along three approximate, although not perfectly aligned, transects. An orthogonal projection was performed to accurately position each station along the transect line. This allowed the identification of the surface receiver closest to each station and thus the extraction of the corresponding results.

The first set of results compares these findings with those of the 1D analyses. Figure 6.23 shows the same 19 previously selected points with response functions

calculated as the ratio between the Fourier amplitude spectra and the Fourier amplitude spectrum recorded at the reference site (station TN02).

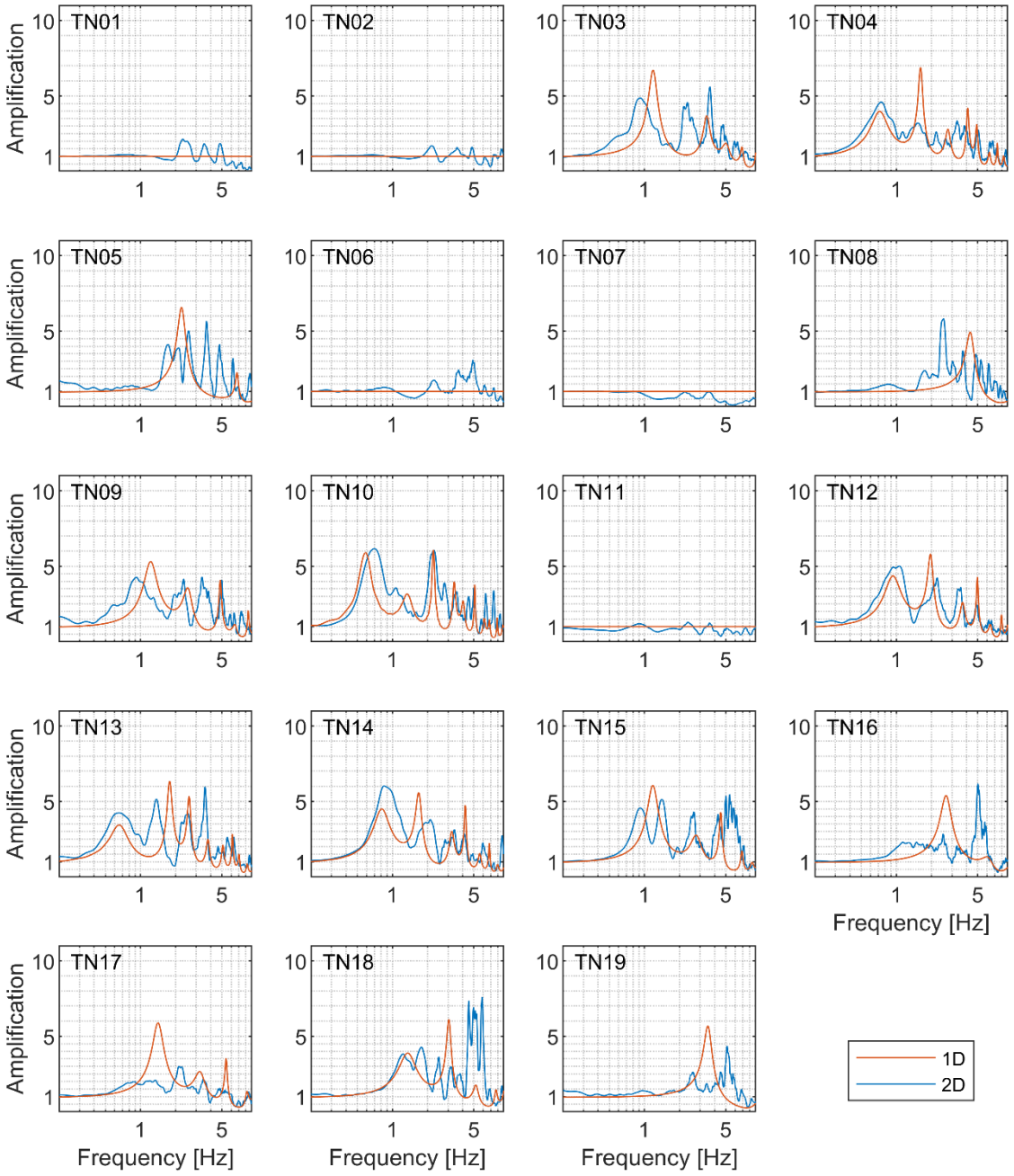


Figure 6.23. Amplification results from 2D simulations compared with 1D simulation results.

The amplification curves show clear differences between 1D and 2D analyses. In some parts of the functions, the 2D analyses show higher amplification values compared to the 1D results, while in other parts the 2D amplification is lower. This is because, as mentioned above, the stratigraphic effect, although important, is just one of the factors influencing the response. In regions where the receivers are

located within the valley, resonance effects related to the morphology of the valley become evident. In contrast, topographical effects predominate in areas with outcropping bedrock. In addition, 2D amplification curves have a higher degree of complexity compared to their 1D counterparts. As 1D analyses are solely influenced by stratigraphy, they produce clearly defined amplification peaks that are localised at specific frequencies. In contrast, 2D curves show more complex and less defined peaks that are often localised at different frequencies than those observed in the 1D results. This complexity reflects the interaction of several factors, such as the topography and geometry of the subsurface, which together influence the behaviour of the amplification curves.

From these results it can be deduced that in areas where the 1D and 2D curves are close to each other, the amplification is predominantly affected by stratigraphic effects. Conversely, where significant differences between the results can be observed, it is clear that the valley effect plays a prevalent role.

Figure 6.24 shows amplification values (the same as in the previous figure, but in a different form) as a function of frequency and spatial variations along the entire profile of the sections. The x-axis represents the length of the section, while the y-axis shows the frequencies on a logarithmic scale. Amplification values are colour coded. Areas with particularly high amplification levels are clearly recognisable.

In the first section, the amplification areas are concentrated near the centre of the larger valley in the west, with a significant intensity between 0.5 and 1 Hz. Another peak with a maximum amplification of 10 is observed within the valley, occurring at frequencies between 2.1 and 2.3 Hz. Moving further to the right, another peak appears in the secondary valley to the east of Monte Brione with a frequency range between 1.5 and 2 Hz.

The second section shows a broader distribution of amplification compared to the first section, with peaks occurring predominantly between 0.5 and 1 Hz showing a lower amplification than the ones in the previous section. This distribution extends over the entire section and is not limited to a specific range. The observed behaviour is related to the spatial configuration of the section, which crosses longitudinally the western valley from the Garda Lake to the bedrock edge in the northeast zone of the valley (see Figure 6.22).

The third section has a more symmetrical amplification pattern than the previous ones, with a high concentration in the centre at frequencies between 0.7 and 1 Hz.

At the edges of the valley, two lateral regions with lower amplification values are visible, occurring between 1 and 1.5 Hz. Beyond the main amplification zones, additional peaks with lower amplitude are observed at higher frequencies, possibly corresponding to higher order modes with regularly spaced fringes.

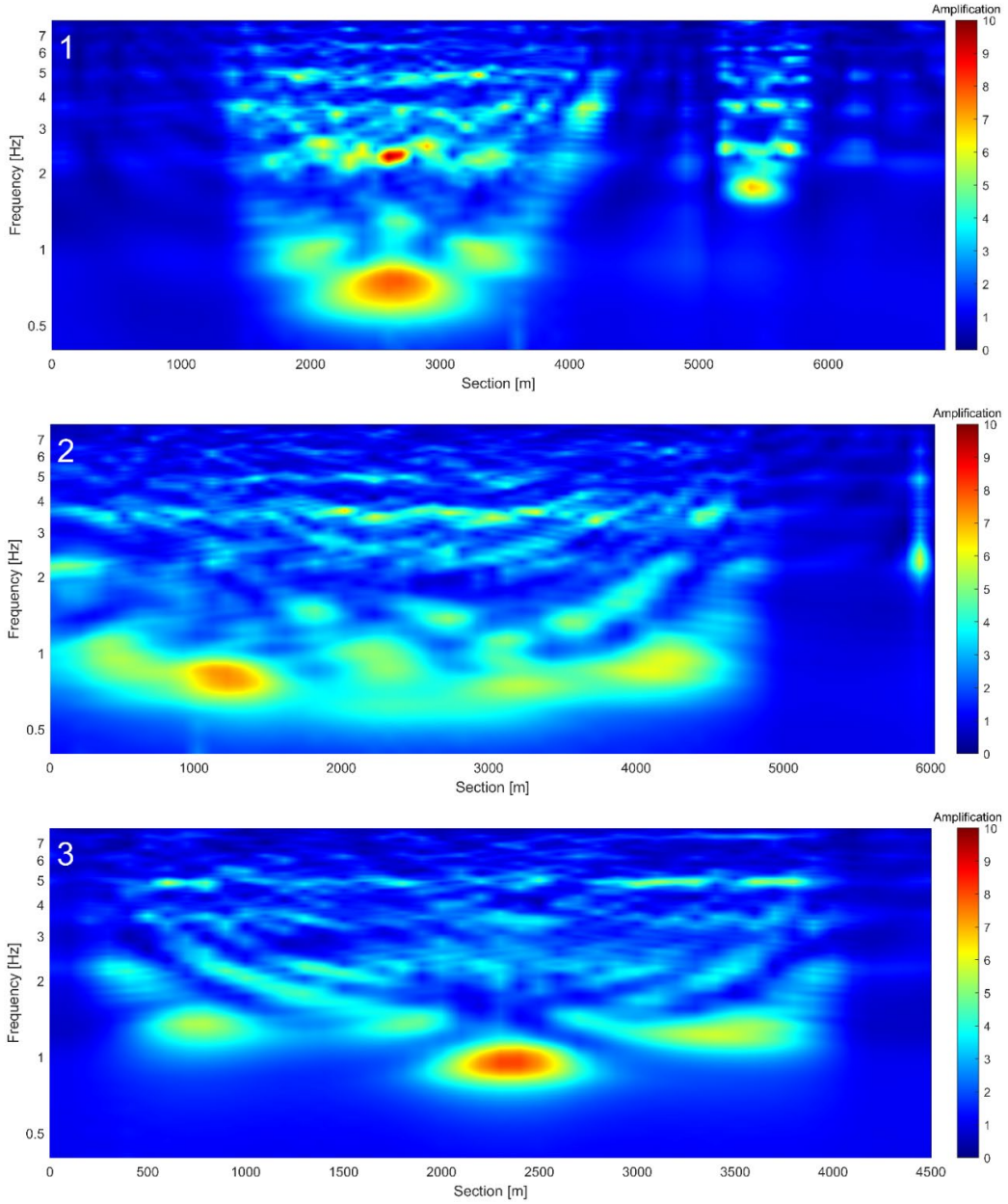


Figure 6.24. Transfer functions plot showing the amplification values along the entire surface profile for the three sections, calculated using the 2D method.

6.1.2.4. 3D simulations

The 3D simulation carried out with the SpecFEM3D software (Peter et al., 2011) corresponds to the final validation test carried out to check the likelihood of the

Geomodeller model. However, it allows a more detailed analysis of the seismic response of the site.

Figure 6.25 shows a comparison of the curves obtained from the 1D, 2D and 3D analyses. The figure shows the response functions calculated as the Fourier spectral ratio between the surface outputs recorded at the 19 temporary station sites and the output recorded at point TN02 (which is considered the reference site for this study area).

The analysis of the curves shows significant differences. The comparison between the 1D and 2D curves shows that although the stratigraphic effect is important, it is not exhaustive to fully capture the seismic response at the site. The 2D simulation already shows amplifications related to the valley effects, while the 3D simulation shows a more complex distribution of amplified frequencies. Stations TN01, TN02, TN06, TN07 and TN11 are located on the bedrock. Nevertheless, a certain amplification can be observed, which is probably due to topographical effects.

It is important to note that the contribution of 3D components does not necessarily lead to greater amplification in all cases. Although this effect is often observed, it is not always present. In particular, a different distribution of amplified frequencies is often observed in the 3D analyses. This observation emphasises the importance of considering all three spatial components, as this ensures a comprehensive understanding of the seismic response.

To further investigate the three-dimensional response, the results were extracted on a grid with a spacing of 50 metres. This allows us to visualise the spatial distribution of the local seismic response within the valley. The analysis shows that in almost all areas of the valley, the recorded amplifications are more than five times larger than the shaking recorded on the bedrock. It is important to note that this value represents the final amplification resulting from the cumulative effect of all existing seismic influences. A more detailed analysis can be performed using Figure 6.26, which illustrates the amplification across different frequency ranges. The response functions were calculated as the ratio of the Fourier spectra relative to the reference site. The resulting curve was divided into six frequency bands and the average amplification within each band was calculated. It is noticeable that amplification values in all frequency bands are relatively high for most areas of the

valley. However, certain fundamental frequencies need to be considered for a proper seismic zonation planning.

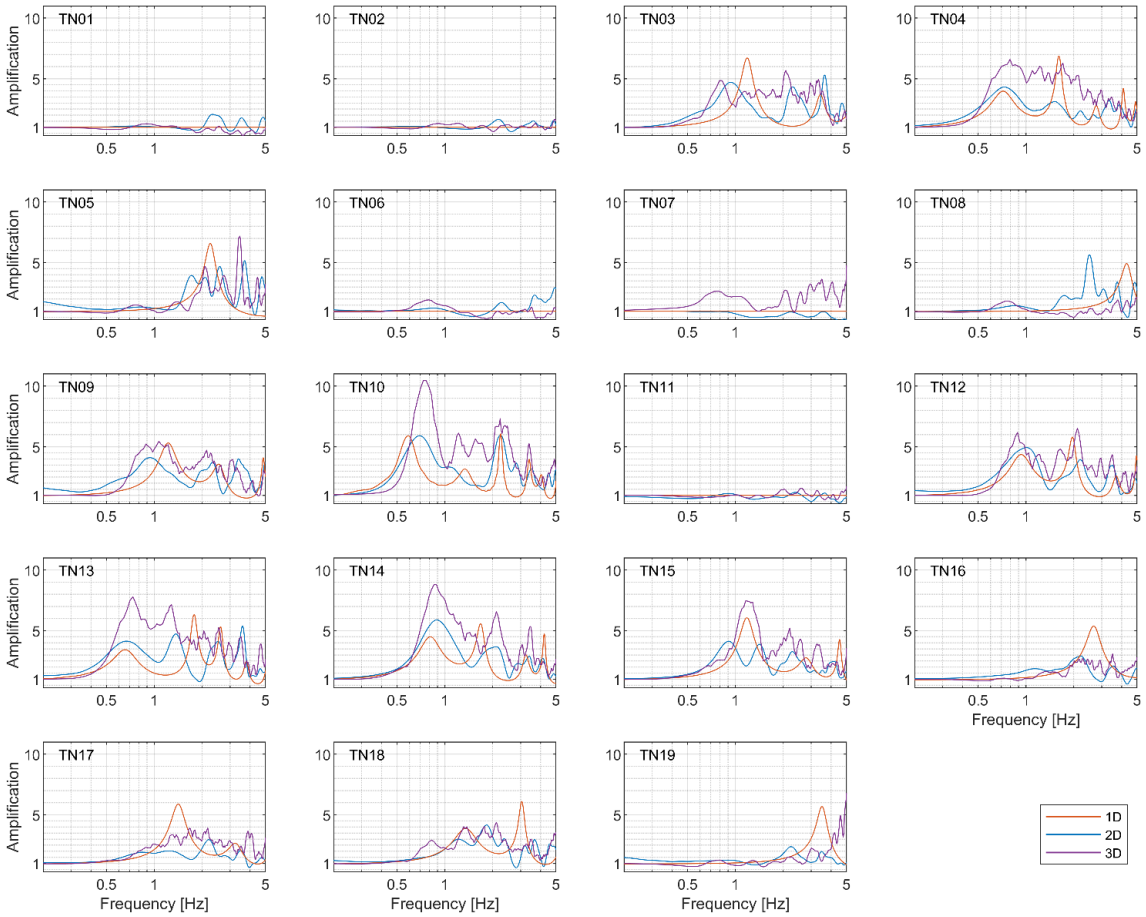


Figure 6.25. Comparison of the response functions calculated from 1D (orange curves), 2D (blue curves) and 3D (violet curves) numerical simulations.

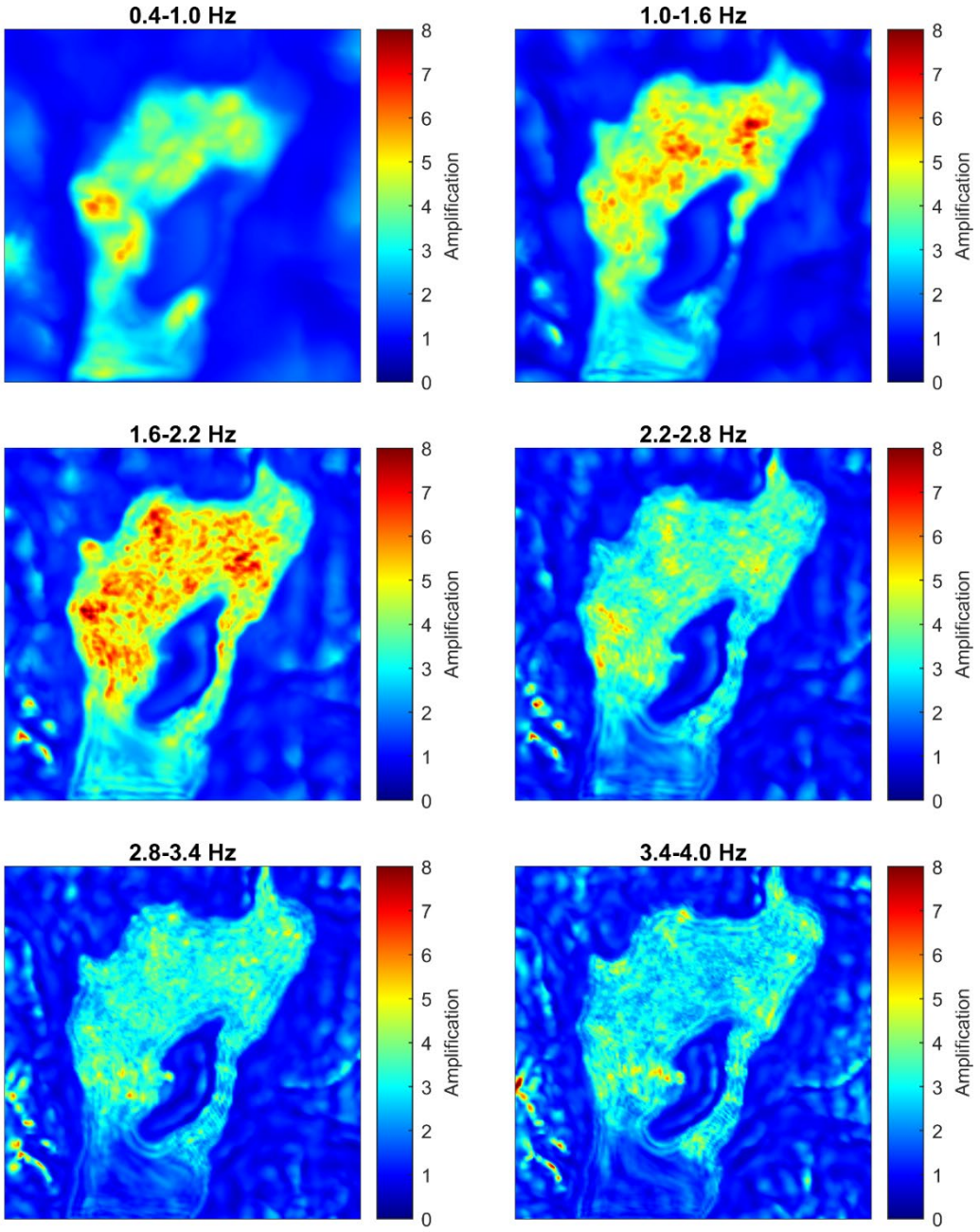


Figure 6.26. Spatial distribution of seismic amplification values, averaging of the three motion components, divided into 6 frequency ranges.

The 1.6–2.2 Hz range appears to be the most amplified, reaching values between 5 and 8, and this is true for almost all areas of the valley except the edges. The 1–1.6 Hz range also shows a generally high level of amplification (from 4 to 7), with two principal areas in the northern part of the valley showing greater amplification. However, the small valley to the east of Monte Brione shows only minimal amplification up to 3, in this frequency range. The range from 0.4 to 1 Hz is less uniform; in particular, the eastern area is not affected at all, while the western valley

shows two main regions: the southern one is clearly amplified, reaching also values of 6, while the northern one is less amplified (from 3 to 5). The trend from 2.2 to 4 Hz is quite similar, with the averaged values showing no clear pattern.

To better understand the subdivision of the zones at different frequencies, Figure 6.27 shows a map in which the frequency corresponding to the peak of the response function curve is plotted for each point in the valley. Only the peaks with an amplification value greater than 2 are taken into account.

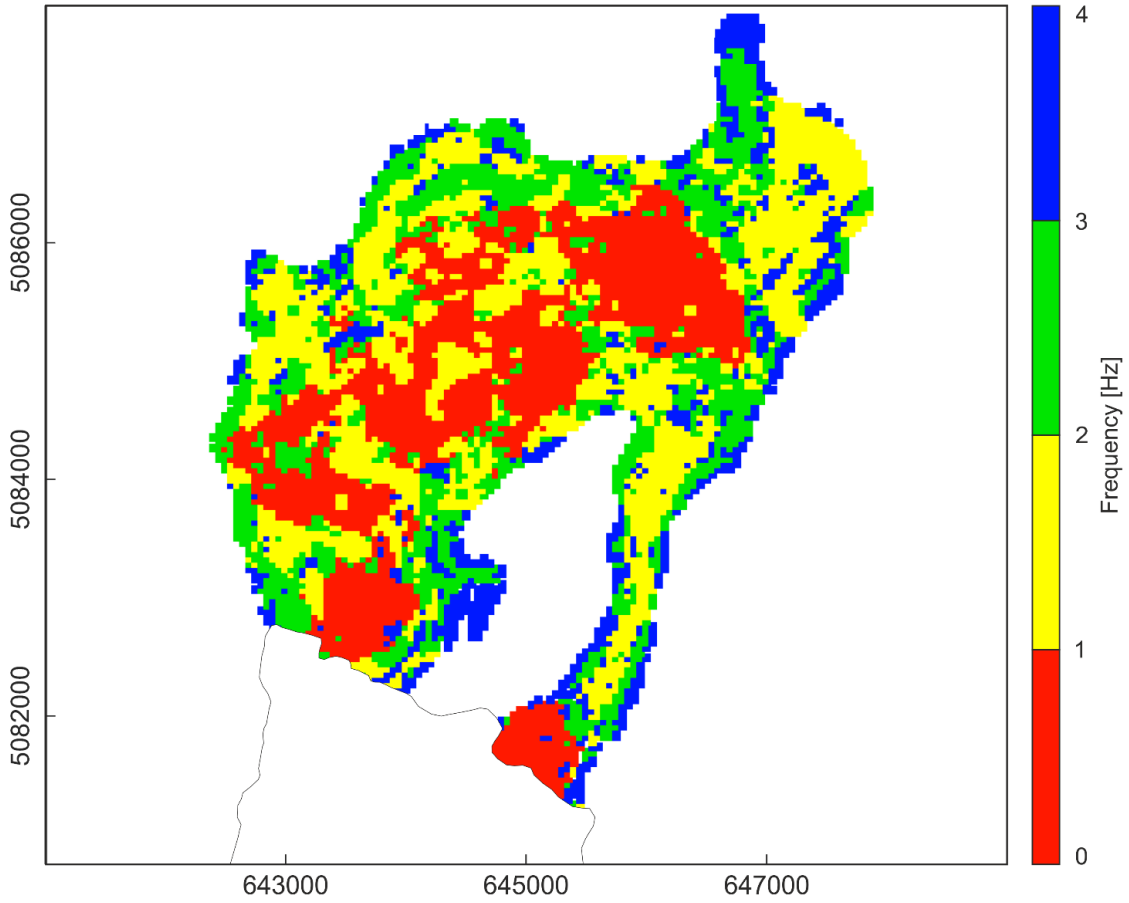


Figure 6.27. Spatial distribution of the frequencies corresponding to the amplification peaks.

A pronounced valley effect can be seen in Figure 6.28, which shows a series of snapshots extracted during the seismic propagation. Approximately 1 second after the event, the arrival of the wave is observed, followed shortly thereafter (at 1.5 seconds) by the generation of surface waves at the edges of the valley. Subsequent images show that the waves are trapped in the sediments, resulting in amplification and a longer duration of motion. Although the initial period of oscillation is an impulse (see Chapter 4 for more details on seismic input), oscillations of more than 13 seconds duration were observed within the valley.

Although this phenomenon is already known, the results emphasise its importance for the analysis of seismic responses in terms of possible damages induced by the shaking energy transmitted from the ground to the structures.

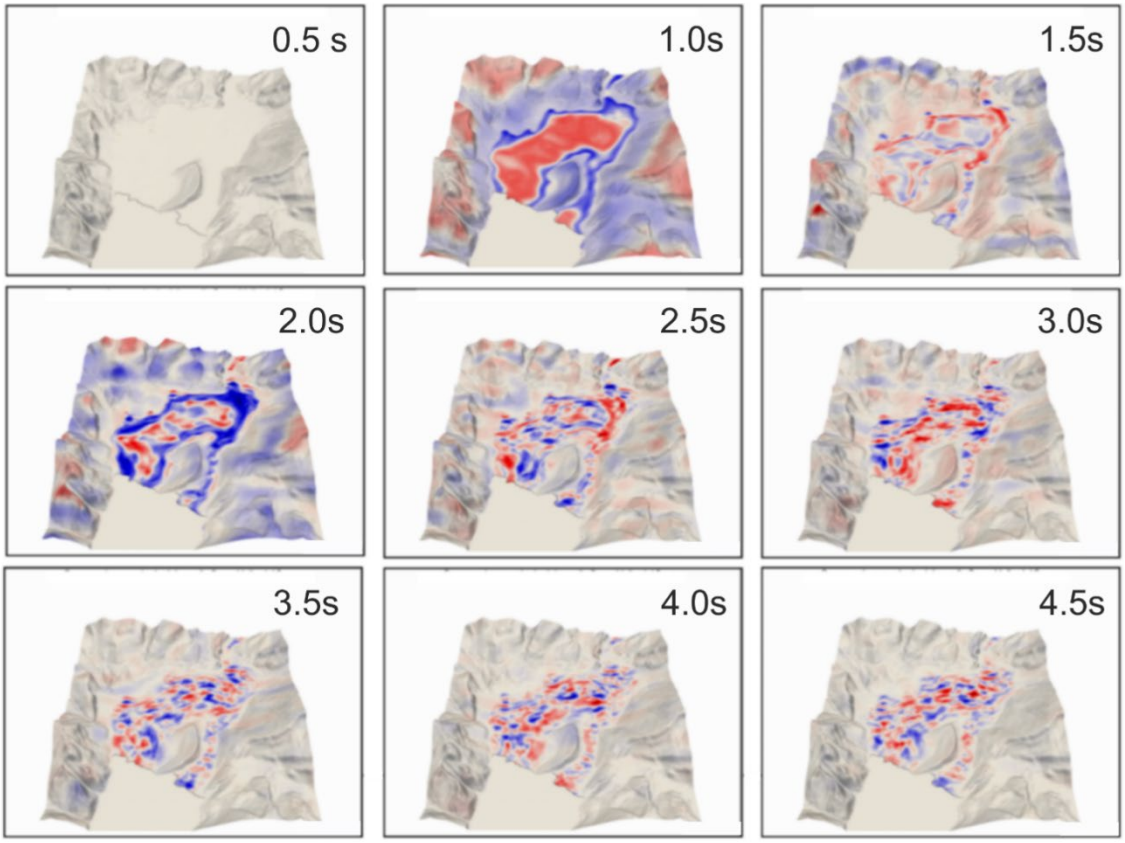


Figure 6.28. Snapshots of the wave field (resulting from the three components) at the surface at different propagation times.

6.2. Arquata del Tronto

The Arquata del Tronto site was initially analysed as the case study of my master's thesis and later published by Primofiore et al. (2020). The methodology used for the reconstruction of the 3D model and its validation through comparison with experimental records is consistent with the approach used for the Sarca Valley study area. Several data acquisition methods were integrated for the subsurface model reconstruction, such as Down Hole surveys, Seismic Reflection profile, Electrical Resistivity Tomography, Multichannel Analysis of Surface Waves, Horizontal to Vertical Spectral Ratio technique and Generalized Inversion Techniques. During the calibration and validation phase, experimental curves from two temporary seismic stations were compared with numerical curves derived from seismic simulations. This iterative comparison ensured a high degree of model accuracy and reliability, as described in detail in Primofiore et al. (2020).

Model validation was initially performed using SpecFEM3D software with a viscoelastic approach. Given the limited extent of the study area, a more detailed analysis is now performed with a constitutive law highlighting the non-linear behaviour typical of soils. The commercial software Flac3D was used for this purpose. Figure 6.29 shows the three-dimensional reconstruction of the subsoil volume of 800 m x 800 m x 200 m, which was created with the internal mesher of Flac3D.

Table 6.7 summarises the physical-mechanical properties of the lithological units in the study area, which were determined by an integrated analysis of the experimental data and the existing literature. These properties are crucial for defining the seismic response characteristics of the model and provide a solid basis for accurate simulations of seismic wave propagation.

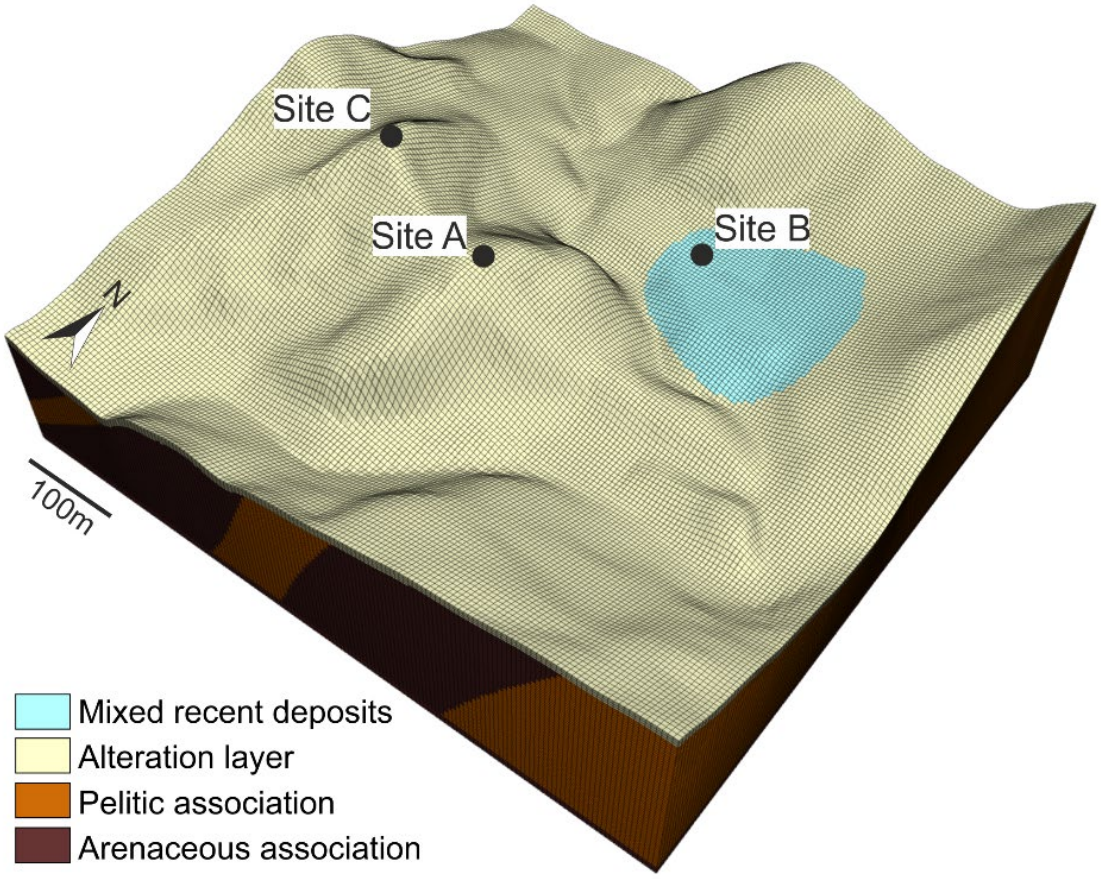


Figure 6.29. Reconstruction within the Flac3D software used for seismic numerical simulations. The model is described by Primofiore et al. (2020). The three sites investigated are site A, which corresponds to the old town of Arquata del Tronto, site B, which is identified with the hamlet of Borgo located in a small alluvial valley, and site C, which harbours an ancient castle. Further finds from these sites were discussed in Chapter 5.

Table 6.7. Stratigraphic column of the 3D model for the Arquata del Tronto site with a geophysical characterisation of the individual lithological units. The properties listed include S-wave velocity, P-wave velocity, density, Poisson's ratio, shear damping factor, volumetric damping factor and total damping coefficient.

Lithological units	Vs (m/s)	Vp (m/s)	ρ (kg/m3)	υ	Qs	Qk	D
Mixed recent deposits	450	1100	1800	0.45	45	160	Rollins et al.,1998
Alteration layer	700	1700	2000	0.4	70	245	Linear 0.7%
Pelitic association	900	2250	2100	0.4	90	315	Linear 0.55%
Arenaceous association	1000	2250	2200	0.38	100	350	Linear 0.5%

Therefore, the first step of this study is to reproduce the results obtained with SpecFEM3D with Flac3D, both configured with a viscoelastic setting to verify how much affected are the results from different numerical methods implemented into the two software packages. This calibration step is important to ensure reliable cross-comparisons. The Flac3D mesh has been refined to achieve higher discretisation accuracy. An unstructured hexahedral mesh with an element size of 5 m in the x and y directions and a variable size of 4 m to 6 m in the z direction is used. In contrast, the SpecFEM3D model used a coarser mesh with 20 m spacing in the x and y directions and 18-22 m in the z direction. Thanks to this mesh refinement in Flac3D, the results achieve a validity of up to 14 Hz. On the other hand, the limited size of the spatial domain restricted the accuracy of the model for frequencies below 1 Hz.

An impulsive plane wave was used as input motion (details in Chapter 4), and the surface response functions were calculated at three predefined points of interest (locations A, B and C). The method used to analyse the output data was the same as that used for the Sarca Valley site.

Figure 6.30 illustrates the good agreement between the curves generated by the two software. The solutions were limited to frequencies up to 8 Hz, as the SpecFEM3D simulation, due to its mesh size, is reliable only for frequencies up to this value.

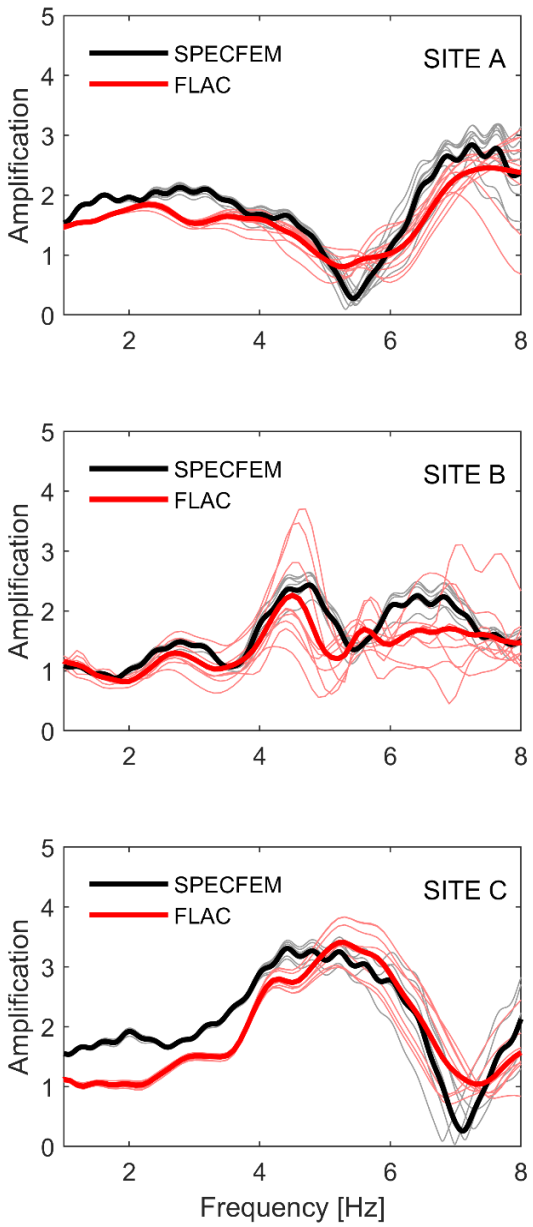


Figure 6.30. Comparison between the simulations performed with Flac3D and SpecFEM3D. The plots show the average of the response function for the three components calculated at specific points within the areas of the three selected sites (Site A, Site B and Site C). The thin lines represent the response functions at individual points, which were then averaged, while the thick lines indicate the average response function for each site.

6.2.1. Comparisons between linear and non-linear simulations

After confirming the consistency of the analysis, a linear-equivalent response analysis of the study area was conducted using a hysteretic damping model, and the results were compared with those of the viscoelastic response, both computed using Flac3D.

The methodology used to derive the damping formulae using a linear-equivalent constitutive model in Flac3D was explained in Chapter 4. Here we focus on the results of this procedure.

The behaviour of the soil was simulated numerically with hysteretic damping, while Rayleigh damping was applied for rocky lithological units.

To formulate this latter type of damping, it is necessary to determine the damping value and the associated natural frequency. The values of the Qμ-factor were converted into values of the D-ratio according to the relationship of Siebert (1986). The results are summarised in the last column of Table 6.7. To determine the natural frequency of the system, we observed free vibrations that resulted in an average central frequency of 3.08 Hz.

To model the non-linear behaviour of soils in the sediment-filled valley of Borgo, we applied hysteretic damping using the literature curves developed by Rollins et al. (1998). Calibration of these curves was required prior to their application in Flac3D. Among the available formulas, we chose a sigmoidal curve whose parameters were fitted with the function sig4: 1.12, -0.72, -1.09 and 0.03. To account for the negligible energy dissipation at low cyclic strain values, which is typical of hysteretic damping, a small Rayleigh damping component was added, which shifts the curve slightly upwards. The values used for the integration were a D-ratio of 0.011 and a natural frequency of 2.88 Hz.

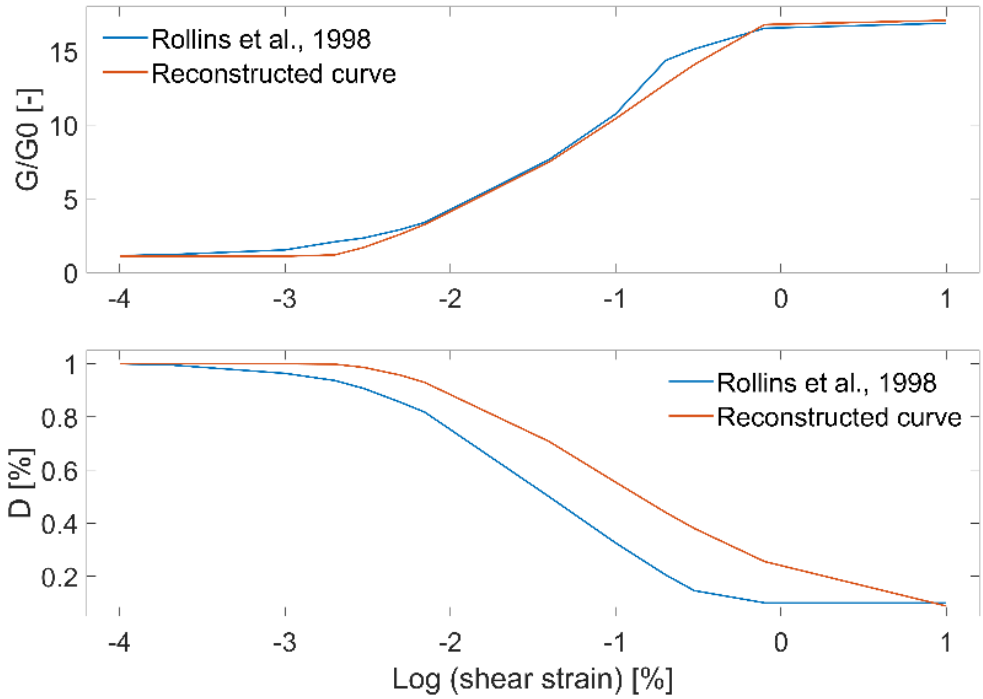


Figure 6.31. Left: Comparison between the experimental Shear modulus reduction factor curve of Rollins et al. (1998) and the curve reproduced with the Flac3D function after calibration. Right: Comparison between the experimental Damping ratio curve of Rollins et al. (1998) and the curve resulting from the calibration.

The response functions are calculated as Fourier ratios with respect to a reference site consisting exclusively of rocks and without topographical effects (plain conditions). These results are obtained by extracting the results on a regular grid of receivers at a distance of 20 m above the topographic surface of the model. In order to observe the non-linear behaviour of the soils, the comparison is only carried out at the recording points within the Borgo valley (site B), as hysteretic damping is only applied in this area.

A shift of the amplification peaks towards lower frequencies is observed (Figure 6.32), which is consistent with the expected response for nonlinear soil behaviour based on previous literature studies (Xu et al., 2003). The nonlinear damping mechanisms in loose soils, modelled by the hysteretic damping approach, lead to a reduction in stiffness with increasing strain and hence a reduction in natural resonance frequencies.

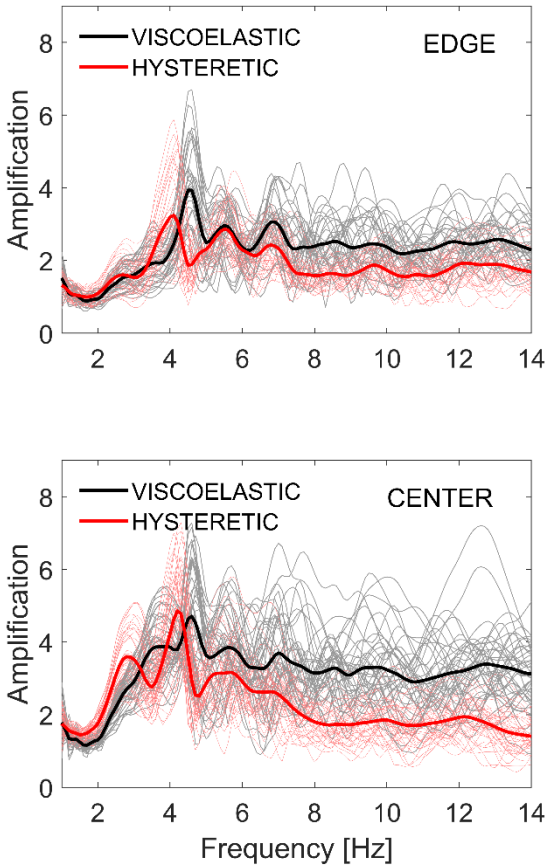


Figure 6.32. Comparison between simulations with viscoelastic and linear-equivalent behaviour with hysteretic damping. The plots show the average of the components of the response function calculated for all points of the valley, divided into the edge zone and the central zone. Thin lines: Response functions of the individual points; thick lines: Average response function for each zone.

This shift in peak frequencies is a direct consequence of the hysteretic damping model, which better captures the reduction in stiffness and the resulting decrease in resonance frequencies. This is a crucial aspect of seismic response modelling as it significantly affects the predicted resonance frequencies and potential damage in areas with such soils.

At higher frequencies, lower amplification values are observed compared to the results obtained through viscoelastic behaviour. This reduction is due to the improved energy dissipation mechanisms of the hysteretic model, which more accurately represents the non-linear deformation and energy loss in soils during seismic events.

It is noteworthy that a clear amplification is observed at the valley margins, even in areas with thinner deposits. This behaviour underlines the pronounced influence

of the 3D edge effect in small valleys, where wave reflections and interference at the edges lead to complex amplification patterns. The concentration of energy near the edges results from the geometric and material contrasts between the valley deposits and the surrounding bedrock, leading to localised constructive interference that is likely to be even more pronounced in smaller valleys such as the Borgo Valley.

6.2.2. Directional effects

The focussing of seismic waves is a phenomenon that is often analysed in reliefs and is known as a topographical effect. In asymmetric reliefs with preferential elongation, the cumulative site effect results from both topographical and polarisation influences. It is therefore useful to carry out a separate analysis for the horizontal directions of oscillation. In the case of the Arquata del Tronto ridge, the natural east-west orientation of the ridge simplified the analysis, as the components of the seismic input did not need to be rotated for orientation.

Figure 6.33 shows the amplification peaks of the response functions from simulations performed with seismic inputs polarised along the north-south and east-west oscillation directions. In the upper panel, which represents the E-W oscillations, there are no significant effects of wave focussing. In contrast, in the lower panel, which corresponds to the N-S input oscillation, a stronger amplification is observed along the ridge oriented perpendicular to the seismic input. This amplification is consistent with the results of He et al. (2020) and Pischiutta et al. (2010), who found similar behaviour. This amplification effect can be attributed to the particular geometry of the terrain and plays a decisive role in the assessment of seismic risk in mountainous regions. It suggests that sections for two-dimensional analyses should ideally be aligned perpendicular to the steepest slope.

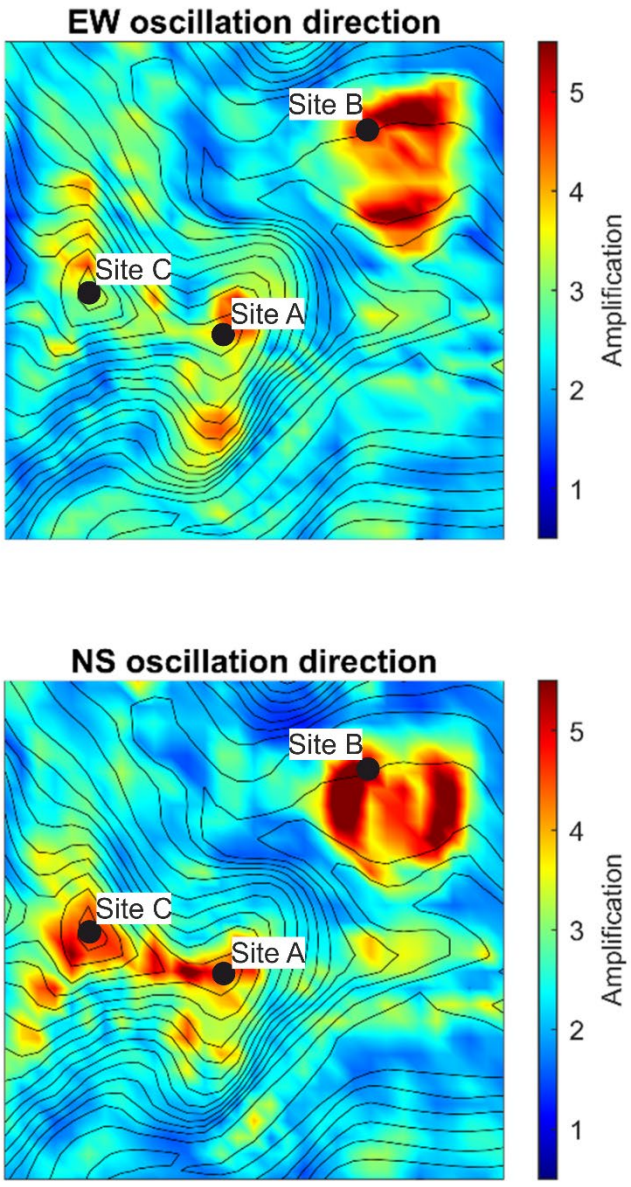


Figure 6.33. Peak value of the response function, for each acquisition point on the surface, for the 2 horizontal components of the seismic motion. Upper panel: polarisation of input motion in east-west direction; lower panel: polarisation of input motion in north-south direction.

In addition to topographic morphology, it is important to consider the orientation of lithological units that run parallel to the north-south direction of the ridge (see Chapter 5 for a detailed description of stratigraphic features). This orientation is the result of selective erosion processes in which the more erosion-resistant arenaceous layers stand out clearly distinguished topographically from the pelitic associations. This alternation between layers with different properties has the potential to significantly influence the direction of seismic wave oscillations and contribute to wave polarisation in addition to topographic influences. Previous

studies by Pischiutta et al. (2017) support this hypothesis and show how geological structures can alter seismic oscillation patterns. The combination of lithological and morphological factors makes the seismic response of this ridge particularly complex. Therefore, when selecting a 2D seismic analysis section, it is important that it is orientated as perpendicular as possible to the layer sequence. However, this approach has its limitations in more complex, planar scenarios where 3D analysis is required.

In the polarisation analyses, a pronounced seismic response was observed within the small valley at Site B, which does not behave as a single coherent body. The polarisation of the oscillations contributes to increased seismic motion in certain areas, particularly along the valley margins. This behaviour is most pronounced where the edges are aligned parallel to the direction of seismic vibrations. The combined influence of edge orientation and site geometry appears to control wave propagation, resulting in an uneven distribution of seismic responses.

6.2.3. Torsional motions

Torsional (or rotational) motions, defined as rotations around the vertical axis, are caused by the interaction between seismic waves and topographic or stratigraphic heterogeneities. This motion is expressed by the angular velocity, which is calculated from the time histories of the velocity components recorded along the three spatial directions at the surface. Since this is a quantity derived from seismic time series data, it was necessary to convolve the response functions (obtained with an impulsive input in the numerical simulation) with an actual seismic signal. The reference event chosen for this analysis is the earthquake of 30 October 2016, which is characterised by a moment magnitude Mw=6.5 and a hypocentre at a depth of 9.2 km with coordinates 42.8322°N and 13.1107°E. The seismic recording used comes from station MZ10, located in Amatrice in the San Cipriano district (42.625117°N, 13.299850°E), 27.7 km far from the epicentre. This recording is shown in Figure 6.34 both in the time domain and as a response spectrum.

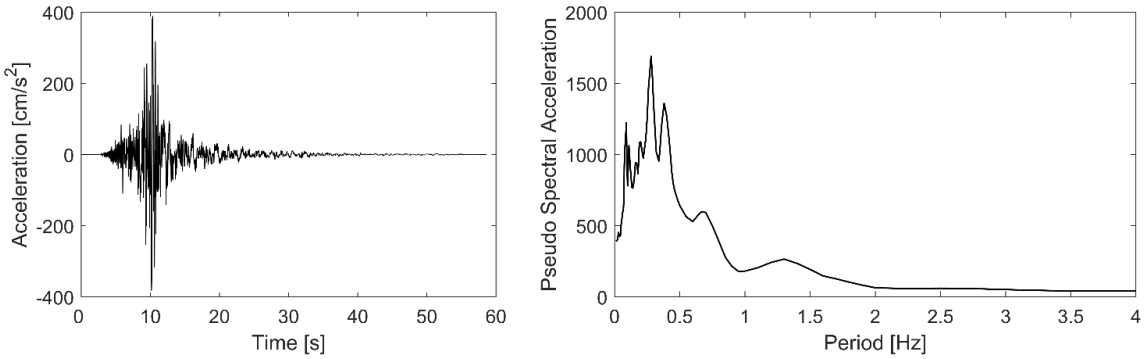


Figure 6.34. Graphical representation of the Mw=6.5 earthquake recorded in Amatrice on 30 October 2016. This event was used as a reference motion for the convolution with synthetic signals and the subsequent calculation of the torsional motions.

With a peak ground acceleration of 390 cm/s², this recording effectively represents the average acceleration that occurred at this study site during the 2016 seismic sequence in central Italy.

The time history is convolved with the 3x3 output components of the numerical simulation for each surface recording point of the output shaking.

The angular velocity is then calculated for each point and for each instant of the time history by calculating the spatial derivatives of the translational components. They are then averaged and Figure 6.35 shows the peak angular velocity about the z-axis (PGω). Further details on the calculation of this parameter can be found in Chapter 4.

Although the peak angular velocity values, expressed in milliradians per second (mrad/s), are relatively low, the observed magnitude is consistent with values reported in the literature in similar cases, e.g. Spudich and Fletcher (2008).

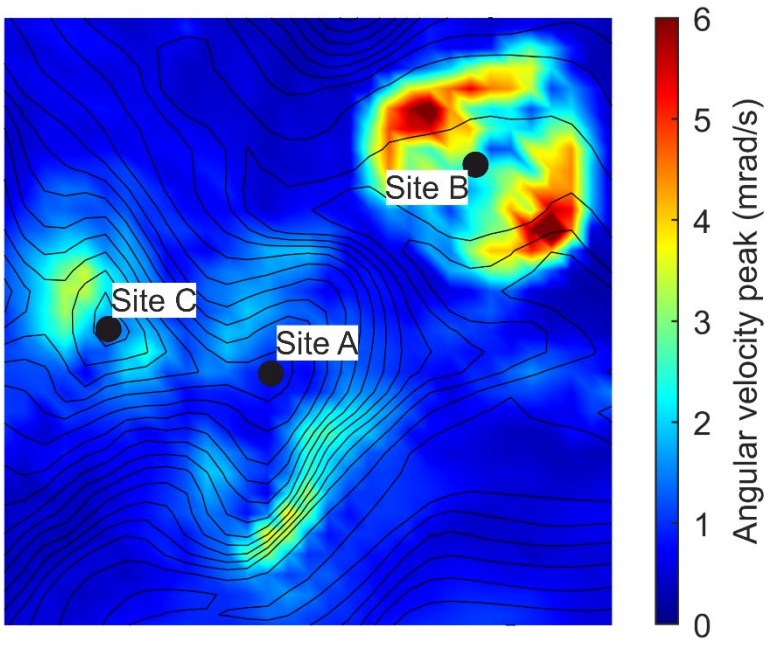


Figure 6.35. Spatial distribution of the peak values of the angular velocity around the z-axis.

The figure clearly shows that a localised increase in angular velocity can be observed in the Borgo valley, where sedimentary deposits appear to act as an amplifying factor. This indicates that the lithological properties have a significant influence on the distribution of this parameter. Another important factor influencing the angular velocity is the topographic slope: Areas with steeper slopes show a greater variability of the parameter, although this effect is less significant than the one related to lithological characteristics. In contrast, sites A and C, characterised by moderate slopes, do not show high values of angular velocity, indicating a lower susceptibility to strong torsional motions in the soil.

This spatial distribution indicates a complex interaction between soil properties and surface morphology and underlines the need for further analyses to determine the specific role of each factor in controlling rotational motions.

A direct comparison can be made with the rotation values of Stupazzini et al. (2009), who used the same method. Their simulation, based on a magnitude 6.0 earthquake comparable to the event used in this study, calculates rotation peaks of about 1 mrad and maximum angular velocities of 10 mrad/s. In contrast, the results of our analysis, shown in Figure 6.35, show peak angular velocities of up to 6 mrad/s, while Figure 6.36 shows rotation peaks (obtained from the time derivative of the angular velocity) with maximum values of 1.5 mrad. These results emphasise

the importance of the valley area and illustrate the considerable influence of the stratigraphy on the rotation effects.

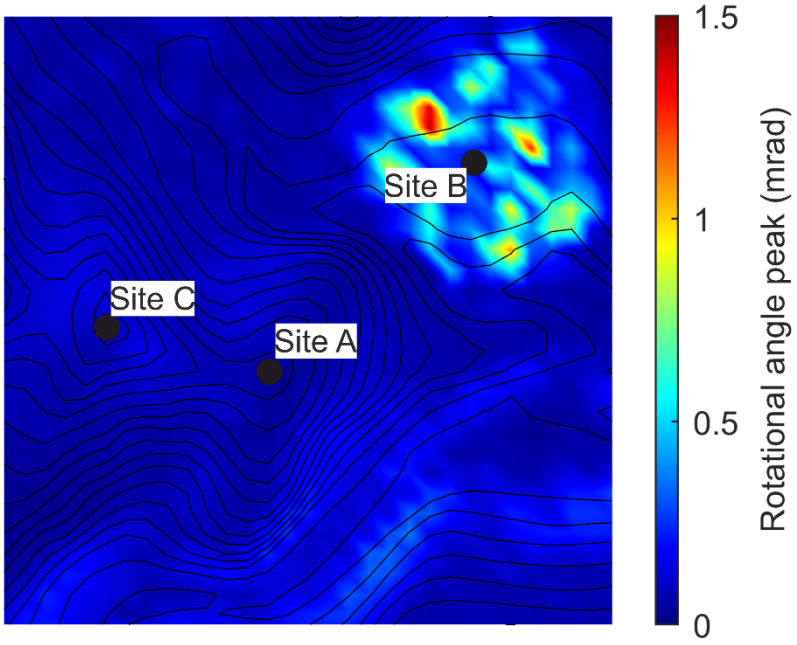


Figure 6.36. Spatial distribution of the peak values of the rotation around the z-axis.

The strong agreement between the results of this study and the values reported by Stupazzini et al. (2009), as well as with other studies summarised in their review, demonstrates the consistency and validity of the methodology used.

The issue of earthquake-induced torsion of buildings is still controversial, as shown by the different criteria in the building codes and the contradictory results in the literature (Anagnostopoulos et al., 2015). Therefore, one aspect that should be analysed is the transfer of such torsional motion from the ground to the building and the impact on structural stability.

CONCLUSIONS

The extent of the potential destruction of earthquake ground shaking depends largely on the dynamic behaviour of subsoil in the affected area. This evidence emphasises the crucial role of the accurate reconstruction of the subsurface geometry and mechanical properties of the geologic formations when studying the seismic site effects.

The results of this work aim to contribute to both territorial prevention and scientific progress: (1) by providing tools useful for urban planning and civil protection by mapping areas with higher seismic vulnerability; and (2) by deepening the understanding of three-dimensional seismic shaking modes, contributing to the advancement of scientific knowledge on the relevant features of the seismic effects.

The assessment of ground motion modification, through simulations of wave propagation, was supported by digital models that accurately and faithfully represent the subsurface. Based on geological, geotechnical and geophysical subsurface characterisation, two case studies are modelled numerically in three dimensions. The reconstruction of these models, therefore, describes the subsurface setting of different lithotypes which exhibit different seismic behaviour.

Three-dimensional simulations of seismic wave propagation applied to two particularly complex study areas were accomplished: the Sarca Valley and the Arquata del Tronto Ridge.

- The first study area is the terminal part of the Sarca river valley (northern Italy) and is a flat sediment-filled valley. This region is highly urbanised and characterised by extensive tourist and industrial activities. The sedimentary basin, with complex buried morphologies, properties heterogeneities, and a thickness of almost 400 m at its deepest point, immediately indicates a potential for significant seismic amplification. In this area, the study highlights two significant effects: the spatial variation of the amplification values with the associated amplified

frequencies and the significant increase in the duration of seismic shaking during wave propagation.

- Analysing the amplification in different frequency ranges, it shows various patterns throughout the valley. The 1.6–2.2 Hz range shows the highest amplification, with values ranging between 5 and 8 consistently observed in most areas except at the edges. The 1–1.6 Hz range also shows a clear amplification with values between 4 and 7, with particularly notable concentrations in the northern part of the valley. In the 0.4–1 Hz range, the amplification is less uniform: the eastern areas remain unaffected, while the western valley has two prominent regions The southern part reaches values of up to 6, while the northern area shows lower amplification with values ranging between 3 and 5. At frequencies above 2.2Hz, there is no clear pattern of amplification and the average values show considerable variability throughout the study area.

- During the seismic propagation, a pronounced increase in the duration of the shaking can be observed. The incident wave is followed by the generation of surface waves at the edges of the valley: these waves get trapped in the sediments. Although the input oscillation was characterised as an impulse, the oscillations within the valley persisted for over 13 seconds. This phenomenon results in amplification and prolonged duration of the motion and emphasises the critical role in assessing the seismic response and potential damage caused by energy transferred from the ground to structures.

- The second study area, Arquata del Tronto, is located in the central Apennines and is characterised by a high seismic reference hazard. This region was completely devastated by the 2016 seismic sequence in central Italy. The configuration of the area consists of an asymmetric ridge, alternating folded and fractured layers and a small closed valley. The analysis at this study site focused on three aspects of the seismic motion modification: the shift to lower frequencies when the equivalent linear constitutive models are used for soils, the polarisation of oscillations and torsional motions.

- In the area of the small valley of Borgo, where loose soils were present, a shift of the amplification peaks by about 1 Hz to lower frequencies was

observed due to the non-linear soil behaviour. This finding confirms previous studies and underlines the need to include the non-linear behaviour of soils deposits in the seismic wave propagation simulations. The amplification is also pronounced at the valley edges, even with thinner deposits, which can be attributed to 3D boundary effects. Wave reflections and interferences near the edges, due to material and geometry contrasts with the host rock, lead to a local concentration of energy.

- In the case of asymmetric ridges, topographic effects are closely related to the directionality of the ground motion. In Arquata del Tronto, the preferential elongation of the ridge leads to a polarisation of the oscillations perpendicular to the ridge. It is essential to consider also the interactions between seismic waves and buried geological structures. In such contexts, seismic oscillations are likely to be polarised perpendicular to the layers, not only due to the topographical features, but also because seismic waves encounter different resistance depending on the lithological properties of the trespassed layers. Polarisation analyses showed wave amplification within the valley, even for small valleys that do not behave like individual bodies. Oscillations concentrate and produce irregular local effects at the valley edges, especially in areas where the edges are orientated parallel to the direction of oscillation.

- By considering oscillations in three directions, the torsional motions were calculated using the angular velocity around the z-axis. Although the peak angular velocity values are relatively low, they align with magnitudes reported in similar cases in the literature. They are more pronounced in layers with low Vs values and are secondarily influenced by slopes, which amplify them. The analysis identifies a local increase in angular velocity within the Borgo valley, where sediment deposits amplify the rotational motion. A comparison with the model of Stupazzini et al. (2009) shows predicted rotational peaks of about 1 mrad and angular velocities of 10 mrad/s. Although this study is of the same order of magnitude, it shows slightly different values, including angular velocities of up to 6 mrad/s (Figure 6.35) and rotation peaks of up to 1.5 mrad. These results highlight the important role of valley stratigraphy in influencing rotational effects and emphasise the need for further investigation of soil-surface morphology interactions.

Future studies will allow us to investigate out-of-plane and torsional behaviour by applying the method to a larger number of case studies. It will be interesting to observe whether different results occur depending, for example, on the type of constitutive law used in the analysis or depending on the buried morphology or lithological properties of the soil.

The scientific community will be made aware of the importance to take into account three-dimensional seismic effects, which are often overlooked in the design of engineering structures.

APPENDIX

Since 1993, the PAT Geological Survey has collected, codified and computerised the data from drillings in the region area. They can be inspected and downloaded from the Portale Geocartografico Trentino at the site https://webgis.provincia.tn.it/. Here you can found a detailed summary.

ID	N° survey	Location	Date	Altitude (m)	Bedrock depth (m)	X coord	Y coord
7	1	Riva del Garda	27/04/1982	66,2	0	642690,34	5082871,97
8	1	Riva del Garda	08/06/1988	71	0	643157,28	5083222,86
9	1	Arco	26/05/1982	87	0	645385,23	5086777,24
10	2	Arco	02/06/1982	88	9,7	645407,99	5086824,62
11	3	Arco	04/06/1982	100	1	645436,67	5086904,19
12	4	Arco	07/06/1982	87	0	645438,93	5086801,84
13	5	Arco	11/06/1982	88	6	645384,32	5086814,6
14	1	Riva del Garda, Varone	16/05/1988	108,5	0	643129,63	5084843,14
15	2	Riva del Garda, Varone	18/05/1988	108,5	0	643091,52	5084861,64
16	3	Riva del Garda, Varone	23/05/1988	108,5	0	643084,01	5084839,1
17	4	Riva del Garda, Varone	26/05/1988	108,5	0	643116,92	5084819,44
18	2	Riva del Garda	10/06/1988	71	0	643160,68	5083203,45
19	3	Riva del Garda	13/06/1988	71	0	643169,06	5083210,27
20	2	Riva del Garda	28/04/1982	66,2	0	642717,69	5082873,34
21	3	Riva del Garda	29/04/1982	66,2	0	642710,17	5082900,7
22	4	Riva del Garda	03/05/1982	66,2	0	642686,93	5082902,08
23	5	Riva del Garda	06/05/1982	66,2	0	642667,1	5082888,4
31	1	Riva del Garda, Rione 2 giugno	30/05/1988	0	0	643420,9	5084268,52
32	2	Riva del Garda, Rione 2 giugno	01/06/1988	0	0	643407,73	5084260,54
33	1	Riva del Garda	28/04/1980	0	6,5	644256,38	5082301,22
34	2	Riva del Garda	05/05/1980	0	7,3	644276,27	5082321,98
35	3	Riva del Garda	06/05/1980	0	2,1	644310	5082330,63
36	1	Arco	15/04/1980	96,5	0	646835,1	5086783,81
37	2	Arco	15/04/1980	98	0	646831,47	5086817,02
38	3	Arco	15/04/1980	93,5	0	646794,13	5086828,96
556	1	Riva del Garda, Colonia Miralago	27/01/1994	0	0	643316,8	5082585,18
650	1	Arco	05/08/1987	91	0	646120,56	5086778,93
651	2	Arco	07/08/1987	91	0	646117,91	5086801,5
652	3	Arco	10/08/1987	91	0	646077,45	5086816,77
653	4	Arco	12/08/1987	91	0	646089,39	5086777,6
676	1	Riva del Garda	15/03/1983	70	0	643995,48	5083284,38
677	2	Riva del Garda	15/03/1983	70	0	643971,56	5083240,49
678	3	Riva del Garda	15/03/1983	70	0	643932,68	5083253,96
679	4	Riva del Garda	15/03/1983	70	0	643959,59	5083296,35
680	1	Arco, Massone	22/03/1983	116	0	647340,18	5087222,59
681	2	Arco, Massone	28/03/1983	119	0	647307,03	5087167,79
682	3	Arco, Massone	24/03/1983	116	0	647357,48	5087184,37
688	1	Riva del Garda	12/10/1983	71	0	642938,04	5083180,03
689	2	Riva del Garda	19/10/1983	71	0	642899,99	5083193,01

690	1	Riva del Garda	09/01/1985	0	0	643130,86	5082717,56
691	1	Riva del Garda	15/11/1986	77	0	642995,63	5083324,66
692	2	Riva del Garda	15/11/1986	77	0	643005,76	5083350,25
781	1	Riva del Garda	21/03/1980	0	0	642886,67	5083860,86
782	2	Riva del Garda	21/03/1980	0	0	642896,47	5083884,08
783	3	Riva del Garda	21/03/1980	0	0	642854,18	5083876,86
946	1	Riva del Garda	27/09/1993	0	0	643488,53	5082575,38
947	2	Riva del Garda	08/10/1993	0	0	643503,67	5082599,17
967	1	Riva del Garda, S.S. Torbole-Riva	20/01/1982	0	5	644289,06	5081988,22
968	2	Riva del Garda, S.S. Torbole-Riva	22/01/1982	0	2,5	644409,16	5082017,66
969	3	Riva del Garda, S.S. Torbole-Riva	25/01/1982	0	2,7	644553,17	5082035,92
970	4	Riva del Garda, S.S. Torbole-Riva	25/01/1982	0	0	644562,18	5082038,92
971	5	Riva del Garda, S.S. Torbole-Riva	27/01/1982	0	0	644653,28	5082076,16
972	6	Riva del Garda, S.S. Torbole-Riva	27/01/1982	0	1	644657,48	5082077,97
973	7	Riva del Garda, S.S. Torbole-Riva	29/01/1982	0	3,6	644667,69	5082082,77
974	1	Riva del Garda	30/11/1993	0	0	642772,34	5082885,92
975	2	Riva del Garda	06/12/1993	0	0	642773,57	5082879,79
976	3	Riva del Garda	07/12/1993	0	0	642769,73	5082881,87
977	1	Riva del Garda, San Giacomo	06/06/1984	0	0	642379,51	5084195,34
978	2	Riva del Garda, San Giacomo	14/06/1984	0	0	642348,25	5084338,75
988	4	Riva del Garda	07/05/1980	0	1,4	644286,65	5082299,49
989	5	Riva del Garda	07/05/1980	0	1,8	644290,11	5082307,27
990	6	Riva del Garda	07/05/1980	0	7	644271,08	5082305,75
991	1	Riva del Garda	19/05/1982	67	0	642691,86	5082727
992	2	Riva del Garda	21/05/1982	67	0	642708,73	5082756,22
993	1	Arco, Maza	15/06/1983	78	0	646605,9	5083984,53
994	2	Arco, Maza	29/06/1983	80	0	646663,45	5084033,78
995	3	Arco, Maza	29/06/1983	78	2,5	646515,36	5083945,28
996	4	Arco, Maza	30/06/1983	78	10,4	646400,27	5083916,04
997	5	Arco, Maza	04/07/1983	78	0	646387,22	5083962,99
998	6	Arco, Maza	07/07/1983	75	0	646209,3	5083795,44
999	7	Arco, Maza	15/07/1983	78	0	646671,96	5083995,53
1000	8	Arco, Maza	18/07/1983	79	0	646707,26	5083973,99
1002	1	Arco, Maza		0	0	646693,51	5084044,59
1003	2	Arco, Maza		0	0	646744,88	5084038,62
1004	3	Arco, Maza		0	0	646869,2	5084115,48
1005	4	Arco, Maza		0	2,3	646820,06	5084019,96
1006	5	Arco, Maza		0	6,5	646747,86	5083995,34
1007	6	Arco, Maza		0	0	646740,41	5084107,28
1008	7	Arco, Maza		0	0	646780,61	5084153,54
1009	1	Riva del Garda	31/08/1993	0	0	644113,55	5082861,56
1010	2	Riva del Garda	09/07/1993	0	0	644000,36	5082940,07
1011	1	Arco, Provvidenza - Neve	05/03/1984	82	0	646030,41	5085664,88
1012	2	Arco, Provvidenza - Neve	20/03/1984	98,5	0	646931,35	5086371,37
1618	1	Arco	24/09/1996	102	0	647002,83	5086291,61
1619	2	Arco	30/09/1996	103	0	647057,85	5086728,55
1652	1	Riva del Garda, Cimitero	15/12/1993	0	0	643314,16	5083381,05
1653	2	Riva del Garda, Cimitero	18/01/1994	0	0	643325,49	5083366,64
1903	1	Nago Torbole, Monte Brione	26/01/1998	0	2,5	644538,78	5082035,93
1904	2	Nago Torbole, Monte Brione	27/01/1998	0	5,5	644648,09	5082074,6
1905	3	Nago Torbole, Monte Brione	28/01/1998	0	4	644354,65	5082001,94
1906	4	Nago Torbole, Monte Brione	29/01/1998	0	6,2	644257,62	5081989,64
2178	1	Mori, Loppio	01/12/1997	230	0	649950,72	5079788,7

2179	2	Mori, Loppio	04/12/1997	230	0	649936,52	5079747,29
2444	1	Riva del Garda - Arco	01/01/1992	78,5	0	644930,79	5084882,45
2445	2	Riva del Garda - Arco	01/01/1992	78,5	0	644587,16	5085109,24
2446	3	Riva del Garda - Arco	01/01/1992	99	0	643484,93	5085295,55
2447	4	Riva del Garda - Arco	01/01/1992	109	0	643035,04	5084877,77
2448	5	Riva del Garda - Arco	01/01/1992	112	0	642447,51	5084174,73
2449	1	Riva del Garda	14/04/1989	67	0	645613,78	5081177,97
2450	2	Riva del Garda	20/04/1989	67	0	645615,97	5081205,42
2457	1	Riva del Garda	01/09/1986	88	0	643034,14	5083940,2
2458	3	Arco, Provvidenza - Neve	31/03/1984	83	0	645312,6	5085740,25
2460	4	Arco, Provvidenza - Neve	31/03/1984	83	0	645773,65	5085655,99
2461	5	Arco, Provvidenza - Neve	31/03/1984	89	0	646619,68	5086208,12
2462	6	Arco, Provvidenza - Neve	31/03/1984	93	0	646724,12	5086203,01
2463	7	Arco, Provvidenza - Neve	31/03/1984	98	0	646854,02	5086187,67
2464	8	Arco, Provvidenza - Neve	31/03/1984	91	0	646720,3	5086302,65
2465	9	Arco, Provvidenza - Neve	31/03/1984	98	0	646912,61	5086271,99
2744	1	Arco, Porto	11/04/2000	66	0	644976	5081732,5
2846	1	Tenno	27/05/2001	0	45,2	640101,63	5088168,08
2847	2	Tenno	30/05/2001	0	28,5	640010,74	5088114,09
2848	3	Tenno	07/06/2001	0	14,6	640107,31	5088017,46
2849	4	Tenno	15/06/2001	0	0	640379,96	5088246,24
2850	5	Tenno	19/06/2001	0	50,7	640357,24	5088145,35
2912	1	Riva del Garda	28/11/2001	66,9	14,2	642637,29	5082440,41
2913	2	Riva del Garda	30/11/2001	67,5	0	642645,34	5082567,23
2914	3	Riva del Garda	02/12/2001	67,5	16,6	642650,37	5082615,54
2915	4	Riva del Garda	04/12/2001	66,9	6,3	642630,25	5082438,4
3031	1	Riva del Garda, Canale Rocca	01/01/2002	66	0	643007,71	5082770,01
3032	2	Riva del Garda, Canale Rocca	02/01/2002	66	0	643007,3	5082822,48
3033	3	Riva del Garda, Canale Rocca	03/01/2002	66	0	643004,46	5082888,79
3034	4	Riva del Garda, Canale Rocca	04/01/2002	66	0	642978,84	5082894,08
3035	5	Riva del Garda, Canale Rocca	05/01/2002	66	0	642923,13	5082893,67
3036	6	Riva del Garda, Canale Rocca	06/01/2002	66	0	642906,87	5082868,05
3037	7	Riva del Garda, Canale Rocca	07/07/2002	66	0	642901,99	5082825,74
3038	8	Riva del Garda, Canale Rocca	08/01/2002	66	0	642896,7	5082790,76
3039	9	Riva del Garda, Canale Rocca	09/01/2002	66	0	642934,11	5082761,07
3040	10	Riva del Garda, Canale Rocca	10/01/2002	66	0	642975,59	5082794,01
3041	11	Riva del Garda, Canale Rocca	11/01/2002	66	0	642976,81	5082845,26
3042	12	Riva del Garda, Canale Rocca	12/01/2002	66	0	642956,48	5082875,78
3077	1	Arco, Varignano	05/02/1999	83	0	644631,35	5086696,33
3078	2	Arco, Varignano	08/02/1999	84,8	0	644391,51	5086662,97
3079	3	Arco, Varignano	09/02/1999	85	0	644251,69	5086496,19
3081	1	Riva del Garda - Arco	14/09/2000	88	0	643729,73	5085420,96
3082	2	Riva del Garda - Arco	14/09/2000	111	0	643120,12	5084978,81
3083	3	Riva del Garda - Arco	14/09/2000	104,8	0	642608,48	5084137,45
3084	4	Riva del Garda - Arco	11/09/2000	101,5	0	642599,2	5083908,8
3085	5	Riva del Garda - Arco	12/09/2000	98	0	642519,53	5083740,41
3086	6	Riva del Garda - Arco	27/10/2000	101	0	642494,01	5083717,49
3087	7	Riva del Garda - Arco	19/10/2000	155	22,1	642433,43	5083319,07
3088	8	Riva del Garda - Arco	15/09/2000	142	40,8	642477	5083260,95
3089	9	Riva del Garda - Arco	16/09/2000	106	0	642562,06	5083217,87
3092	10	Riva del Garda - Arco	11/09/2000	78,4	0	644719,24	5085534,62
3093	11	Riva del Garda - Arco	11/09/2000	79,8	0	644219,34	5085898,41
3094	12	Riva del Garda - Arco	11/09/2000	100	0	642557,46	5084560,03

3323	1	Arco, San Giorgio	20/12/1997	77,5	272,5	644800,26	5084657,9
3380	1	Tenno, Cologna, Gavazzo nuova		198	4,8	642846,4	5086007,88
3381	2	Tenno, Cologna, Gavazzo nuova		199	5,65	642853,08	5086023,32
3382	3	Tenno, Cologna, Gavazzo nuova		205	7,5	642877,26	5086036,26
3383	1	Tenno	13/03/1980	412	0	641985,79	5086732,76
3384	2	Tenno	13/03/1980	414	0	642019,04	5086754,7
3385	1	Arco	15/04/1980	98	0	646854,81	5086805,6
3386	2	Arco	15/04/1980	94	0	646812,8	5086848,16
3387	1	Arco	15/01/1995	86	37	645408,48	5086786,9
3388	1	Arco	04/07/1994	86	0	645480,68	5086866,2
3389	2	Arco	07/07/1994	90	4,5	645455,17	5086890,49
3390	3	Arco	08/07/1994	86	0	645471,96	5086819,5
3391	4	Arco	13/07/1994	86	0	645417,19	5086756,6
3392	5	Arco	15/07/1994	86	0	645453,91	5086774,66
3403	1	Tenno, Cologna, Val		275	0	642803,9	5086360,76
3480	1	Arco, Romarzollo	22/01/2002	85	0	644801,47	5086840,35
3481	2	Arco, Romarzollo	23/01/2002	85	0	644835,12	5086824,64
3566	1	Arco	21/05/2003	88,5	0	645947,73	5086621,66
3567	2	Arco	22/05/2003	88,5	0	646023,32	5086624,36
3568	3	Arco	28/05/2003	88,5	0	646091,62	5086672,13
3606	1	Riva del Garda, Ischia	11/09/2003	90	0	643376,51	5084466,48
3607	2	Riva del Garda, Ischia	11/09/2003	90	0	643406,86	5084442,08
3608	3	Riva del Garda, Ischia	12/09/2003	90	0	643432,93	5084417,38
3609	4	Riva del Garda, Ischia	12/09/2003	90	0	643452,82	5084436,59
3610	5	Riva del Garda, Ischia	15/09/2003	90	0	643427,44	5084466,79
3611	6	Riva del Garda, Ischia	15/09/2003	90	0	643400	5084500,42
3795	1	Chiarano		89	10,5	645330,99	5086802,7
3796	2	Chiarano		0	9,5	645307,08	5086779,88
3797	3	Chiarano		87	21,1	645350,97	5086756,92
4073	3	Riva del Garda, San Giacomo	22/05/1984	0	39	642273,06	5084799,65
4111	3	Arco	03/09/2001	0	0	647039,9	5086746,62
4112	4	Arco	04/09/2001	0	0	647005,29	5086984,55
4284	1	istituto Enaip	18/10/2010	0	0	646741,472	5086874,743
4285	2	istituto Enaip	15/10/2010	0	0	646707,668	5086856,575
4508	1	San Tommaso	20/09/2001	280	7,2	647386	5082542
4509	2	San Tommaso	21/09/2001	330	2,4	647354	5082716
4510	3	San Tommaso	20/09/2001	270	60	646959	5083708
4511	4	San Tommaso	20/09/2001	120	0,8	646292	5083424
4512	5	San Tommaso	06/09/2001	76,5	0	645996	5084316
4519	1	Riva	01/10/2007	0	0	642981,562	5083985,149
4520	2	Riva	01/10/2007	0	0	643145,695	5083926,622
4521	3	Riva	01/10/2007	0	0	643413,433	5083382,833
4522	1	Albola	16/09/2003	0	0	643461,439	5083457
4523	2	Albola	16/09/2003	0	0	643487,211	5083488,722
4524	3	Albola	17/09/2003	0	0	643476,327	5083499,938
4525	4	Albola	17/09/2003	0	0	643458,101	5083473,118
4526	5	Albola	18/09/2003	0	0	643412,506	5083437,009
4608	1	Riva del Garda	01/09/2008	66,34	0	643023,661	5082682,438
4609	2	Riva del Garda	01/09/2008	66,87	0	643085,369	5082682,234
4610	3	Riva del Garda	01/10/2008	66,1	0	643091,979	5082745,607
4611	4	Riva del Garda	01/10/2008	65,9	0	643060,944	5082785,512

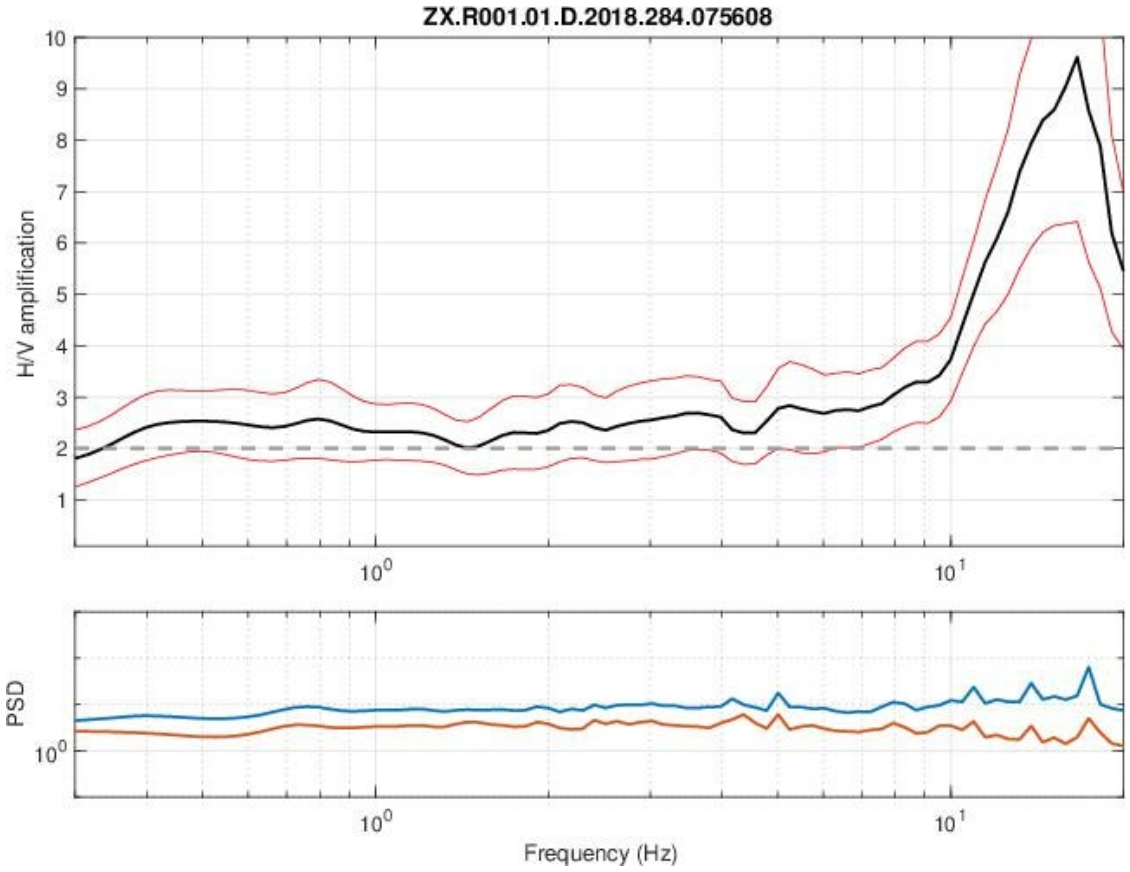
A total of 119 recordings of seismic environmental noise were made as part of the OGS-PAT project in the Sarca Valley. The horizontal and vertical spectral ratio curves (H/V) were derived from these recordings. Here you can found a detailed summary.

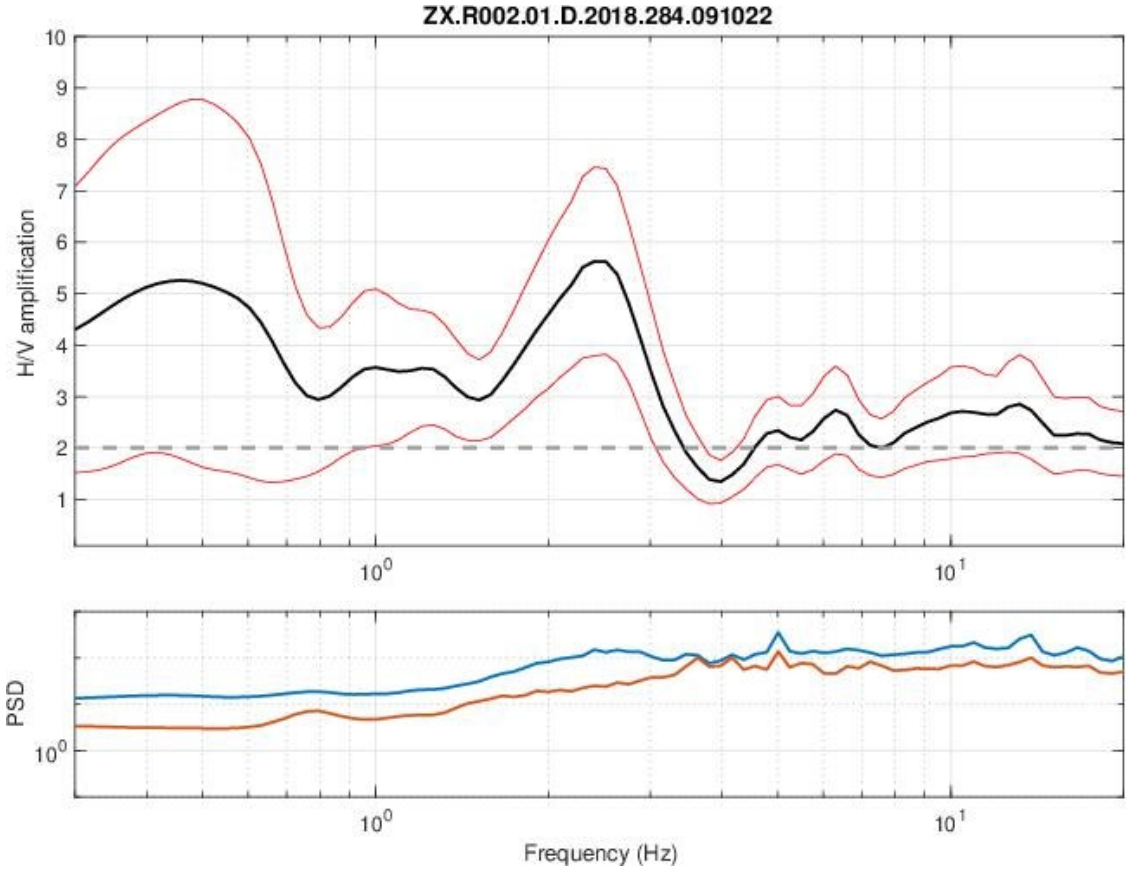
Station	Lat	Lon	f_0 (Hz)	Amplitude f_0 peak	f_1 (Hz)	Amplitude f_1 peak	Location
R001	45,8830	10,8736	16,00	9,00	NaN	NaN	MONTE BRIONE
R002	45,8789	10,8560	2,50	5,70	NaN	NaN	WEST VALLEY
R003	45,8964	10,8575	0,50	6,00	2,30	3,60	WEST VALLEY
R004	45,9139	10,8692	0,70	6,20	NaN	NaN	WEST VALLEY
R005	45,9329	10,8716	NaN	NaN	NaN	NaN	BEDROCK
R006	45,8786	10,8950	0,90	8,00	NaN	NaN	NAGO
R007	45,8864	10,8674	NaN	NaN	NaN	NaN	BEDROCK
R008	45,9395	10,8975	3,50	3,10	NaN	NaN	WEST VALLEY
R009	45,9410	10,9082	4,20	6,20	NaN	NaN	WEST VALLEY
R010	45,9322	10,8970	7,00	4,00	NaN	NaN	WEST VALLEY
R011	45,9126	10,8956	1,10	3,80	7,60	5,20	WEST VALLEY
R012	45,9226	10,8965	1,70	4,00	7,60	4,00	WEST VALLEY
R013	45,9324	10,9089	NaN	NaN	NaN	NaN	BEDROCK
R014	45,9232	10,9077	NaN	NaN	NaN	NaN	BEDROCK
R015	45,8781	10,8687	15,90	4,00	NaN	NaN	EAST VALLEY
R016	45,8680	10,8825	NaN	NaN	NaN	NaN	BEDROCK
R017	45,8871	10,8817	1,50	11,50	NaN	NaN	EAST VALLEY
R018	45,8963	10,8696	1,20	4,20	NaN	NaN	WEST VALLEY
R019	45,9002	10,8665	0,65	4,50	NaN	NaN	WEST VALLEY
R020	45,9058	10,8570	0,70	4,20	NaN	NaN	WEST VALLEY
R021	45,9058	10,8712	0,70	5,00	3,50	3,00	WEST VALLEY
R022	45,9057	10,8450	NaN	NaN	NaN	NaN	BEDROCK
R023	45,9142	10,8556	3,00	5,80	NaN	NaN	WEST VALLEY
R024	45,8810	10,8813	2,70	9,00	NaN	NaN	EAST VALLEY
R025	45,8788	10,8816	NaN	NaN	NaN	NaN	BEDROCK
R026	45,8824	10,8761	1,30	2,80	NaN	NaN	EAST VALLEY
R027	45,8875	10,8564	1,00	4,50	2,40	4,30	WEST VALLEY
R028	45,8901	10,8491	0,66	4,10	2,10	3,30	WEST VALLEY
R029	45,8973	10,8439	0,90	3,80	NaN	NaN	WEST VALLEY
R030	45,8885	10,8430	0,80	5,30	NaN	NaN	WEST VALLEY
R031	45,8965	10,8305	NaN	NaN	NaN	NaN	BEDROCK
R032	45,9047	10,8310	NaN	NaN	NaN	NaN	BEDROCK
R033	45,9415	10,8723	NaN	NaN	NaN	NaN	BEDROCK
R034	45,9242	10,8588	NaN	NaN	NaN	NaN	BEDROCK
R035	45,9231	10,8707	NaN	NaN	NaN	NaN	BEDROCK
R036	45,9059	10,8823	0,90	4,00	NaN	NaN	WEST VALLEY
R037	45,8951	10,8825	1,6	5,1	NaN	NaN	EAST VALLEY
R038	45,9421	10,8851	NaN	NaN	NaN	NaN	BEDROCK
R039	45,9303	10,8830	NaN	NaN	NaN	NaN	BEDROCK
R040	45,9237	10,8828	NaN	NaN	NaN	NaN	BEDROCK

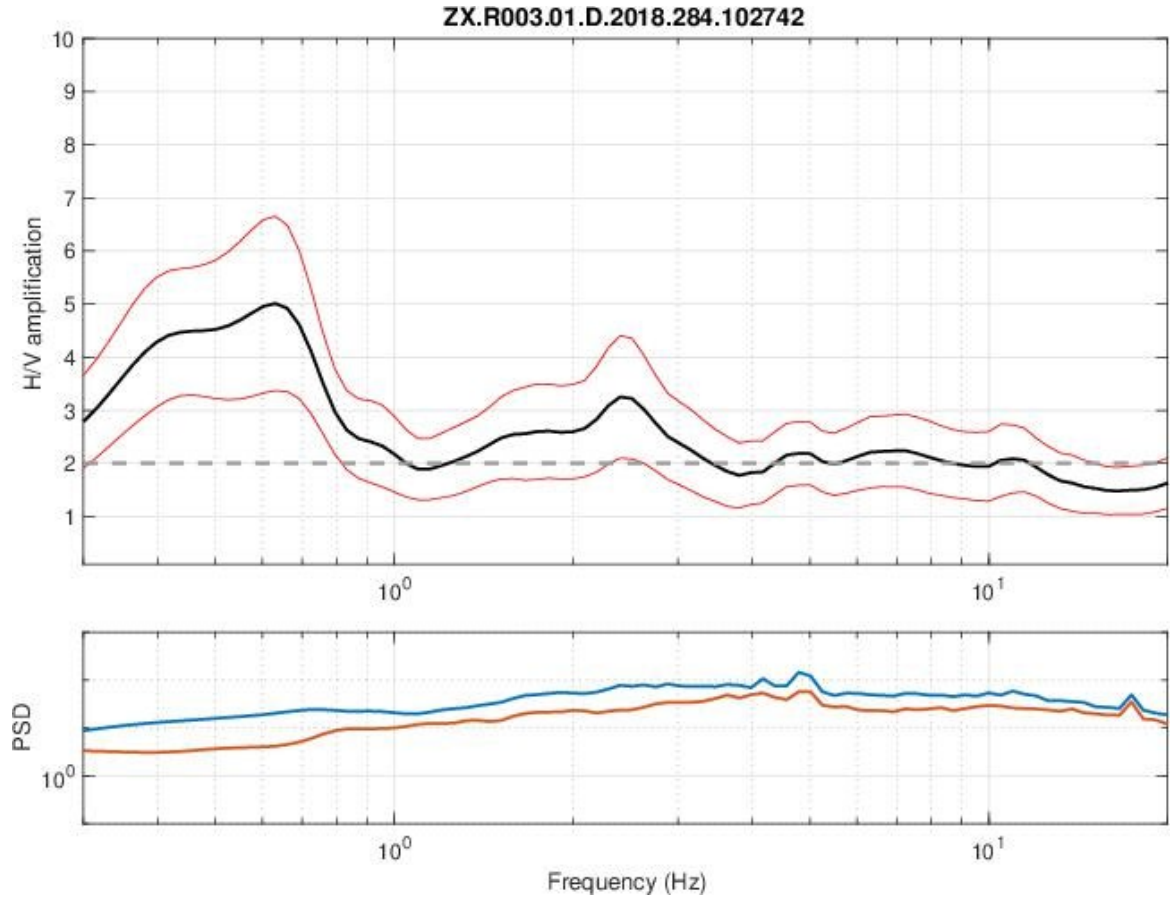
R041	45,9138	10,8827	0,80	5,10	NaN	NaN	WEST VALLEY
R042	45,9090	10,8246	NaN	NaN	NaN	NaN	BEDROCK
R043	45,9051	10,8334	NaN	NaN	NaN	NaN	BEDROCK
R044	45,8799	10,8730	4,00	6,10	NaN	NaN	EAST VALLEY
R045	45,9016	10,8431	NaN	NaN	NaN	NaN	BEDROCK
R046	45,8707	10,8811	NaN	NaN	NaN	NaN	BEDROCK
R047	45,8911	10,8594	1,60	4,70	2,50	3,20	WEST VALLEY
R048	45,8953	10,8538	0,60	4,60	NaN	NaN	WEST VALLEY
R049	45,8775	10,8792	2,60	8,60	NaN	NaN	EAST VALLEY
R050	45,8968	10,8454	0,86	4,70	NaN	NaN	WEST VALLEY
R051	45,8768	10,8805	2,30	9,30	NaN	NaN	EAST VALLEY
R052	45,9058	10,8958	1,27	10,60	NaN	NaN	EAST VALLEY
R053	45,9057	10,9065	NaN	NaN	NaN	NaN	BEDROCK
R054	45,9138	10,9096	1,50	3,80	NaN	NaN	WEST VALLEY
R055	45,8849	10,8397	1,20	6,00	NaN	NaN	WEST VALLEY
R056	45,8840	10,8432	0,70	4,80	2,40	3,10	WEST VALLEY
R057	45,8773	10,8794	2,60	6,70	NaN	NaN	EAST VALLEY
R058	45,8698	10,8737	1,40	5,00	NaN	NaN	EAST VALLEY
R059	45,9022	10,8971	3,60	8,70	NaN	NaN	EAST VALLEY
R060	45,8955	10,8922	2,90	5,40	NaN	NaN	EAST VALLEY
R061	45,8790	10,8539	1,30	4,40	3,80	2,80	WEST VALLEY
R062	45,8736	10,8662	0,60	4,20	NaN	NaN	EAST VALLEY
R063	45,8800	10,8969	1,00	7,50	NaN	NaN	NAGO
R064	45,8791	10,8984	2,60	4,90	NaN	NaN	NAGO
R065	45,8864	10,8674	NaN	NaN	NaN	NaN	BEDROCK
R066	45,8961	10,8571	0,55	4,70	NaN	NaN	WEST VALLEY
R067	45,9216	10,8615	2,40	6,00	NaN	NaN	WEST VALLEY
R068	45,9210	10,8610	2,10	7,20	NaN	NaN	WEST VALLEY
R069	45,9212	10,8576	4,00	4,80	NaN	NaN	WEST VALLEY
R070	45,9181	10,8791	1,50	5,80	3,60	3,20	WEST VALLEY
R071	45,9181	10,8711	NaN	NaN	NaN	NaN	BEDROCK
R072	45,9133	10,9062	NaN	NaN	NaN	NaN	BEDROCK
R073	45,9030	10,8625	0,55	7,50	2,70	3,70	WEST VALLEY
R074	45,9130	10,8741	0,70	5,80	3,30	2,70	WEST VALLEY
R075	45,9164	10,8893	2,20	4,40	NaN	NaN	WEST VALLEY
R076	45,8756	10,8734	1,20	5,00	NaN	NaN	EAST VALLEY
R077	45,8989	10,8884	1,90	6,50	NaN	NaN	EAST VALLEY
R078	45,9066	10,8816	NaN	NaN	NaN	NaN	BEDROCK
R079	45,9092	10,8897	NaN	NaN	NaN	NaN	BEDROCK
R080	45,9186	10,8945	NaN	NaN	NaN	NaN	BEDROCK
R081	45,9323	10,9087	NaN	NaN	NaN	NaN	BEDROCK
R082	45,9329	10,8716	NaN	NaN	NaN	NaN	BEDROCK
R083	45,9082	10,8570	0,90	3,00	NaN	NaN	WEST VALLEY
R084	45,9051	10,8636	0,54	4,00	NaN	NaN	WEST VALLEY
R085	45,8986	10,8687	0,85	3,20	NaN	NaN	WEST VALLEY
R086	45,8831	10,8594	NaN	NaN	NaN	NaN	BEDROCK

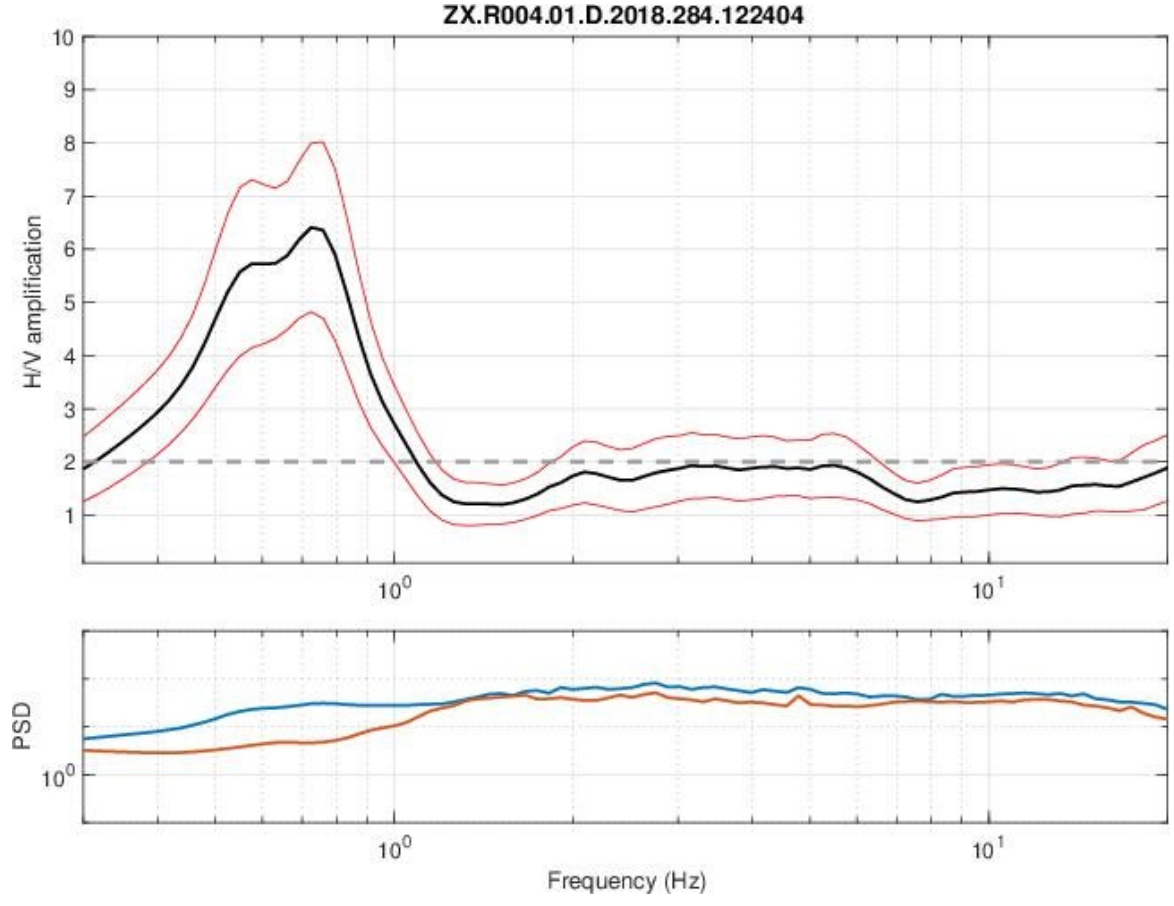
R087	45,9097	10,9056	NaN	NaN	NaN	NaN	BEDROCK
R088	45,9167	10,9092	1,55	5,20	NaN	NaN	WEST VALLEY
R089	45,9016	10,8513	1,10	3,50	NaN	NaN	WEST VALLEY
R090	45,8793	10,8638	NaN	NaN	NaN	NaN	BEDROCK
R091	45,8783	10,8708	1,90	4,70	NaN	NaN	EAST VALLEY
R092	45,8961	10,8767	3,40	4,40	NaN	NaN	MONTE BRIONE
R093	45,8737	10,8665	0,70	4,55	NaN	NaN	EAST VALLEY
R094	45,9397	10,9019	6,90	7,00	NaN	NaN	WEST VALLEY
R095	45,9360	10,9006	2,10	4,00	6,60	3,50	WEST VALLEY
R096	45,9343	10,8954	2,30	4,91	NaN	NaN	WEST VALLEY
R097	45,9311	10,8951	5,30	5,18	NaN	NaN	WEST VALLEY
R098	45,9272	10,8942	4,50	4,60	NaN	NaN	WEST VALLEY
R099	45,9238	10,8898	NaN	NaN	NaN	NaN	BEDROCK
R100	45,8774	10,8893	5,20	7,80	NaN	NaN	NAGO
R101	45,8740	10,8926	3,70	6,10	NaN	NaN	NAGO
R102	45,8797	10,8955	2,60	5,90	NaN	NaN	NAGO
R103	45,8754	10,8967	6,50	6,27	NaN	NaN	NAGO
R104	45,9197	10,9021	3,70	4,10	NaN	NaN	WEST VALLEY
R105	45,9202	10,8798	2,80	4,80	NaN	NaN	WEST VALLEY
R106	45,9082	10,8895	1,15	3,90	NaN	NaN	WEST VALLEY
R107	45,8883	10,8639	6,50	10,30	NaN	NaN	BASE BRIONE
R108	45,8842	10,8647	12,50	16,90	NaN	NaN	BASE BRIONE
R109	45,8956	10,8389	NaN	NaN	NaN	NaN	BEDROCK
R110	45,8995	10,8369	NaN	NaN	NaN	NaN	BEDROCK
TN01	45,8707	10,8812	NaN	NaN	NaN	NaN	BEDROCK
TN02	45,8677	10,8826	NaN	NaN	NaN	NaN	BEDROCK
TN03	45,8912	10,8594	1,60	3,80	NaN	NaN	WEST VALLEY
TN04	45,8954	10,8537	0,60	4,70	1,90	2,90	WEST VALLEY
TN05	45,8776	10,8792	2,30	11,00	NaN	NaN	EAST VALLEY
TN06	45,8864	10,8674	NaN	NaN	NaN	NaN	BEDROCK
TN07	45,9091	10,8244	NaN	NaN	NaN	NaN	BEDROCK
TN08	45,8799	10,8731	4,00	6,20	NaN	NaN	EAST VALLEY
TN09	45,9016	10,8432	1,30	4,00	NaN	NaN	WEST VALLEY
TN10	45,8969	10,8453	0,60	4,00	NaN	NaN	WEST VALLEY
TN11	45,9051	10,8336	NaN	NaN	NaN	NaN	BEDROCK
TN12	45,8855	10,8445	0,80	4,20	2,20	3,20	WEST VALLEY
TN13	45,9031	10,8626	0,55	6,00	2,90	4,00	WEST VALLEY
TN14	45,9131	10,8739	0,70	4,00	NaN	NaN	WEST VALLEY
TN15	45,9157	10,8893	1,20	3,30	NaN	NaN	WEST VALLEY
TN16	45,9132	10,9062	1,50	3,10	NaN	NaN	WEST VALLEY
TN17	45,9180	10,8791	1,50	7,70	3,60	3,00	WEST VALLEY
TN18	45,9180	10,8703	2,10	4,50	NaN	NaN	WEST VALLEY
TN19	45,9212	10,8575	4,20	4,60	NaN	NaN	WEST VALLEY
TN20	45,9210	11,0237	NaN	NaN	NaN	NaN	BEDROCK

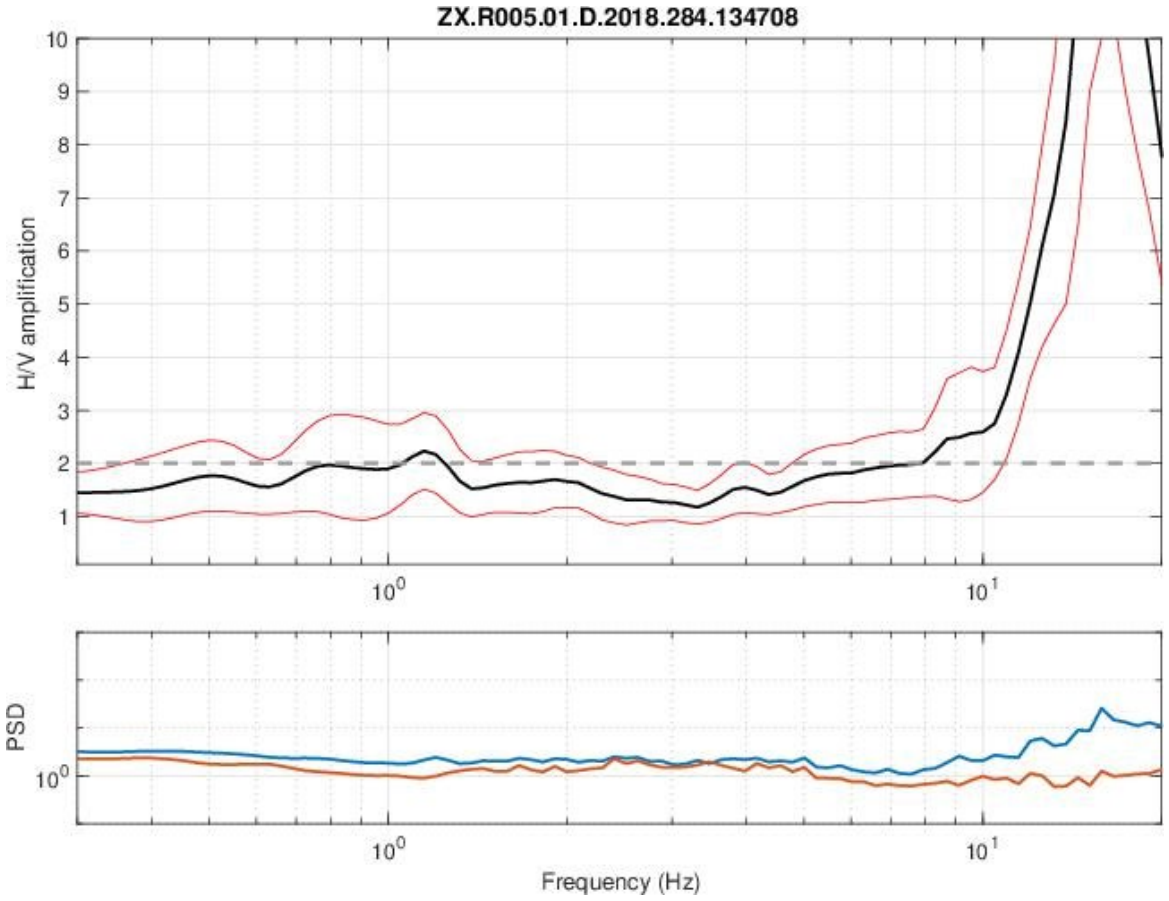
Here follows a summary of the H/V and the associated Power Spectral Density curves, relating to the above data.

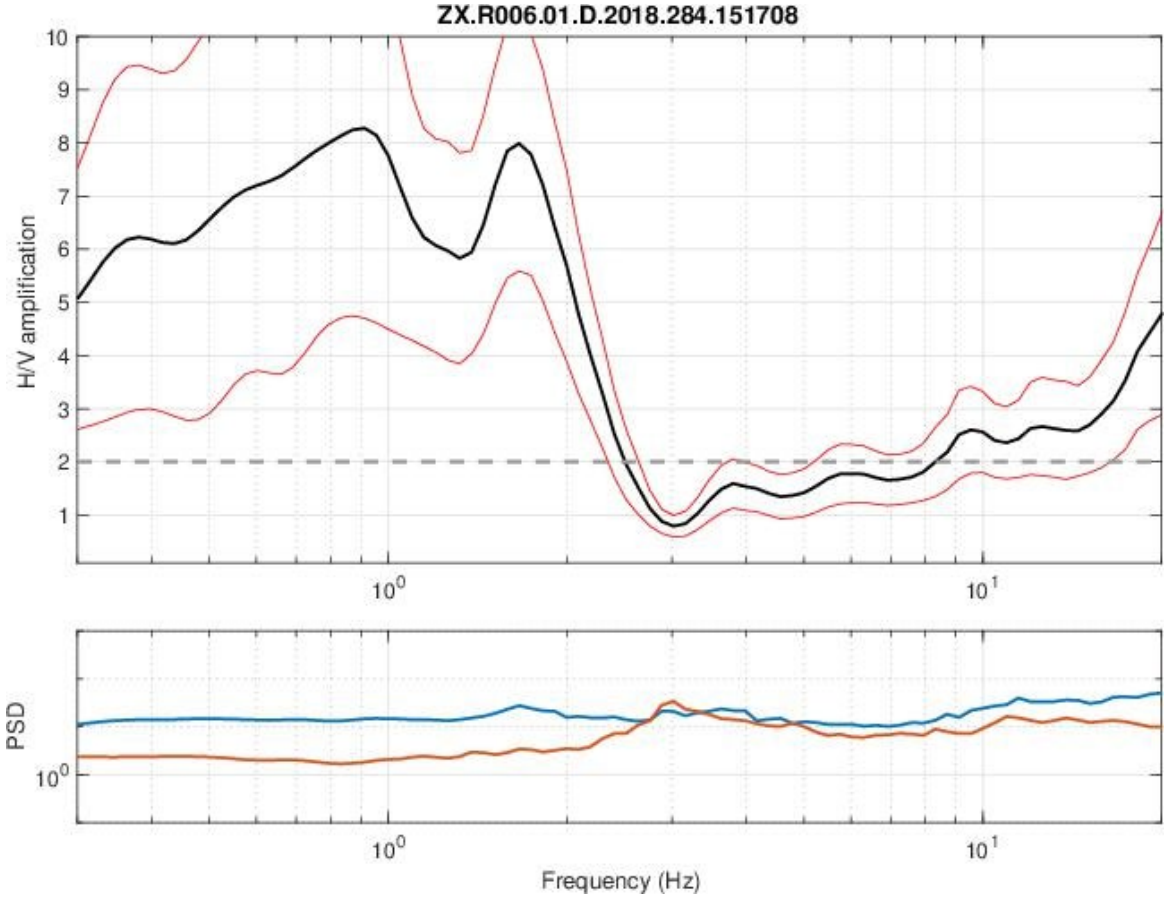


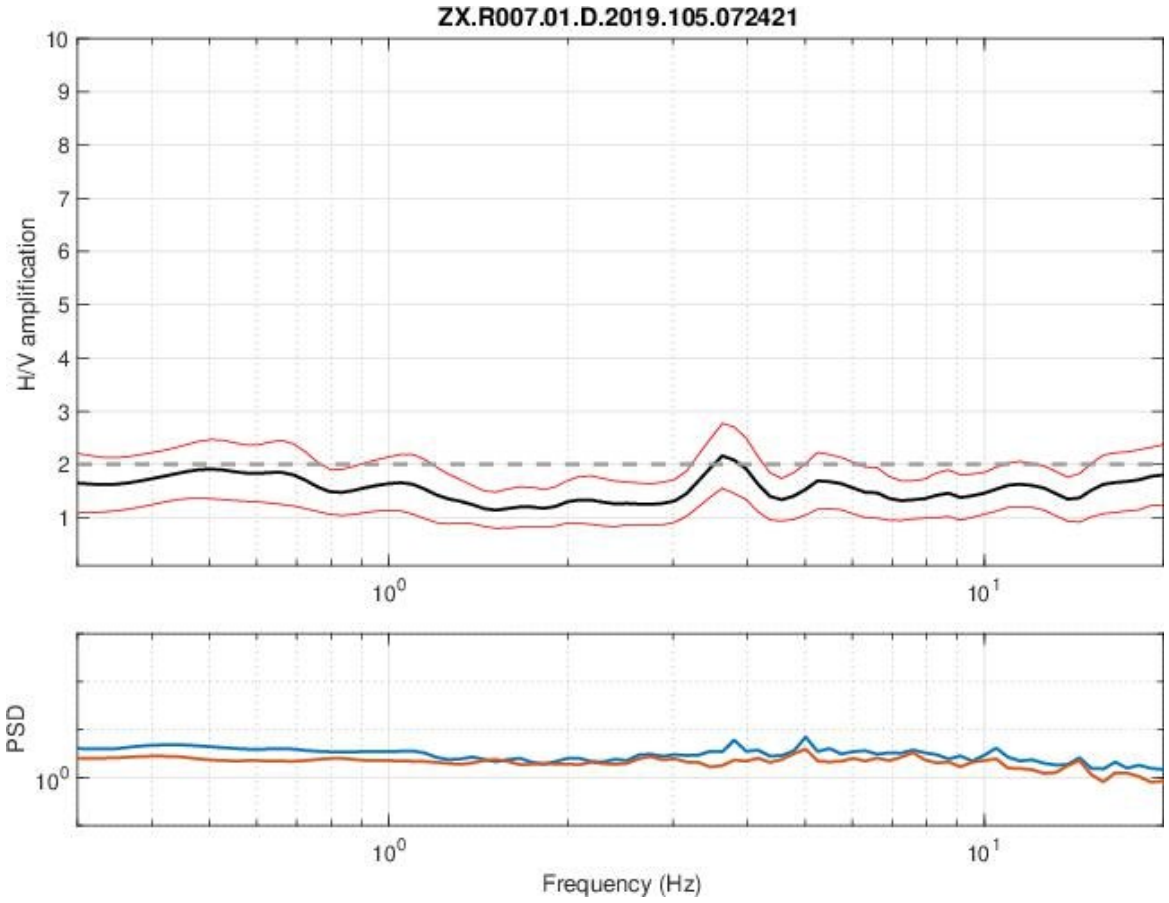


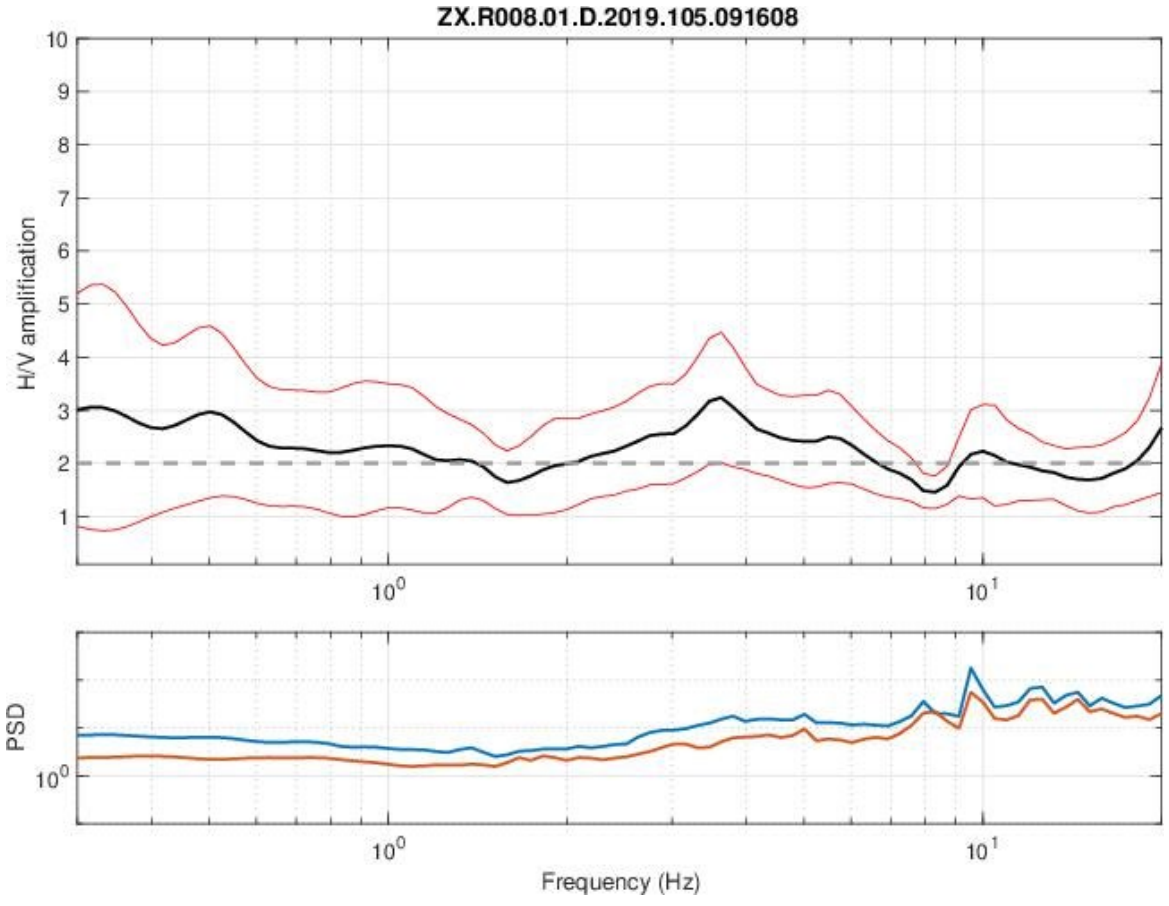

ZX.R003.01.D.2018.284.102742
H/V amplification
PSD
Frequency (Hz)

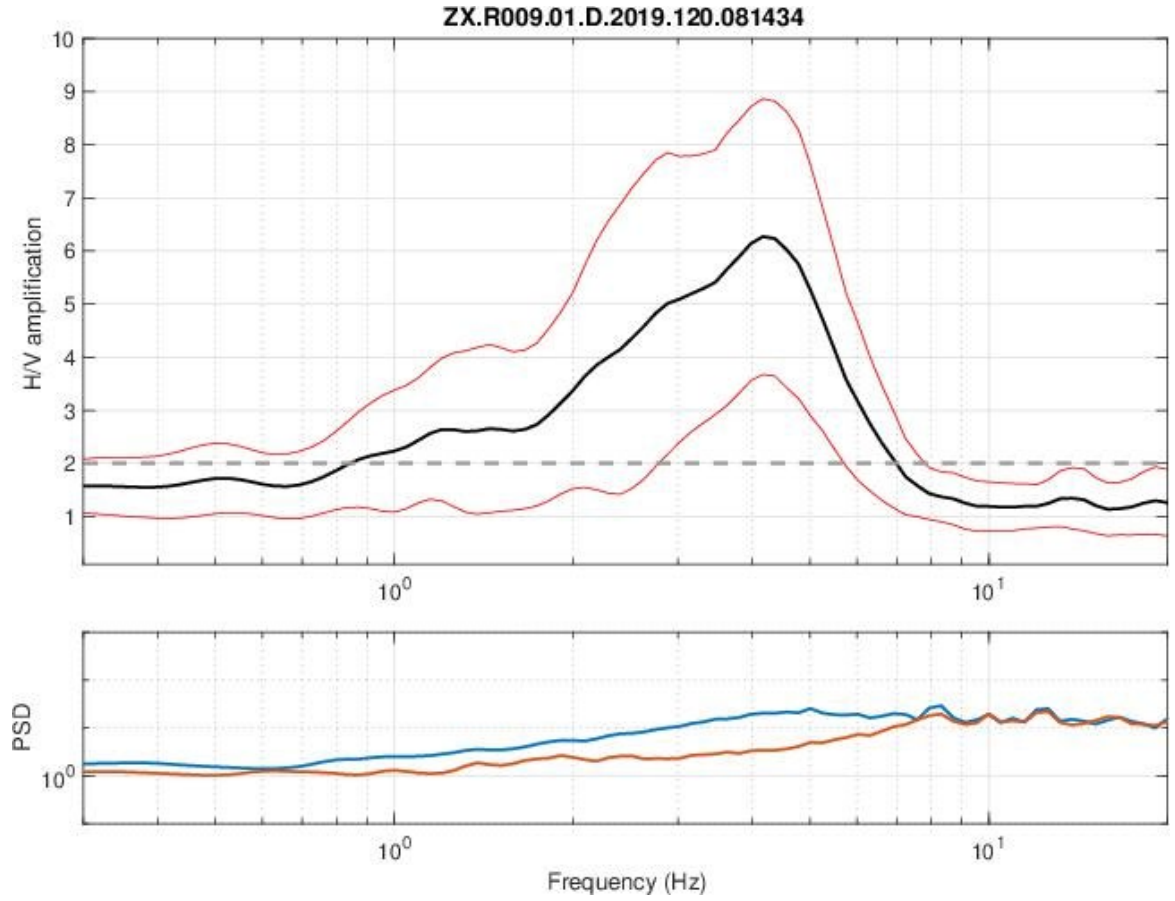

ZX.R004.01.D.2018.284.122404
H/V amplification
PSD
Frequency (Hz)

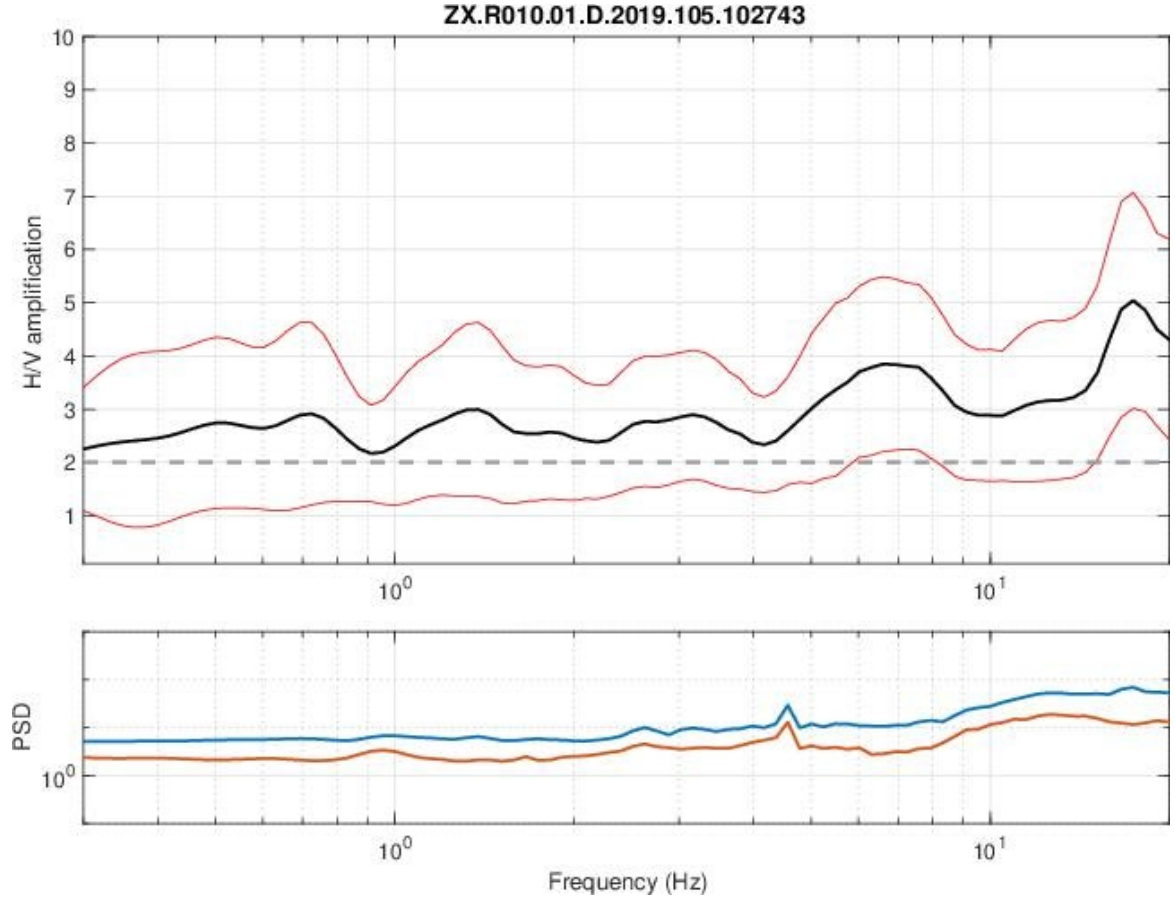

ZX.R005.01.D.2018.284.134708
H/V amplification
PSD
Frequency (Hz)

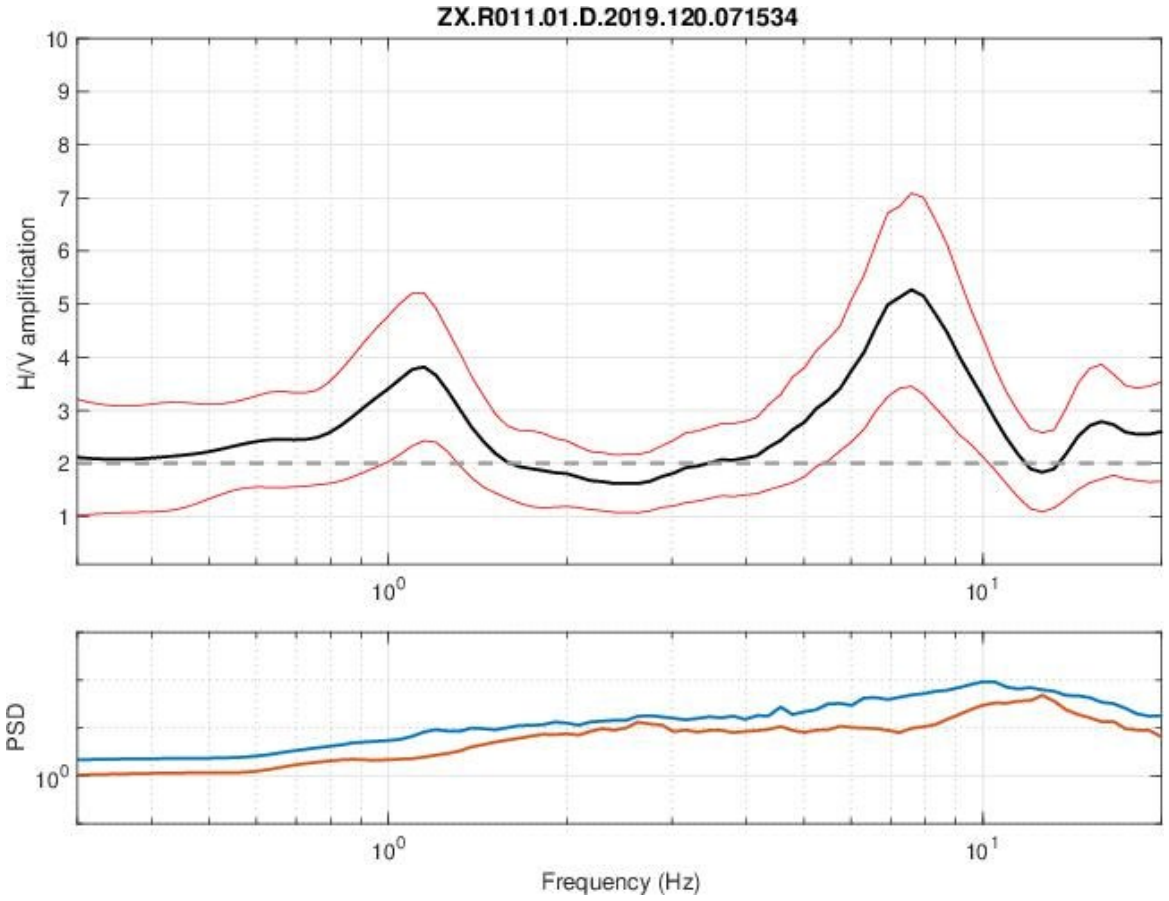

ZX.R006.01.D.2018.284.151708
H/V amplification
PSD
Frequency (Hz)

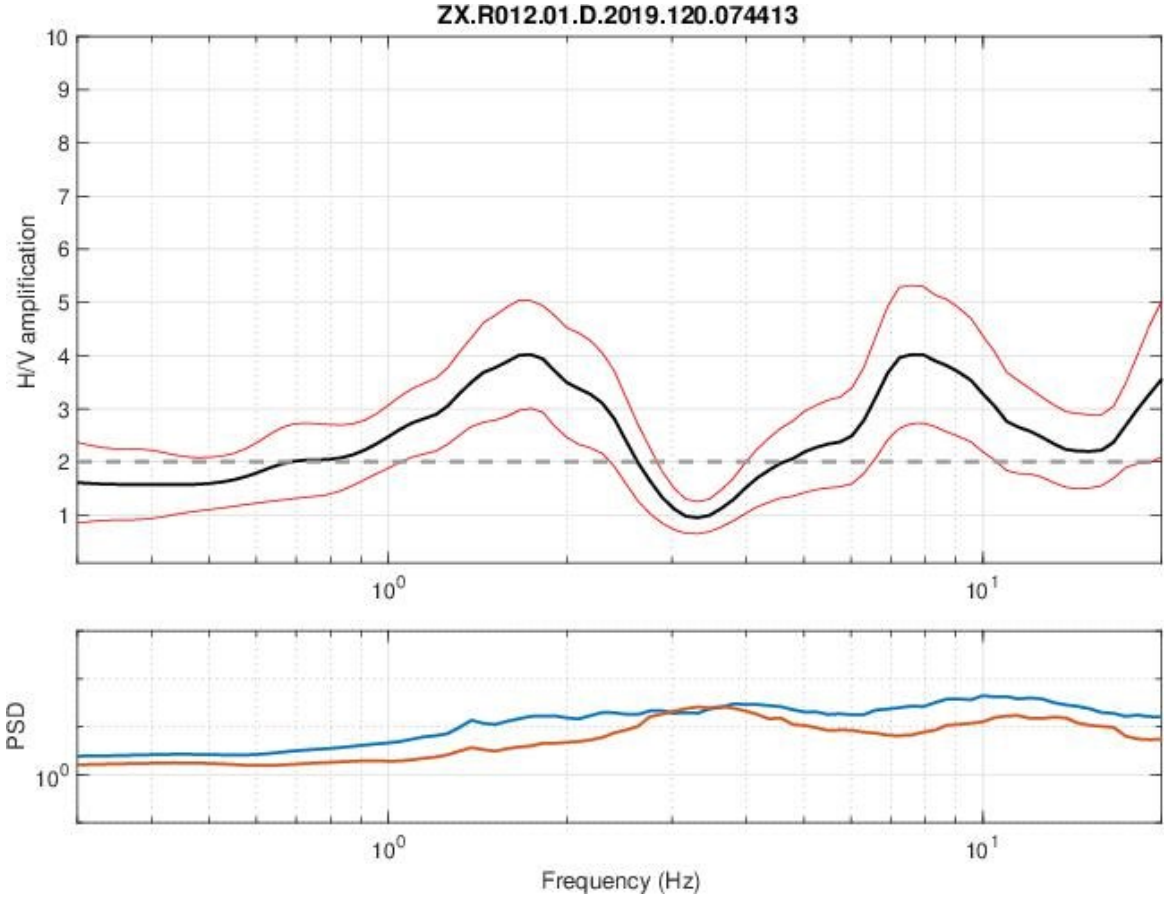

ZX.R007.01.D.2019.105.072421
H/V amplification
PSD
Frequency (Hz)

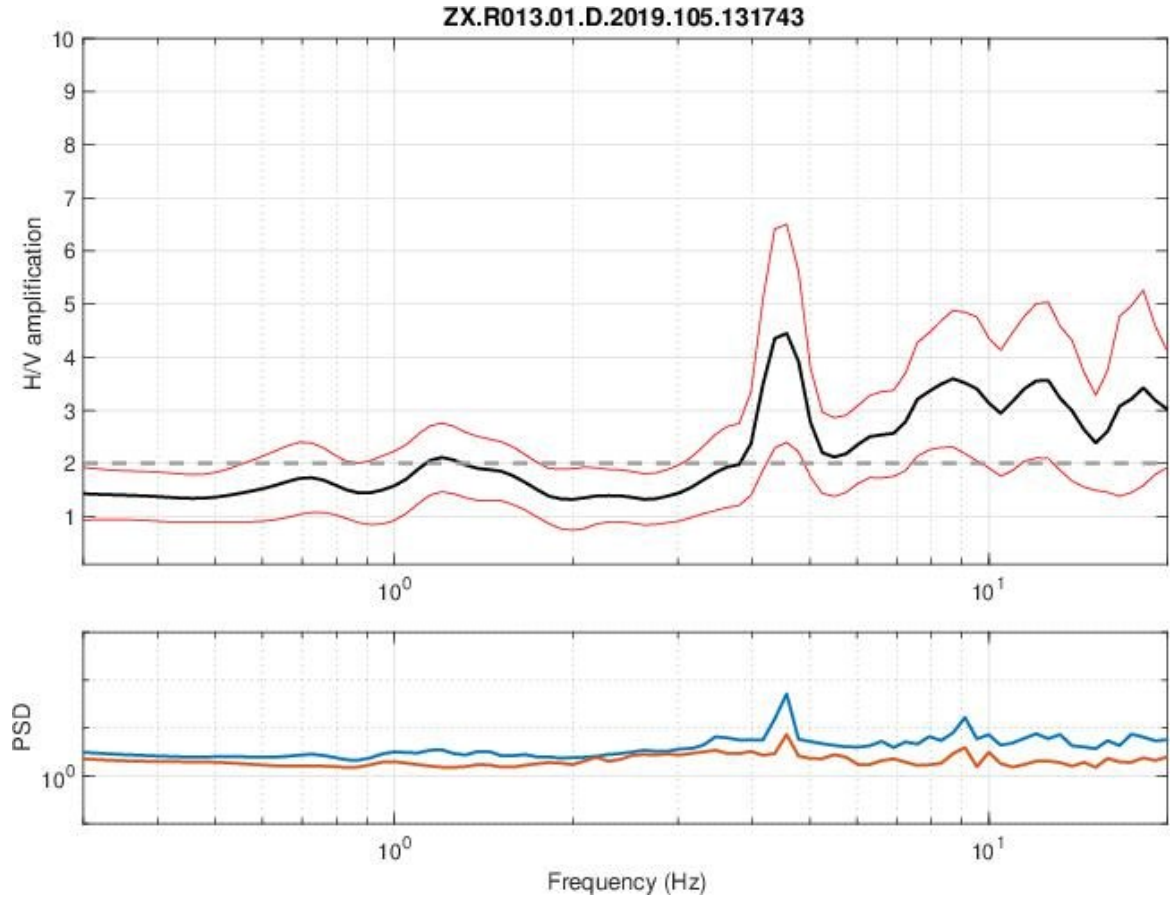

ZX.R008.01.D.2019.105.091608
H/V amplification
PSD
Frequency (Hz)

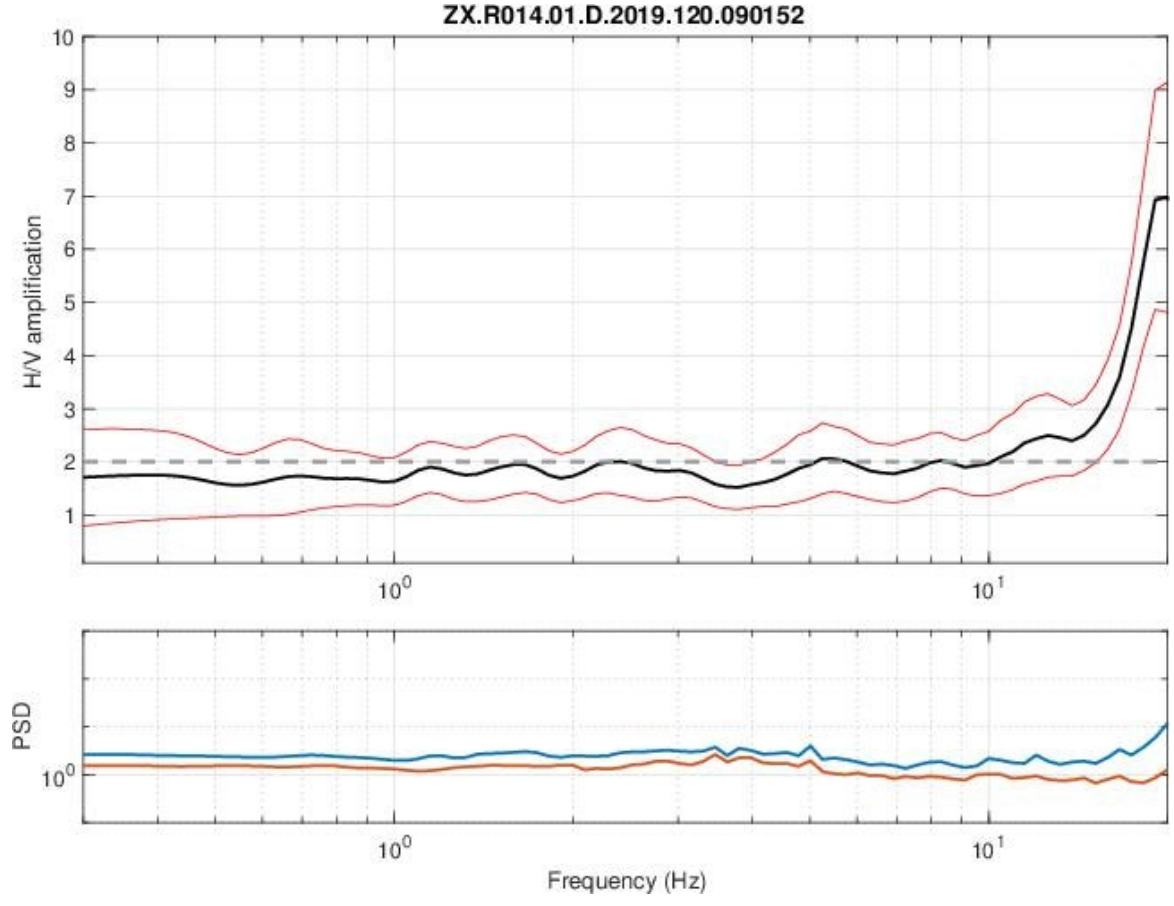

ZX.R009.01.D.2019.120.081434
H/V amplification
PSD
Frequency (Hz)

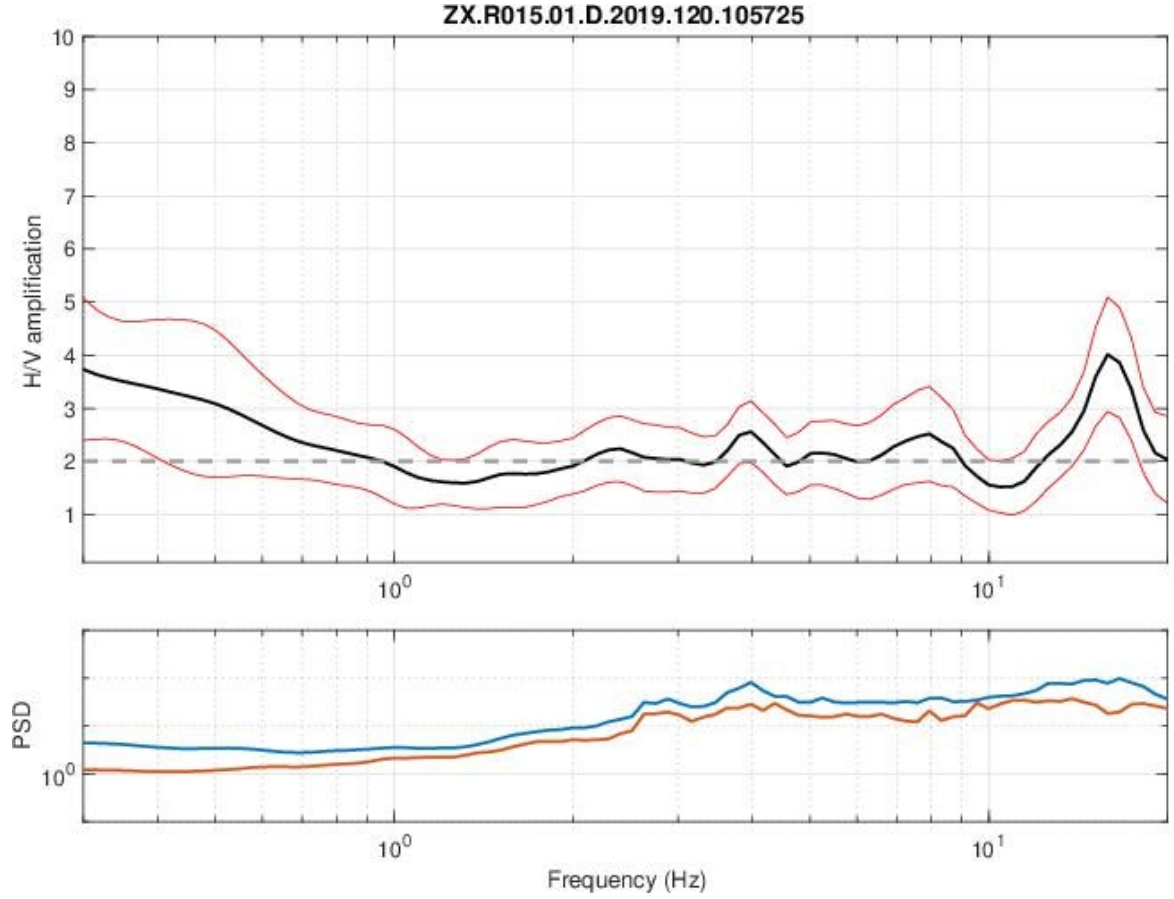

ZX.R010.01.D.2019.105.102743
H/V amplification
PSD
Frequency (Hz)

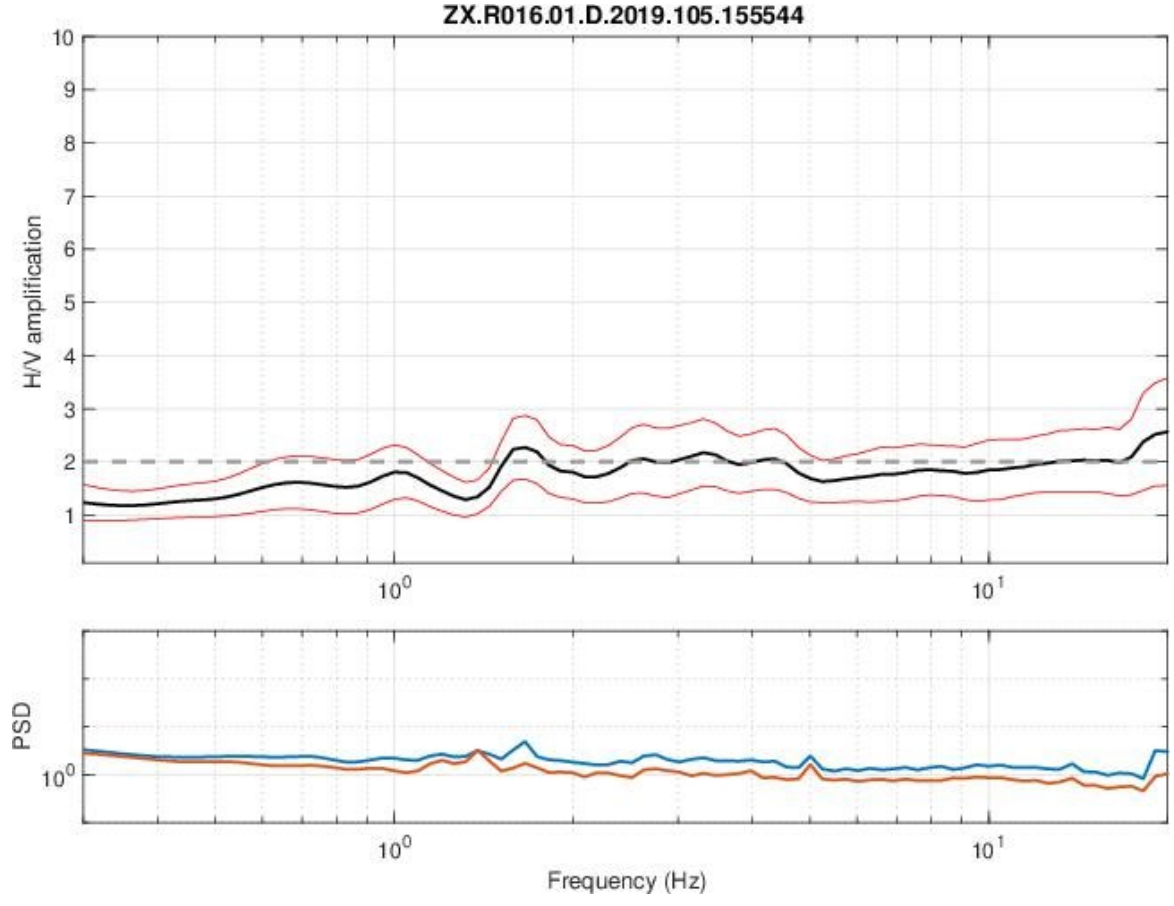

ZX.R011.01.D.2019.120.071534
H/V amplification
PSD
Frequency (Hz)

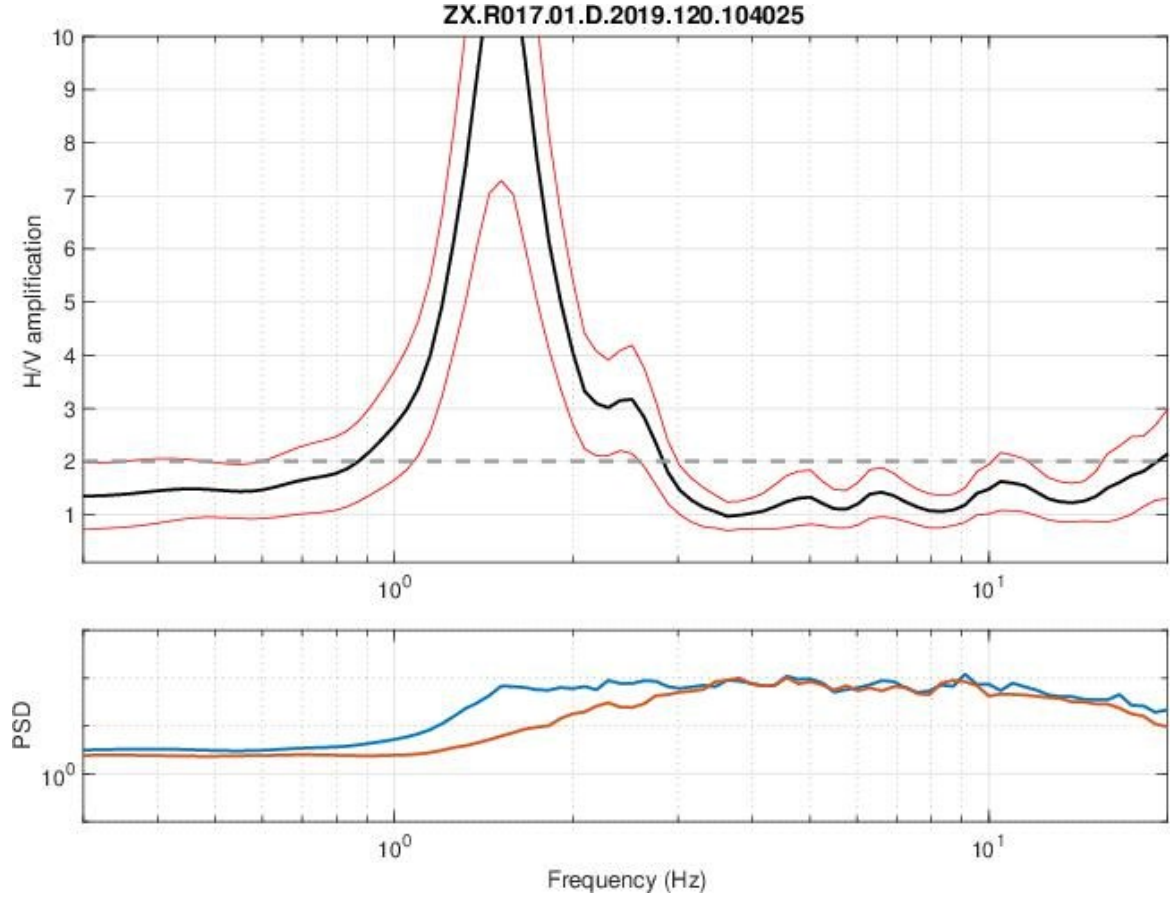

ZX.R012.01.D.2019.120.074413
H/V amplification
PSD
Frequency (Hz)

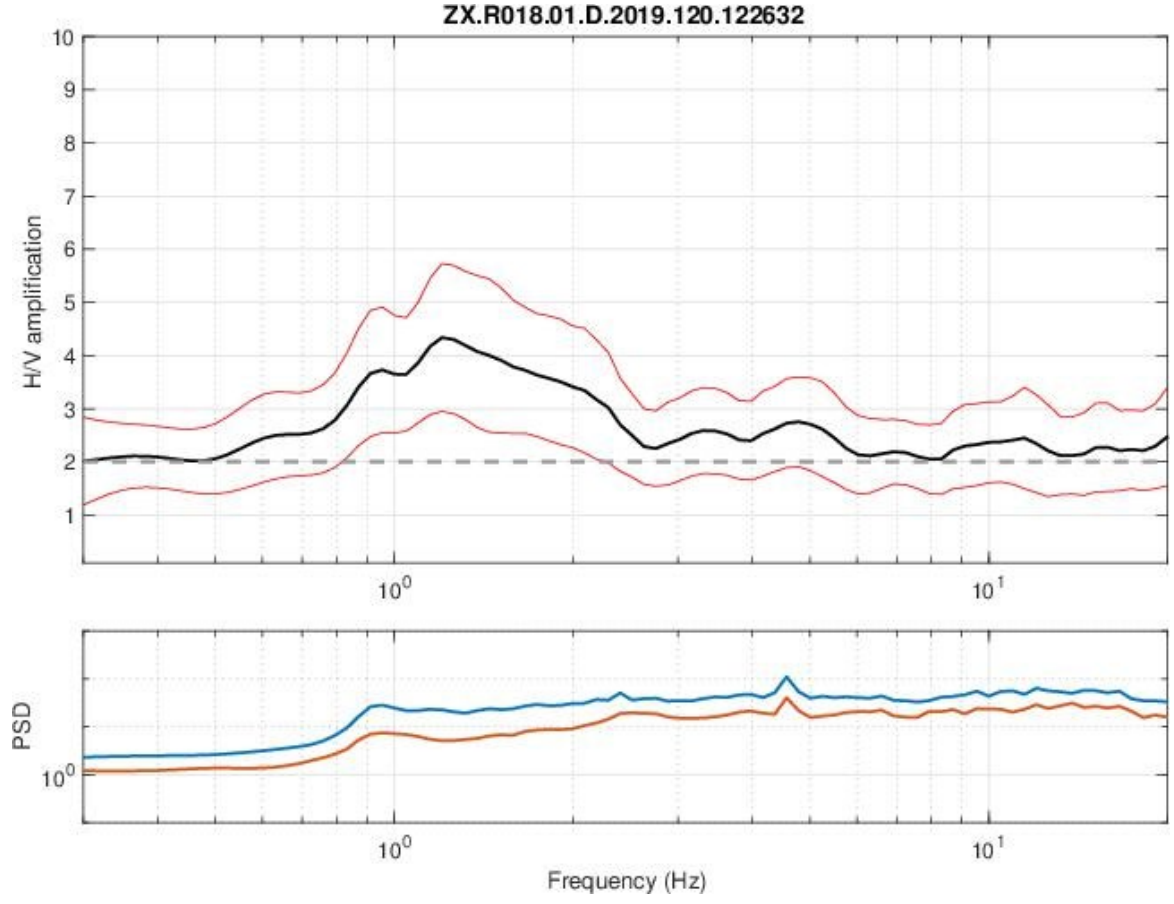

ZX.R013.01.D.2019.105.131743
H/V amplification
PSD
Frequency (Hz)

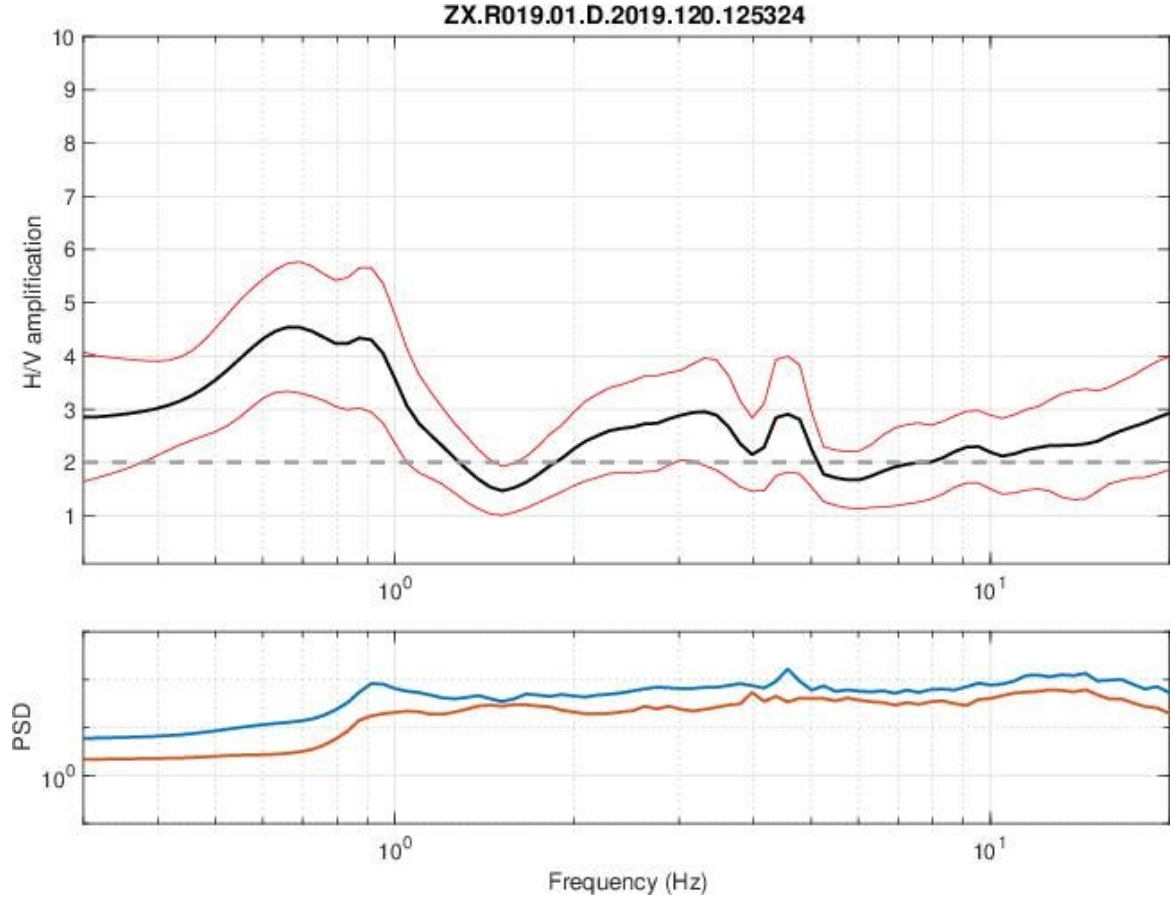

ZX.R014.01.D.2019.120.090152
H/V amplification
PSD
Frequency (Hz)

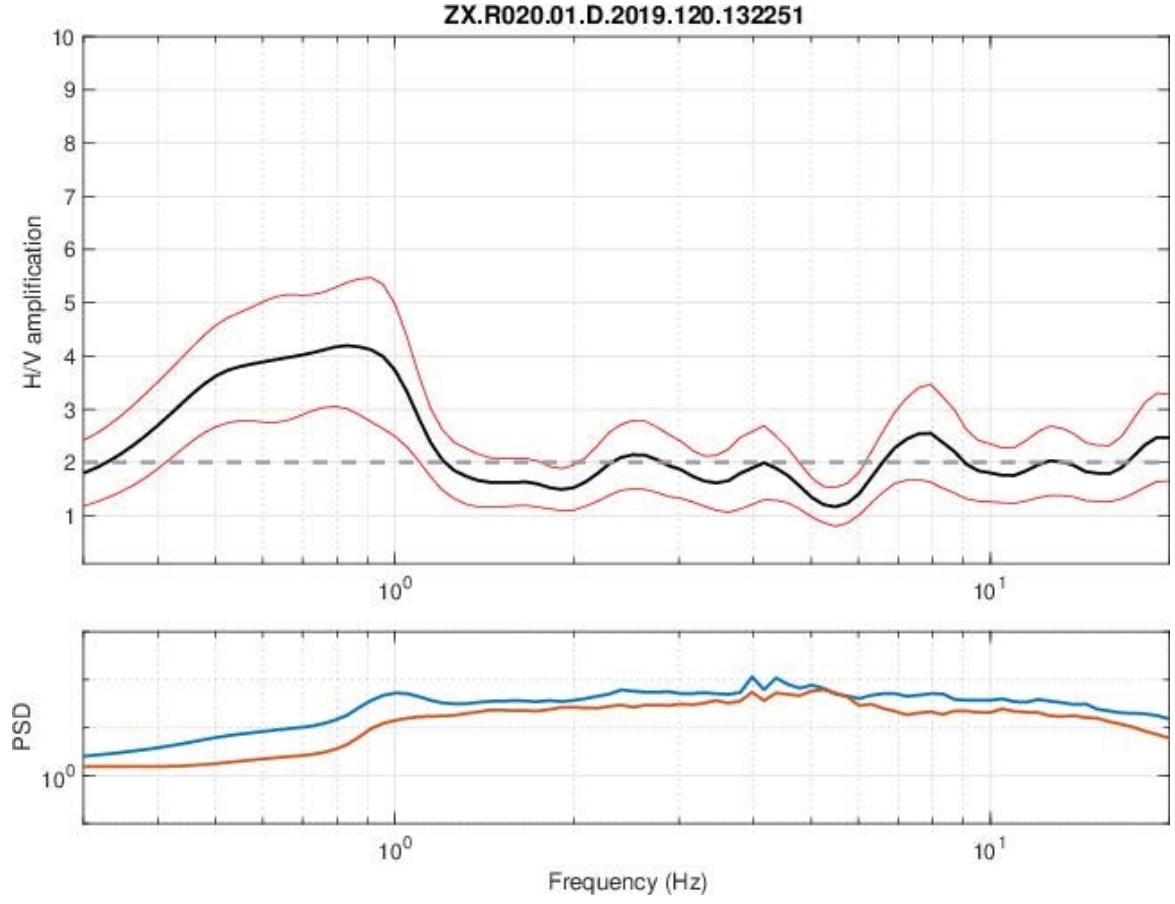

ZX.R015.01.D.2019.120.105725
H/V amplification
PSD
Frequency (Hz)

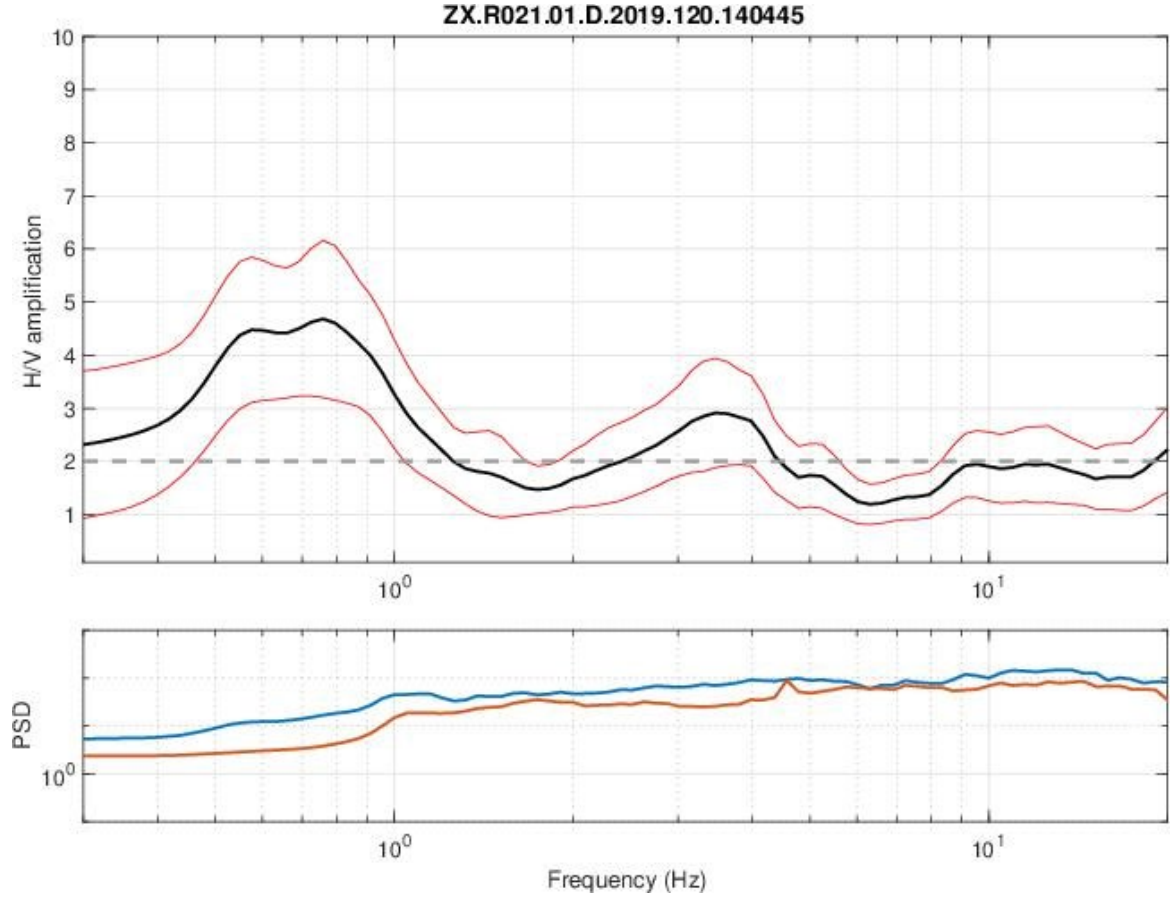

ZX.R016.01.D.2019.105.155544
H/V amplification
PSD
Frequency (Hz)

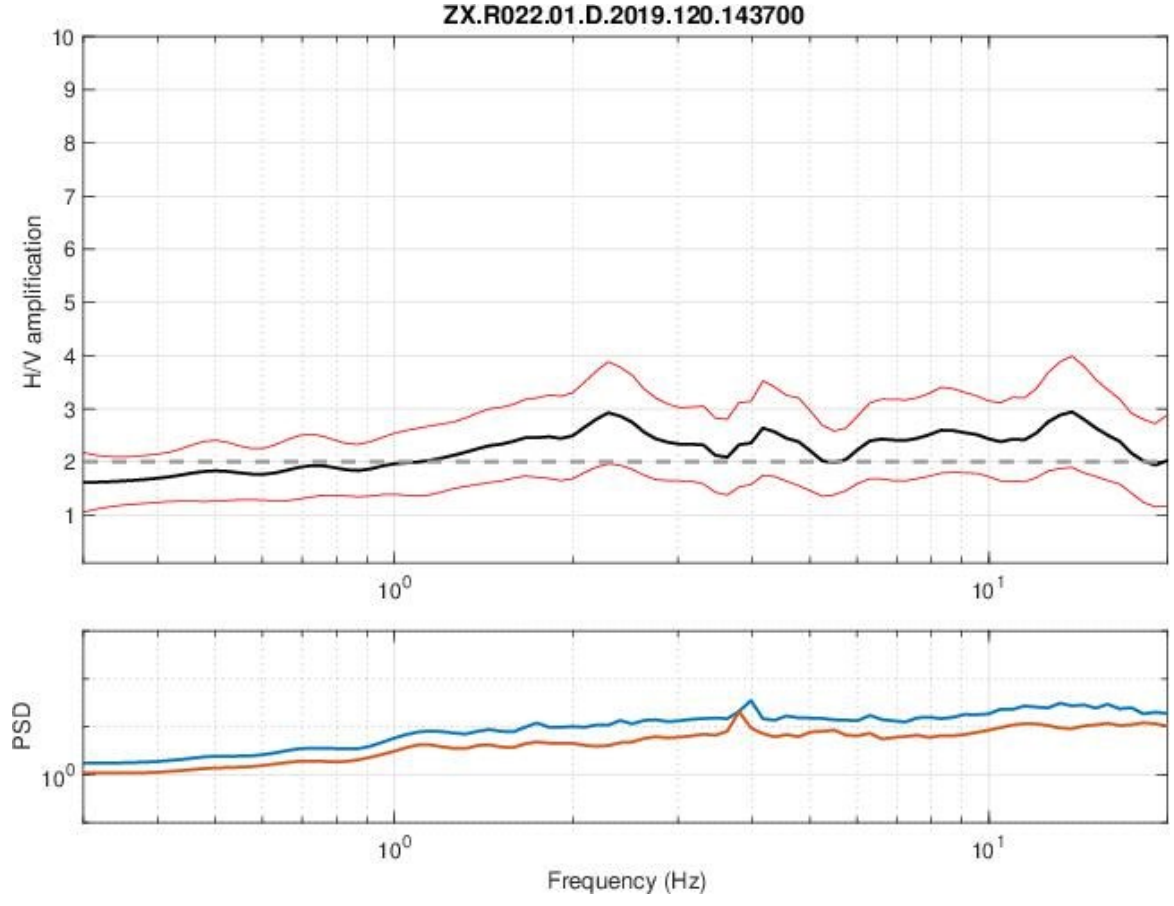

ZX.R017.01.D.2019.120.104025
H/V amplification
PSD
Frequency (Hz)

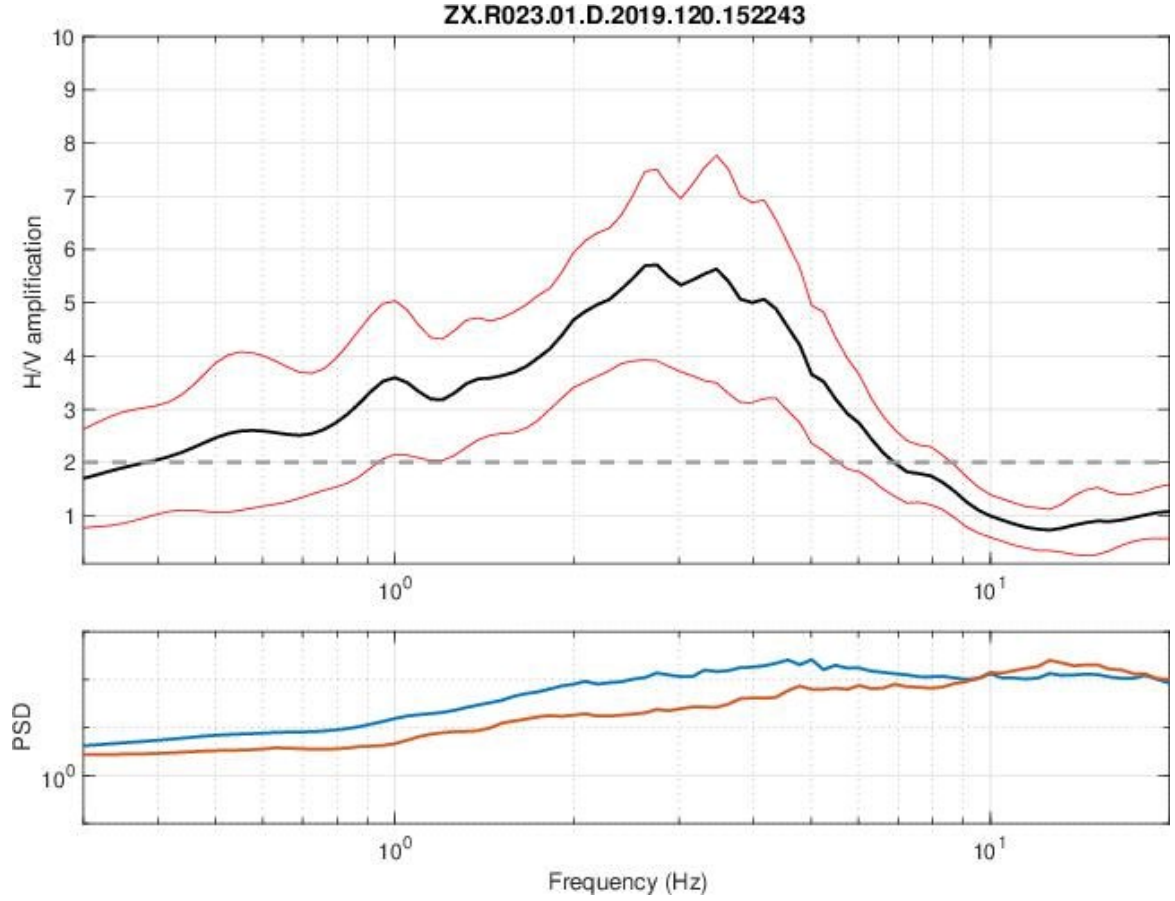

ZX.R018.01.D.2019.120.122632
H/V amplification
PSD
Frequency (Hz)

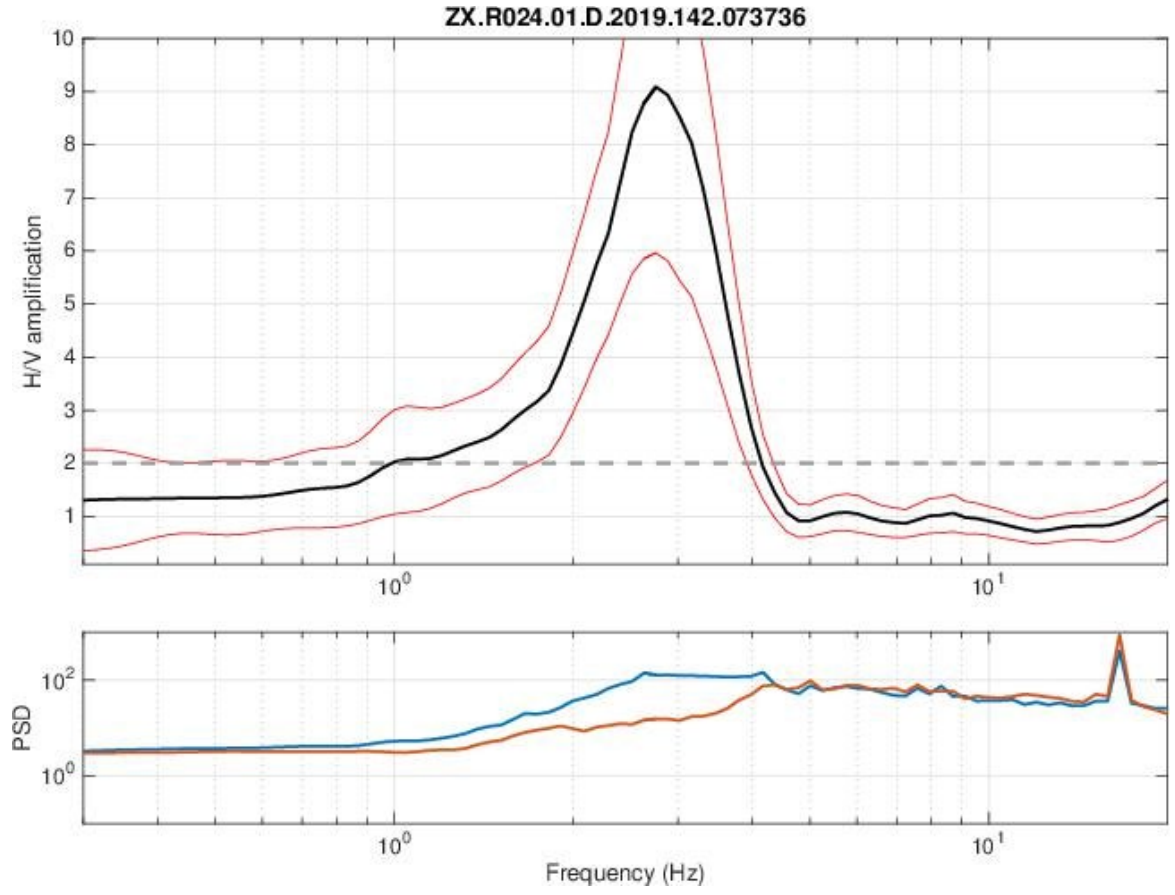

ZX.R019.01.D.2019.120.125324
H/V amplification
PSD
Frequency (Hz)

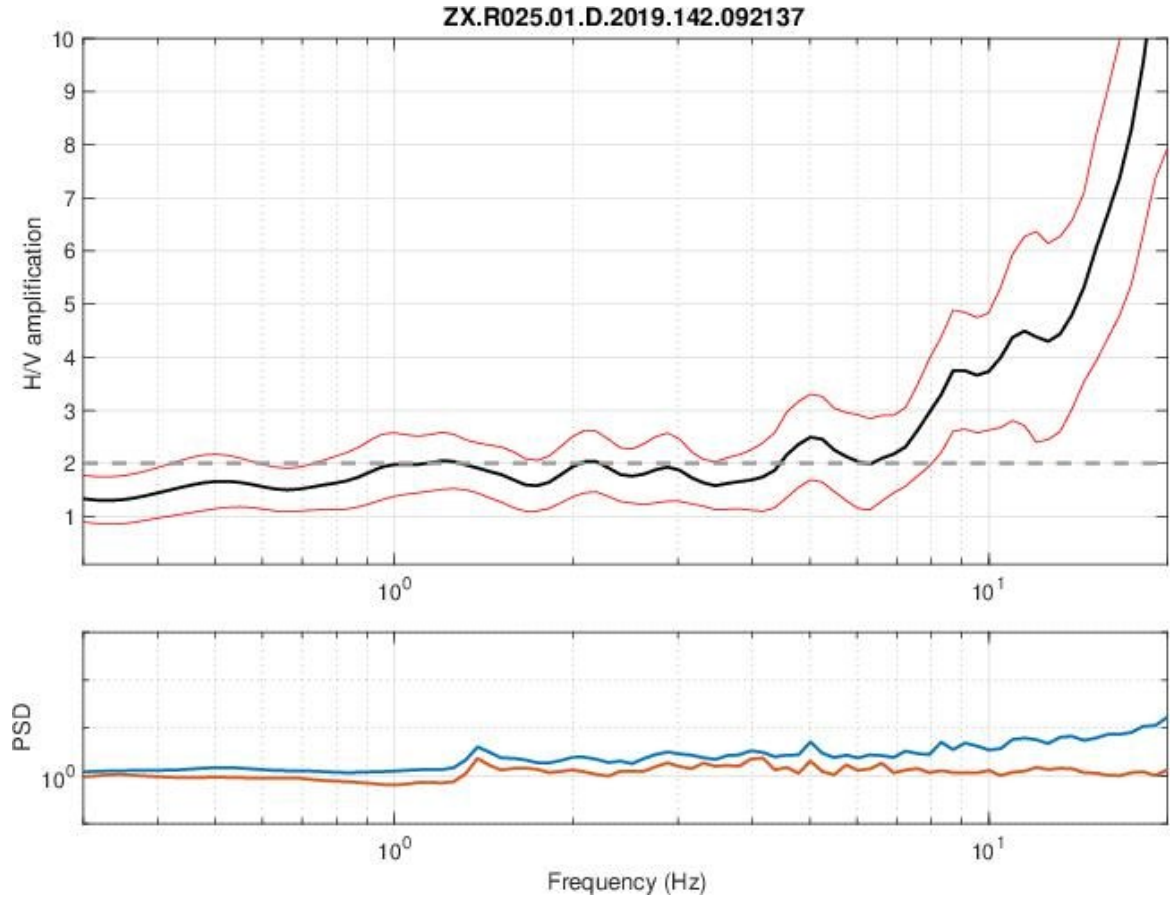

ZX.R020.01.D.2019.120.132251
H/V amplification
PSD
Frequency (Hz)

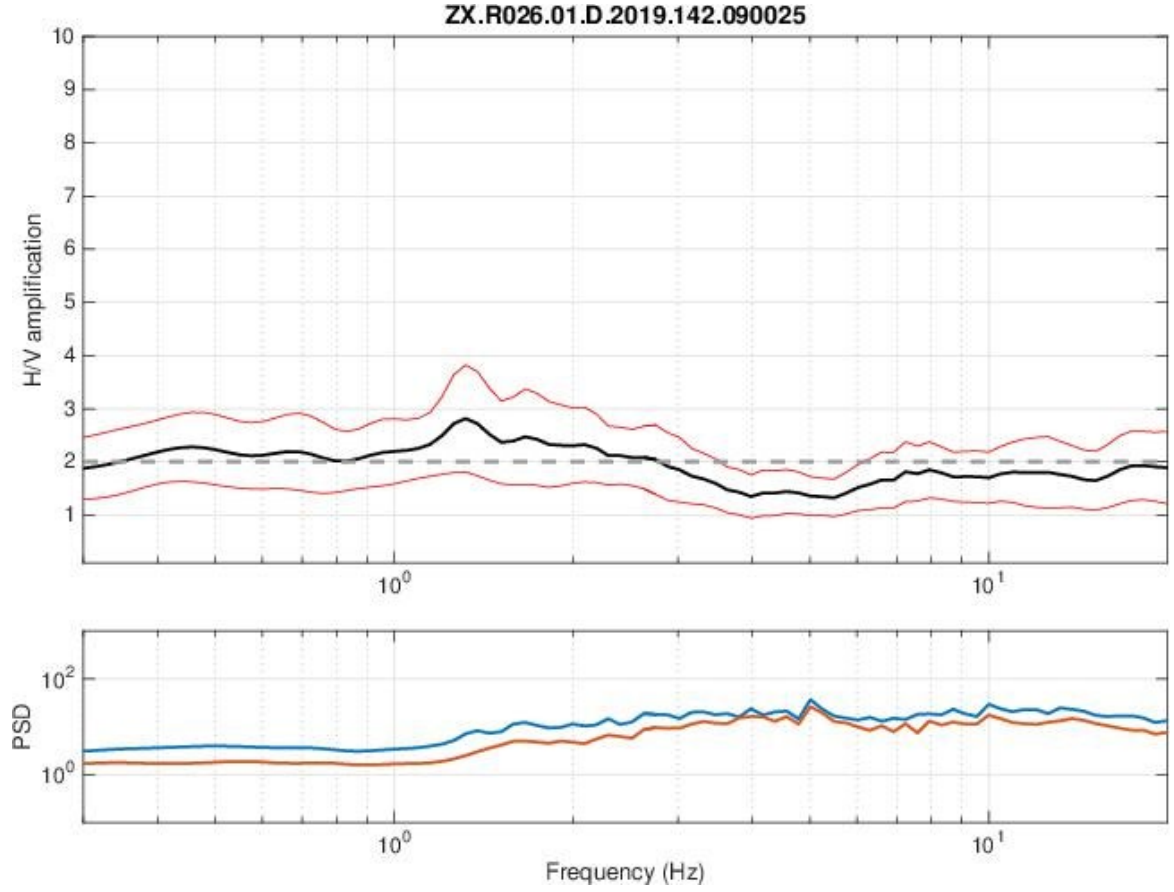

ZX.R021.01.D.2019.120.140445
H/V amplification
PSD
Frequency (Hz)

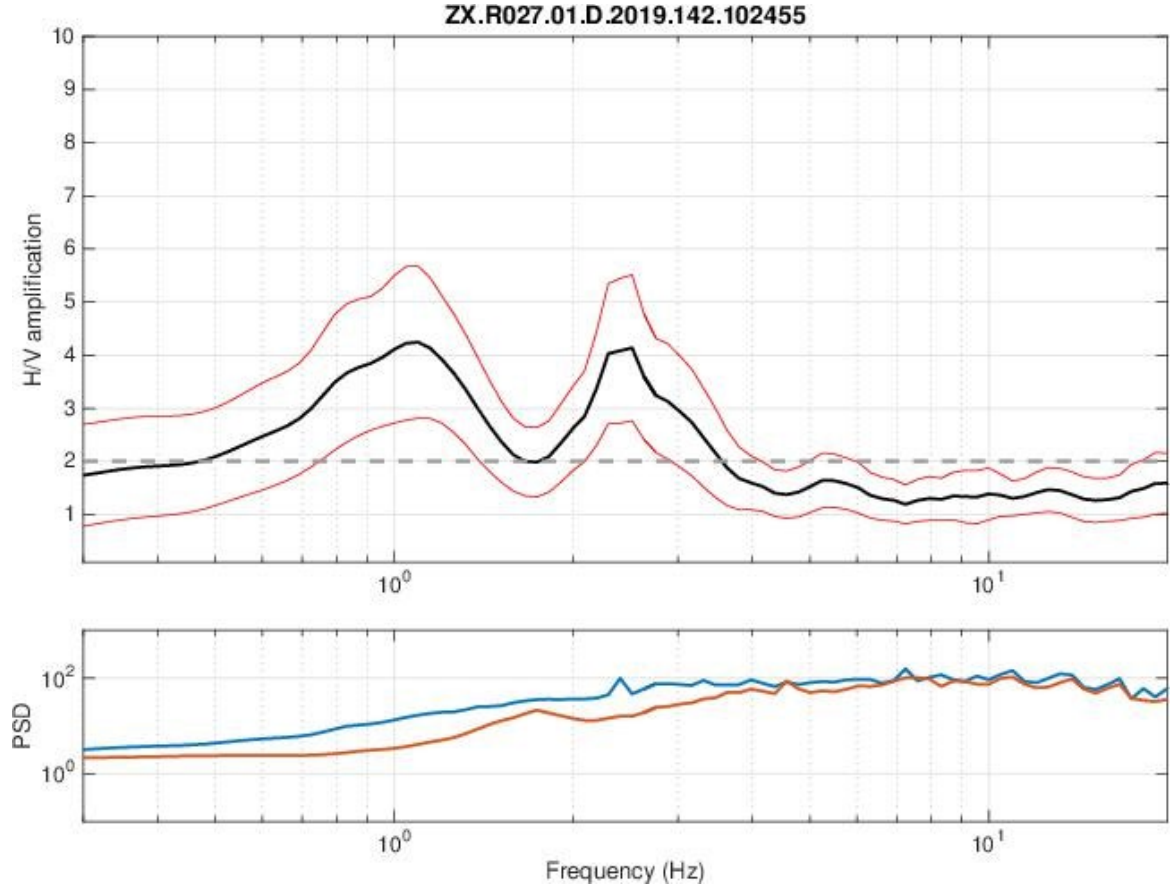

ZX.R022.01.D.2019.120.143700
H/V amplification
PSD
Frequency (Hz)

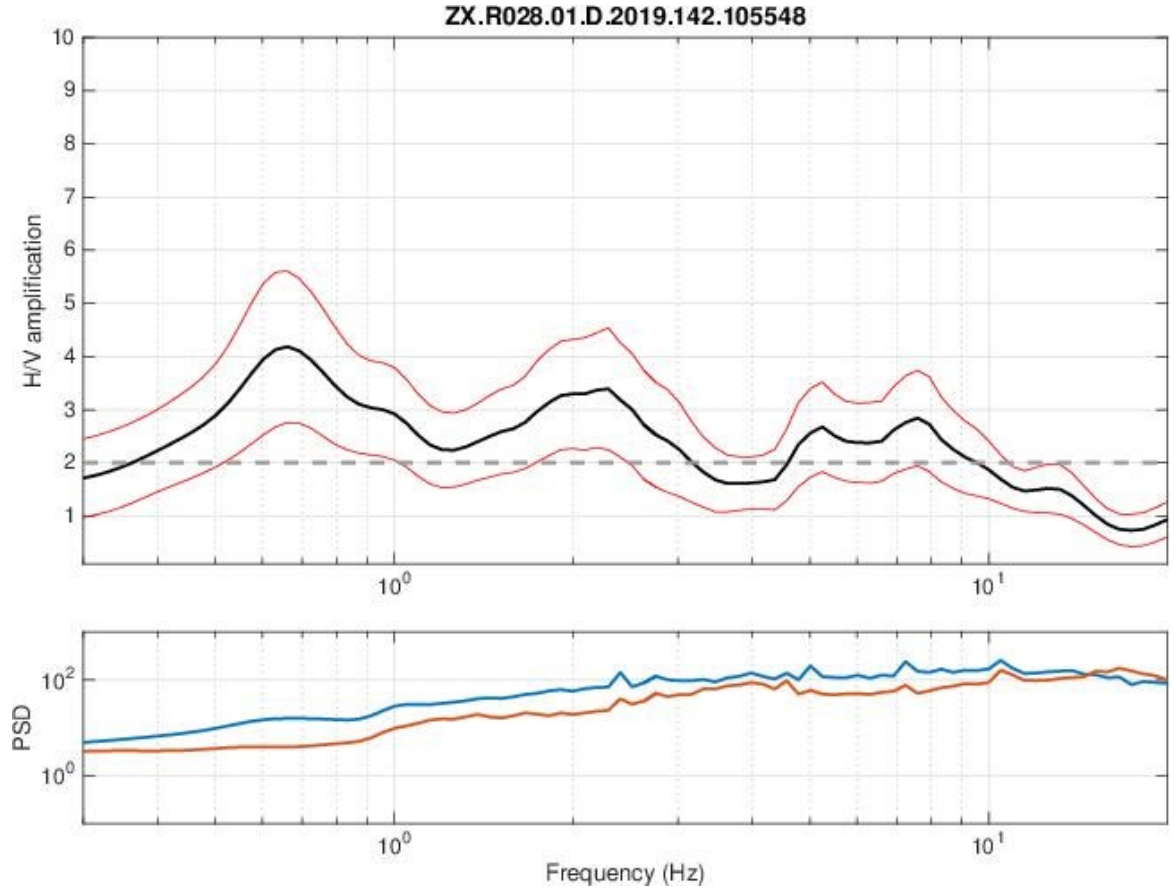

ZX.R023.01.D.2019.120.152243
H/V amplification
PSD
Frequency (Hz)

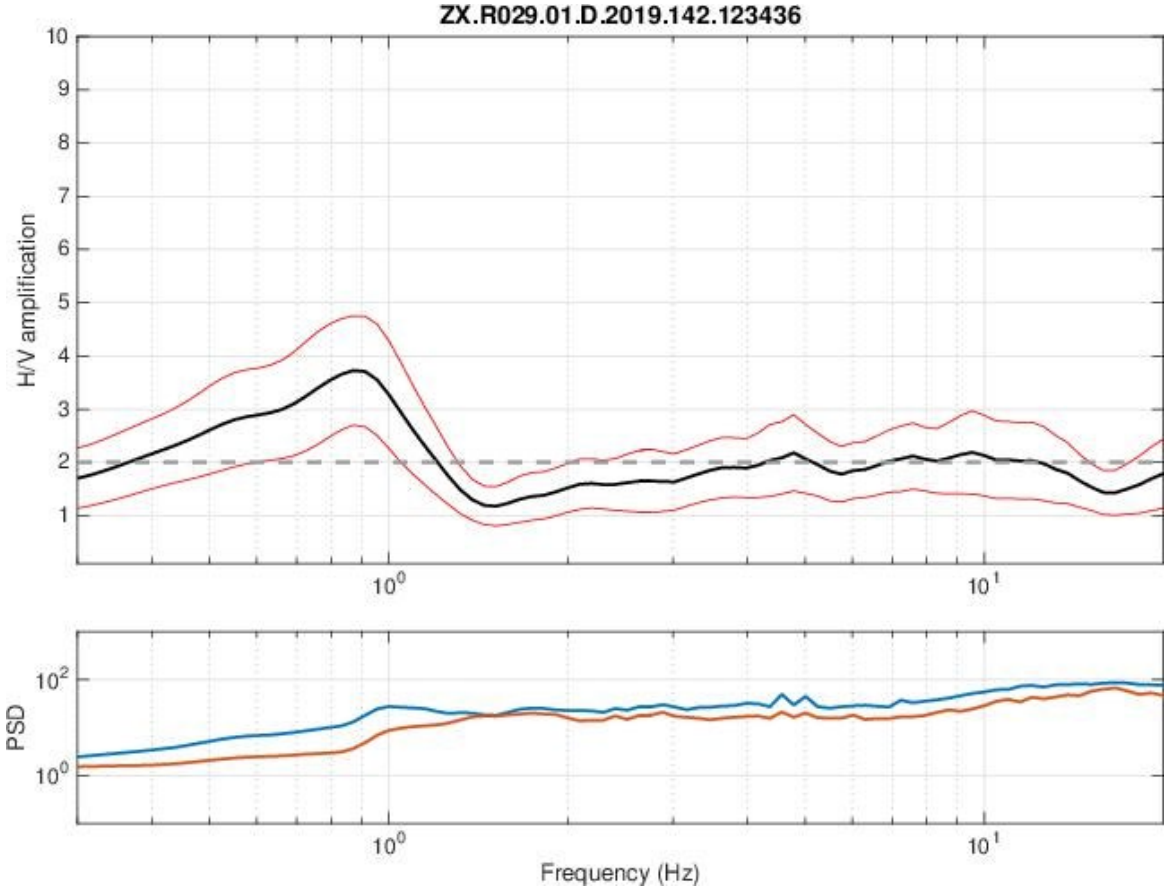

ZX.R024.01.D.2019.142.073736
H/V amplification
PSD
Frequency (Hz)

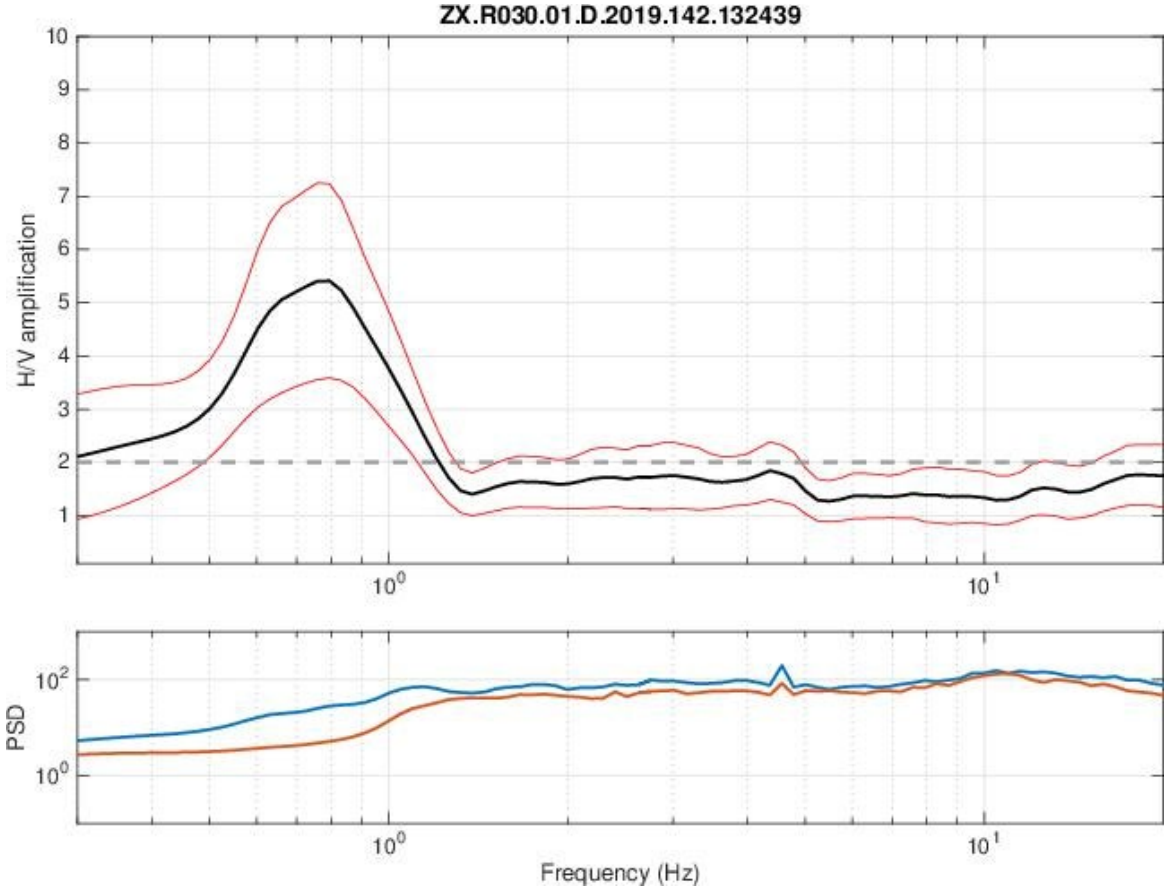

ZX.R025.01.D.2019.142.092137
H/V amplification
PSD
Frequency (Hz)

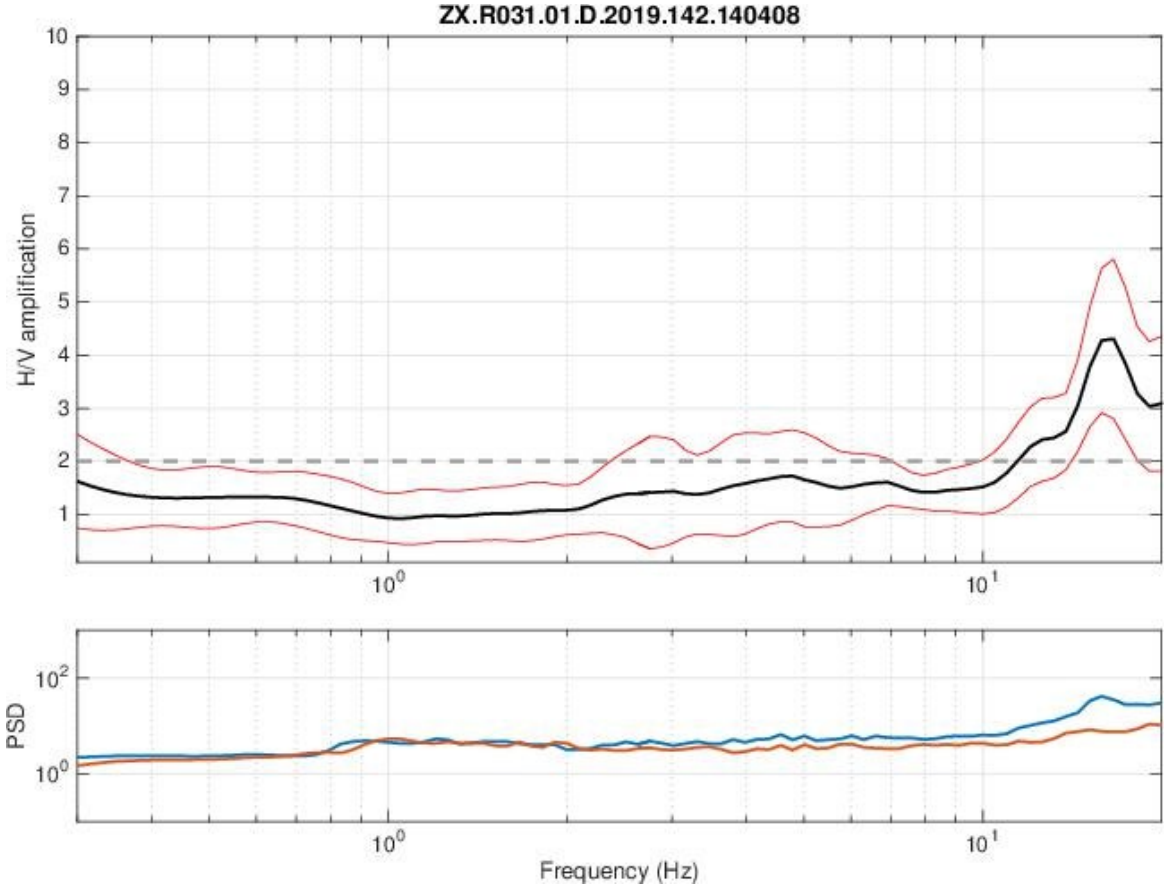

ZX.R026.01.D.2019.142.090025
H/V amplification
PSD
Frequency (Hz)

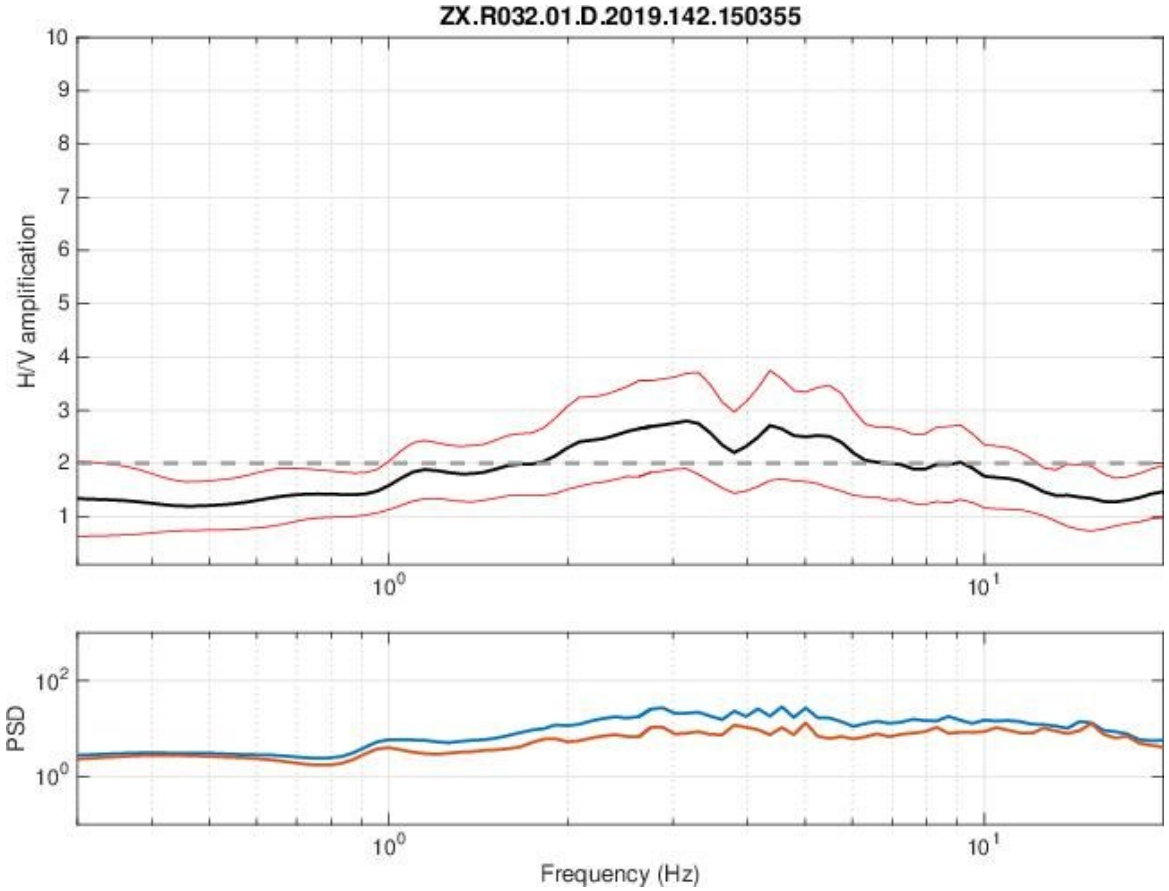

ZX.R027.01.D.2019.142.102455
H/V amplification
PSD
Frequency (Hz)

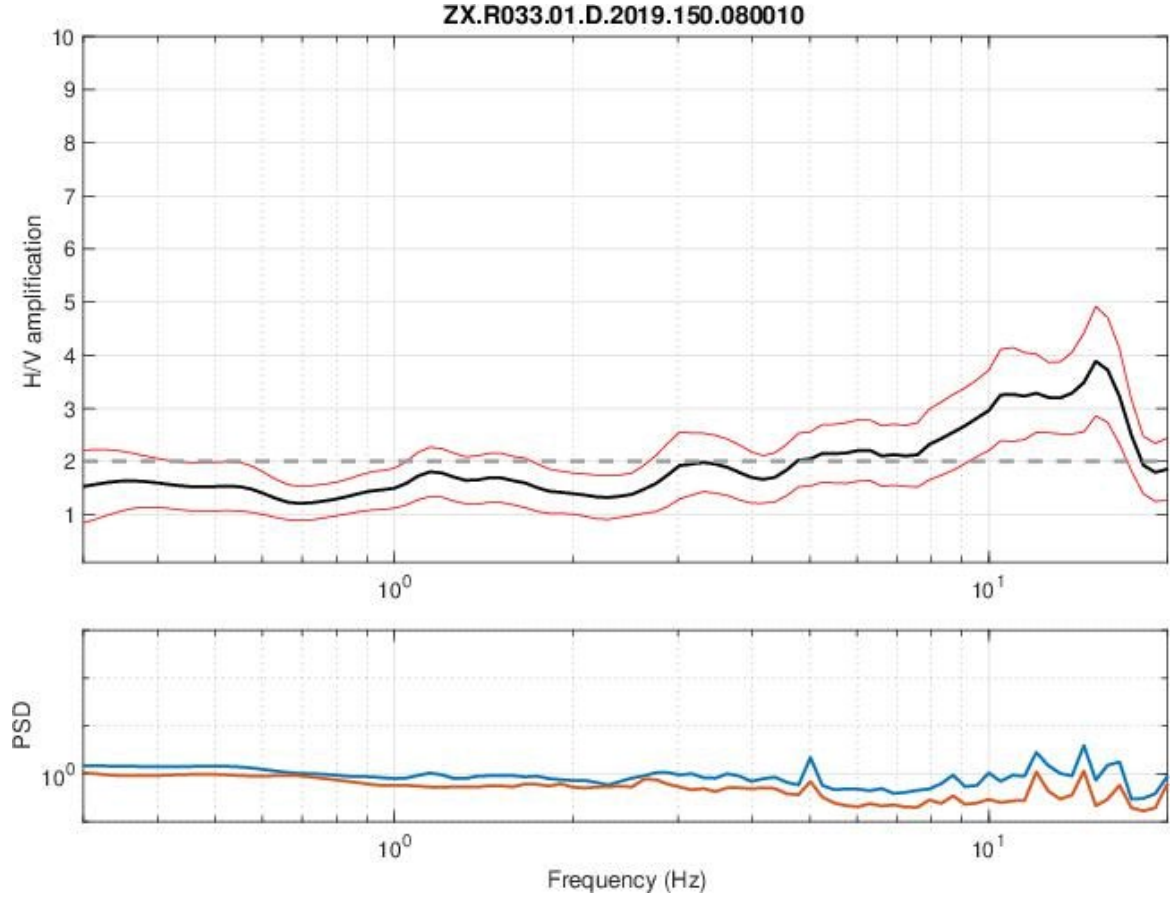

ZX.R028.01.D.2019.142.105548
H/V amplification
PSD
Frequency (Hz)

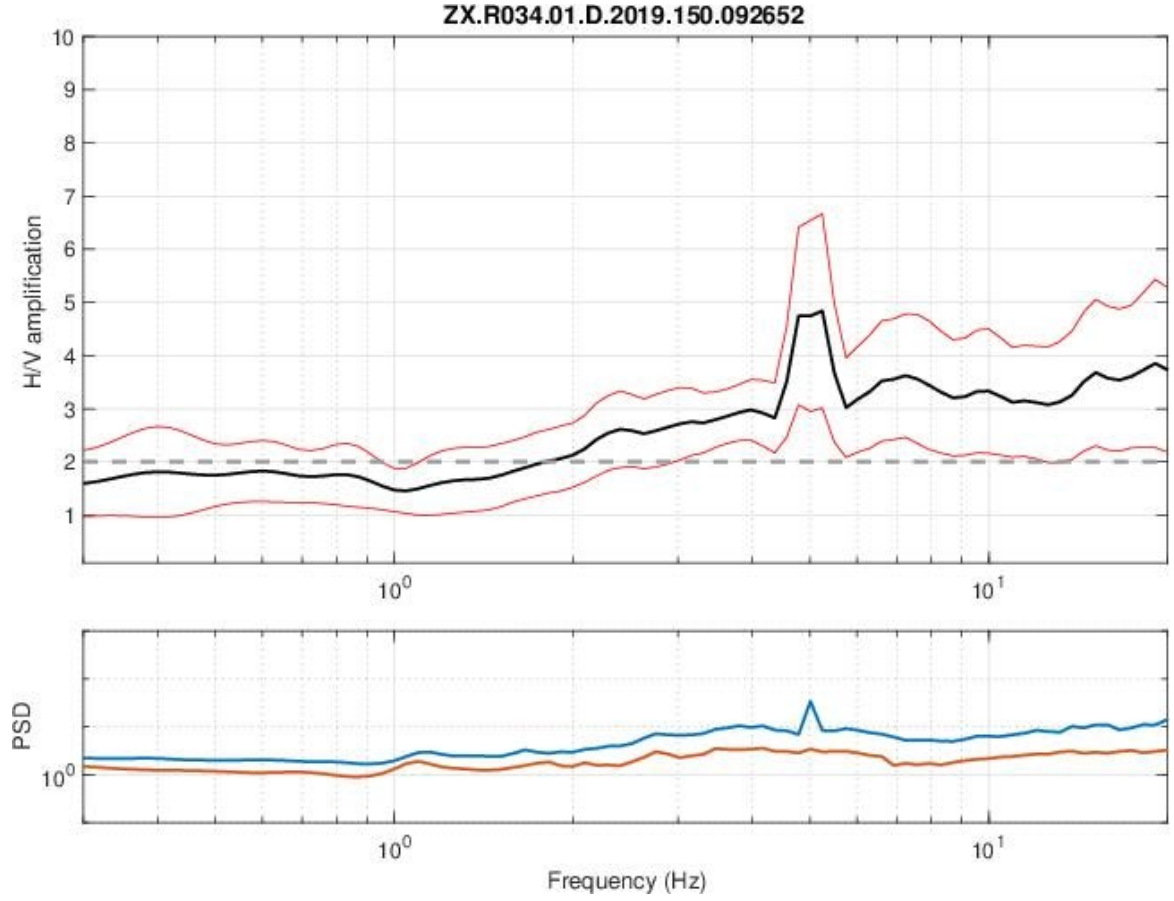

ZX.R029.01.D.2019.142.123436
H/V amplification
PSD
Frequency (Hz)

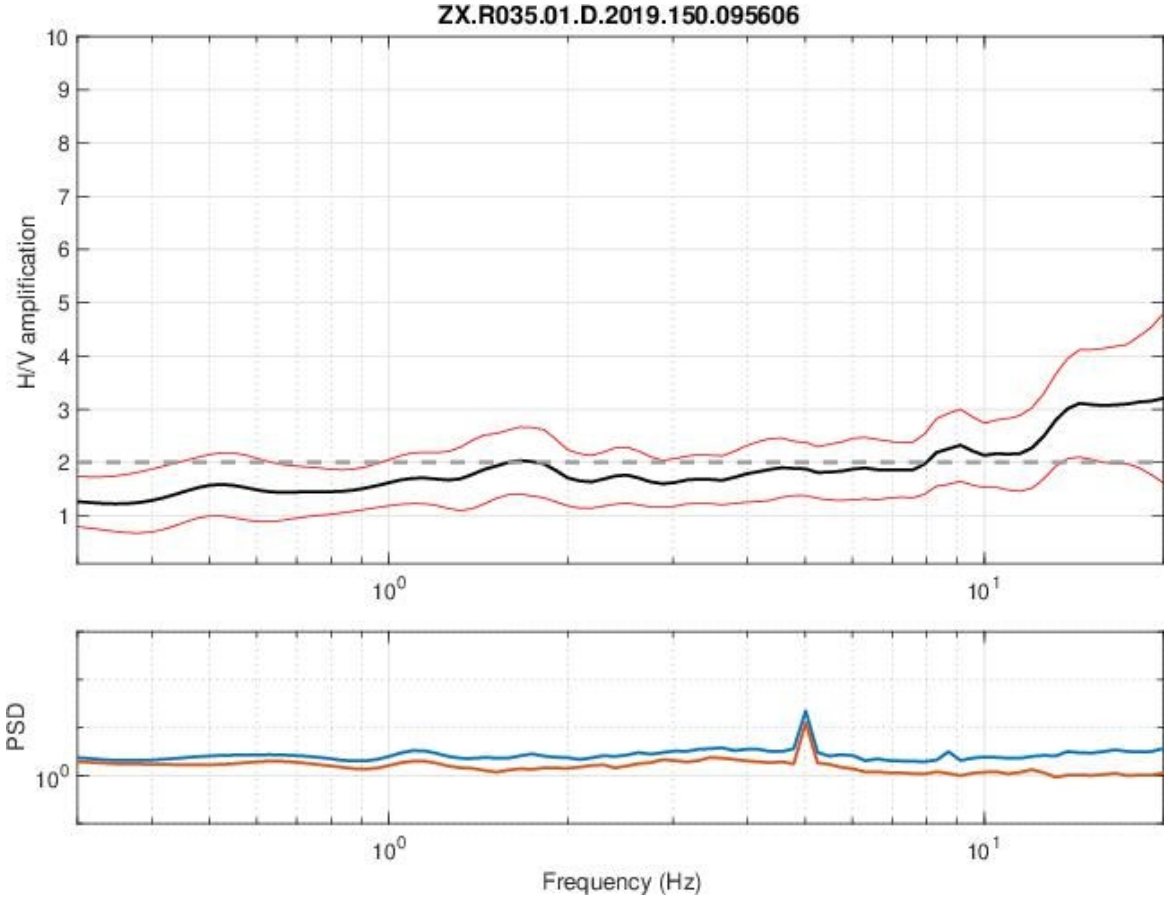

ZX.R030.01.D.2019.142.132439
H/V amplification
PSD
Frequency (Hz)

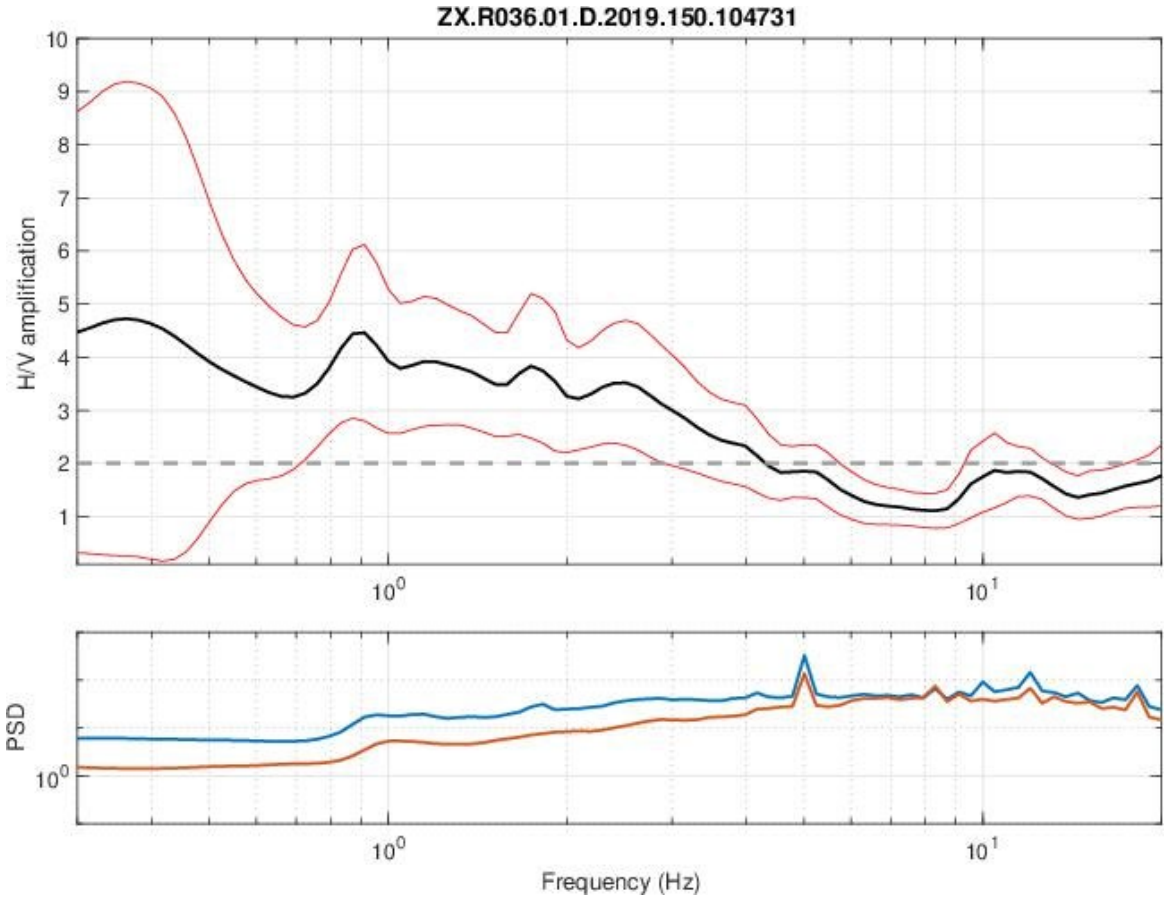

ZX.R031.01.D.2019.142.140408
H/V amplification
PSD
Frequency (Hz)

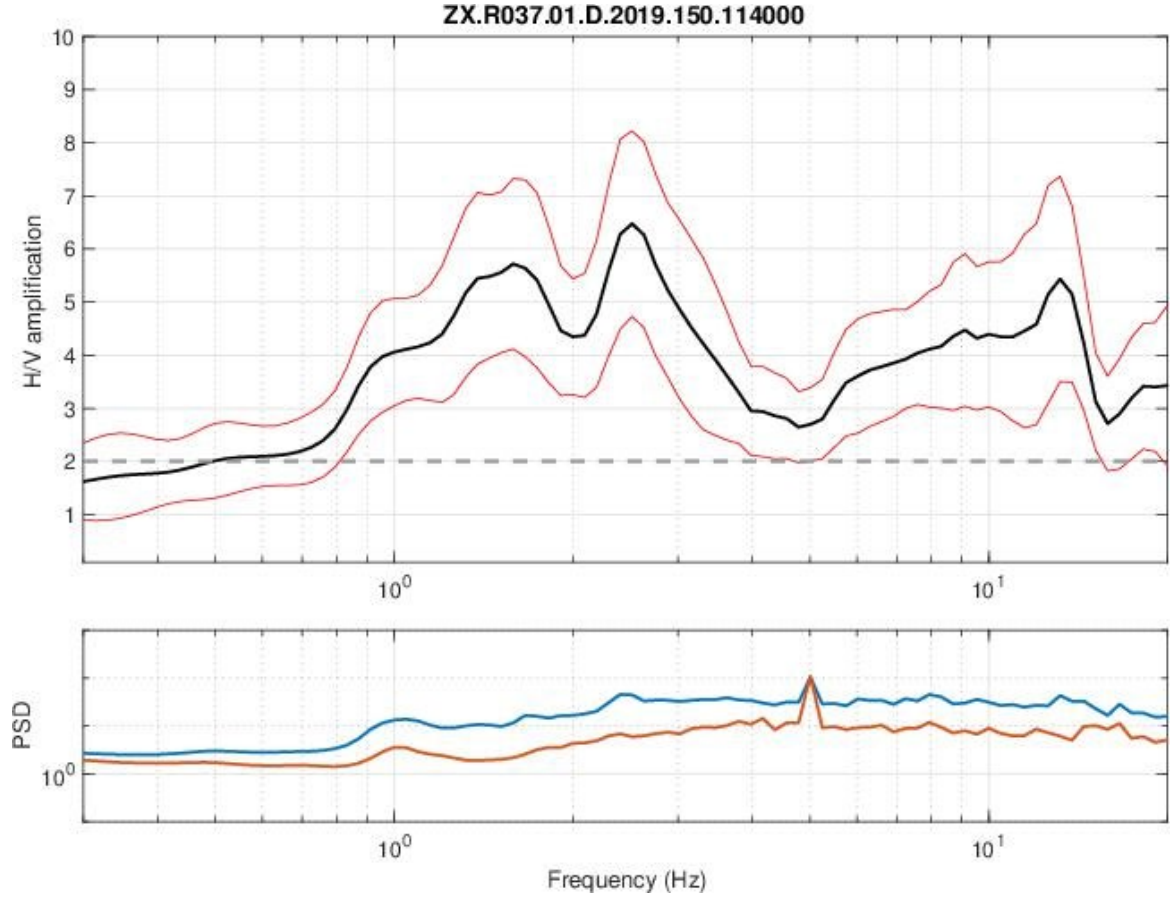

ZX.R032.01.D.2019.142.150355
H/V amplification
PSD
Frequency (Hz)

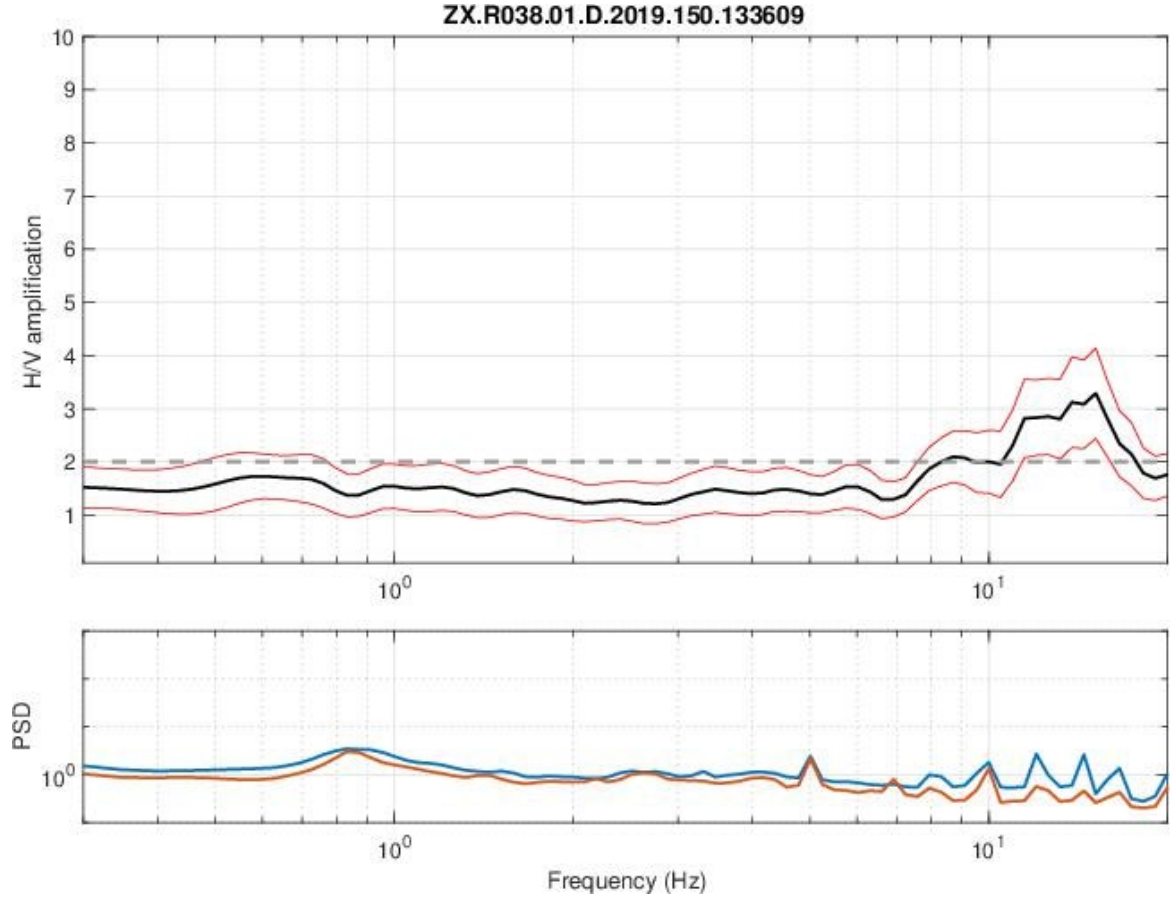

ZX.R033.01.D.2019.150.080010
H/V amplification
PSD
Frequency (Hz)

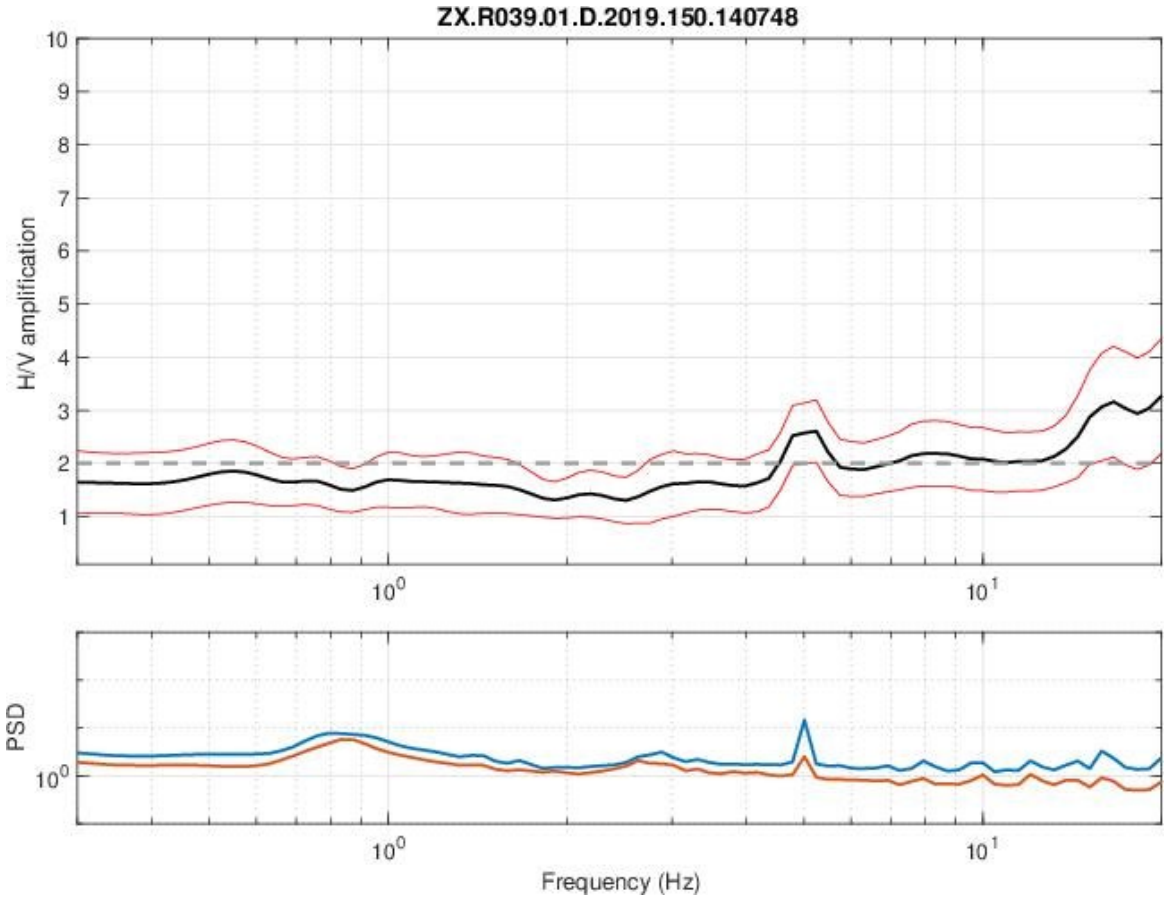

ZX.R034.01.D.2019.150.092652
H/V amplification
PSD
Frequency (Hz)

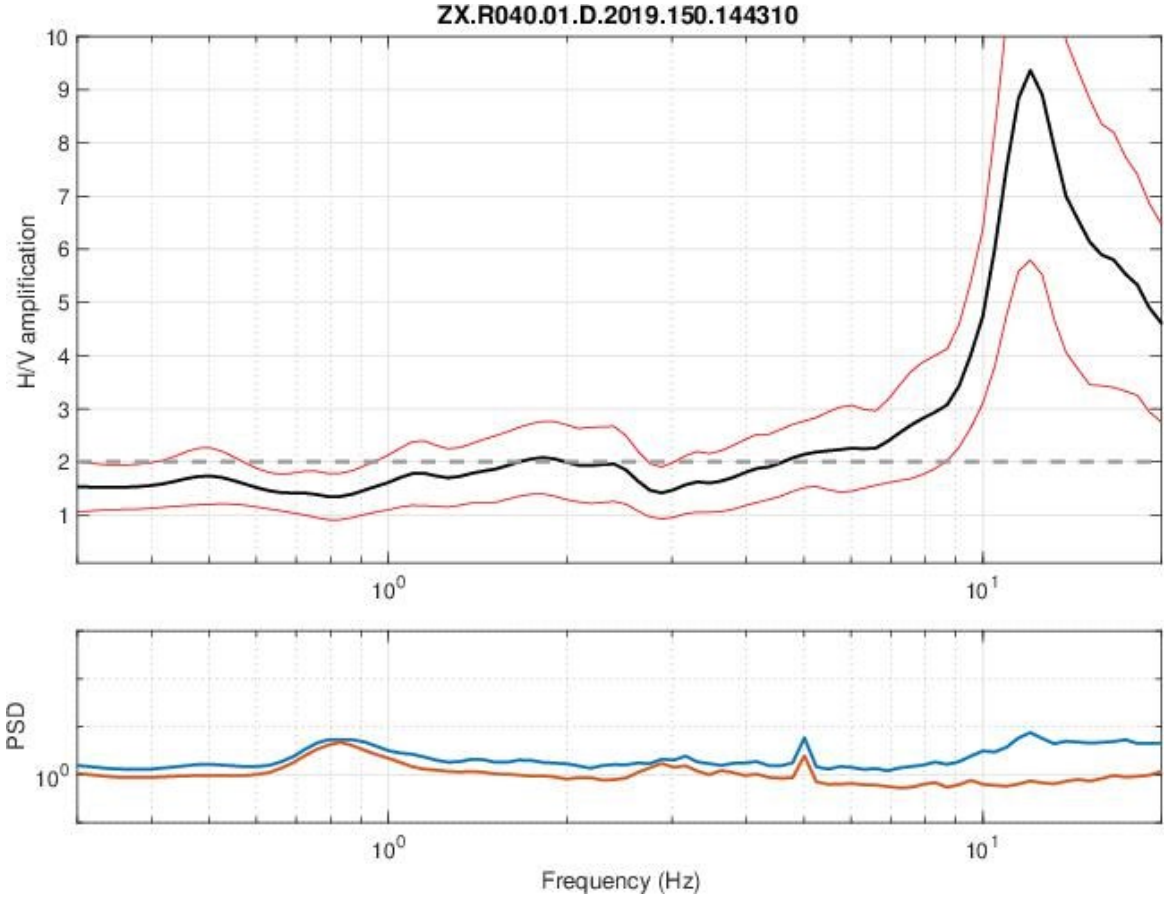

ZX.R035.01.D.2019.150.095606
H/V amplification
PSD
Frequency (Hz)

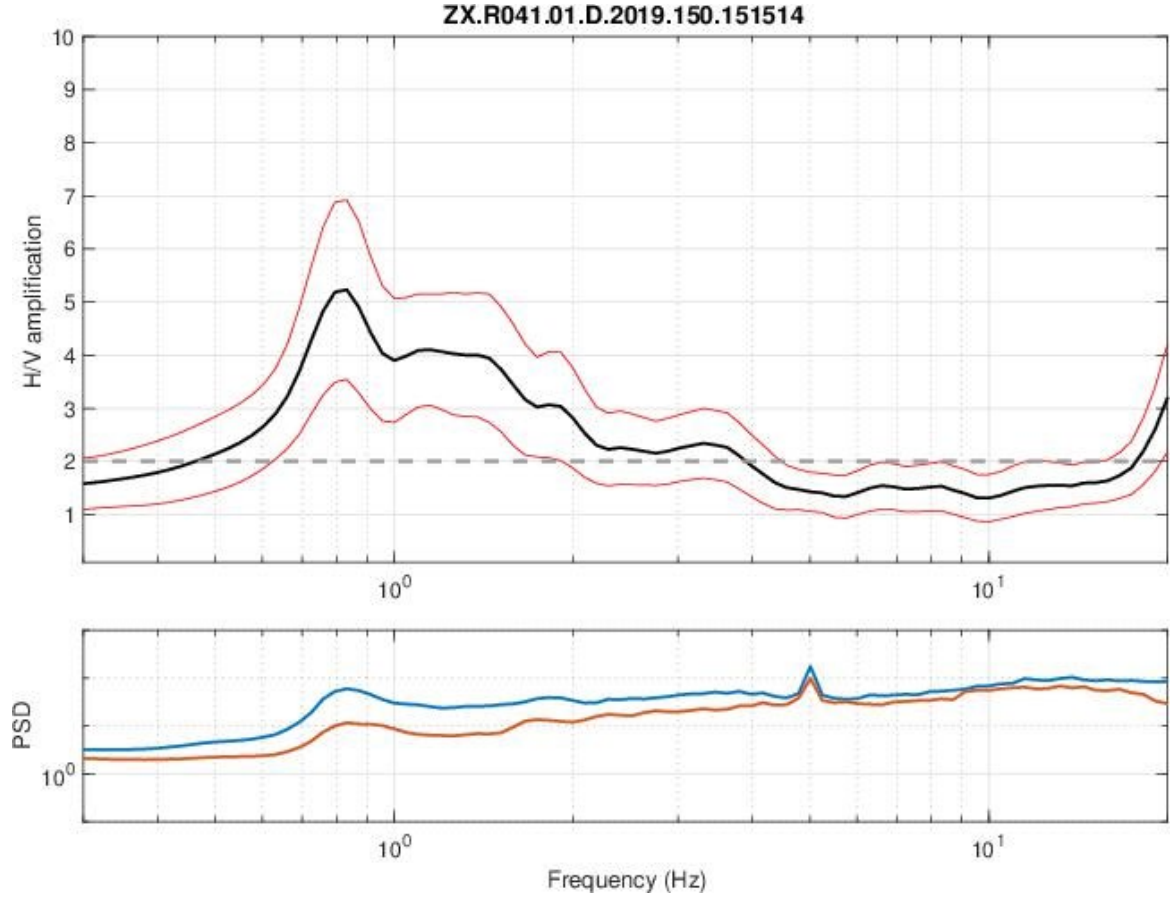

ZX.R036.01.D.2019.150.104731
H/V amplification
PSD
Frequency (Hz)

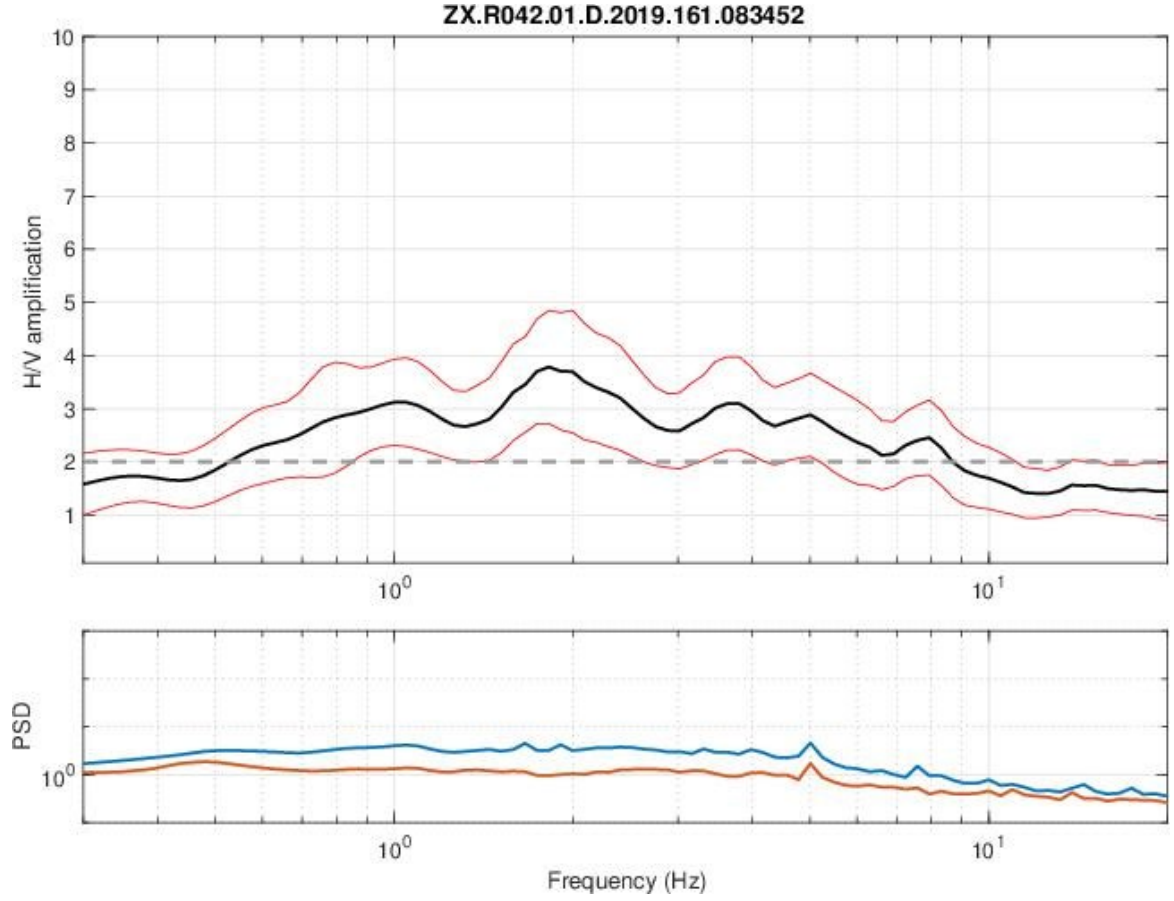

ZX.R037.01.D.2019.150.114000
H/V amplification
PSD
Frequency (Hz)

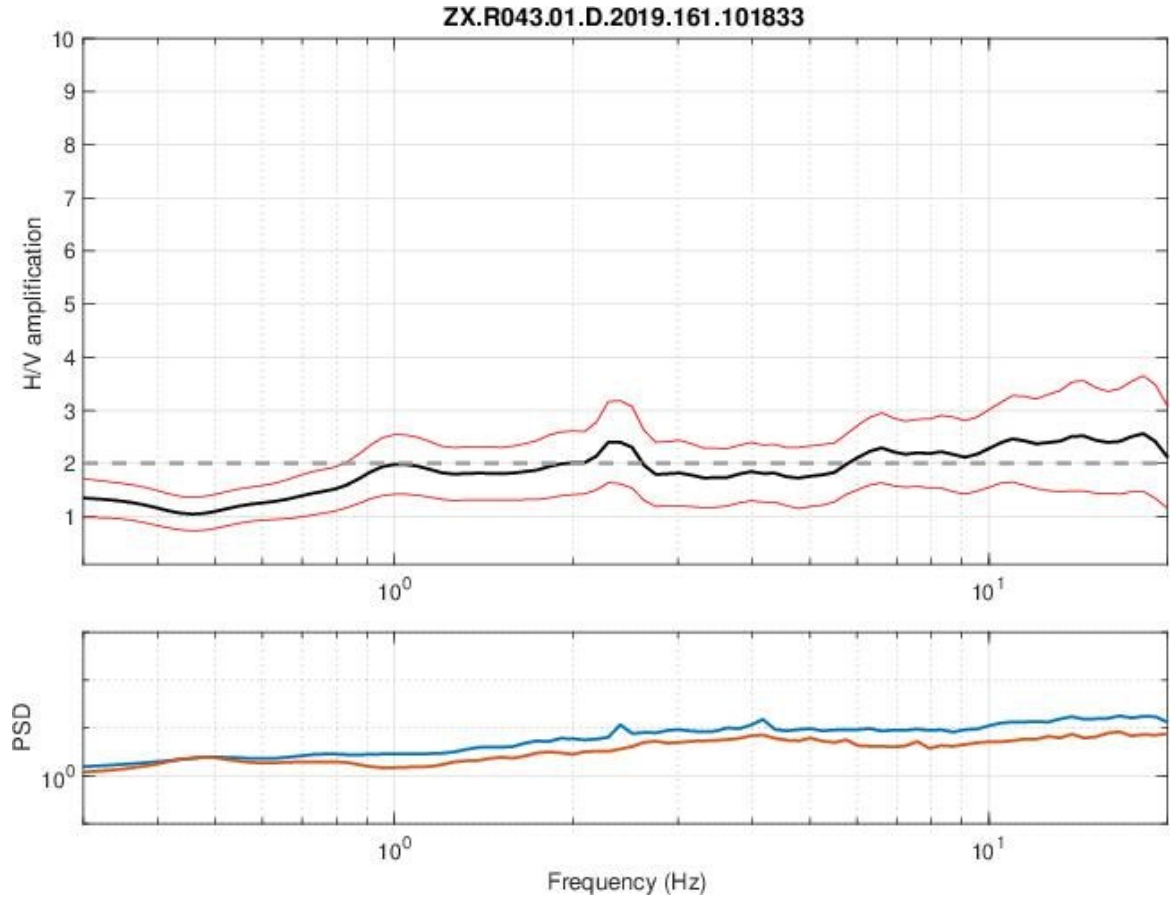

ZX.R038.01.D.2019.150.133609
H/V amplification
PSD
Frequency (Hz)

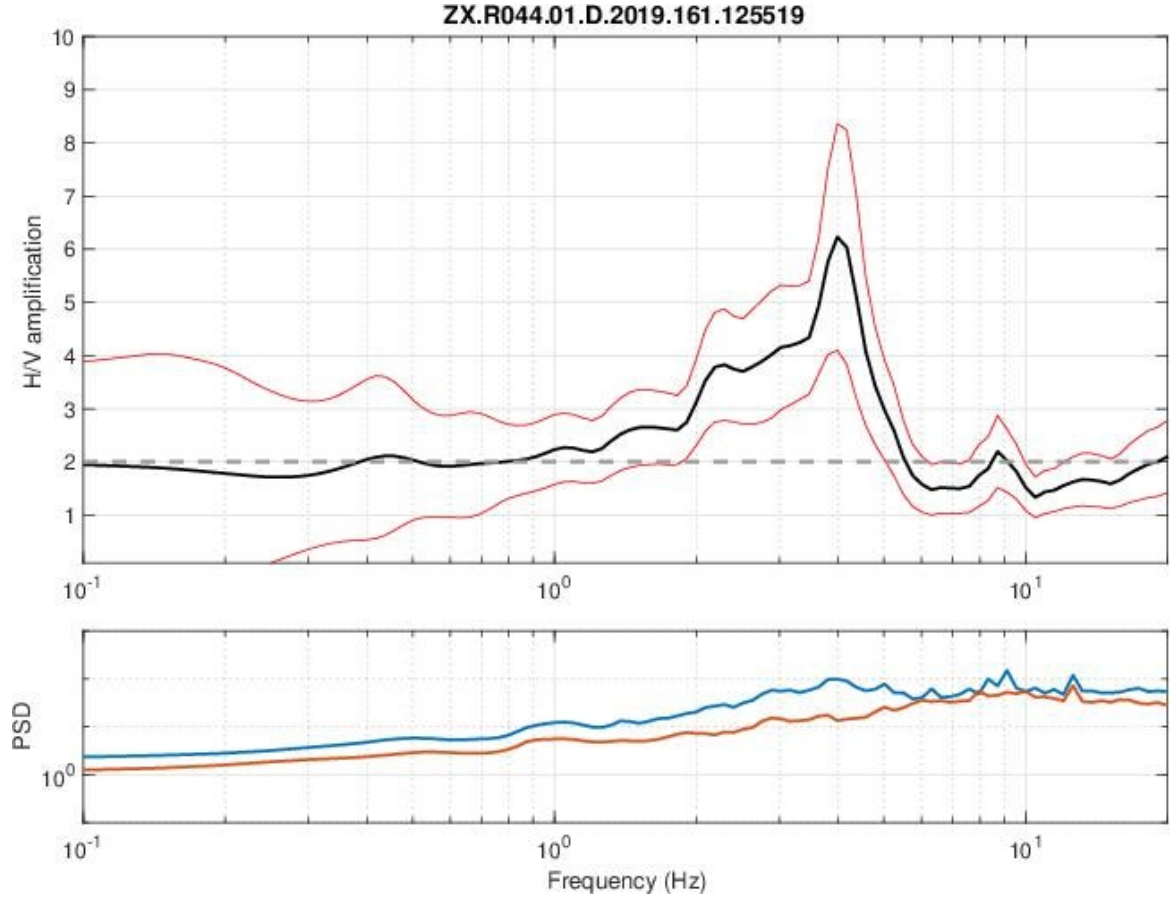

ZX.R039.01.D.2019.150.140748
H/V amplification
PSD
Frequency (Hz)

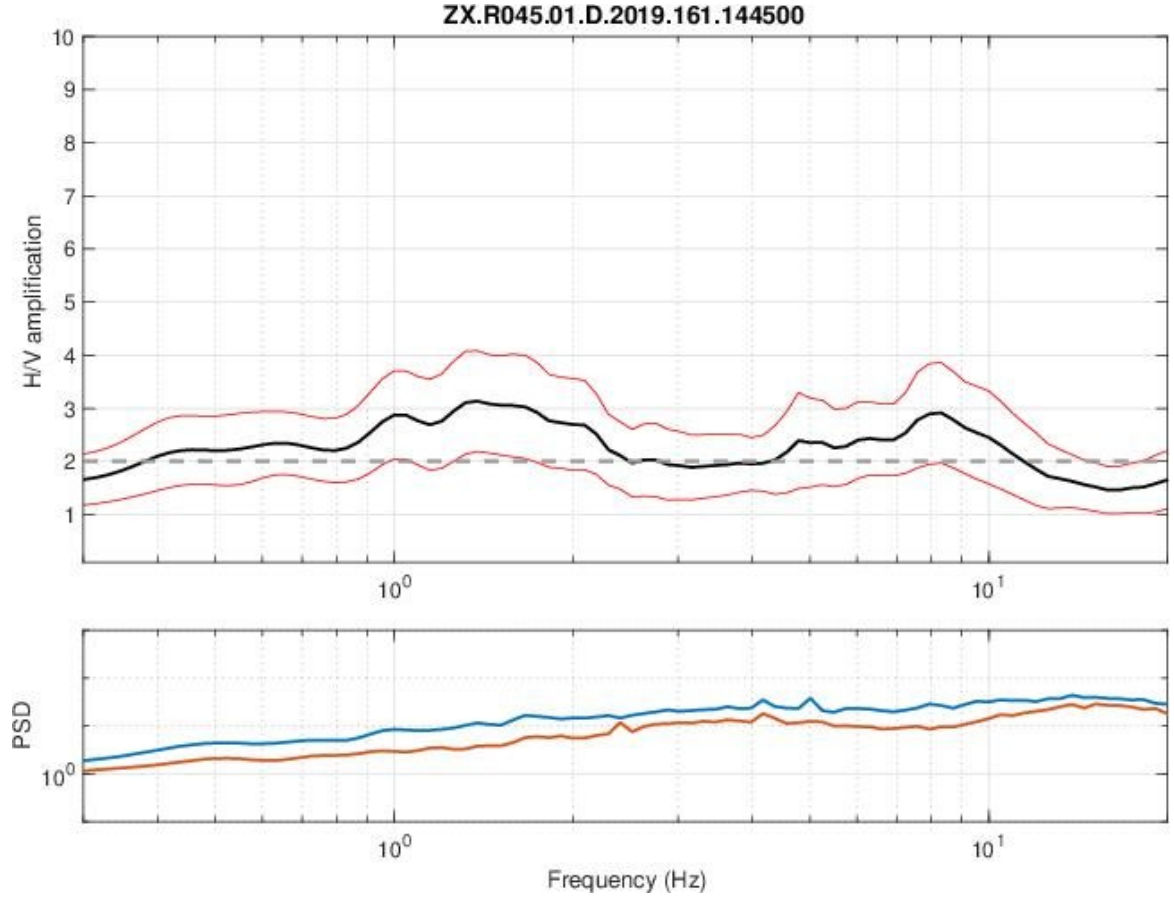

ZX.R040.01.D.2019.150.144310
H/V amplification
PSD
Frequency (Hz)

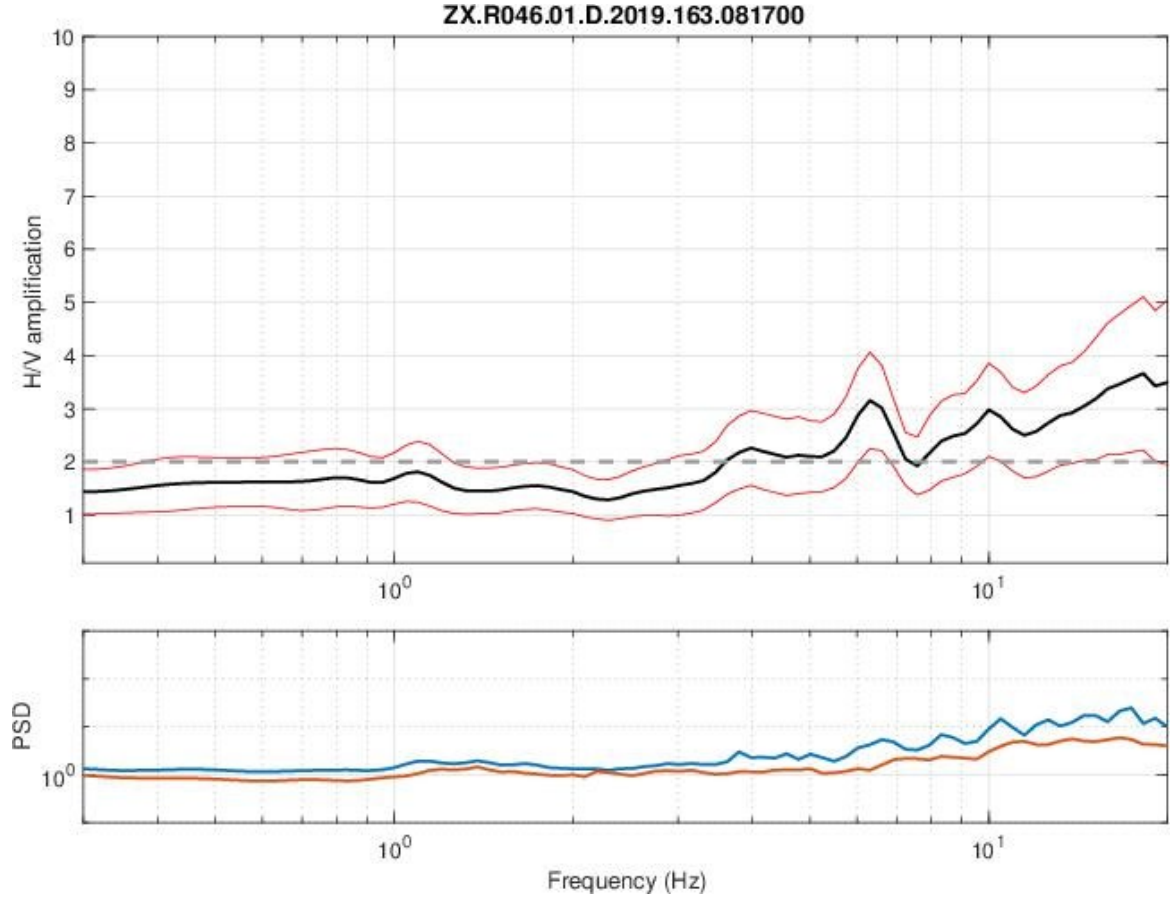

ZX.R041.01.D.2019.150.151514
H/V amplification
PSD
Frequency (Hz)

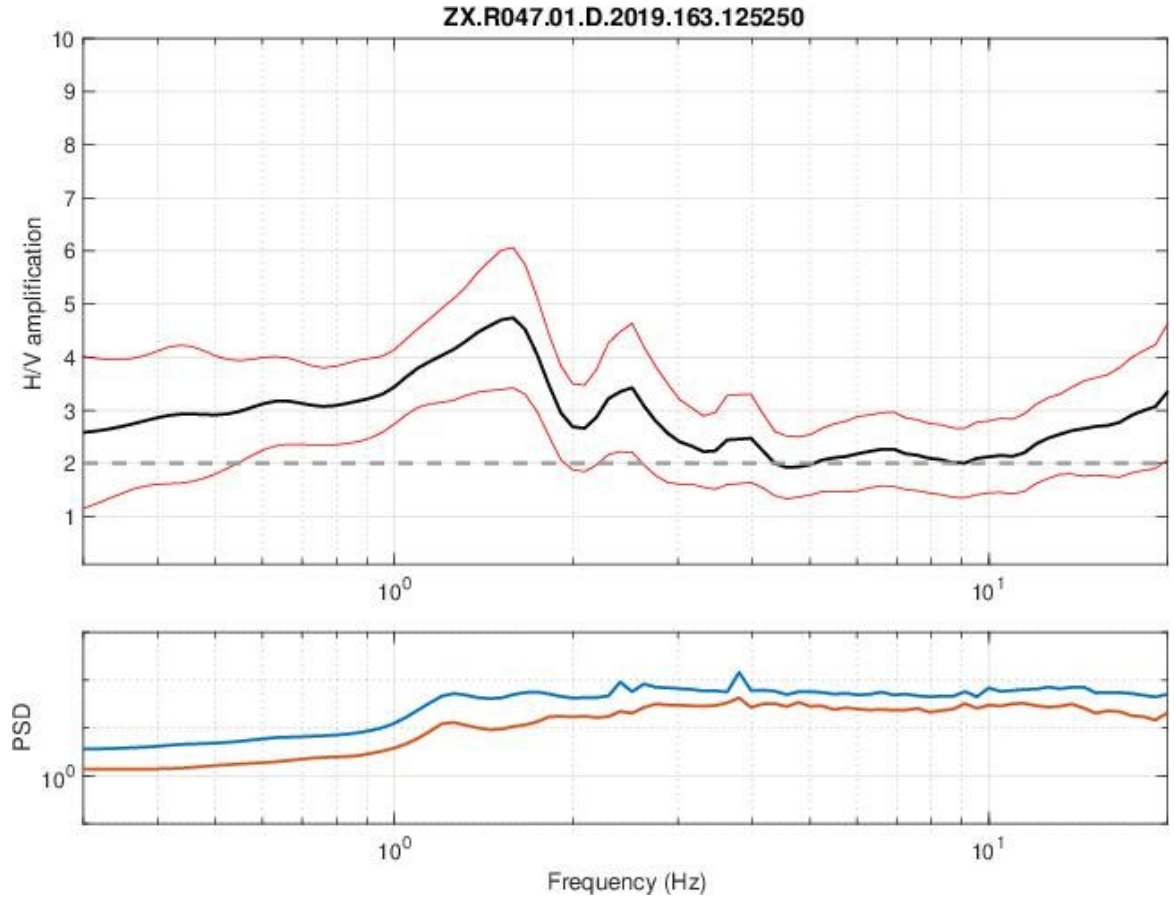

ZX.R042.01.D.2019.161.083452
H/V amplification
PSD
Frequency (Hz)

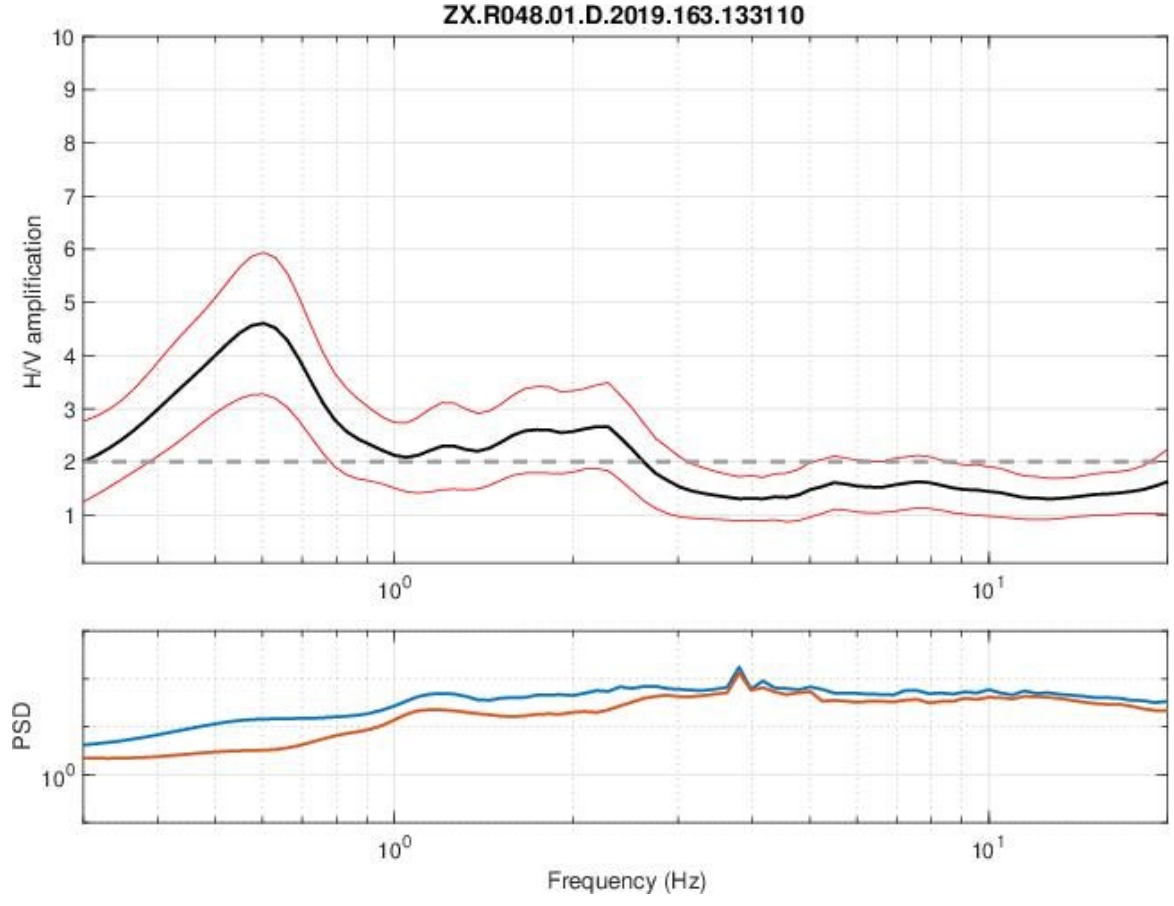

ZX.R043.01.D.2019.161.101833
H/V amplification
PSD
Frequency (Hz)

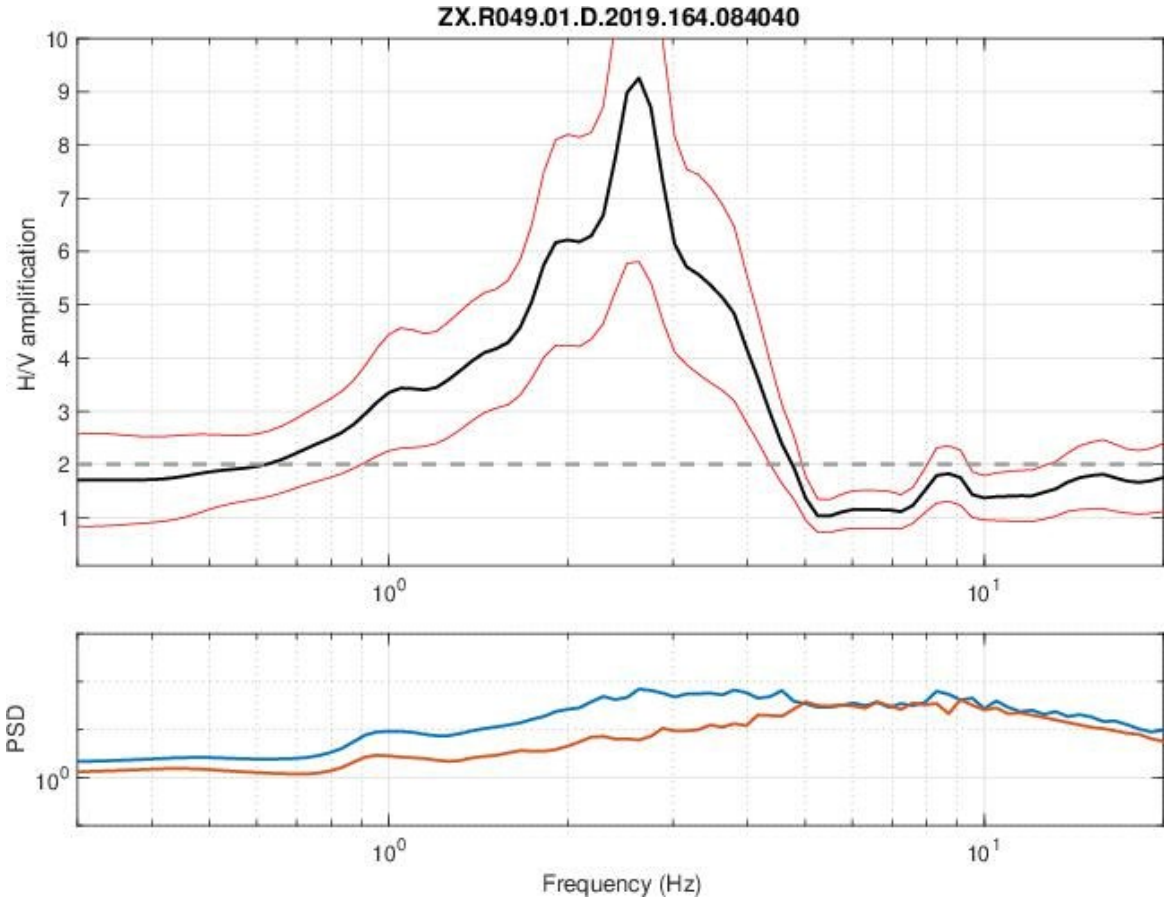

ZX.R044.01.D.2019.161.125519
H/V amplification
PSD
Frequency (Hz)

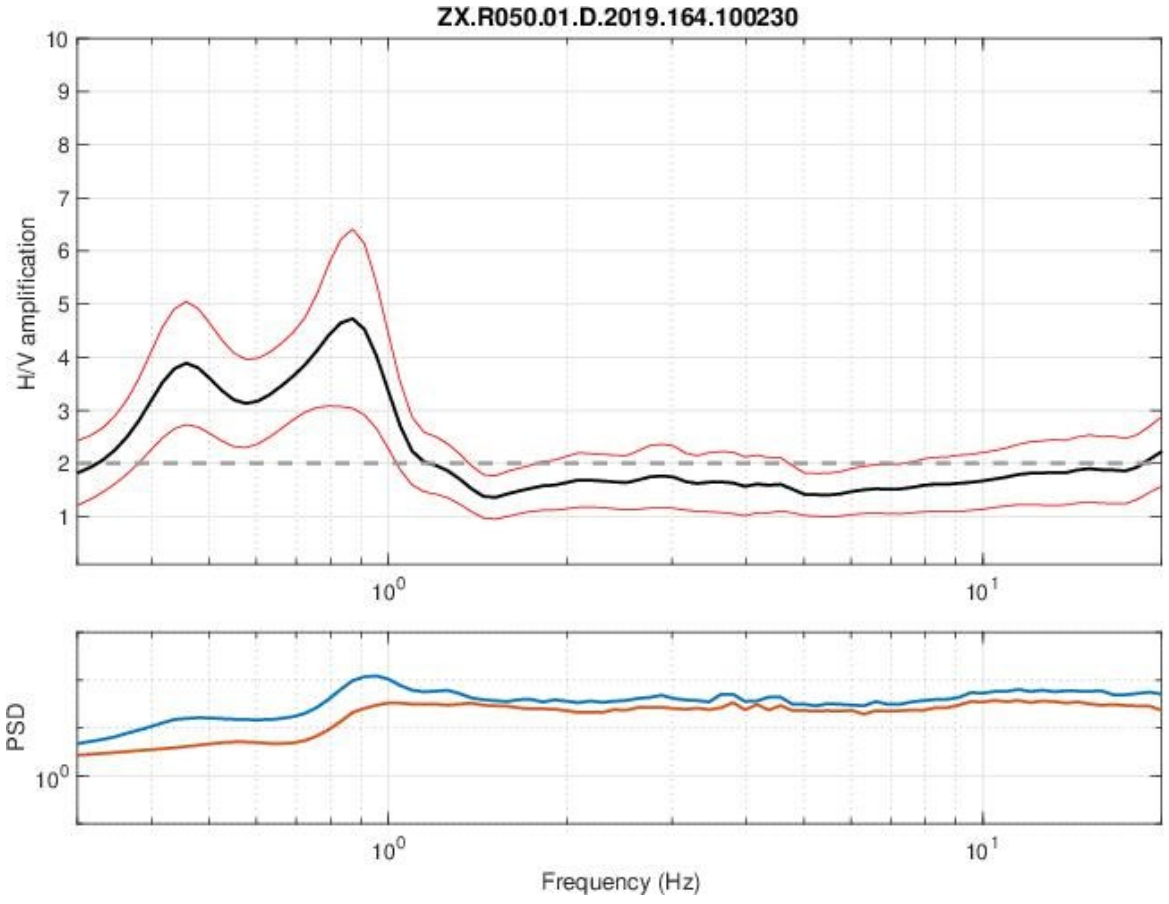

ZX.R045.01.D.2019.161.144500
H/V amplification
PSD
Frequency (Hz)

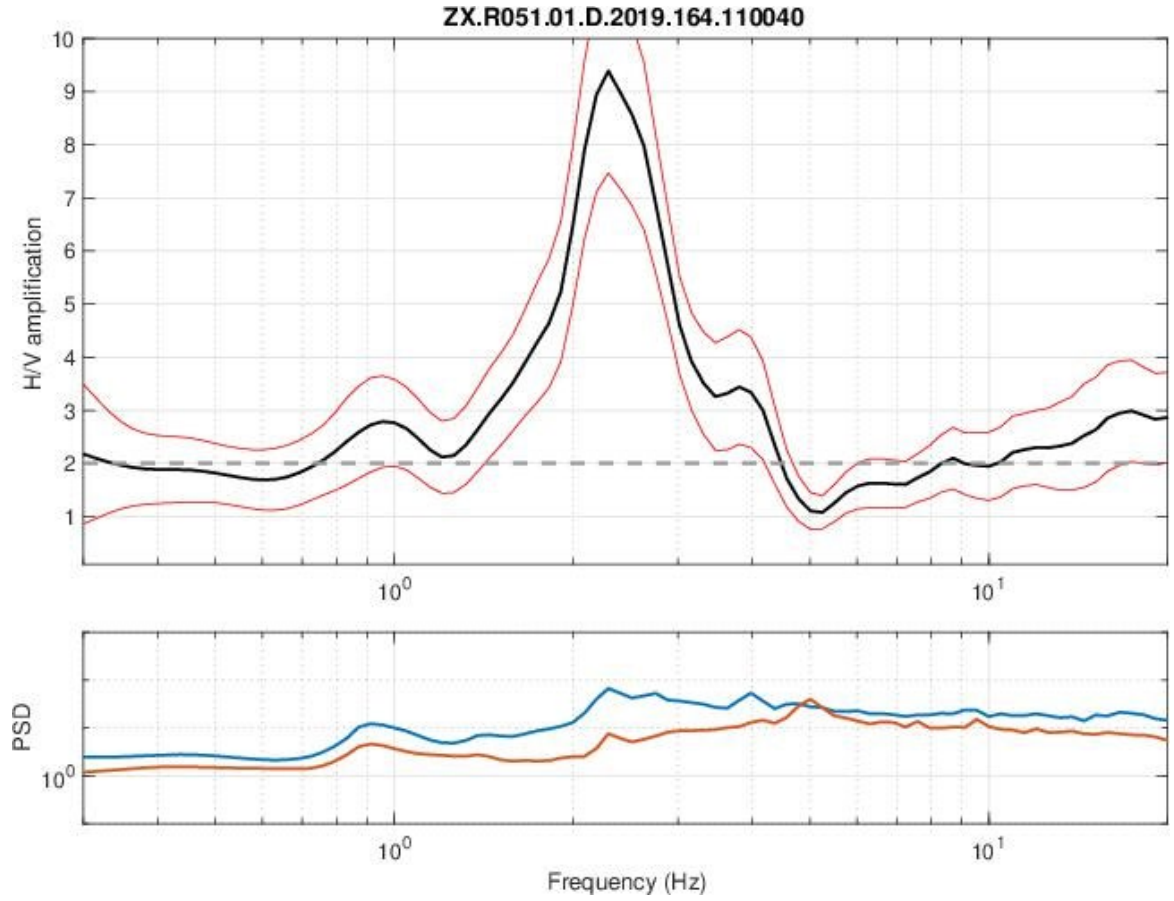

ZX.R046.01.D.2019.163.081700
H/V amplification
PSD
Frequency (Hz)

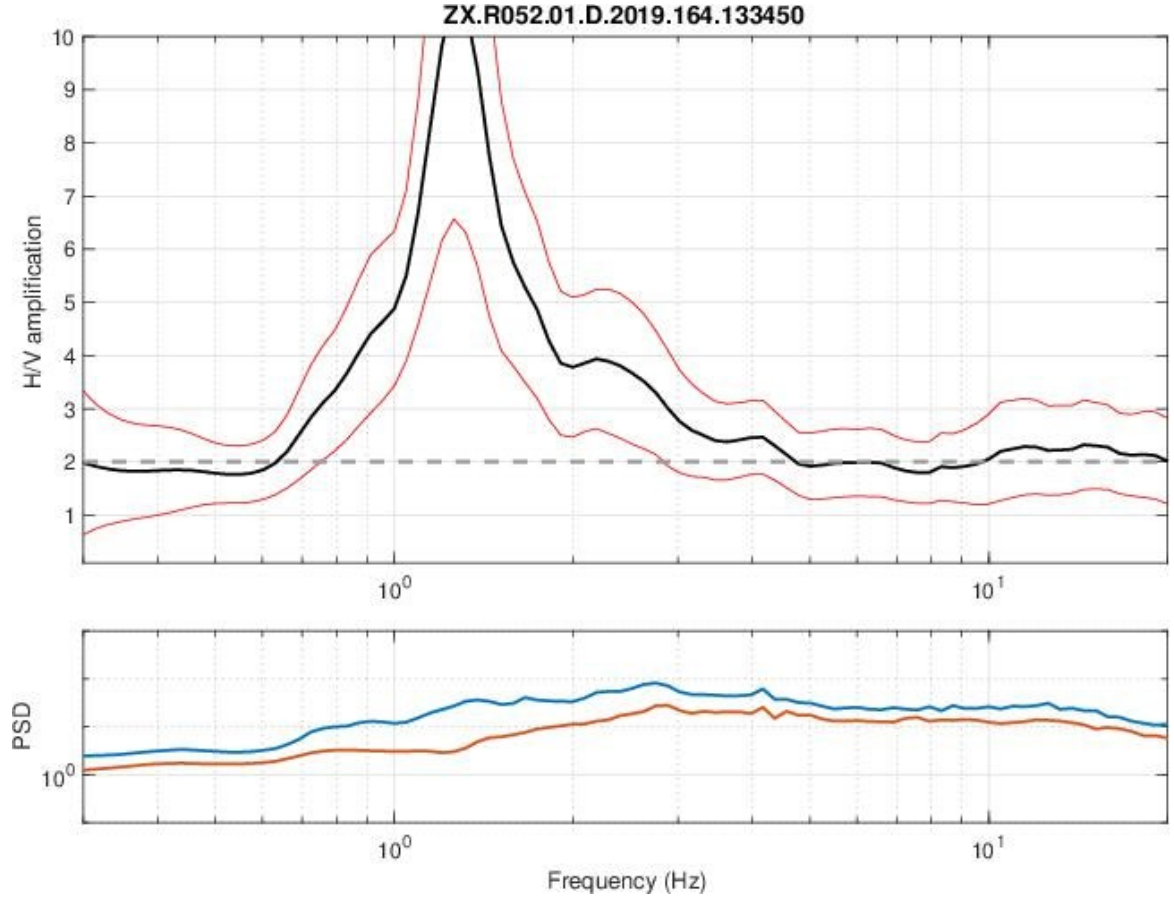

ZX.R047.01.D.2019.163.125250
H/V amplification
PSD
Frequency (Hz)

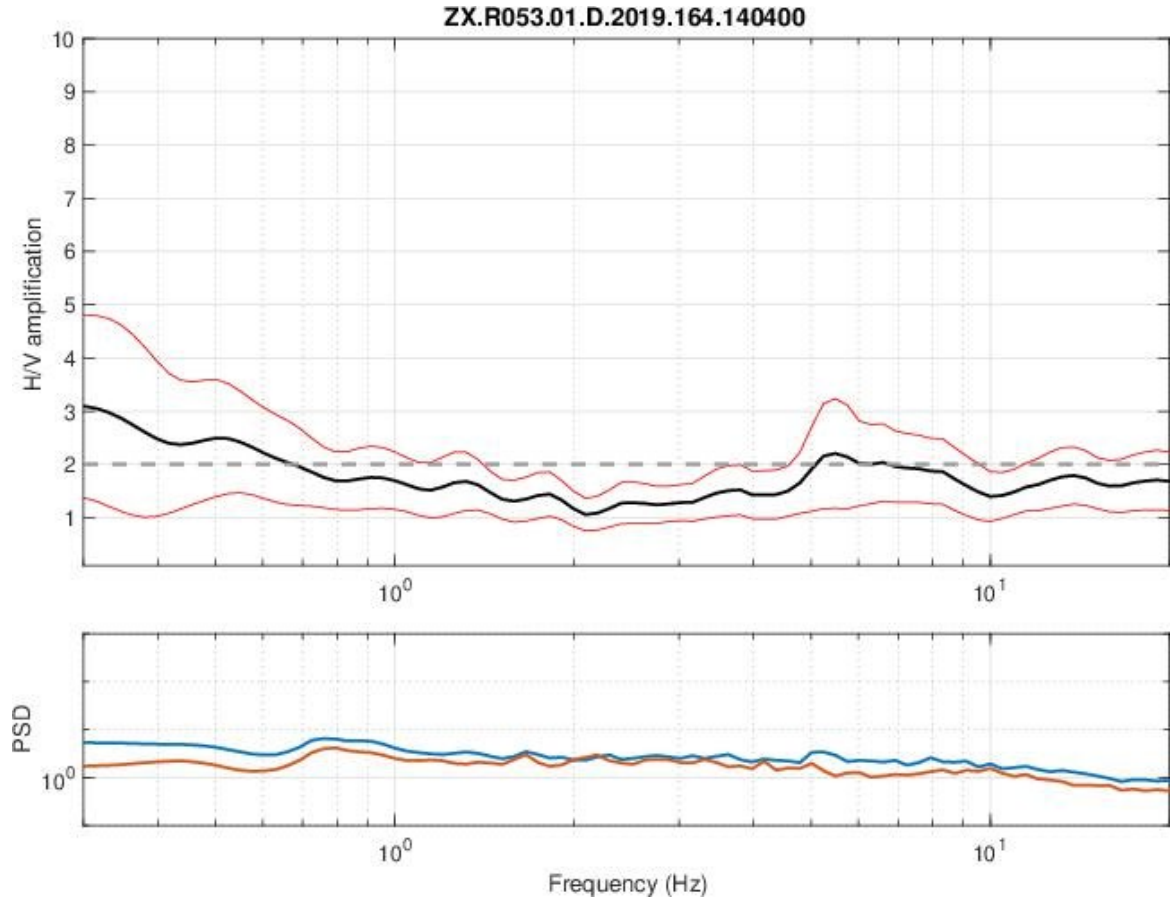

ZX.R048.01.D.2019.163.133110
H/V amplification
PSD
Frequency (Hz)

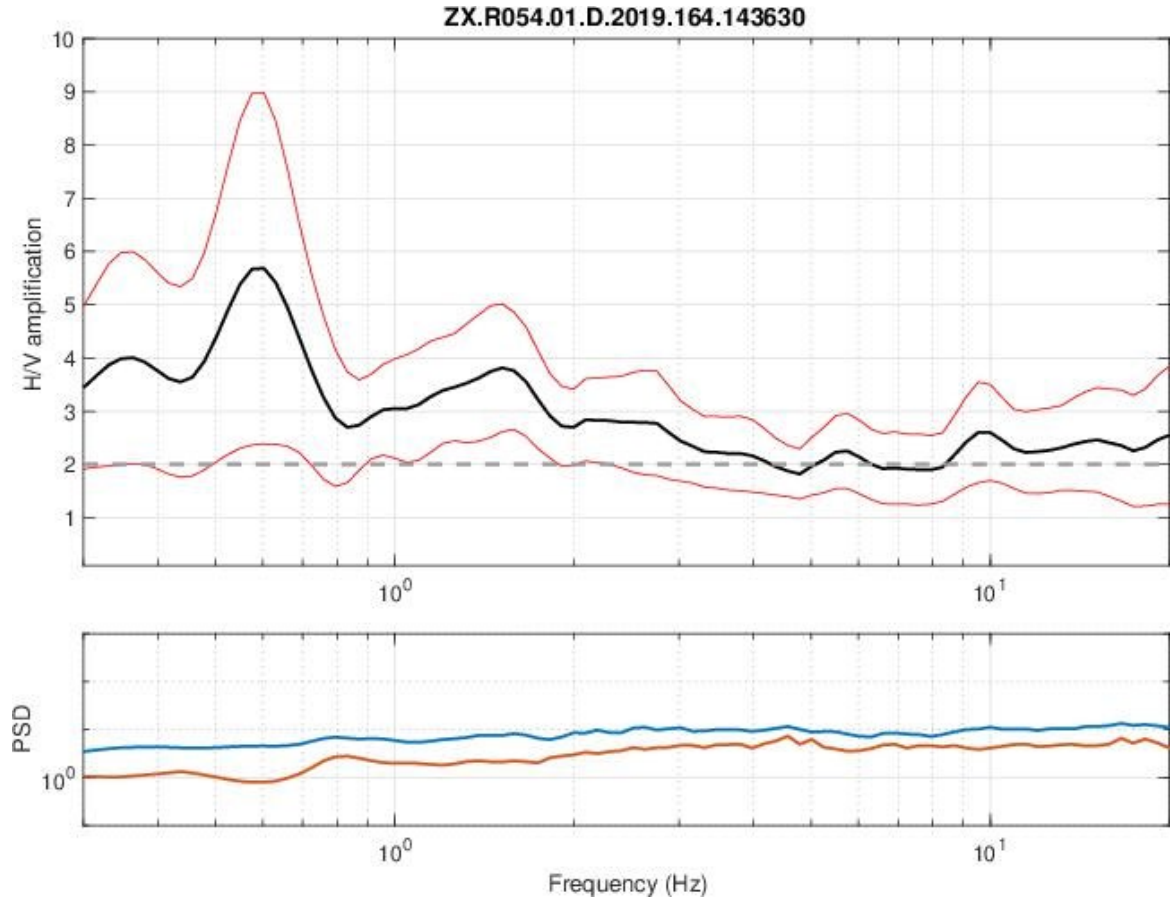

ZX.R049.01.D.2019.164.084040
H/V amplification
PSD
Frequency (Hz)

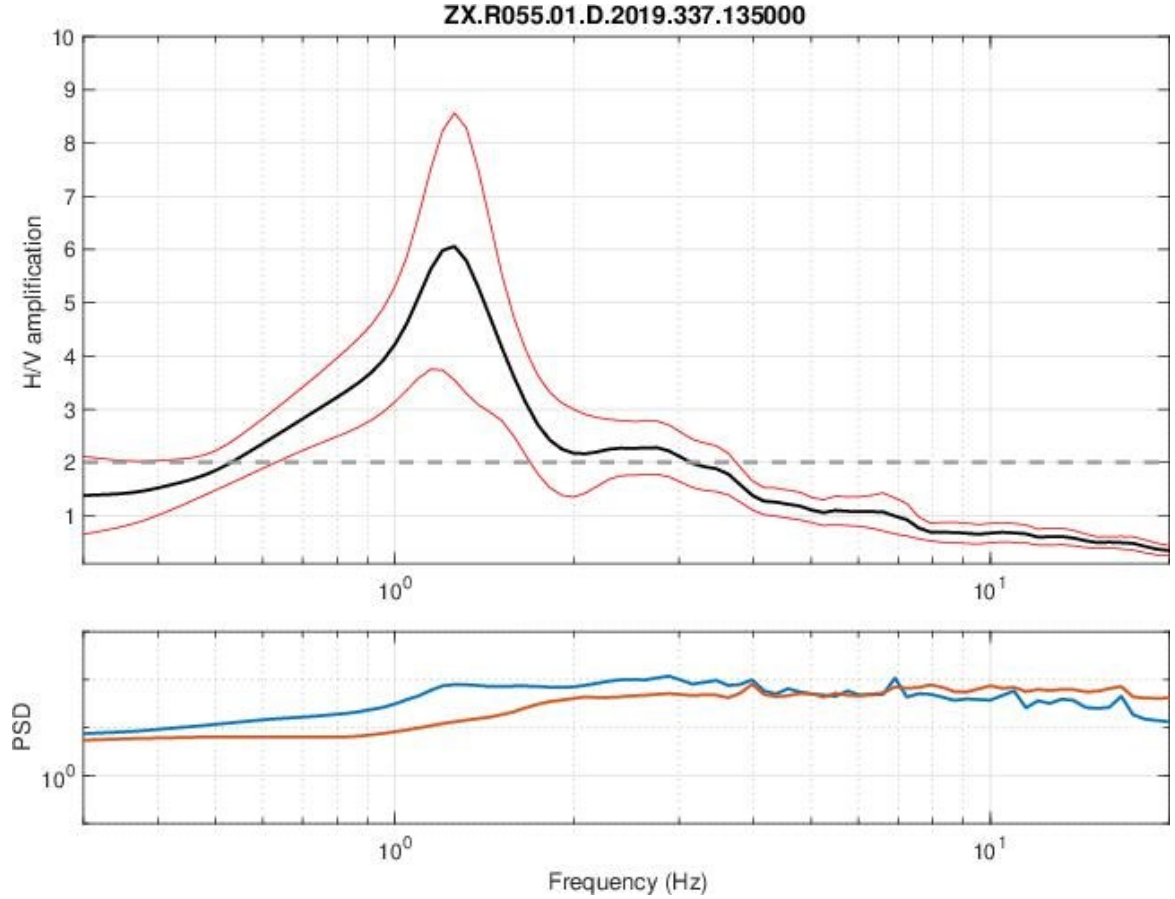

ZX.R050.01.D.2019.164.100230
H/V amplification
PSD
Frequency (Hz)

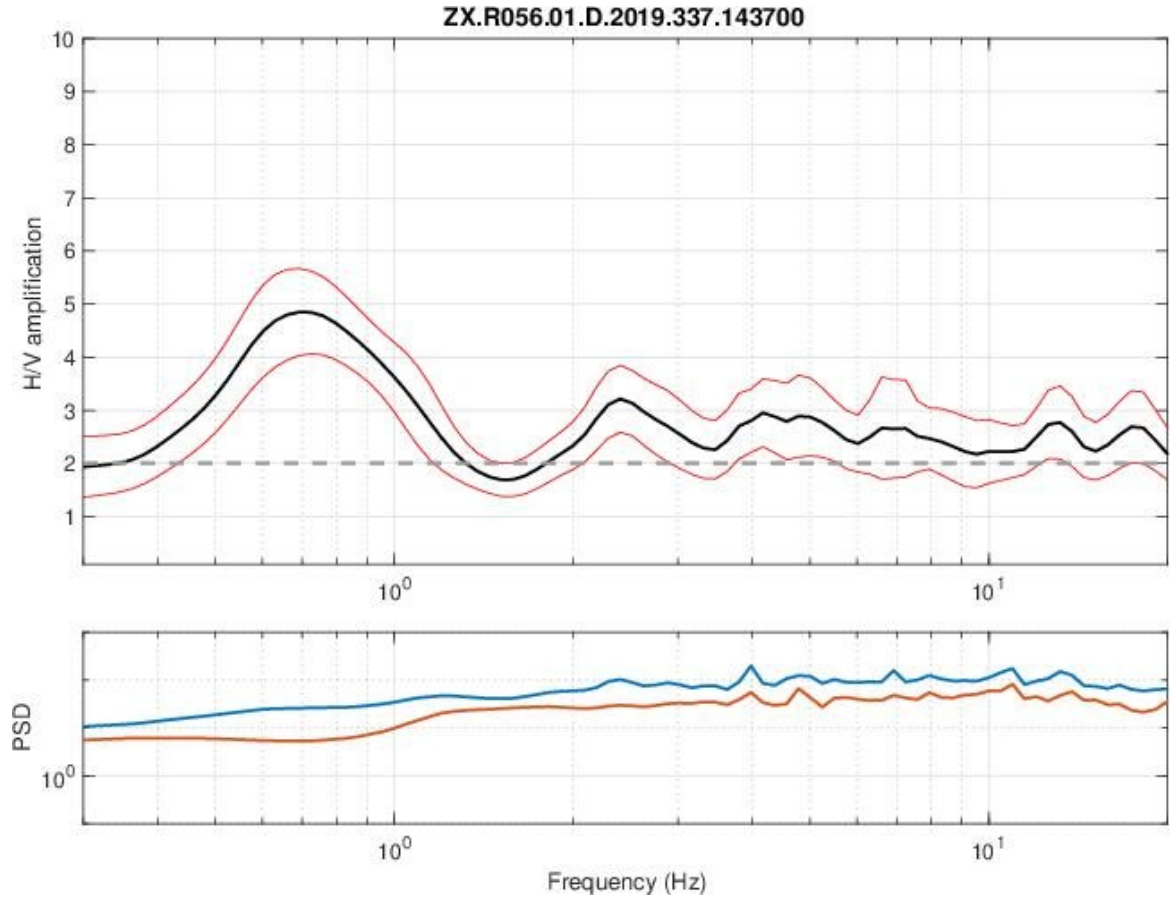

ZX.R051.01.D.2019.164.110040
H/V amplification
PSD
Frequency (Hz)

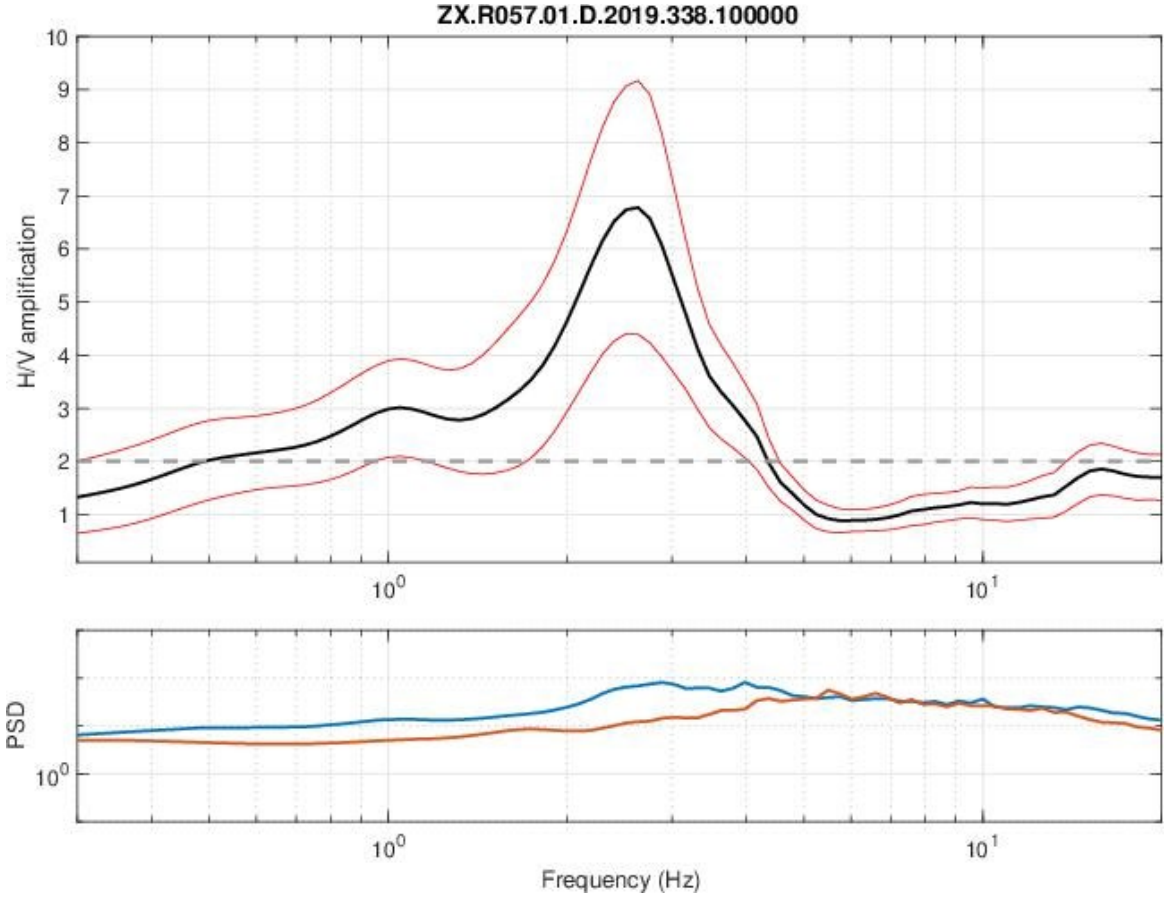

ZX.R052.01.D.2019.164.133450
H/V amplification
PSD
Frequency (Hz)

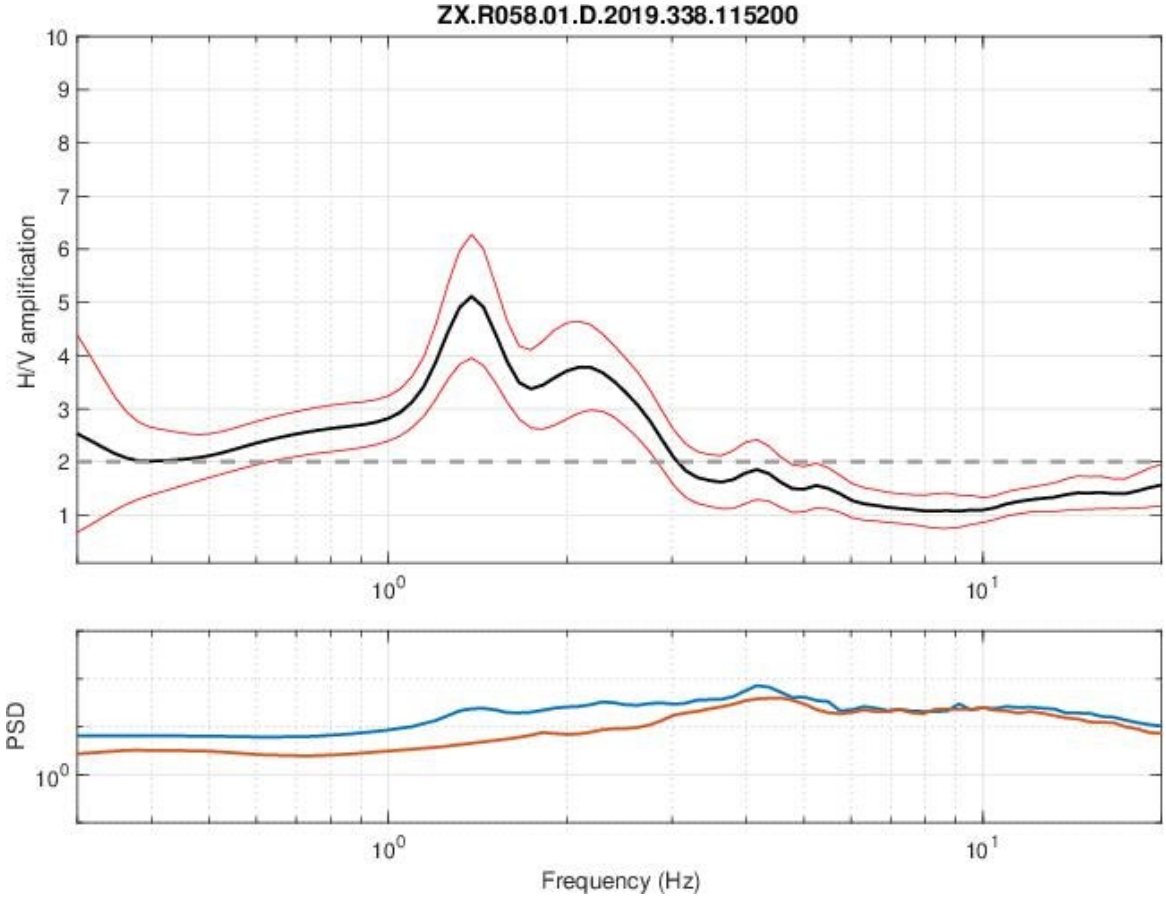

ZX.R053.01.D.2019.164.140400
H/V amplification
PSD
Frequency (Hz)

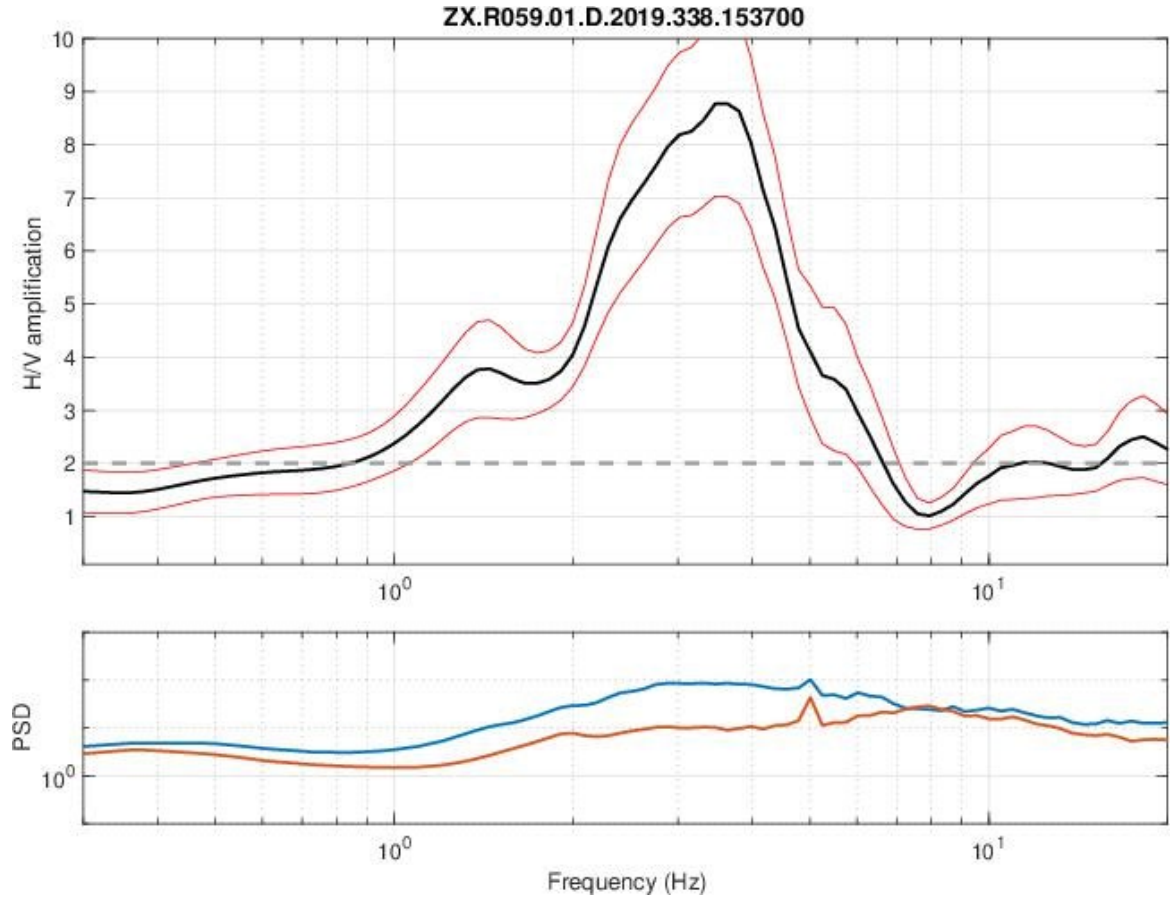

ZX.R054.01.D.2019.164.143630
H/V amplification
PSD
Frequency (Hz)

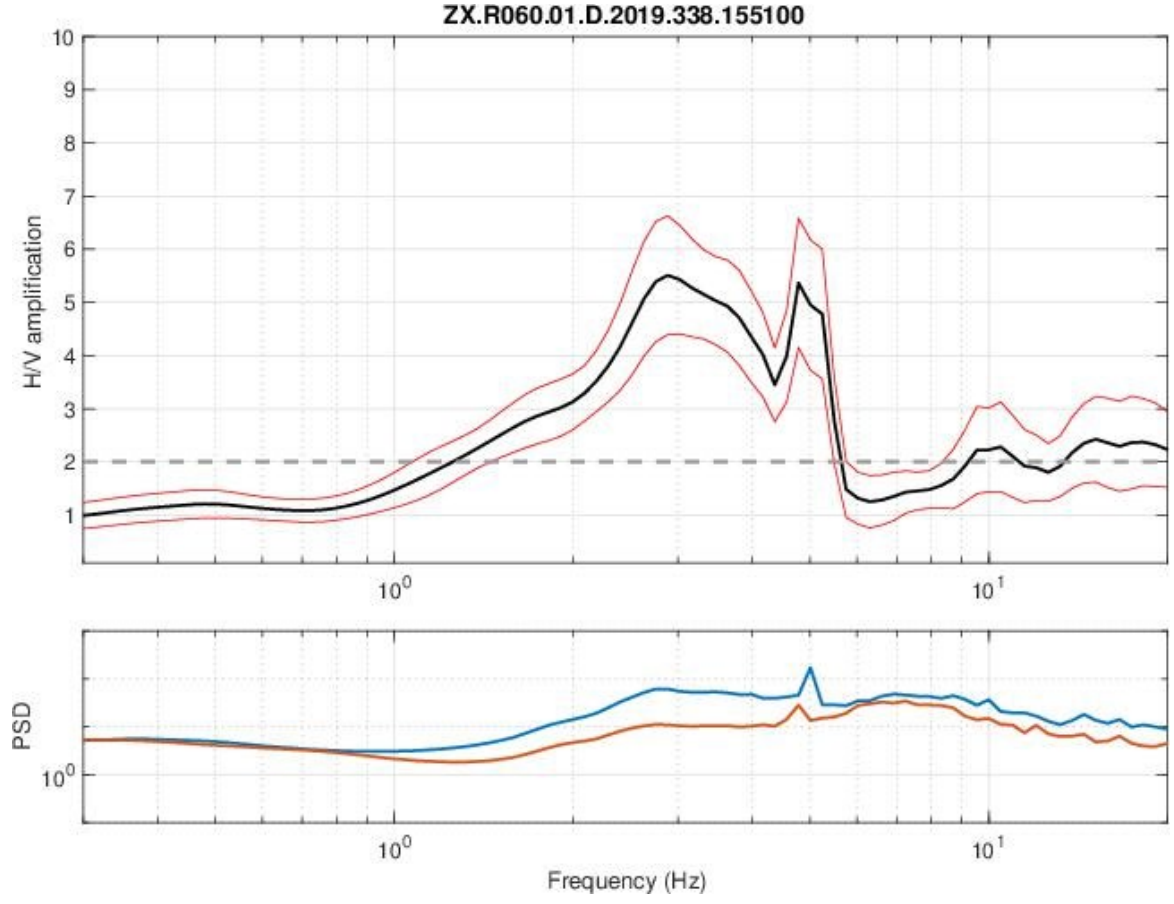

ZX.R055.01.D.2019.337.135000
H/V amplification
PSD
Frequency (Hz)

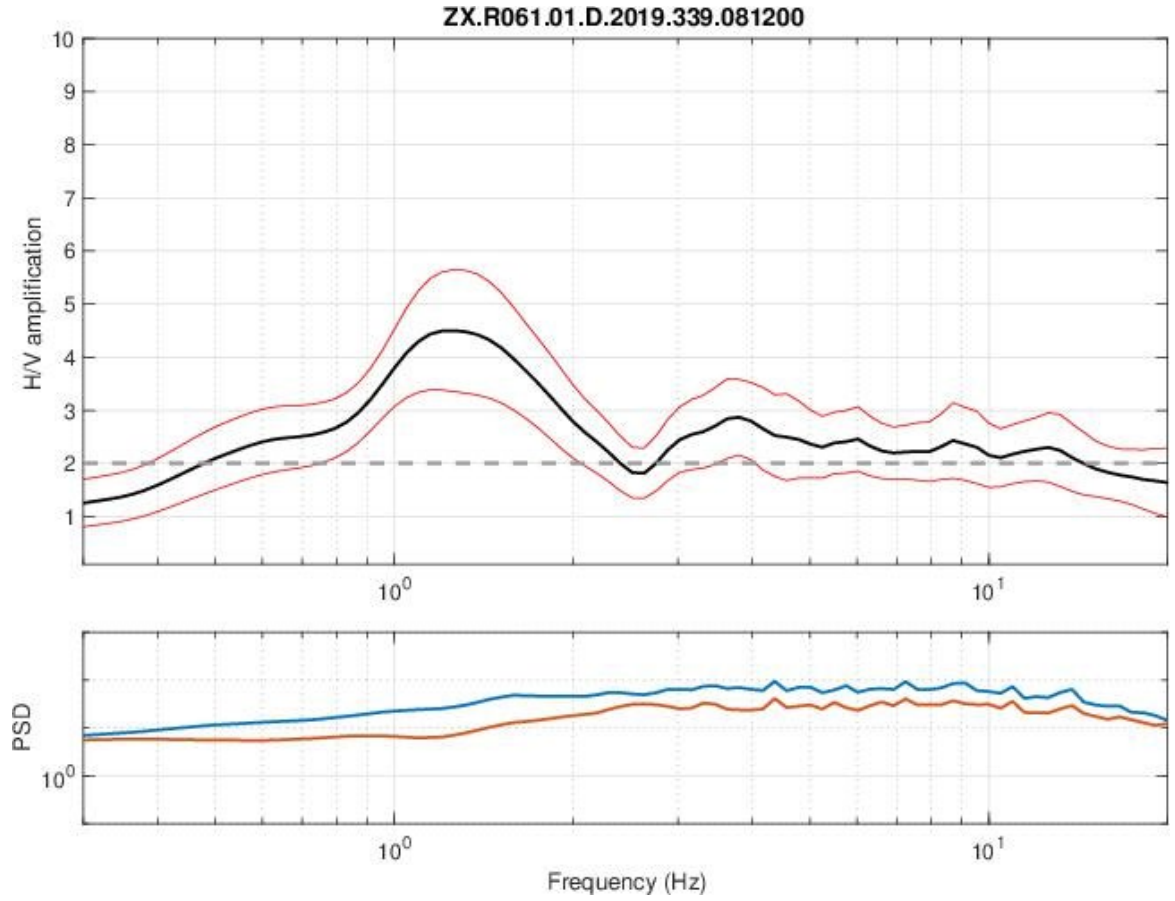

ZX.R056.01.D.2019.337.143700
H/V amplification
PSD
Frequency (Hz)

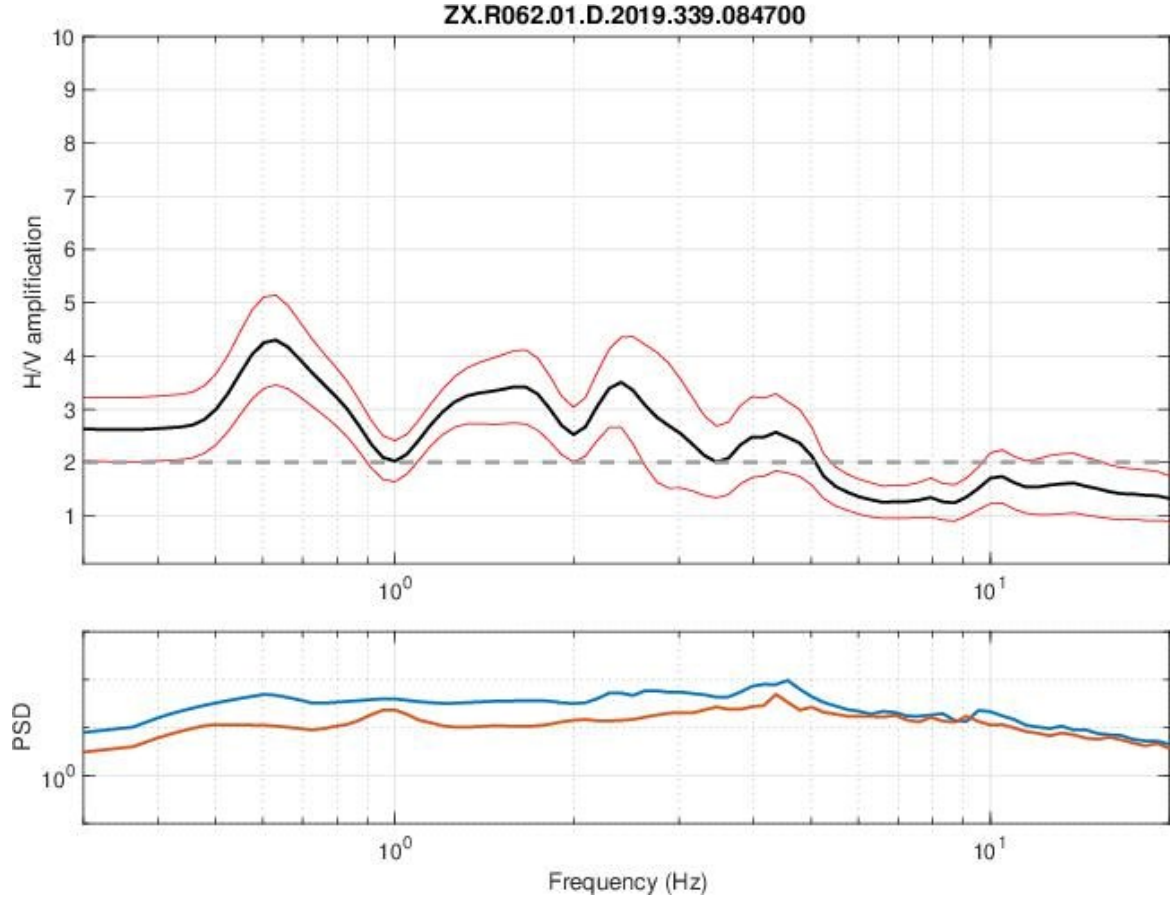

ZX.R057.01.D.2019.338.100000
H/V amplification
PSD
Frequency (Hz)

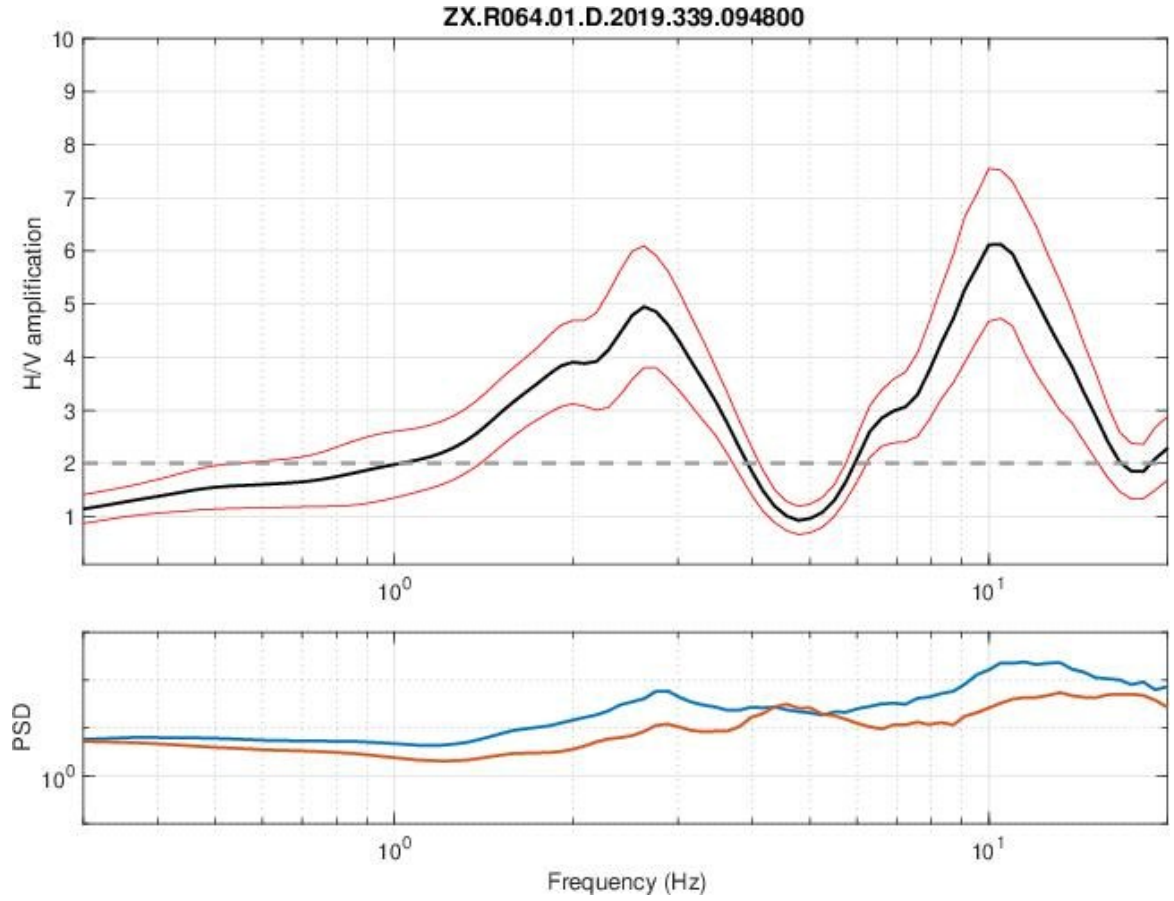

ZX.R058.01.D.2019.338.115200
H/V amplification
PSD
Frequency (Hz)

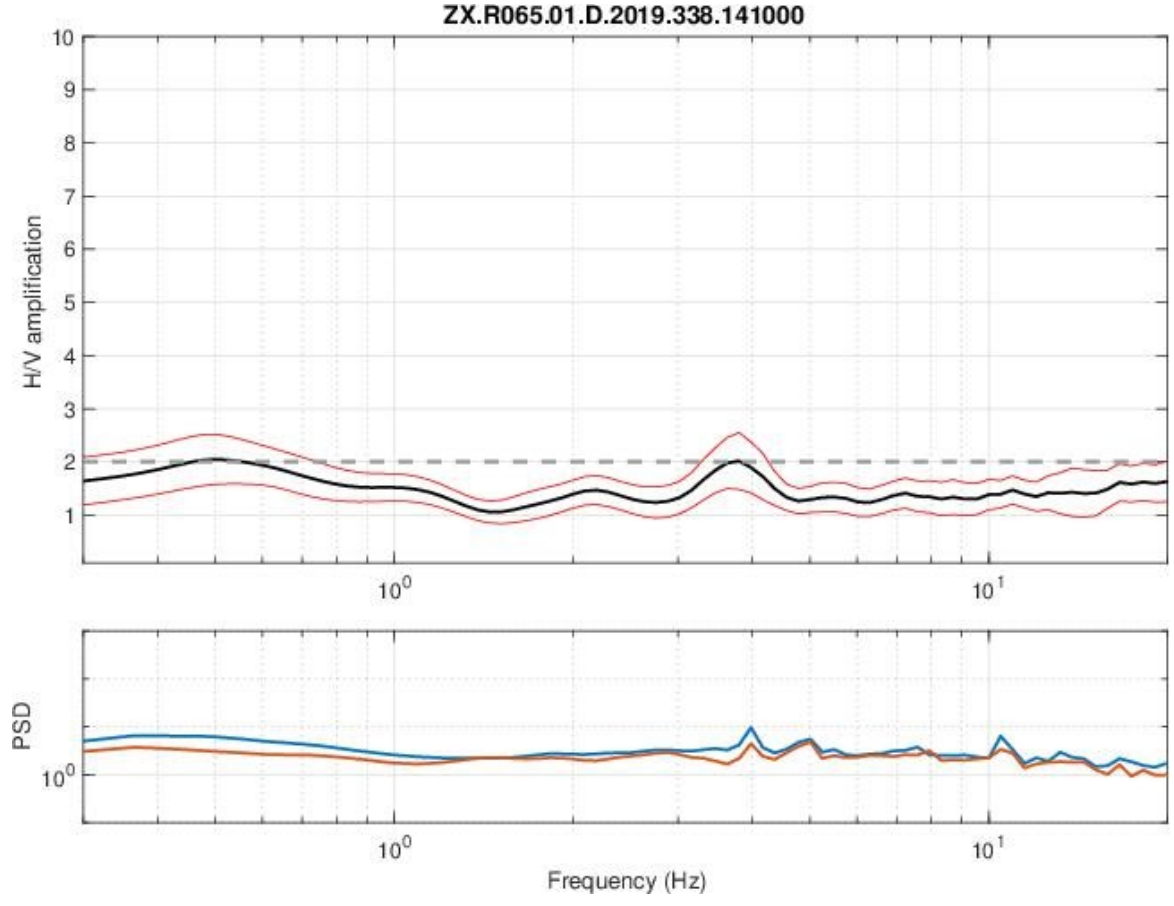

ZX.R059.01.D.2019.338.153700
H/V amplification
PSD
Frequency (Hz)

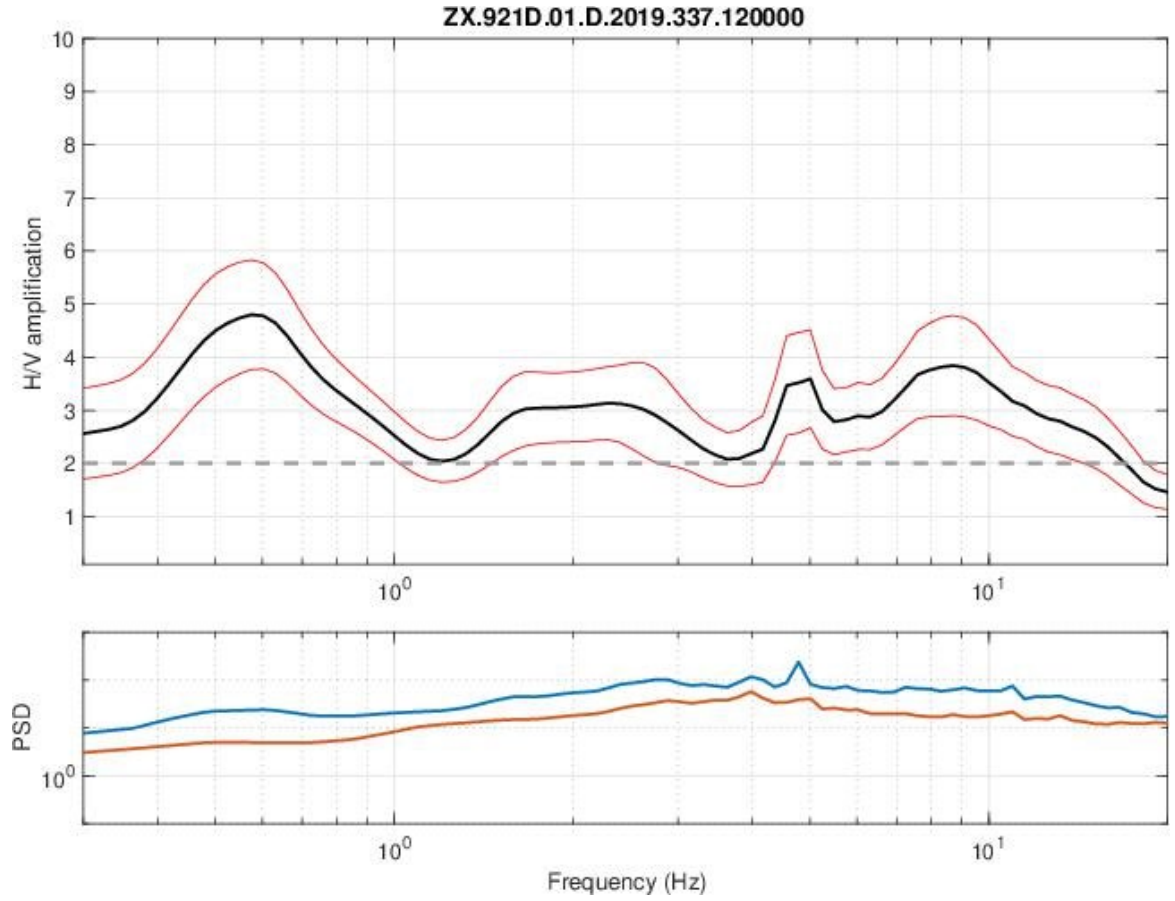

ZX.R060.01.D.2019.338.155100
H/V amplification
PSD
Frequency (Hz)

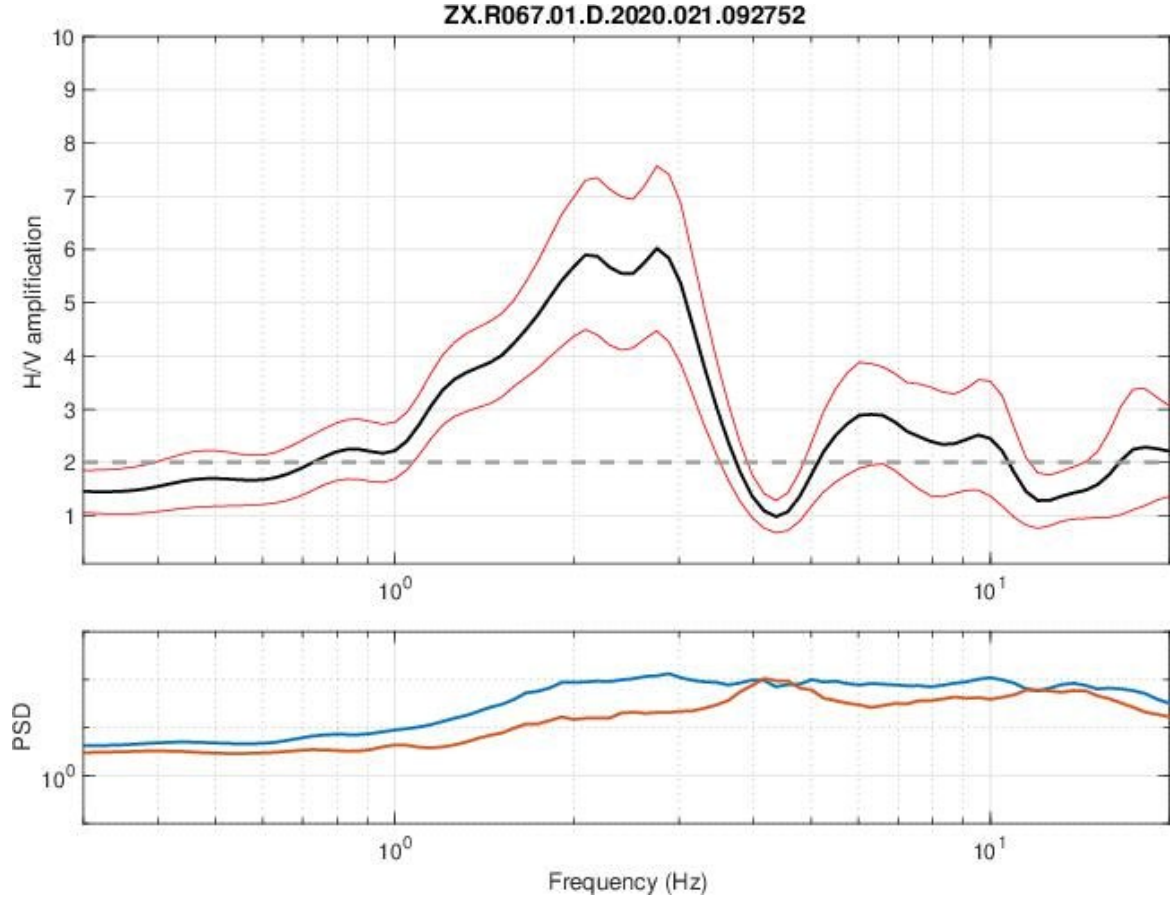

ZX.R061.01.D.2019.339.081200
H/V amplification
PSD
Frequency (Hz)

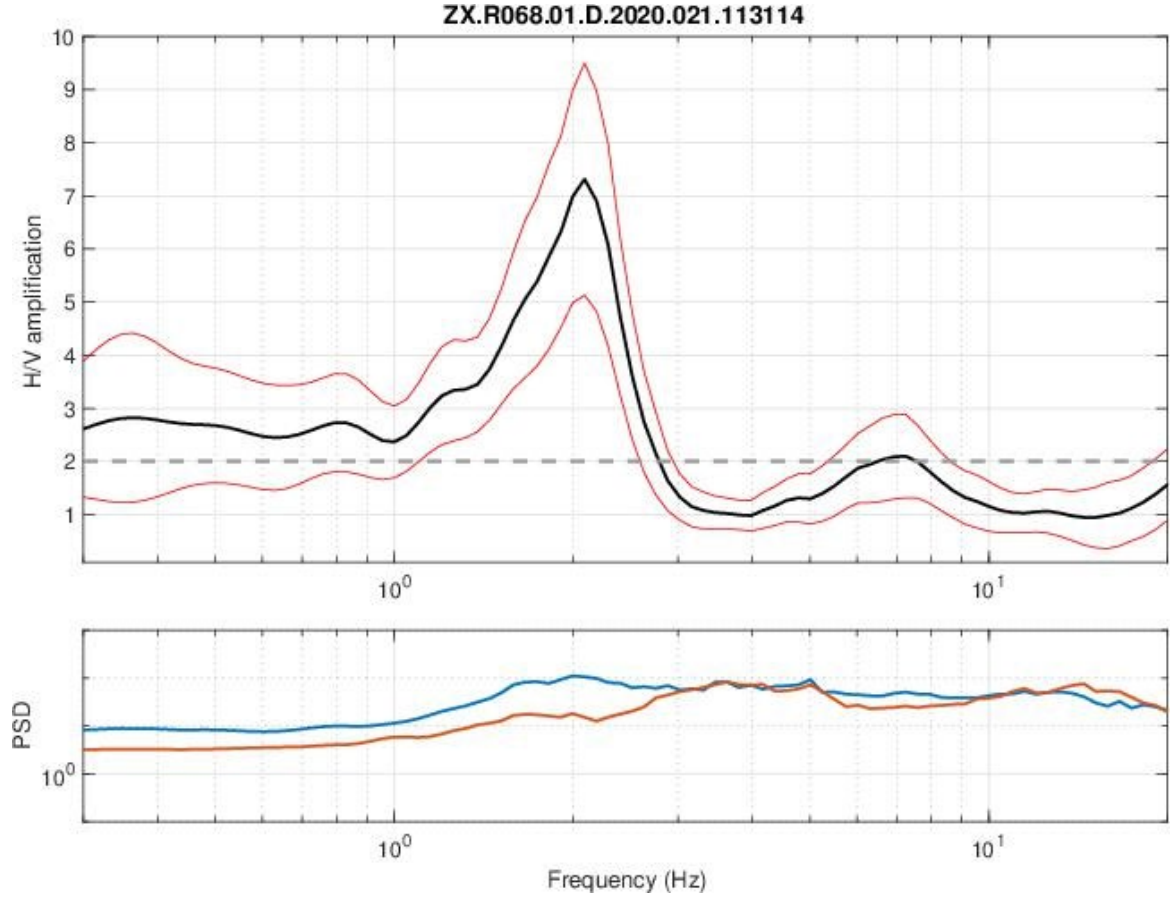

ZX.R062.01.D.2019.339.084700
H/V amplification
PSD
Frequency (Hz)

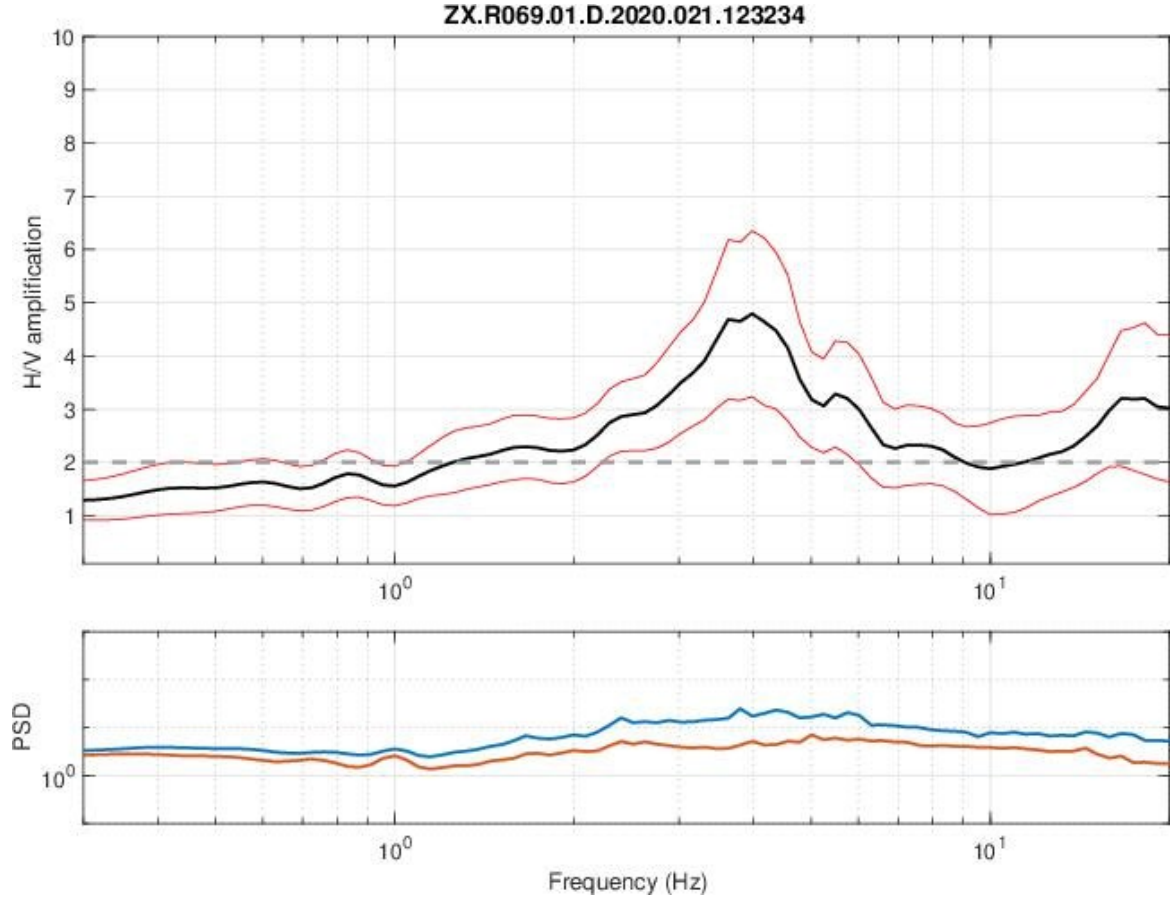

ZX.R064.01.D.2019.339.094800
H/V amplification
PSD
Frequency (Hz)

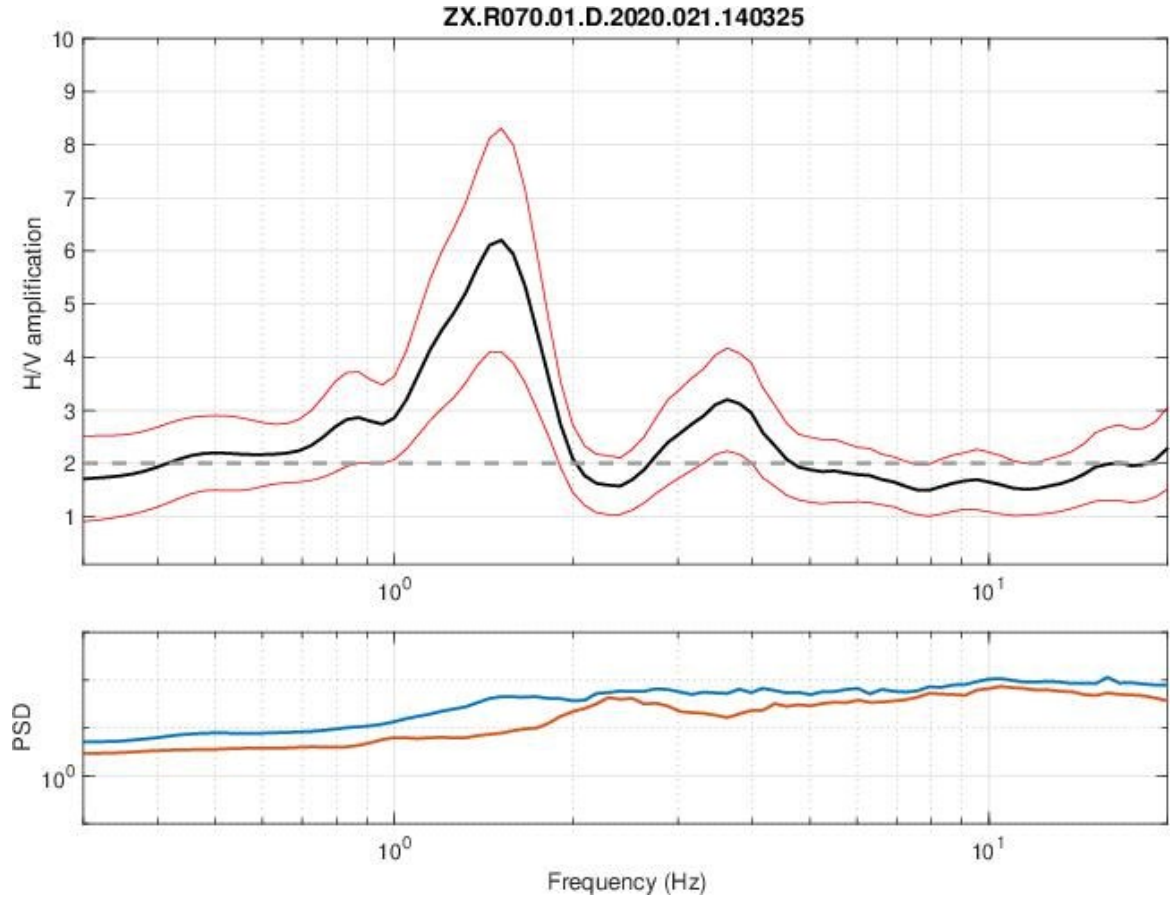

ZX.R065.01.D.2019.338.141000
H/V amplification
PSD
Frequency (Hz)

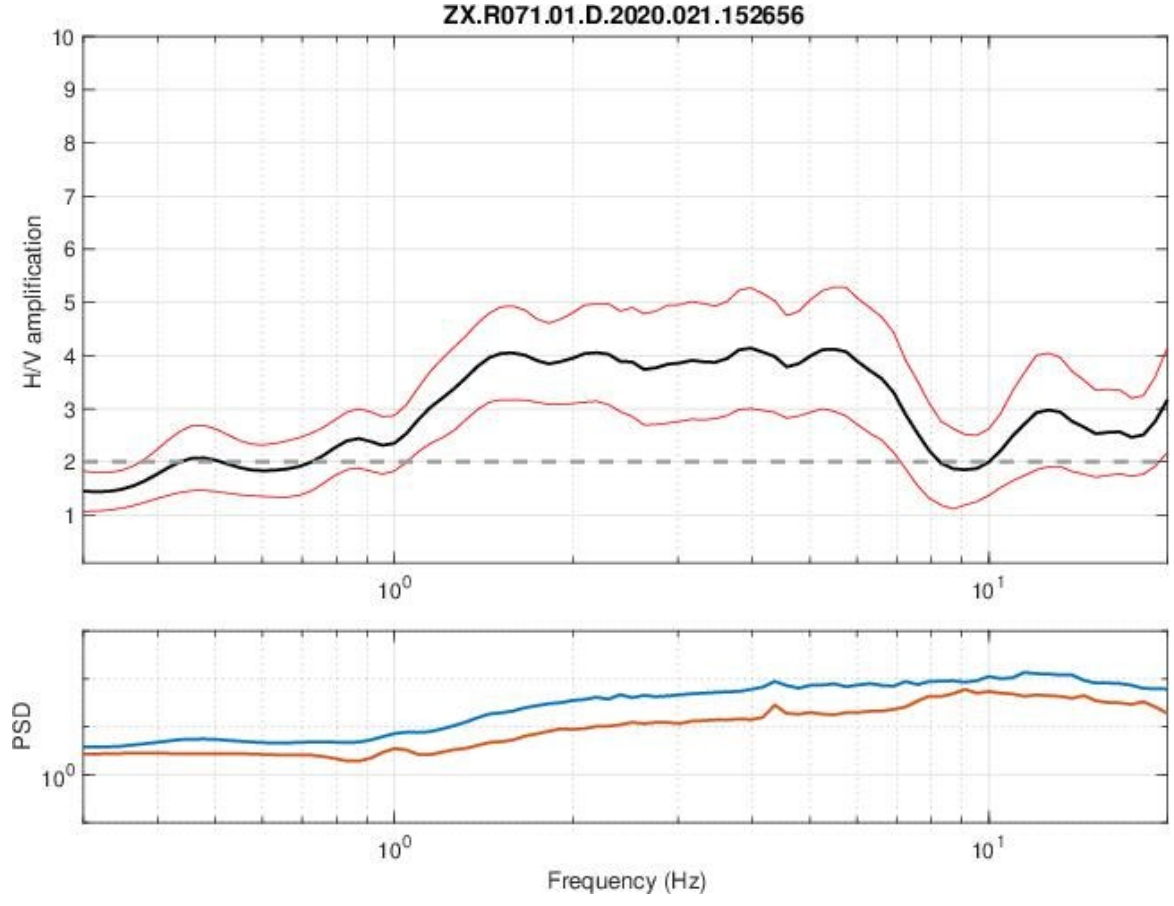

ZX.921D.01.D.2019.337.120000
H/V amplification
PSD
Frequency (Hz)

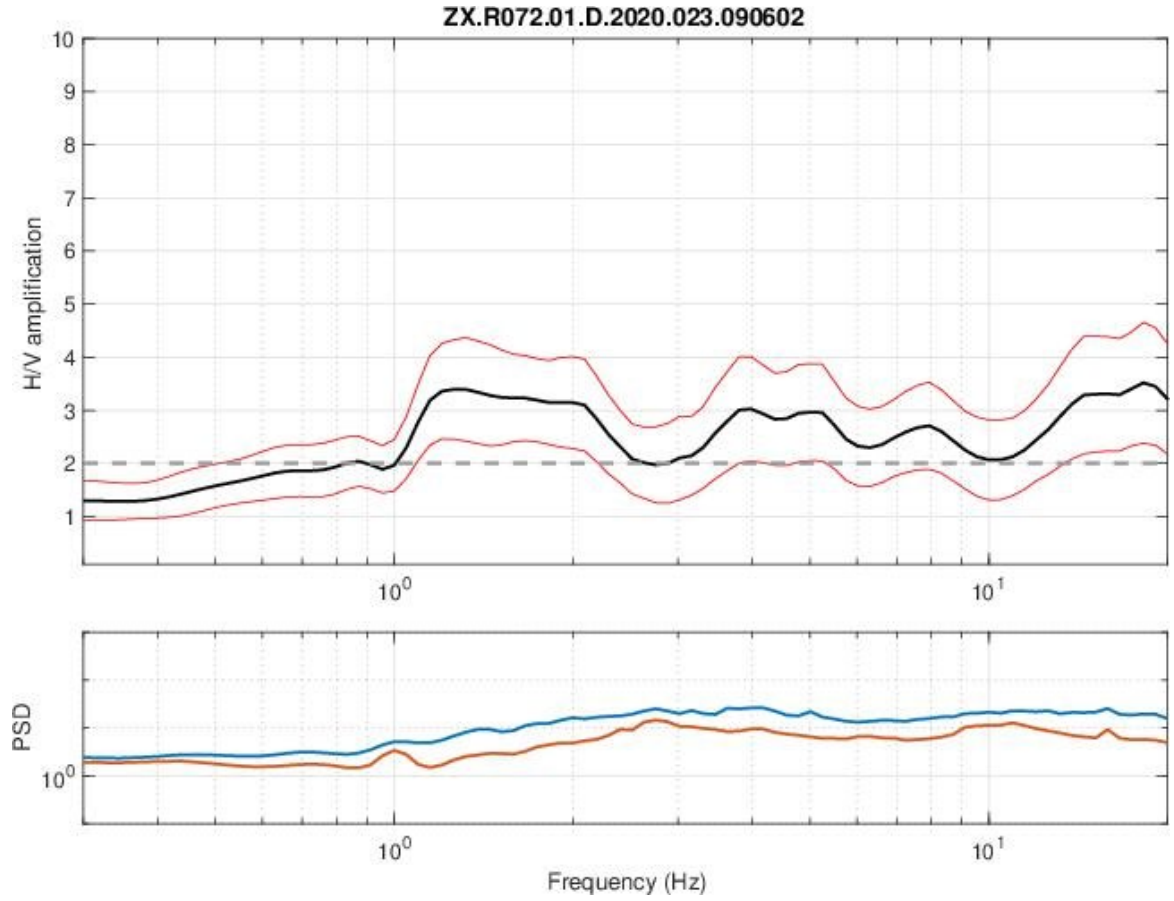

ZX.R067.01.D.2020.021.092752
H/V amplification
PSD
Frequency (Hz)

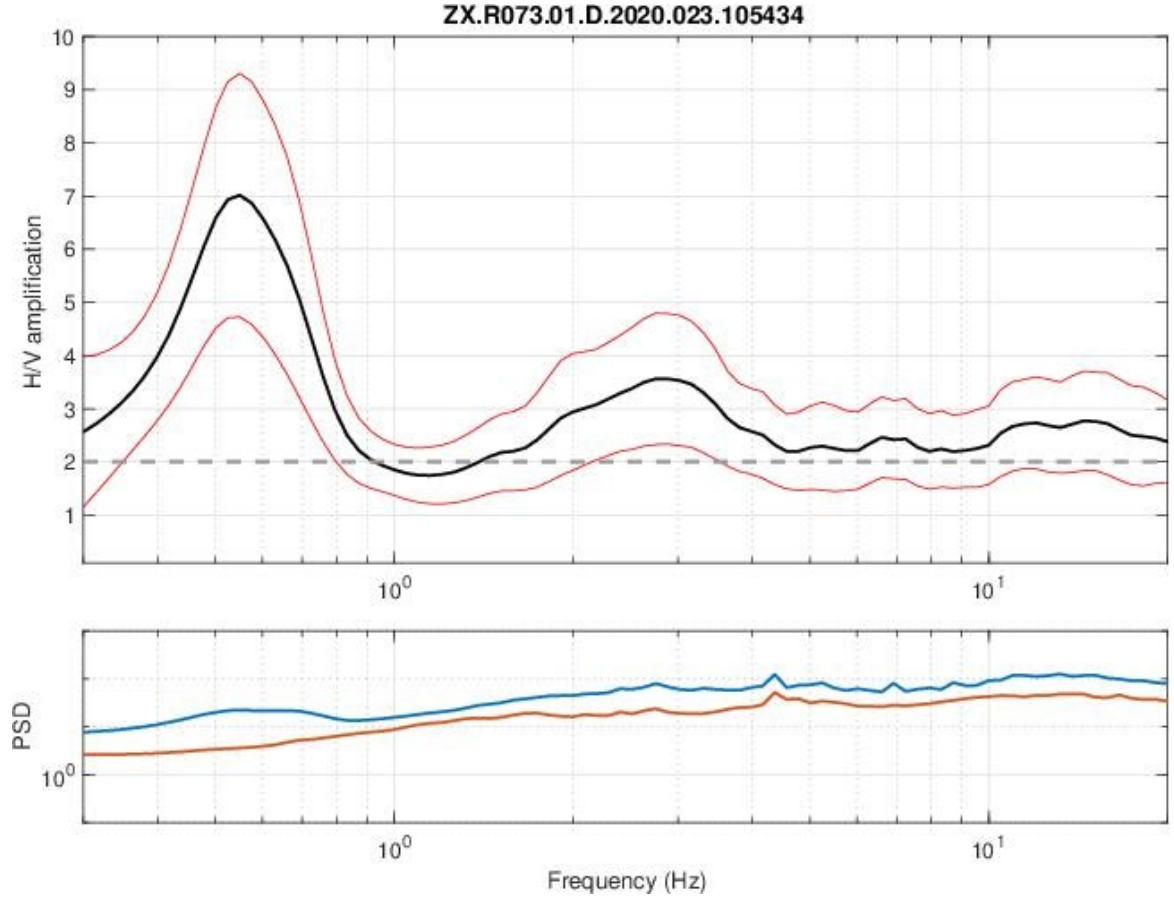

ZX.R068.01.D.2020.021.113114
H/V amplification
PSD
Frequency (Hz)

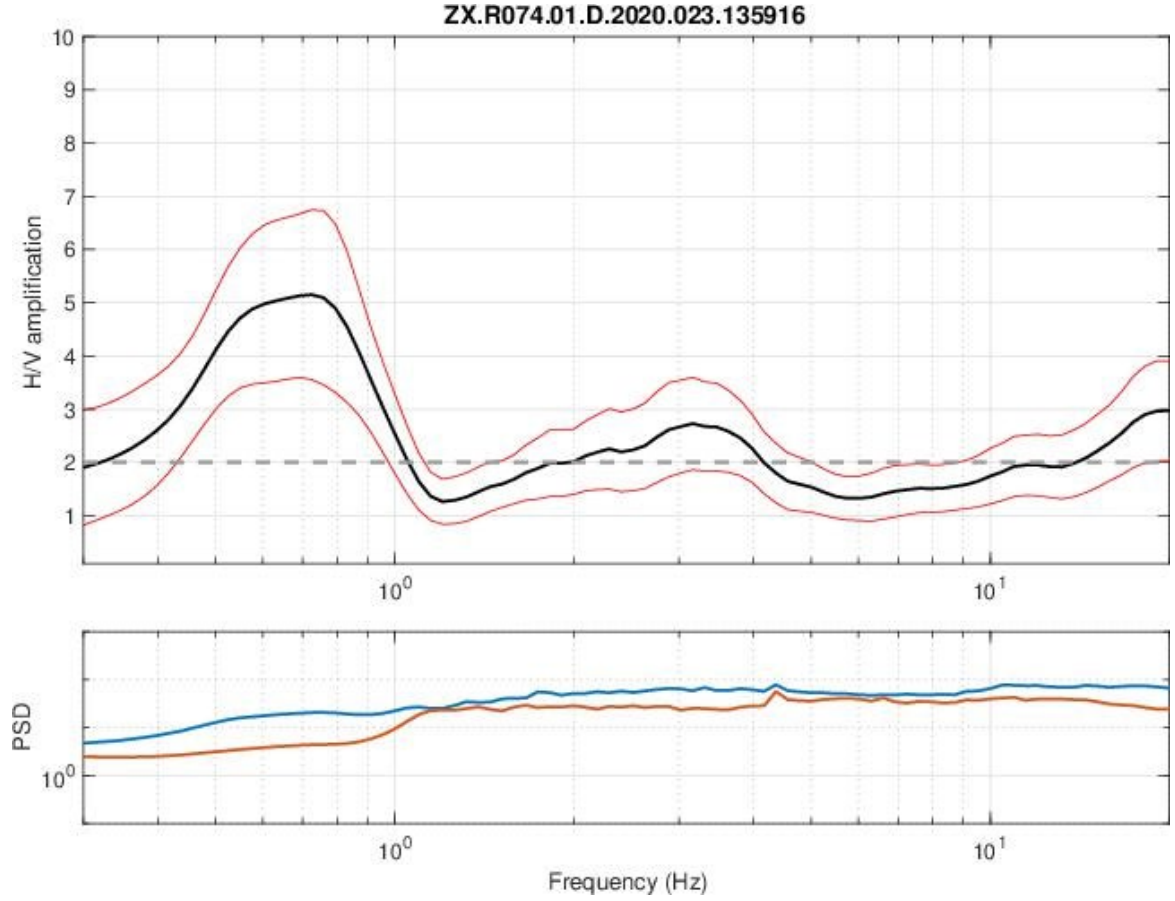

ZX.R069.01.D.2020.021.123234
H/V amplification
PSD
Frequency (Hz)

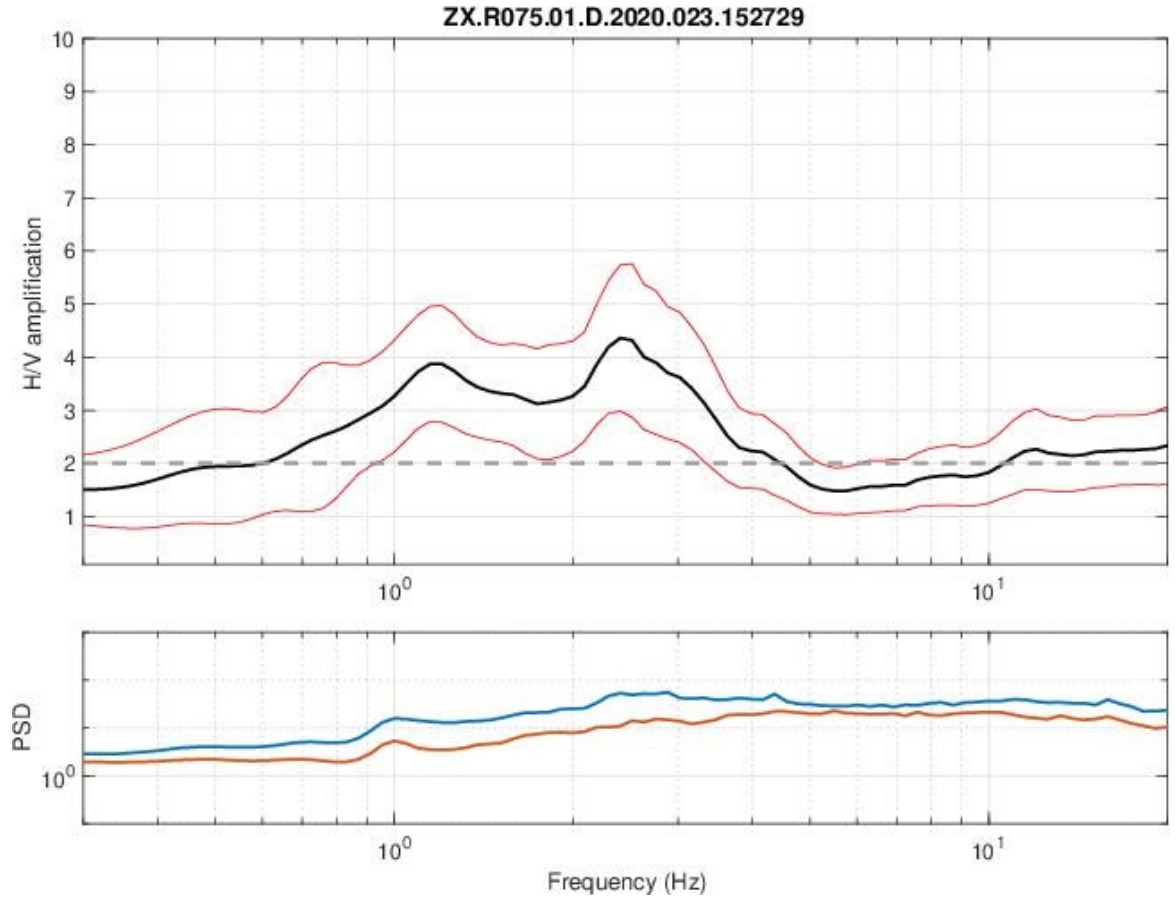

ZX.R070.01.D.2020.021.140325
H/V amplification
PSD
Frequency (Hz)

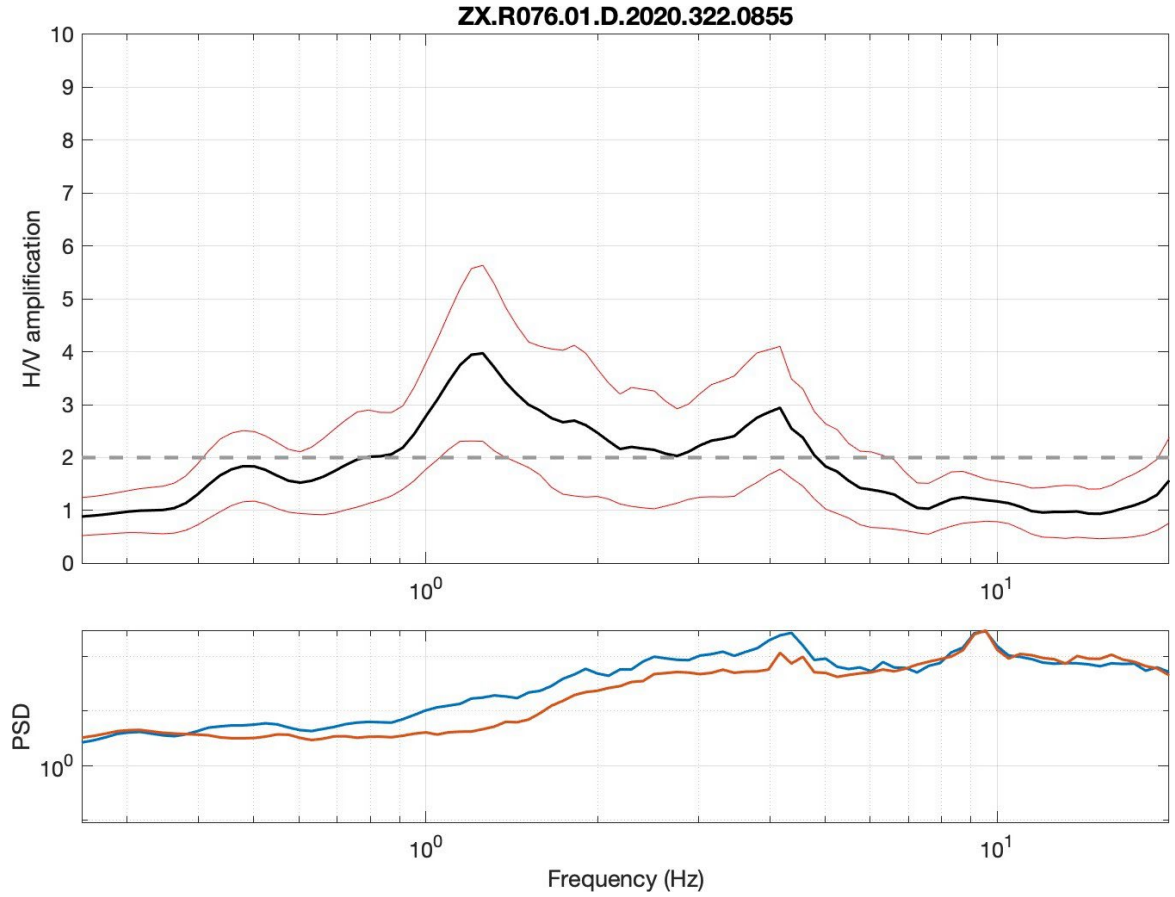

ZX.R071.01.D.2020.021.152656
H/V amplification
PSD
Frequency (Hz)

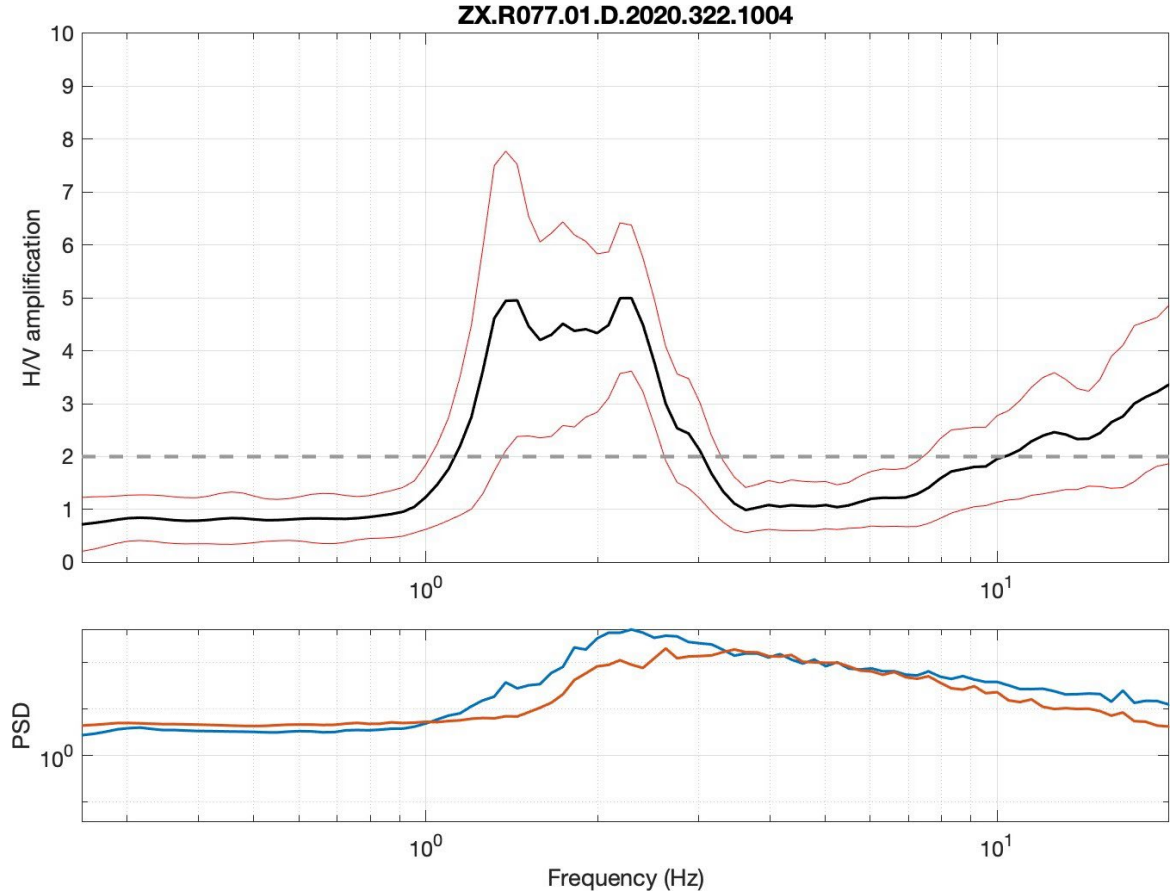

ZX.R072.01.D.2020.023.090602
H/V amplification
PSD
Frequency (Hz)

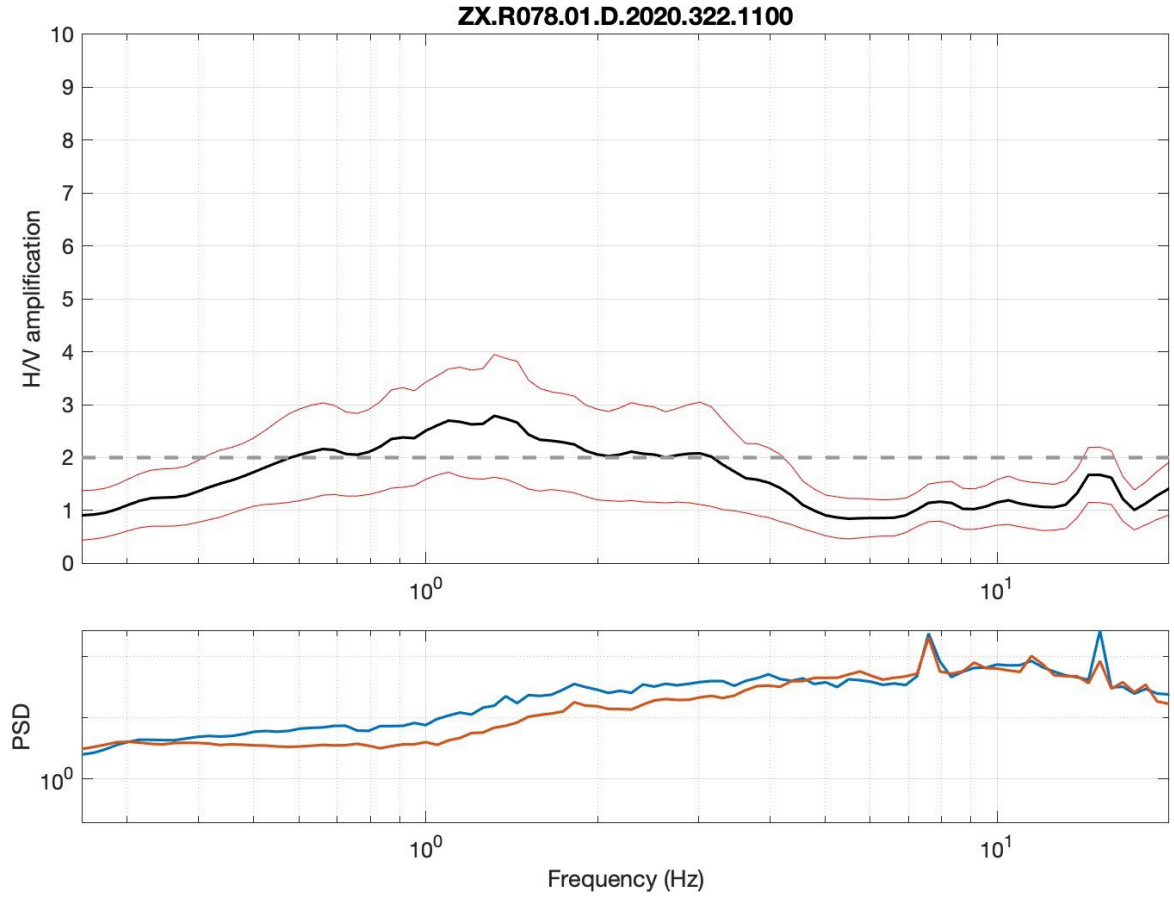

ZX.R073.01.D.2020.023.105434
H/V amplification
PSD
Frequency (Hz)

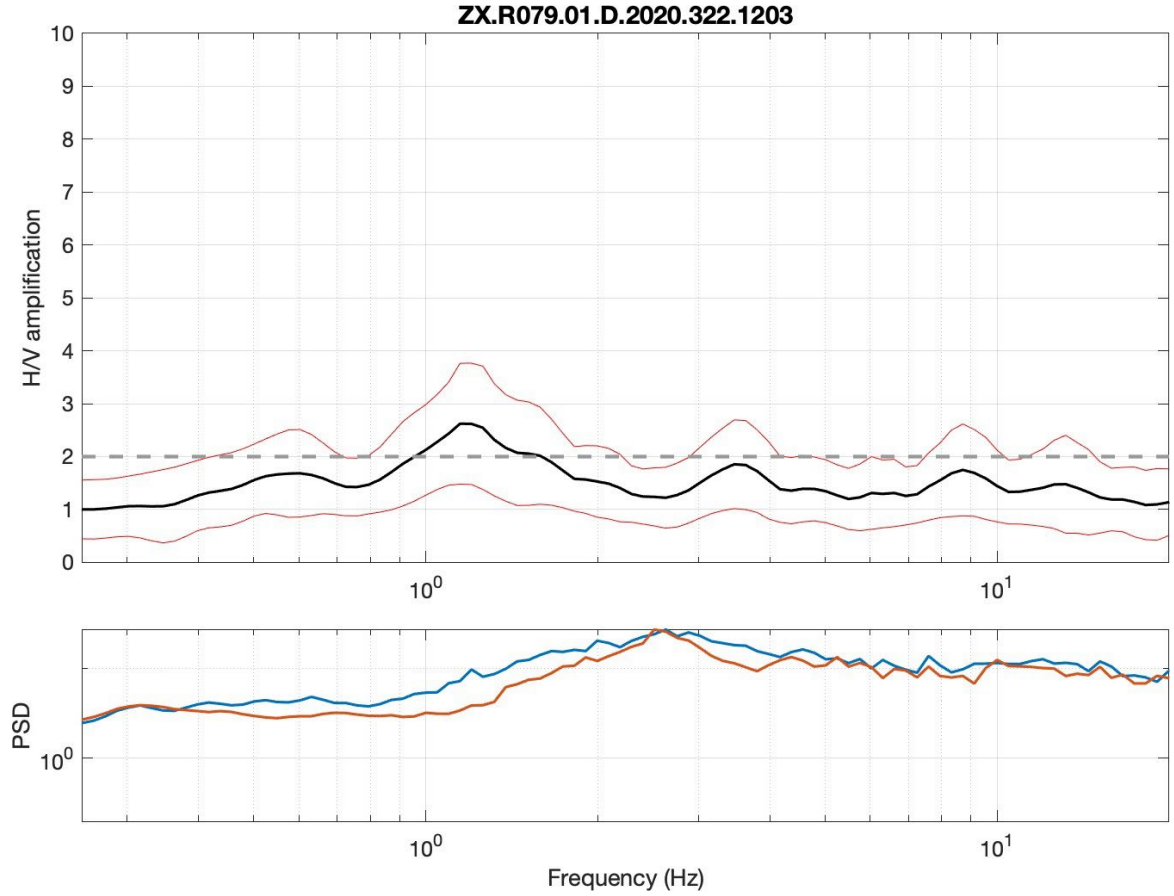

ZX.R074.01.D.2020.023.135916
H/V amplification
PSD
Frequency (Hz)

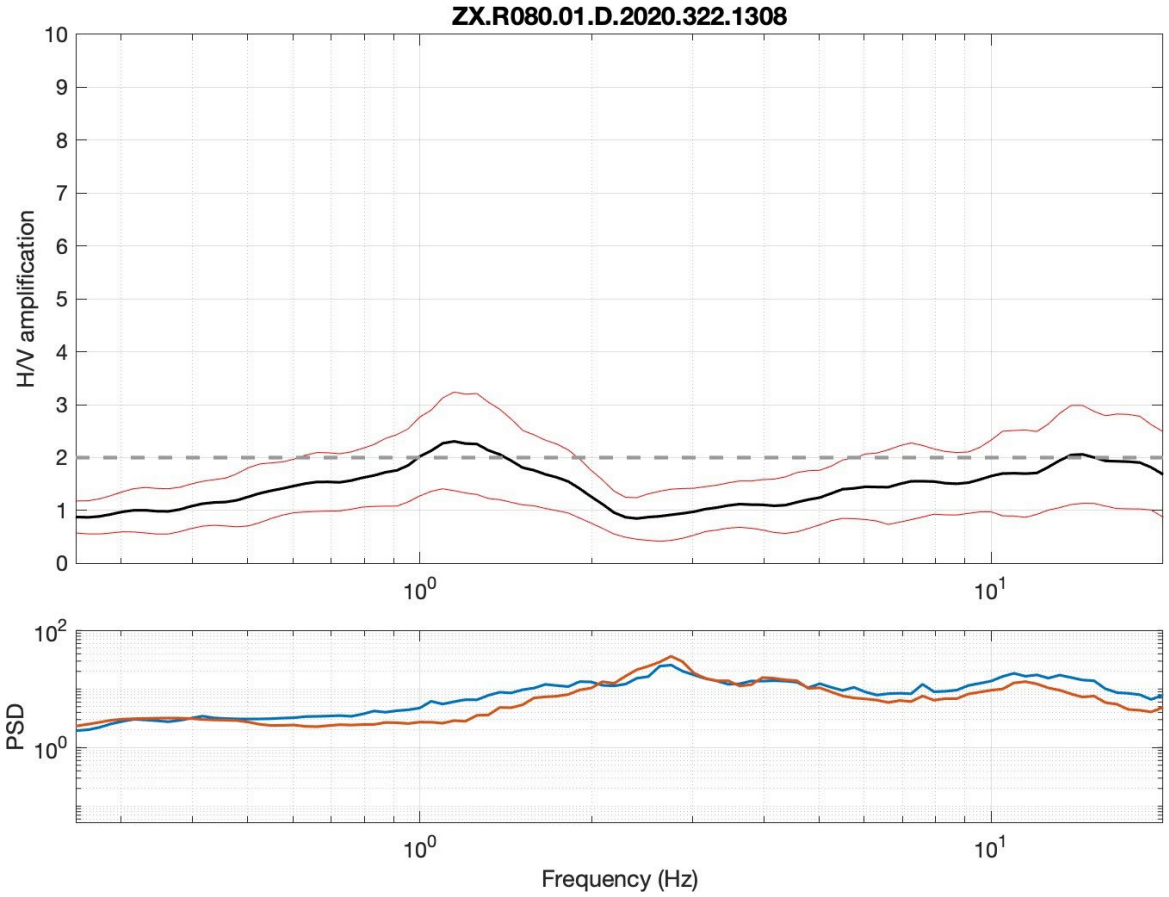

ZX.R075.01.D.2020.023.152729
H/V amplification
PSD
Frequency (Hz)

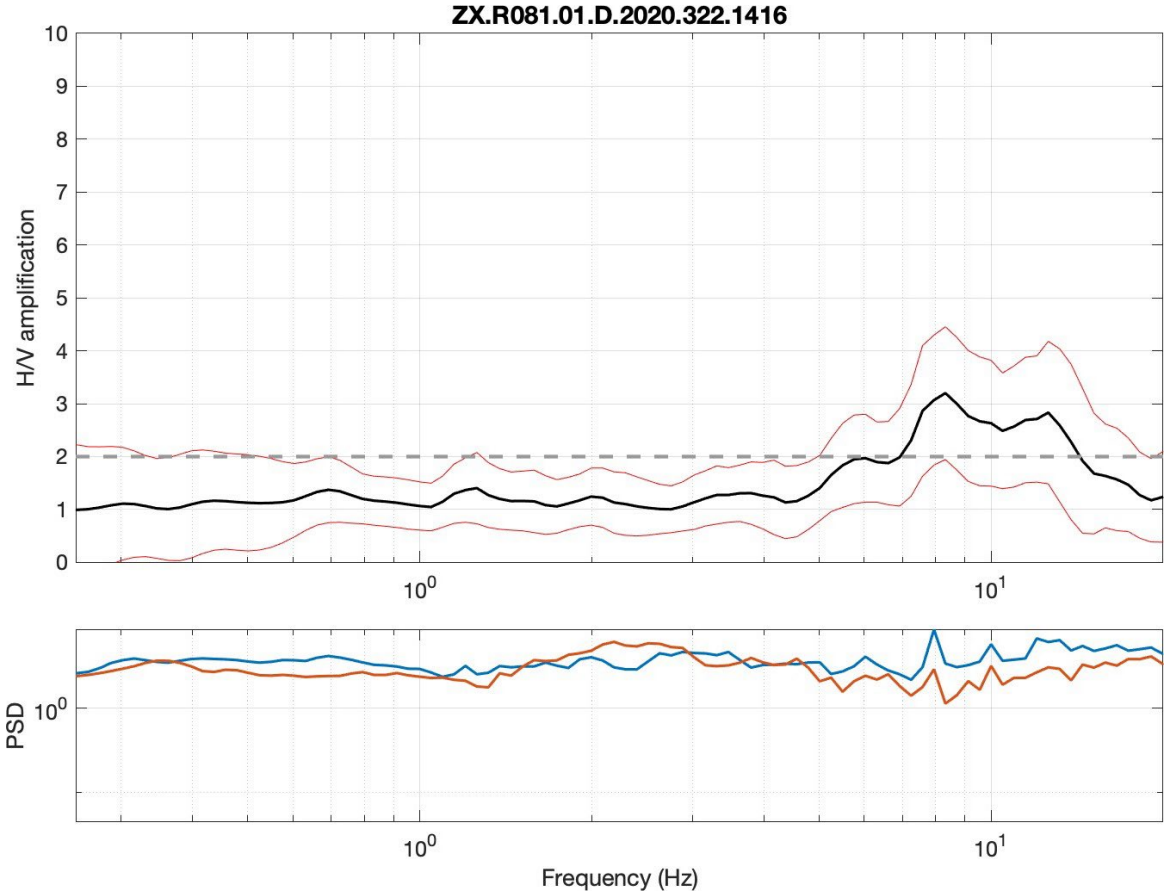

ZX.R076.01.D.2020.322.0855
H/V amplification
PSD
Frequency (Hz)

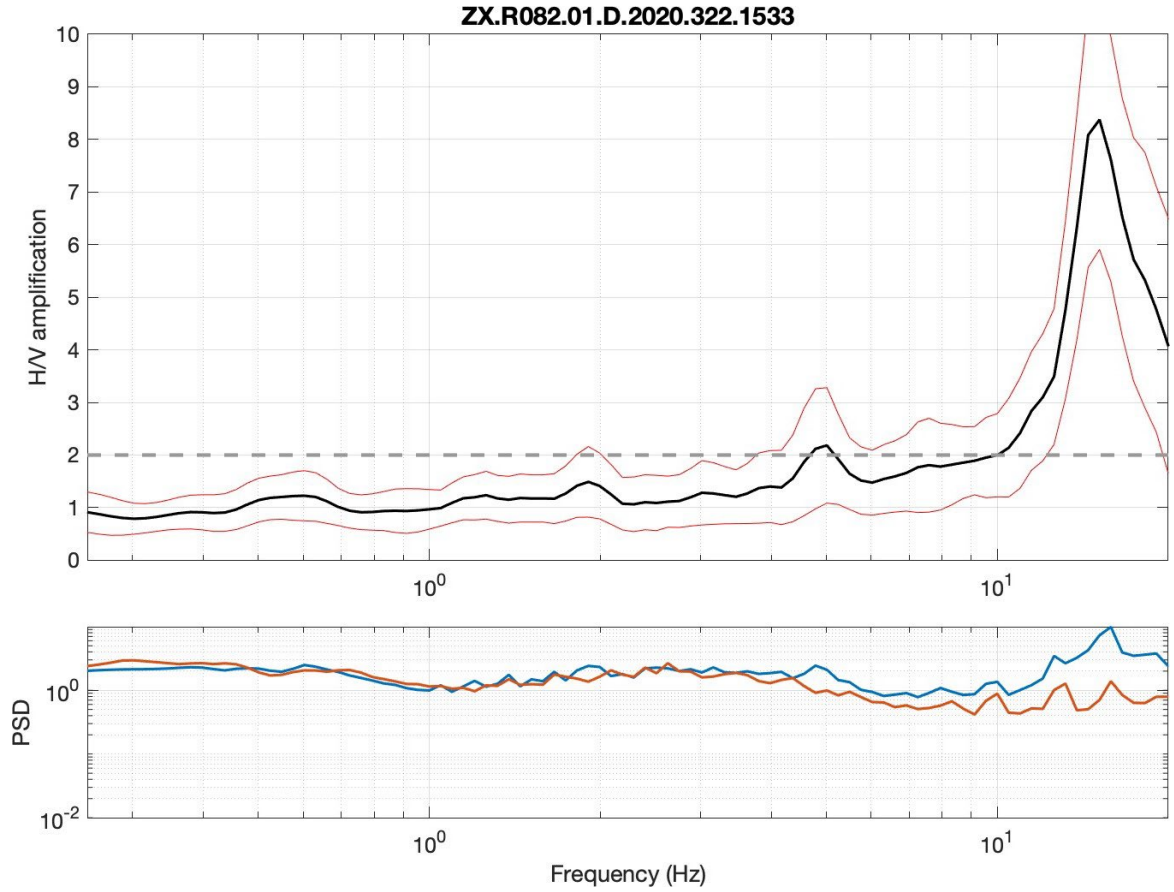

ZX.R077.01.D.2020.322.1004
H/V amplification
PSD
Frequency (Hz)

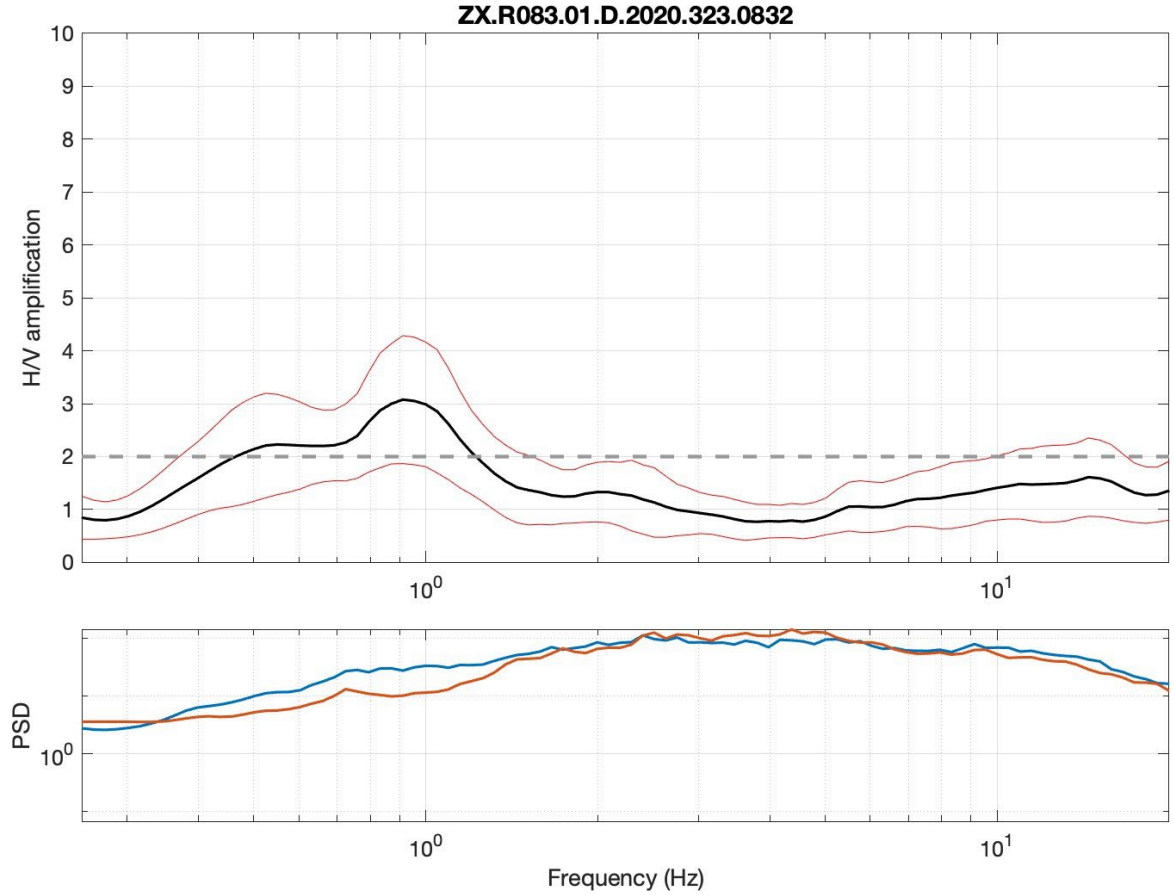

ZX.R078.01.D.2020.322.1100
H/V amplification
PSD
Frequency (Hz)

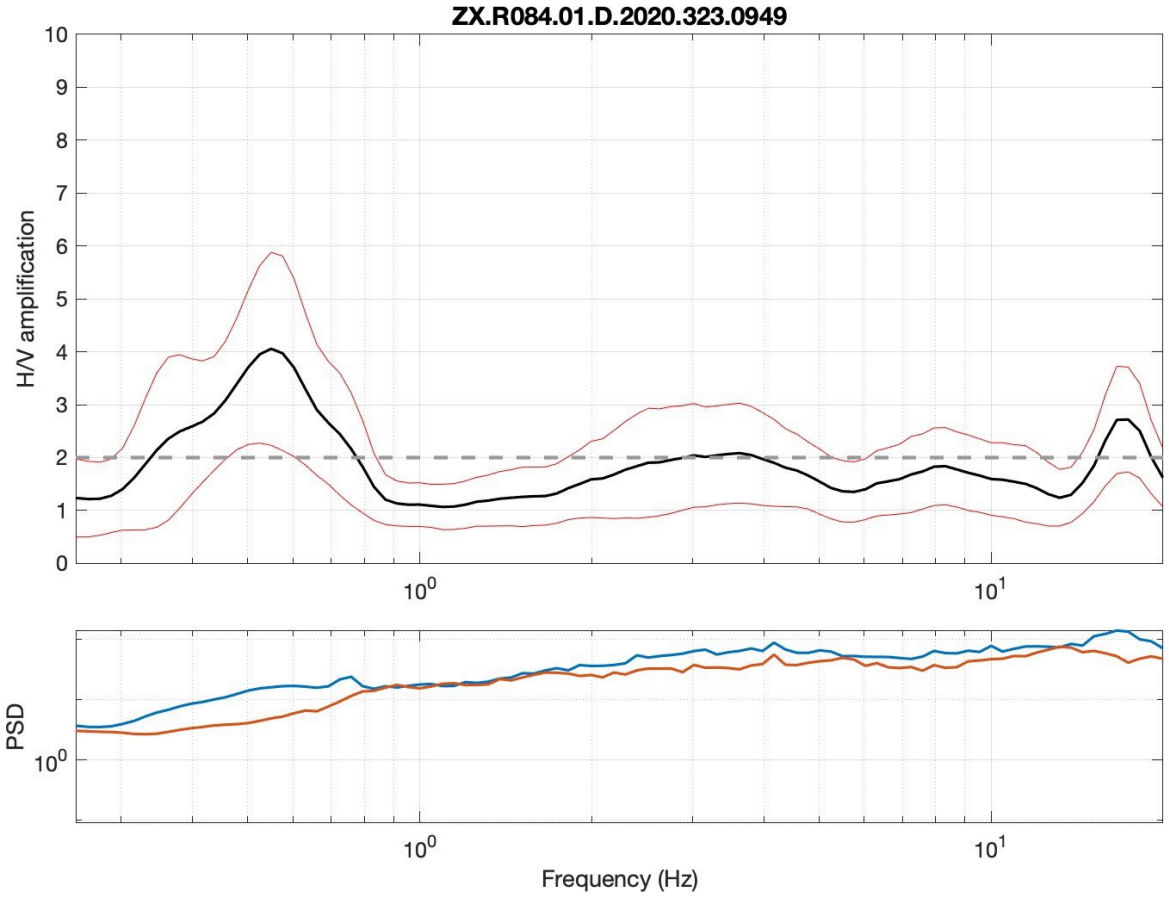

ZX.R079.01.D.2020.322.1203
H/V amplification
PSD
Frequency (Hz)

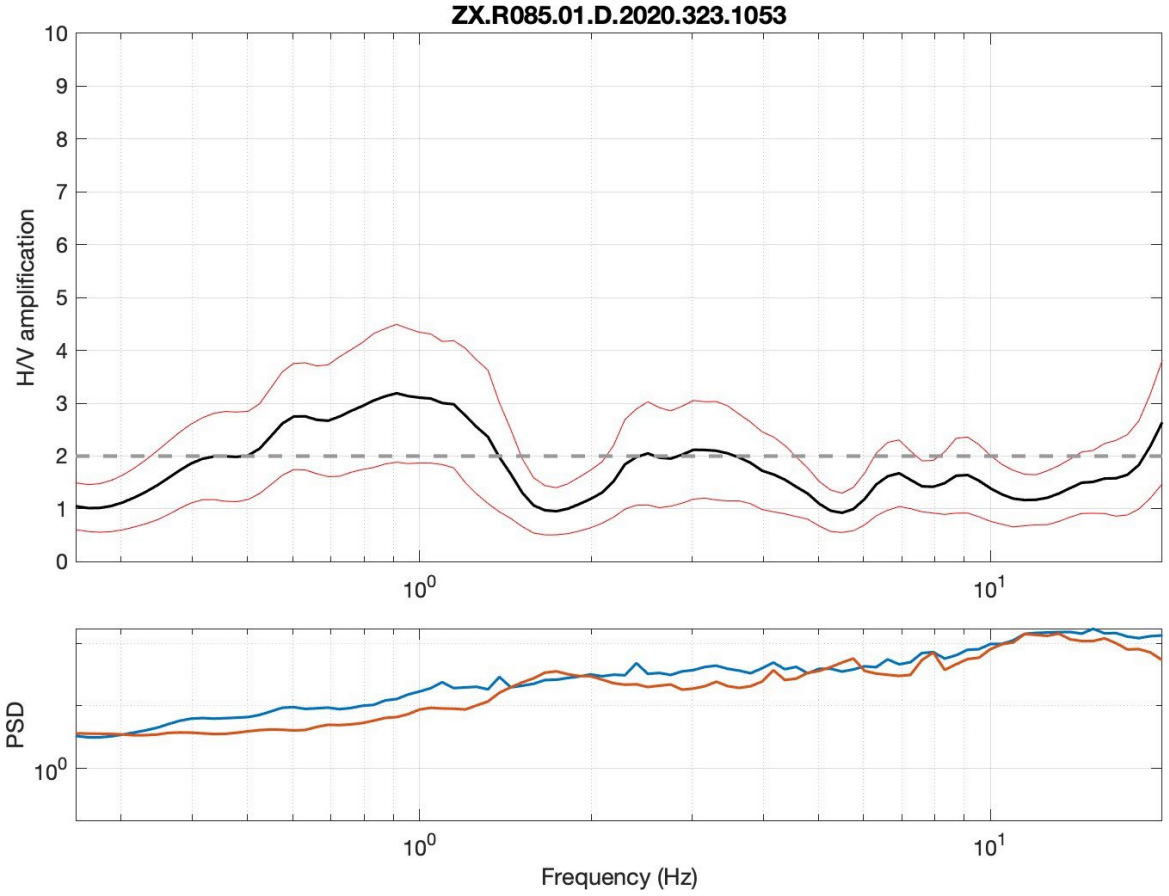

ZX.R080.01.D.2020.322.1308
H/V amplification
PSD
Frequency (Hz)

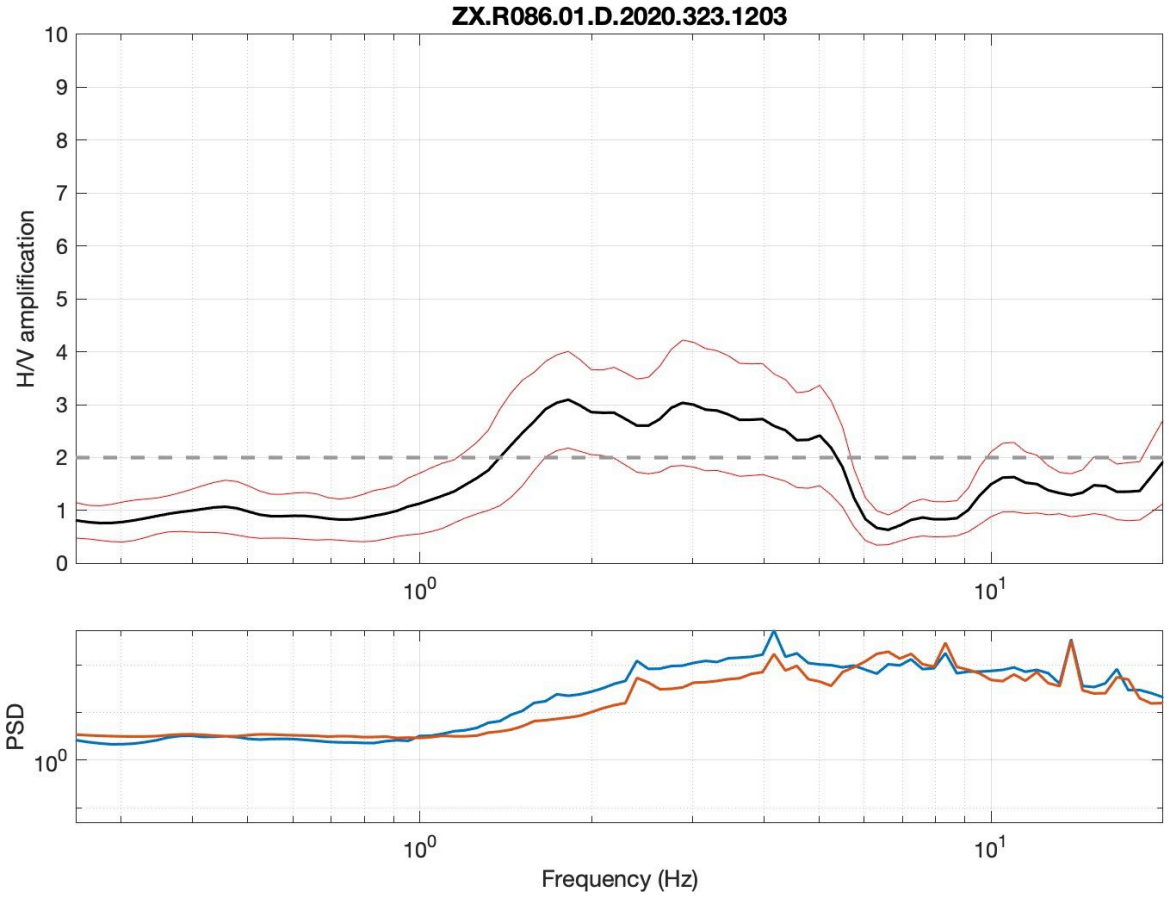

ZX.R081.01.D.2020.322.1416
H/V amplification
PSD
Frequency (Hz)

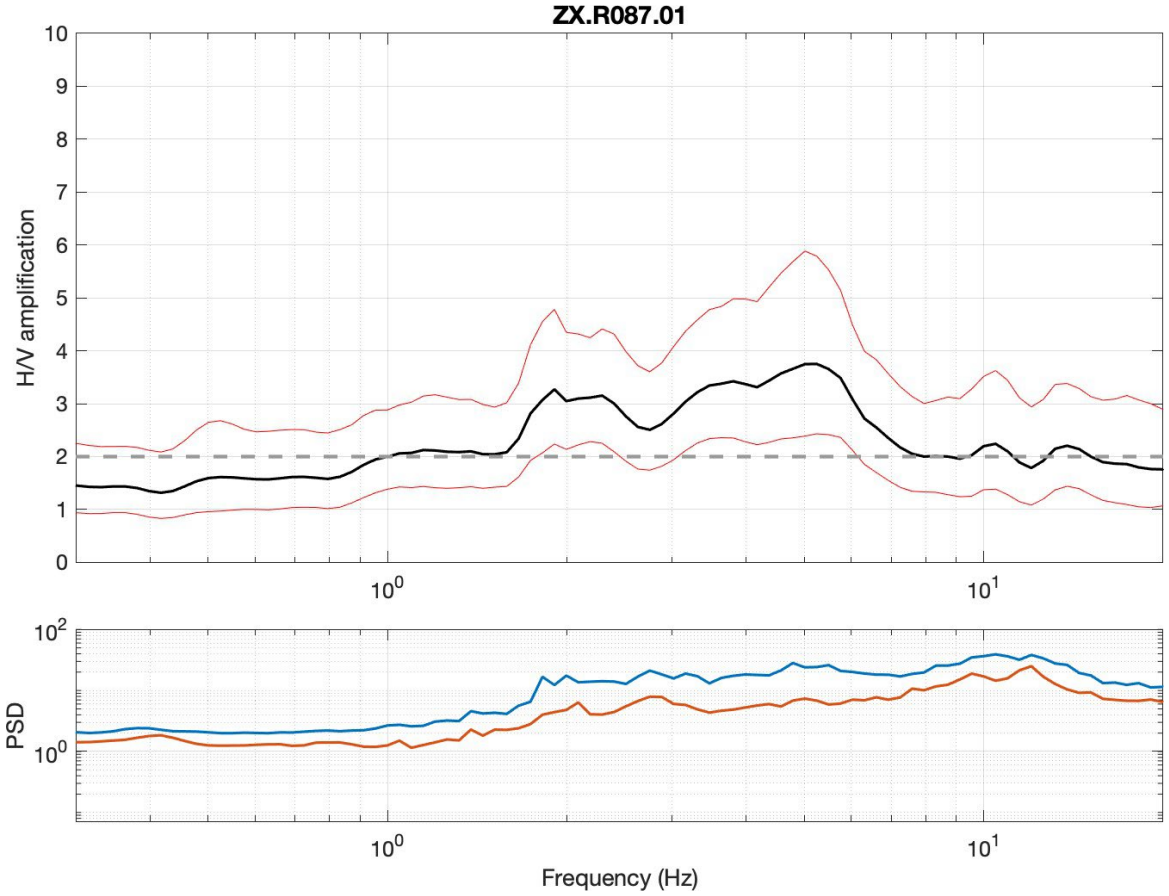

ZX.R082.01.D.2020.322.1533
H/V amplification
PSD
Frequency (Hz)

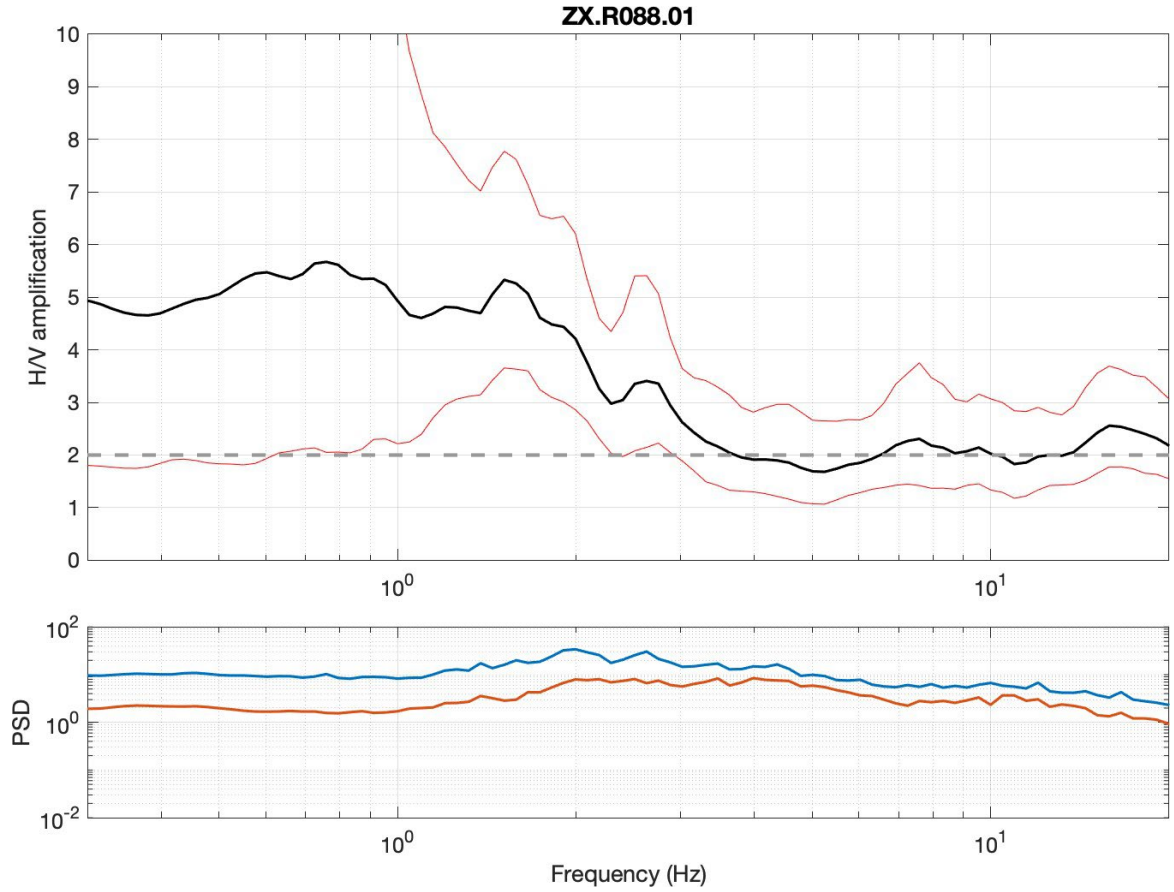

ZX.R083.01.D.2020.323.0832
H/V amplification
PSD
Frequency (Hz)

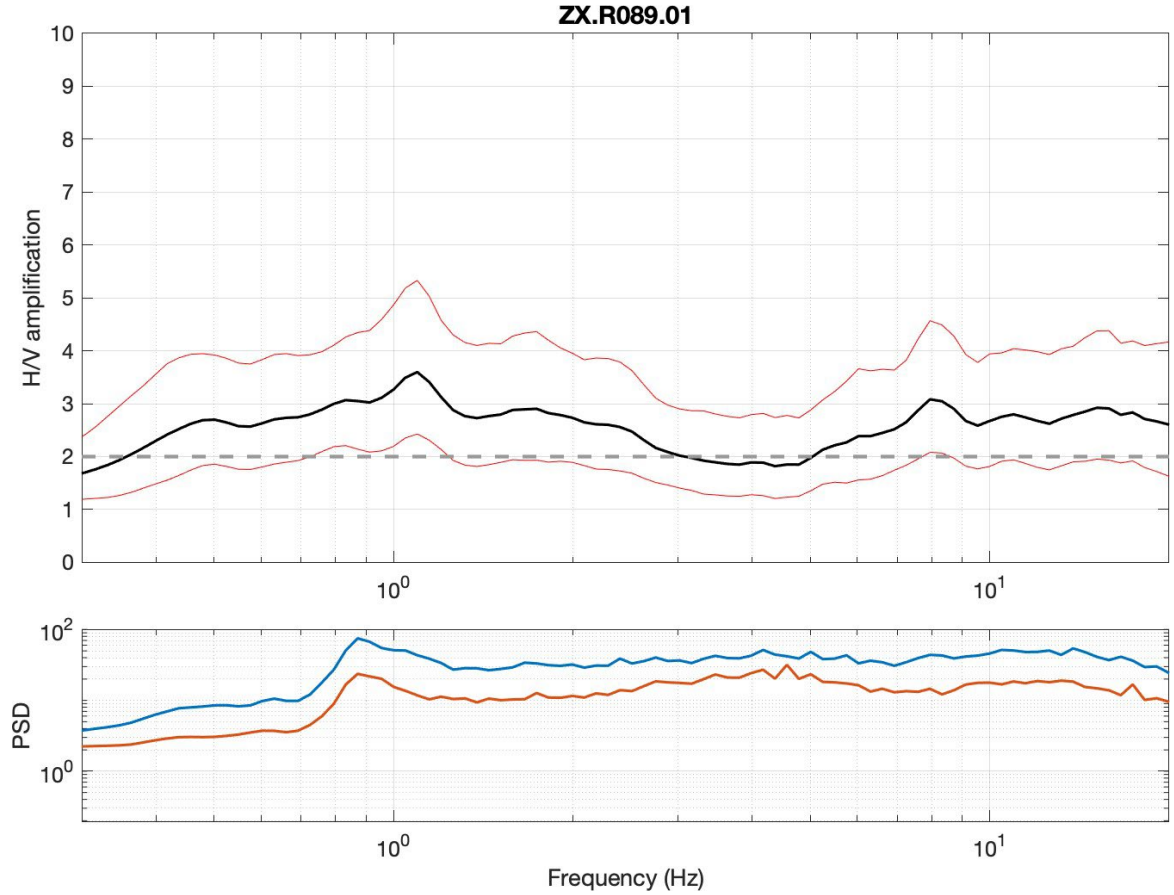

ZX.R084.01.D.2020.323.0949
H/V amplification
PSD
Frequency (Hz)

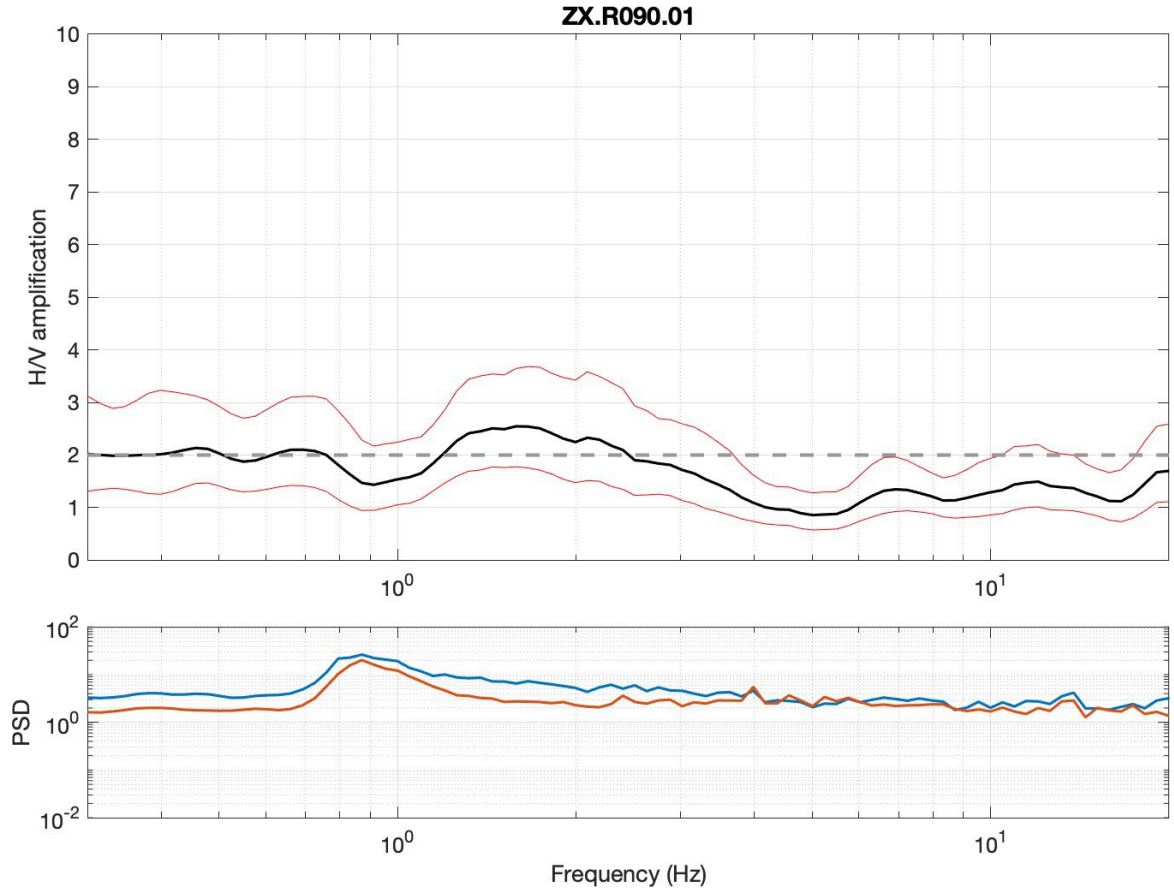

ZX.R085.01.D.2020.323.1053
H/V amplification
PSD
Frequency (Hz)

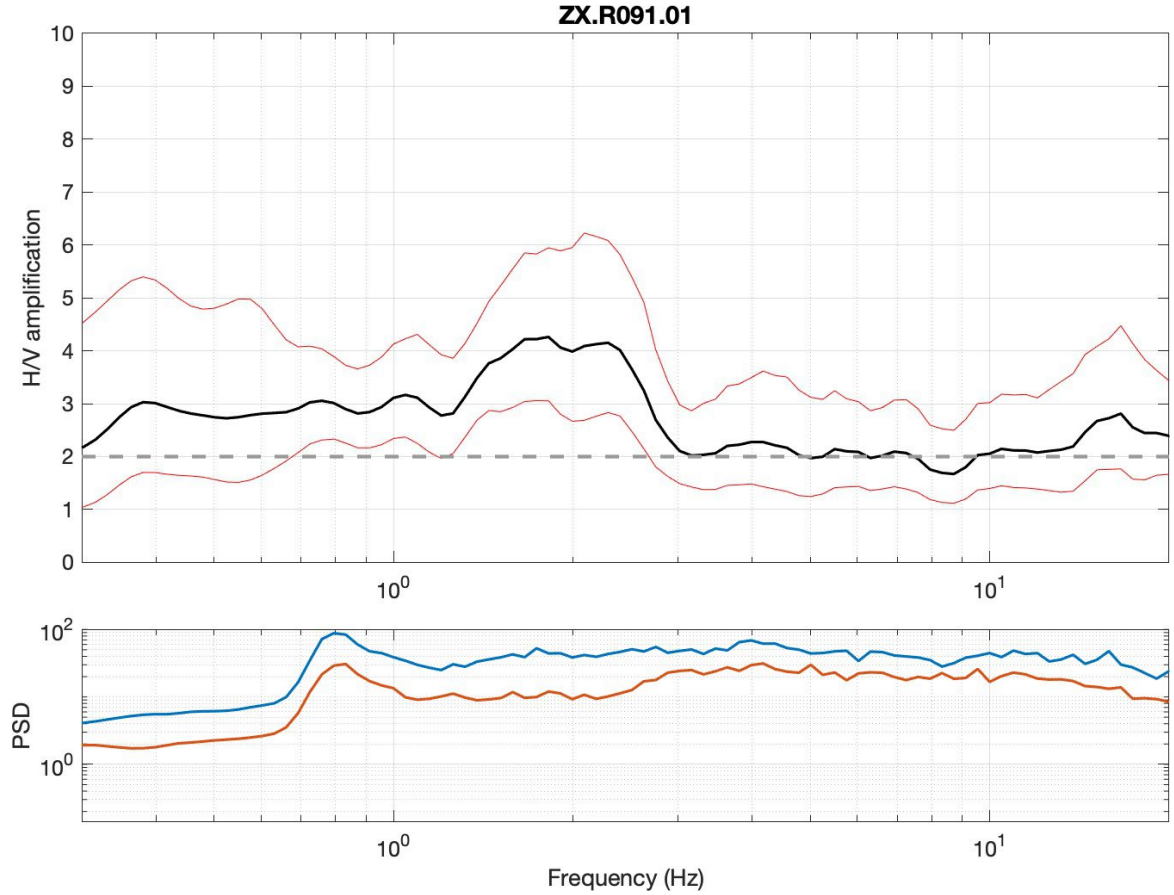

ZX.R086.01.D.2020.323.1203
H/V amplification
PSD
Frequency (Hz)

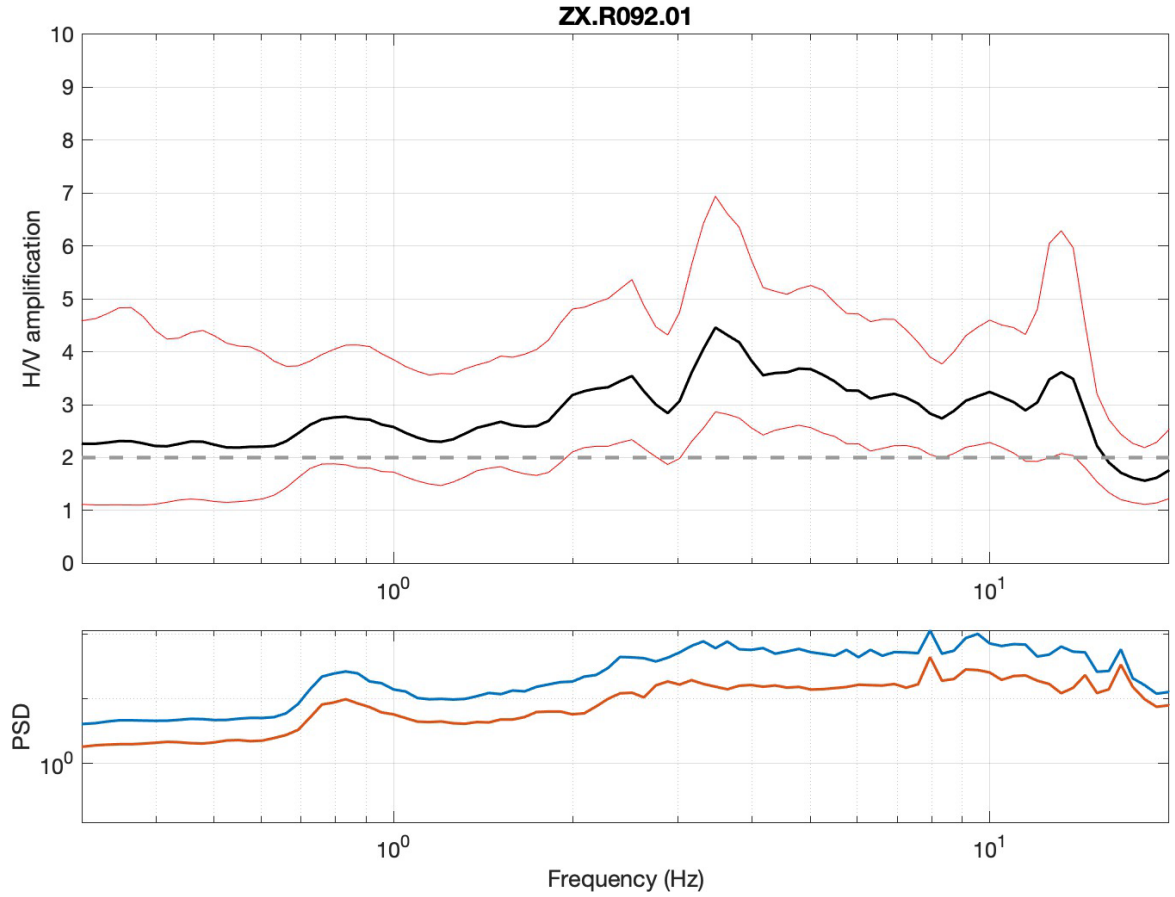

ZX.R087.01
H/V amplification
PSD
Frequency (Hz)

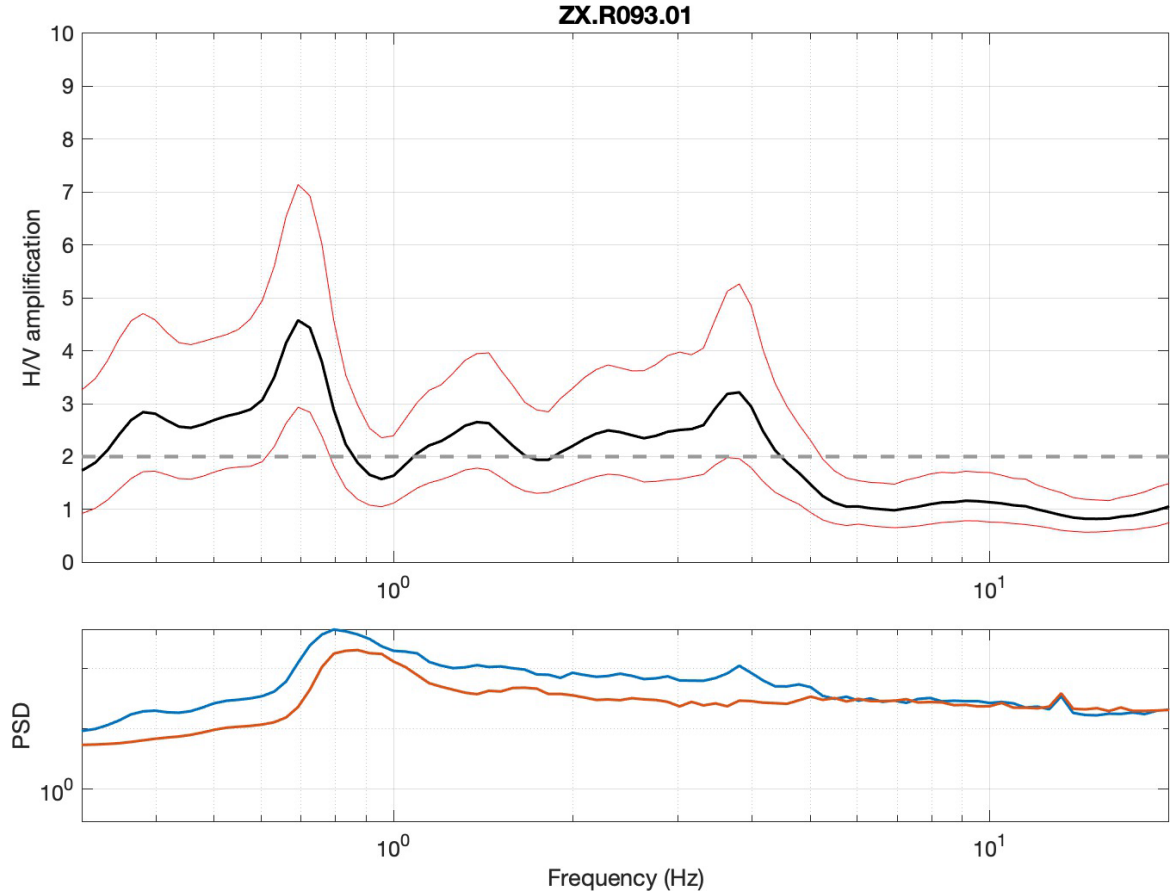

ZX.R088.01
H/V amplification
PSD
Frequency (Hz)

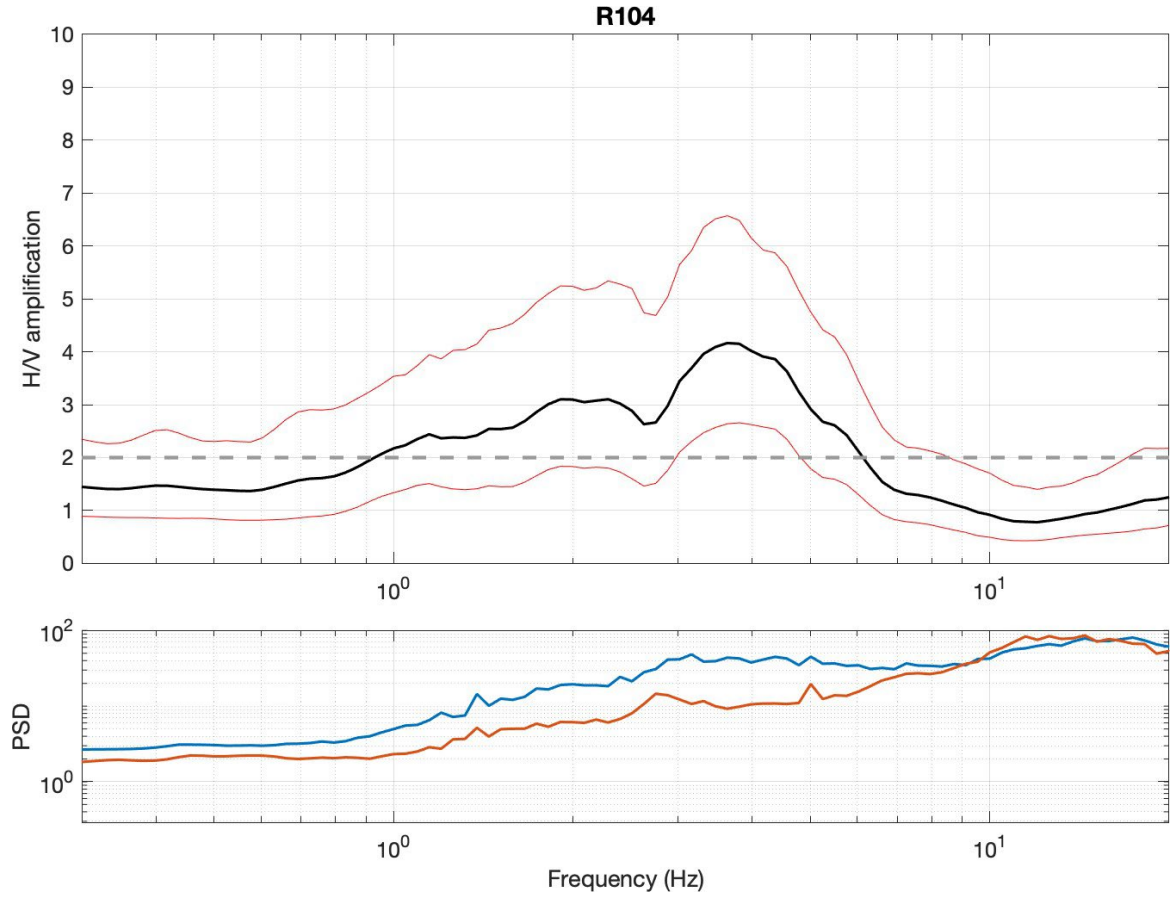

ZX.R089.01
H/V amplification
PSD
Frequency (Hz)

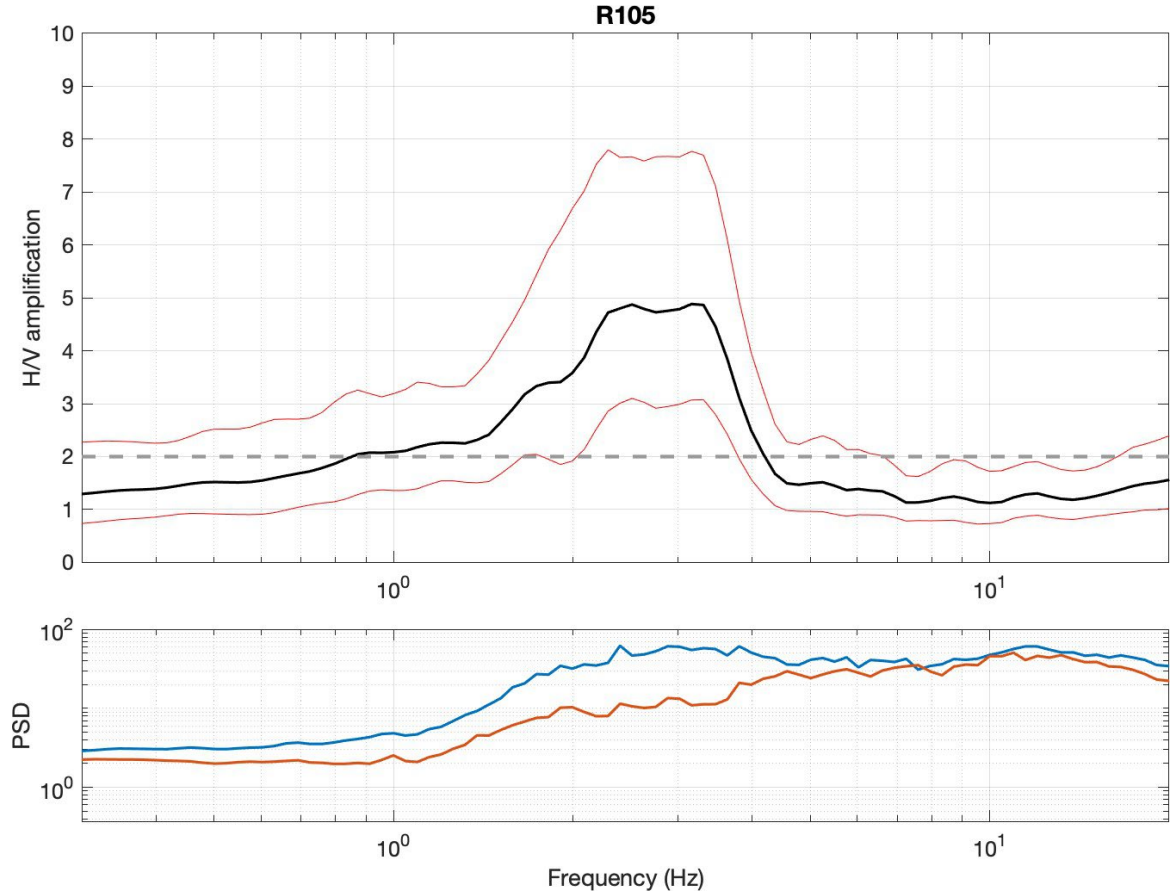

ZX.R090.01
H/V amplification
PSD
Frequency (Hz)

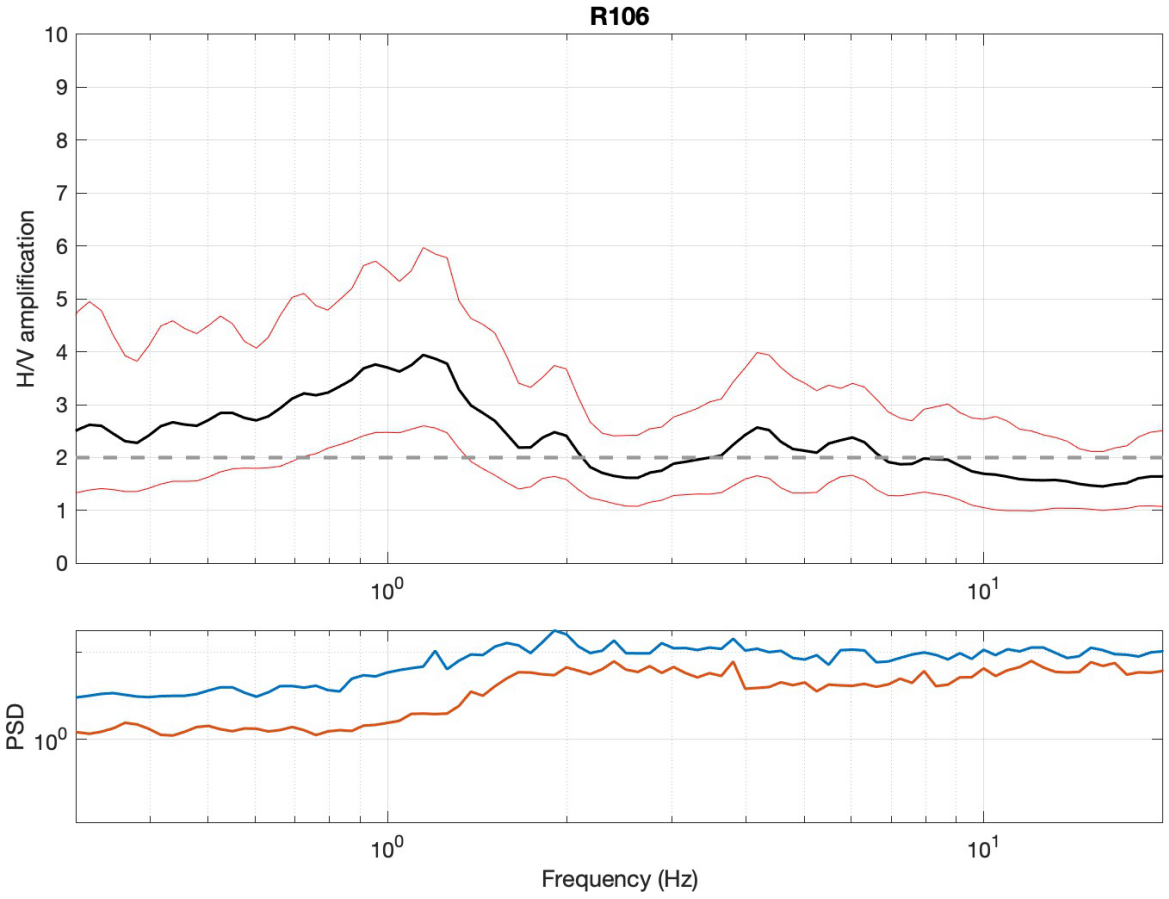

ZX.R091.01
H/V amplification
PSD
Frequency (Hz)

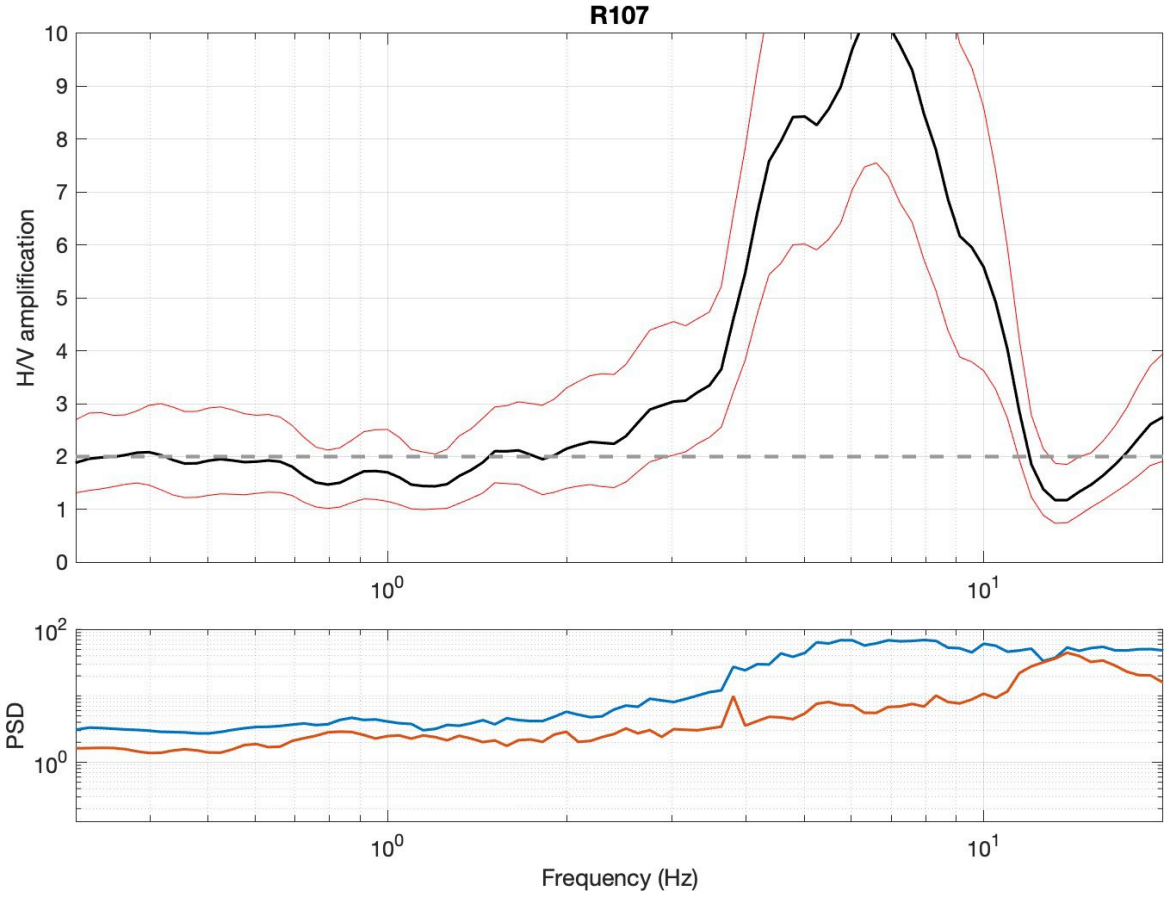

ZX.R092.01
H/V amplification
PSD
Frequency (Hz)

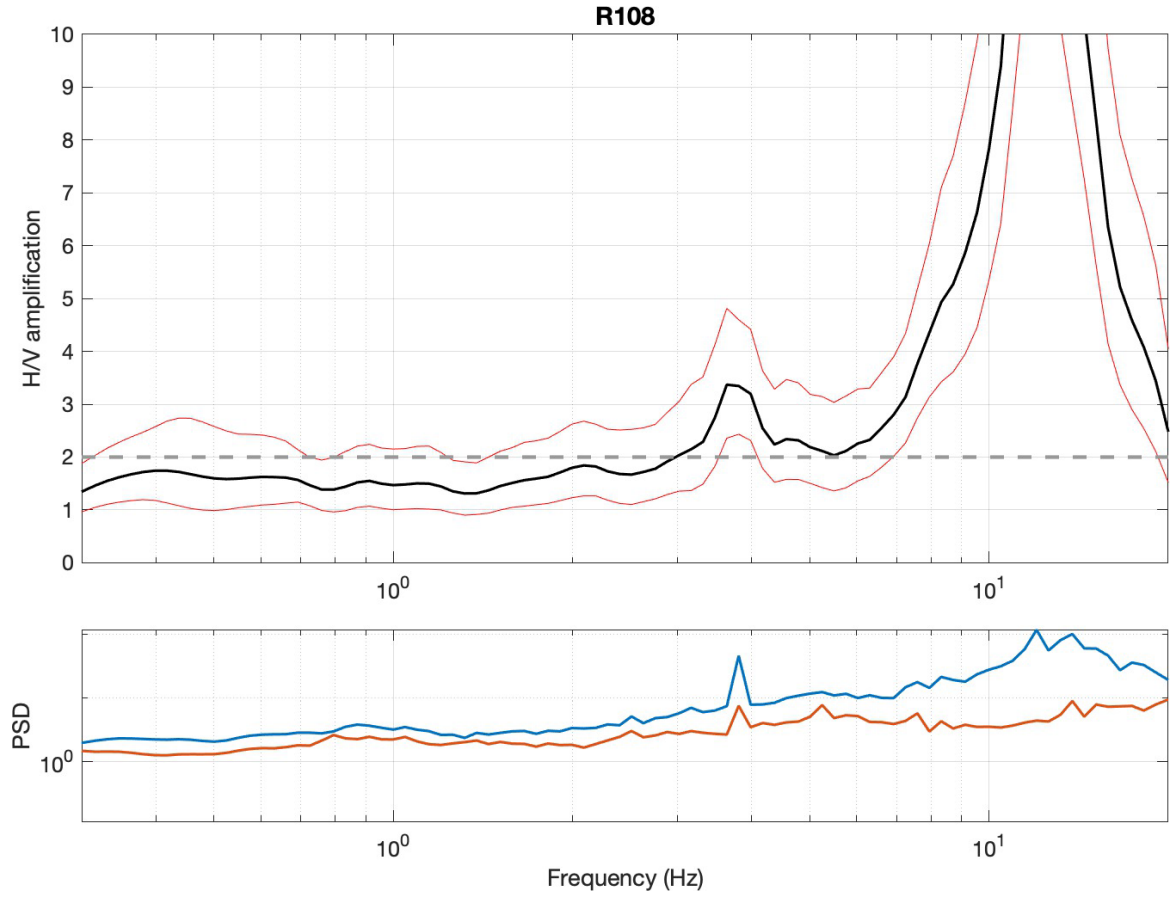

ZX.R093.01
H/V amplification
PSD
Frequency (Hz)

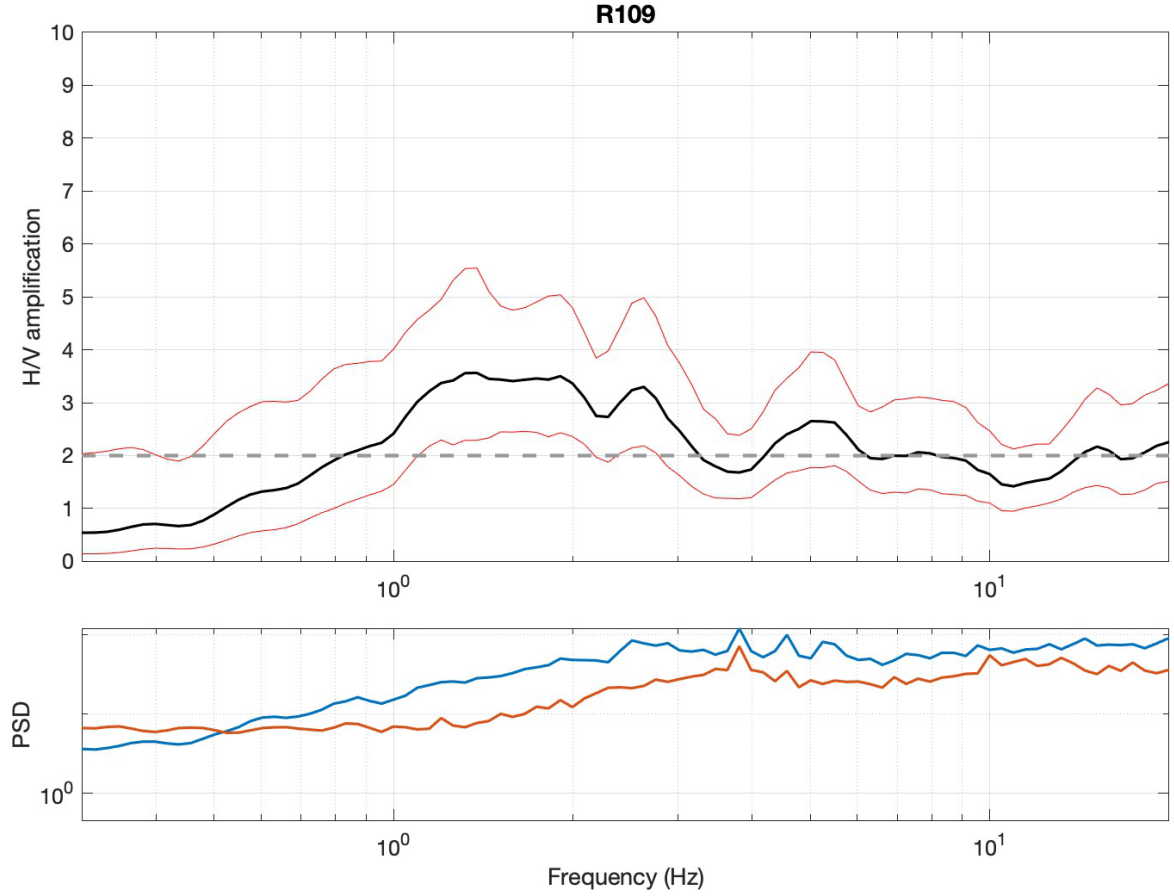

R104
H/V amplification
PSD
Frequency (Hz)

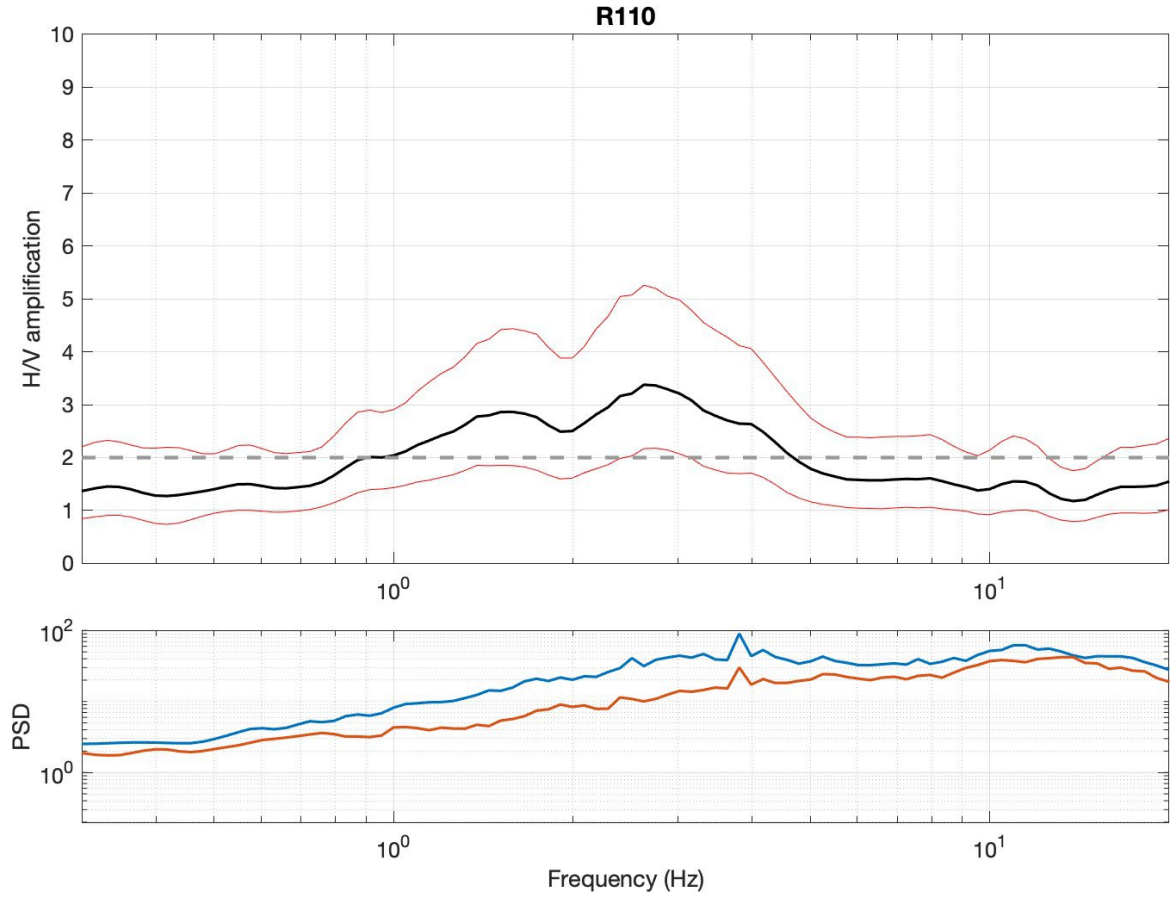

R105
H/V amplification
PSD
Frequency (Hz)

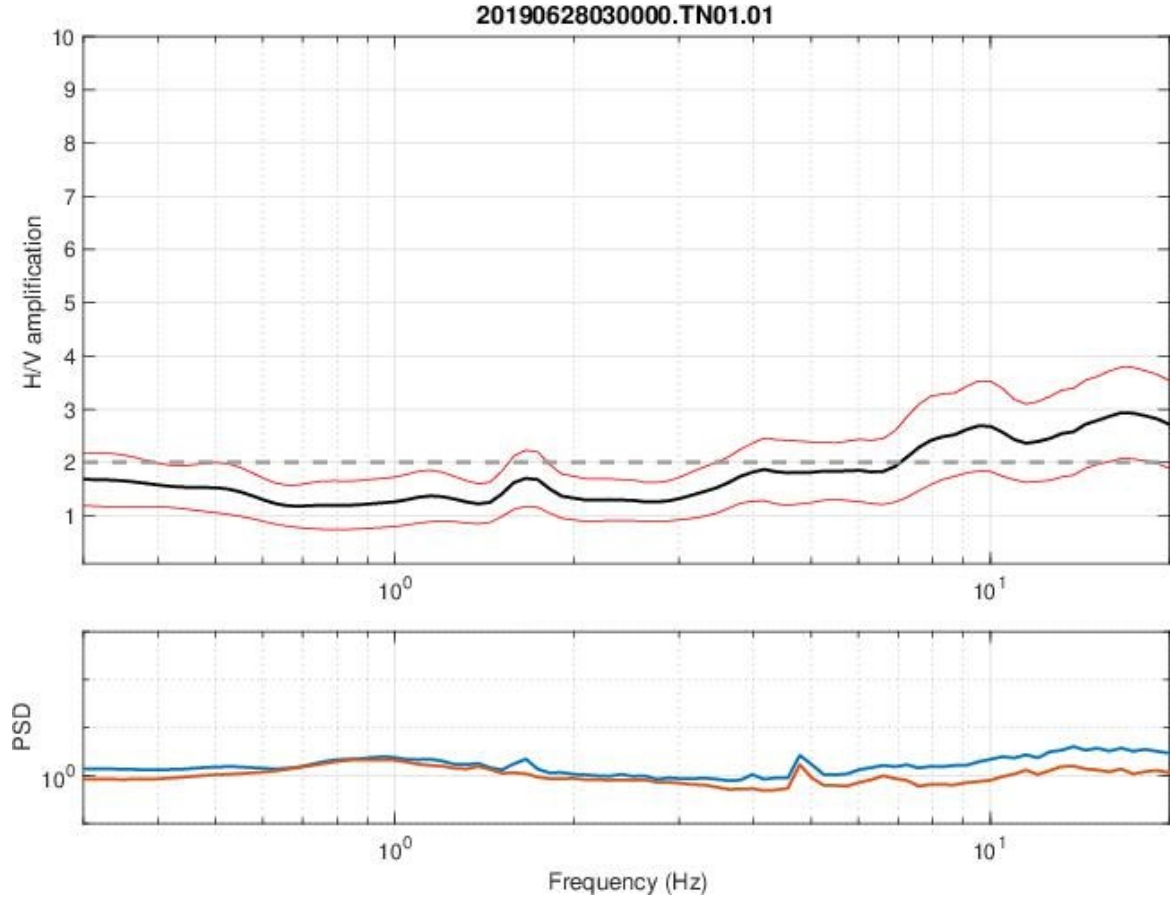

R106
H/V amplification
PSD
Frequency (Hz)

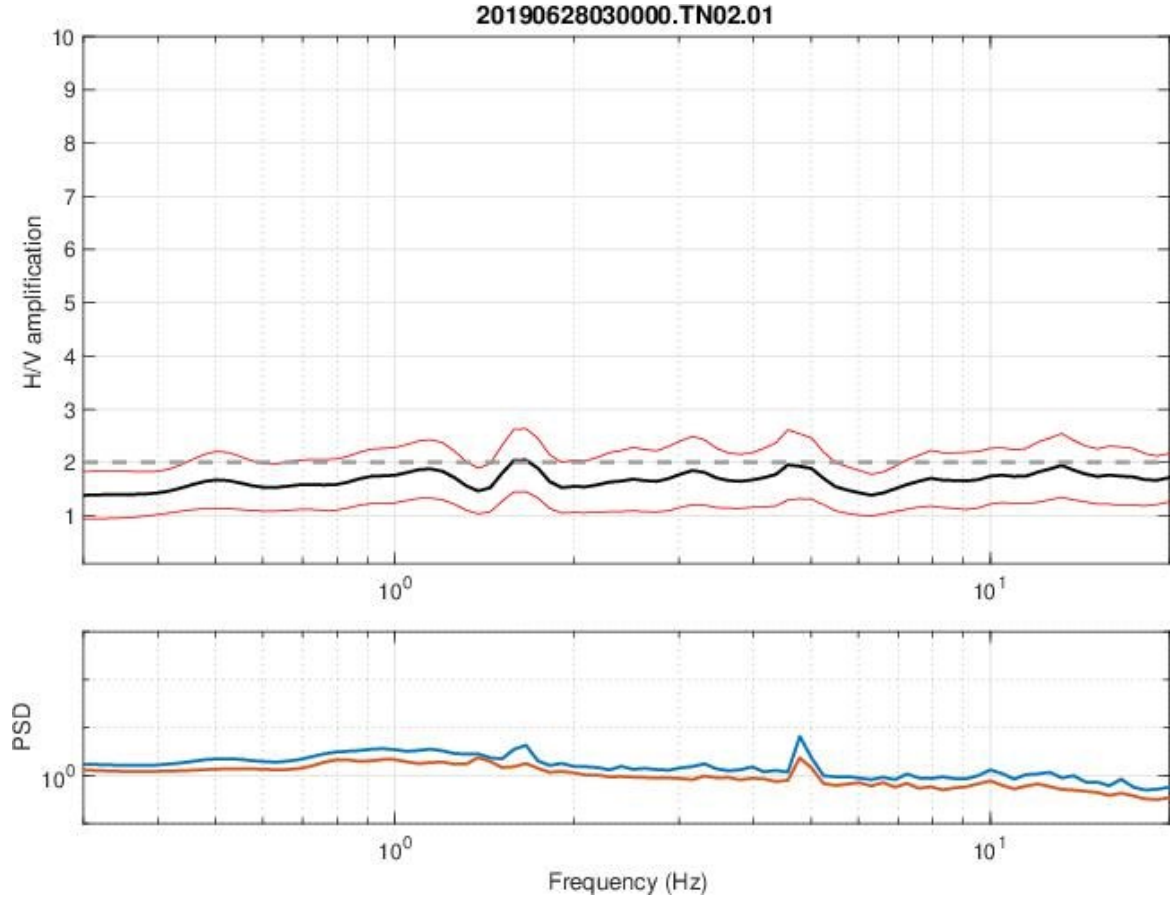

R107
H/V amplification
PSD
Frequency (Hz)

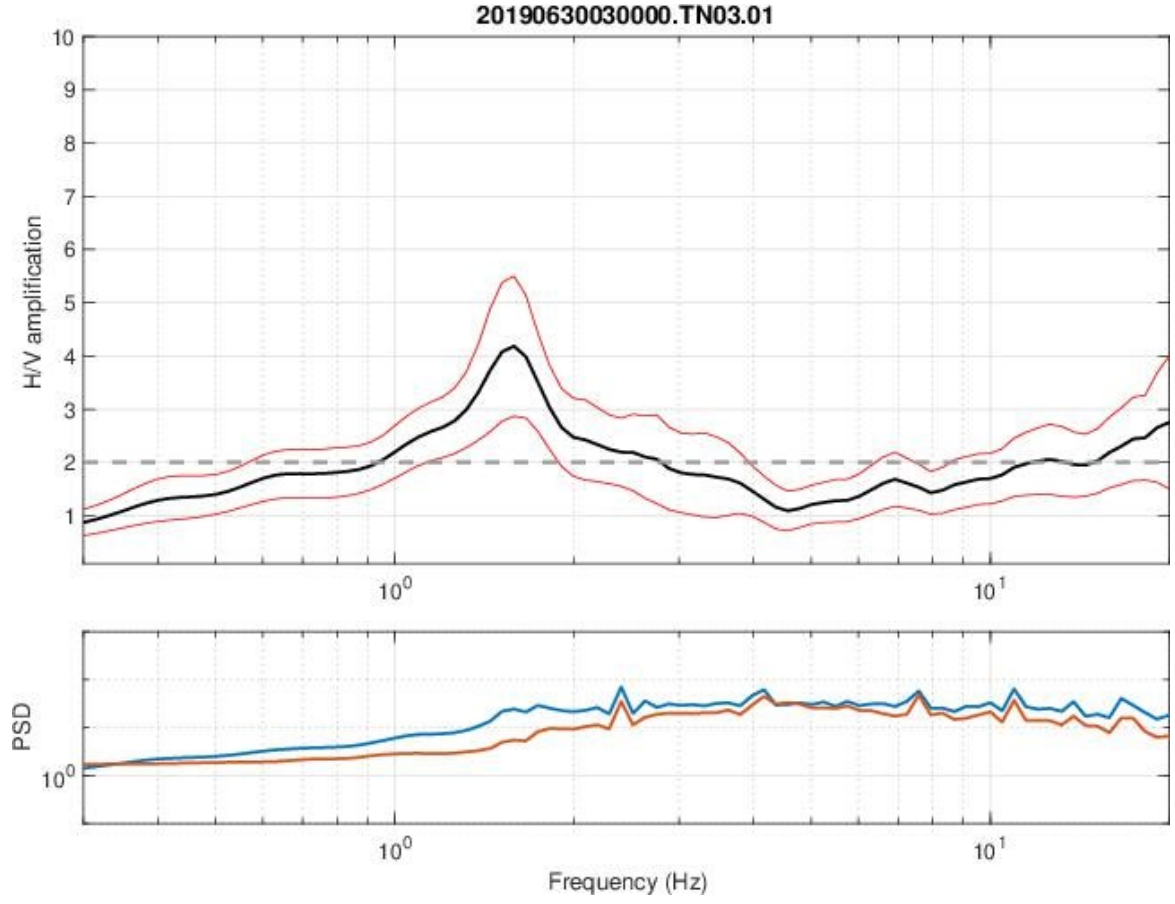

R108
H/V amplification
PSD
Frequency (Hz)

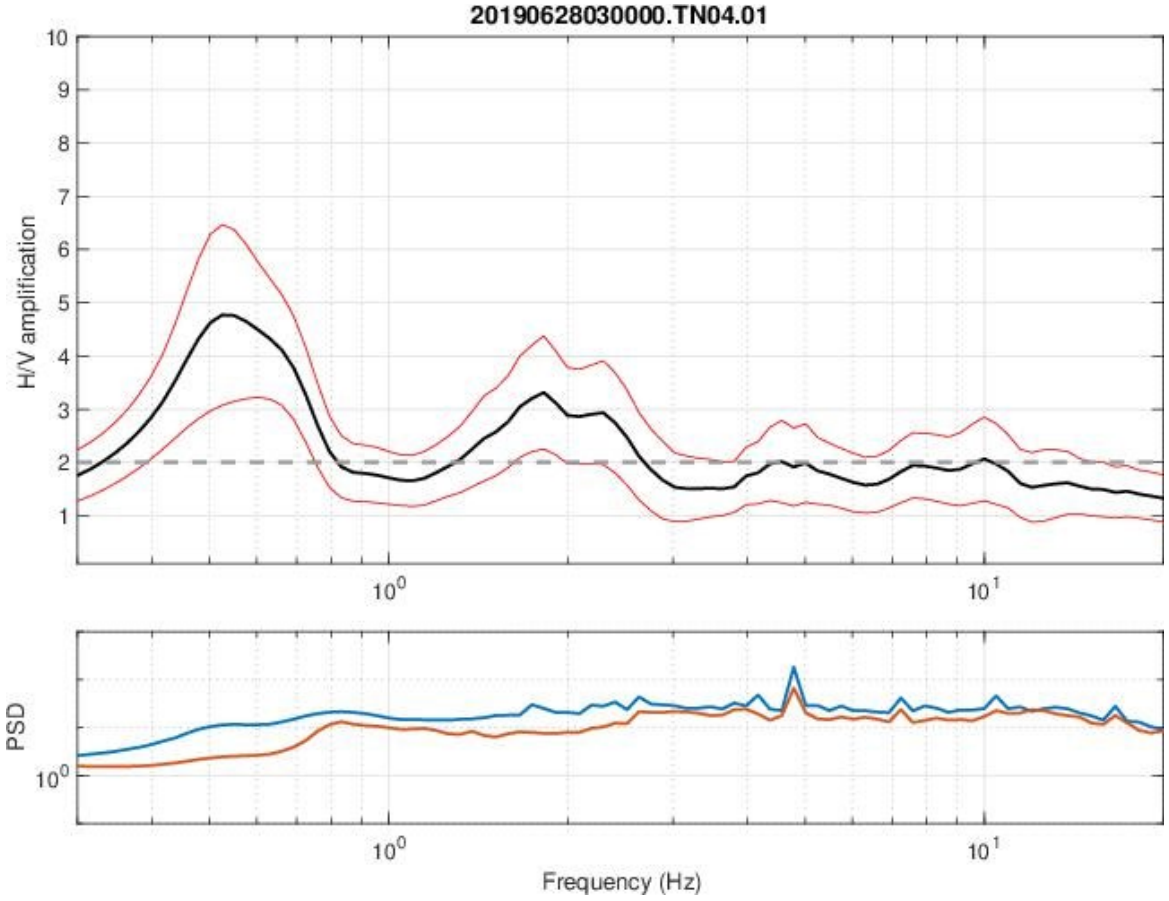

R109
H/V amplification
PSD
Frequency (Hz)

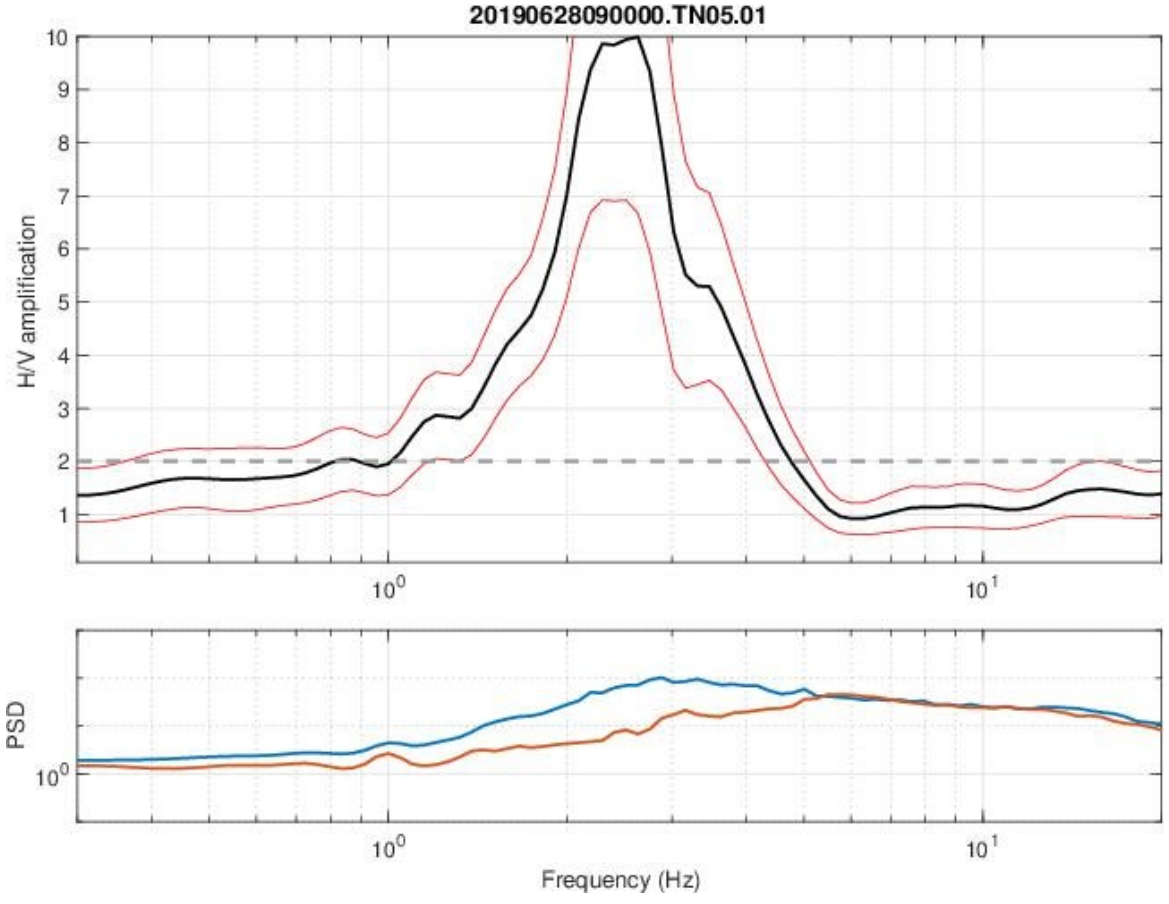

R110
H/V amplification
PSD
Frequency (Hz)

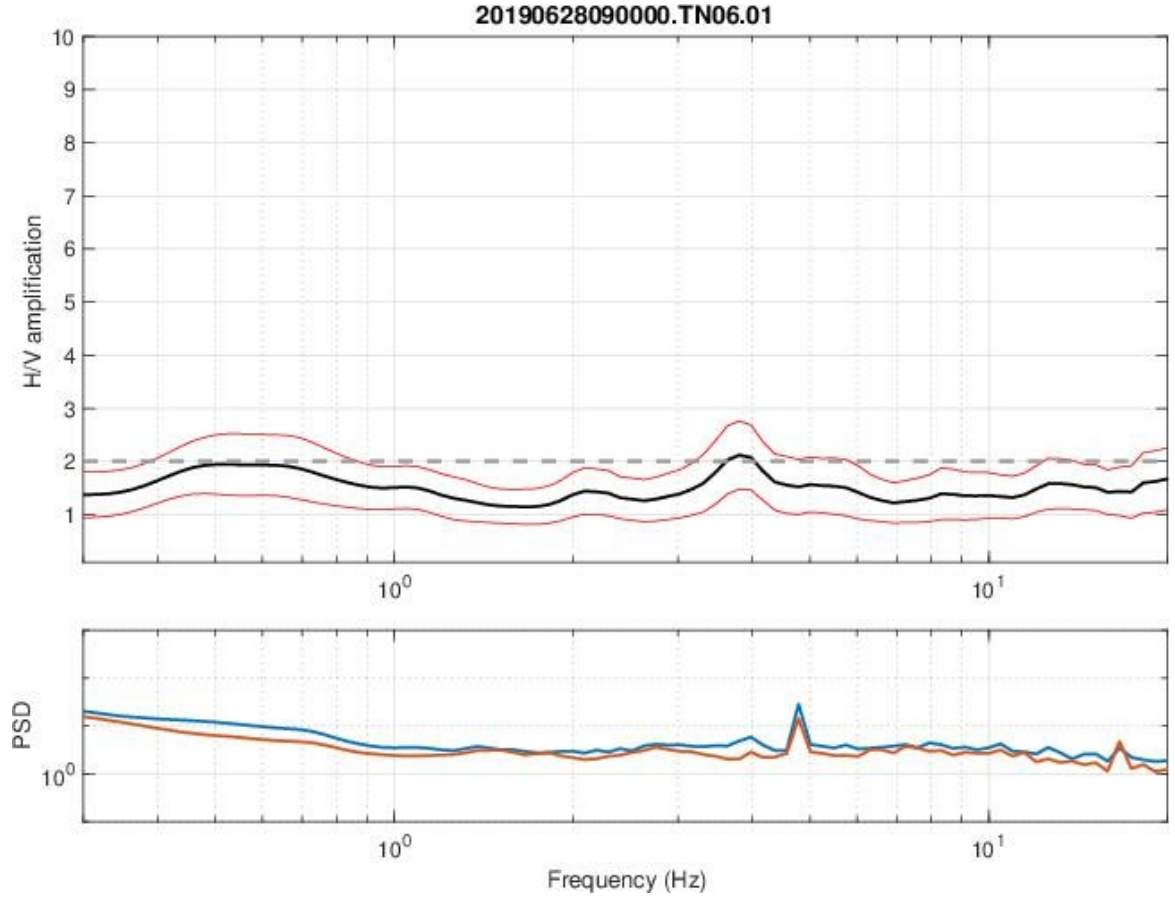

20190628030000.TN01.01
H/V amplification
PSD
Frequency (Hz)

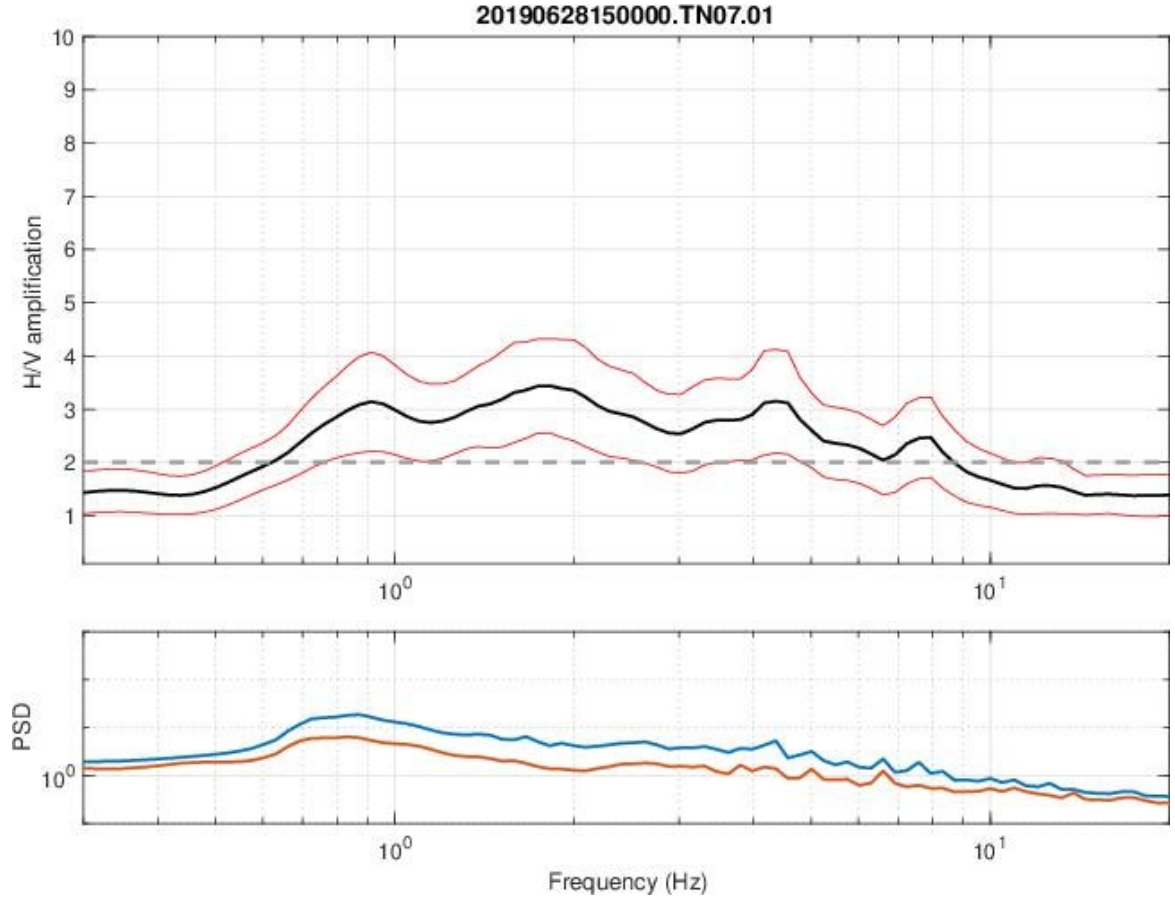

20190628030000.TN02.01
H/V amplification
PSD
Frequency (Hz)

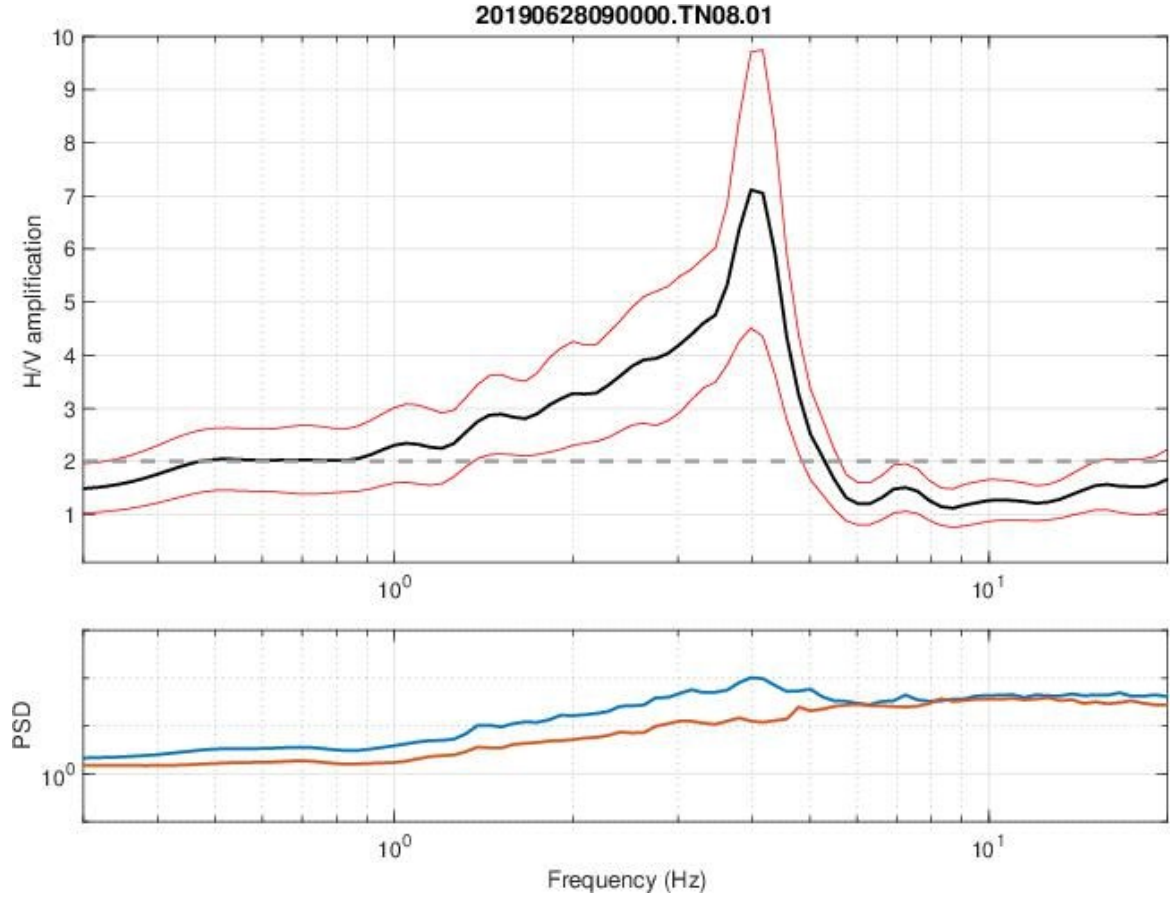

20190630030000.TN03.01
H/V amplification
PSD
Frequency (Hz)

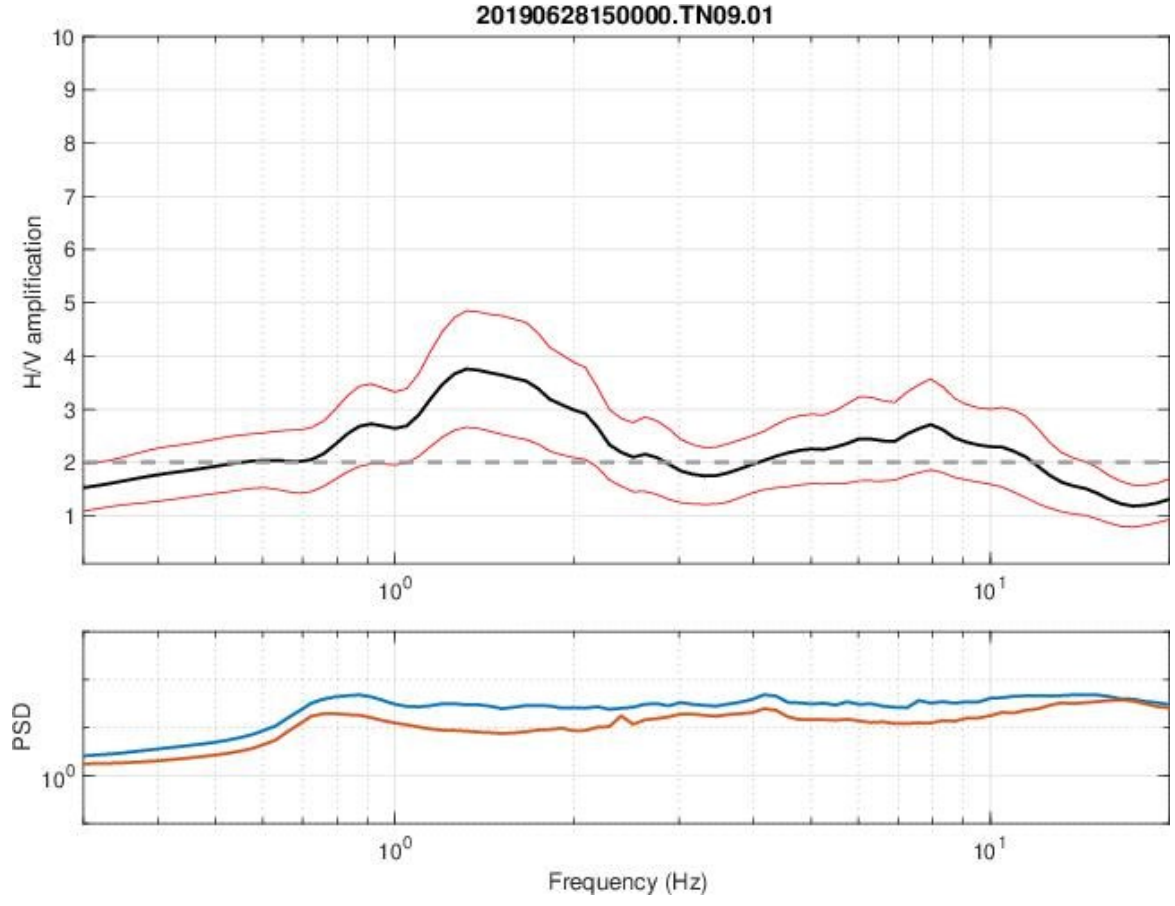

20190628030000.TN04.01
H/V amplification
PSD
Frequency (Hz)

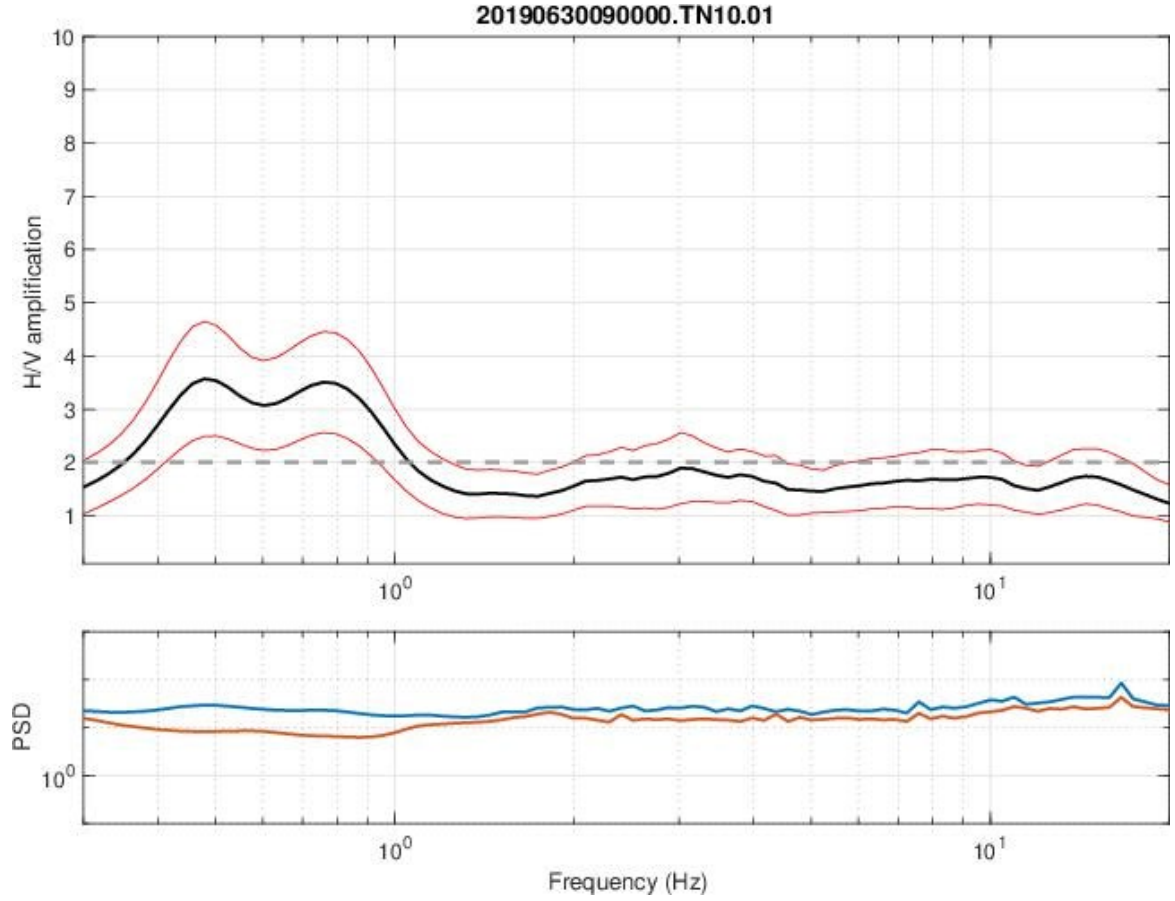

20190628090000.TN05.01
H/V amplification
PSD
Frequency (Hz)

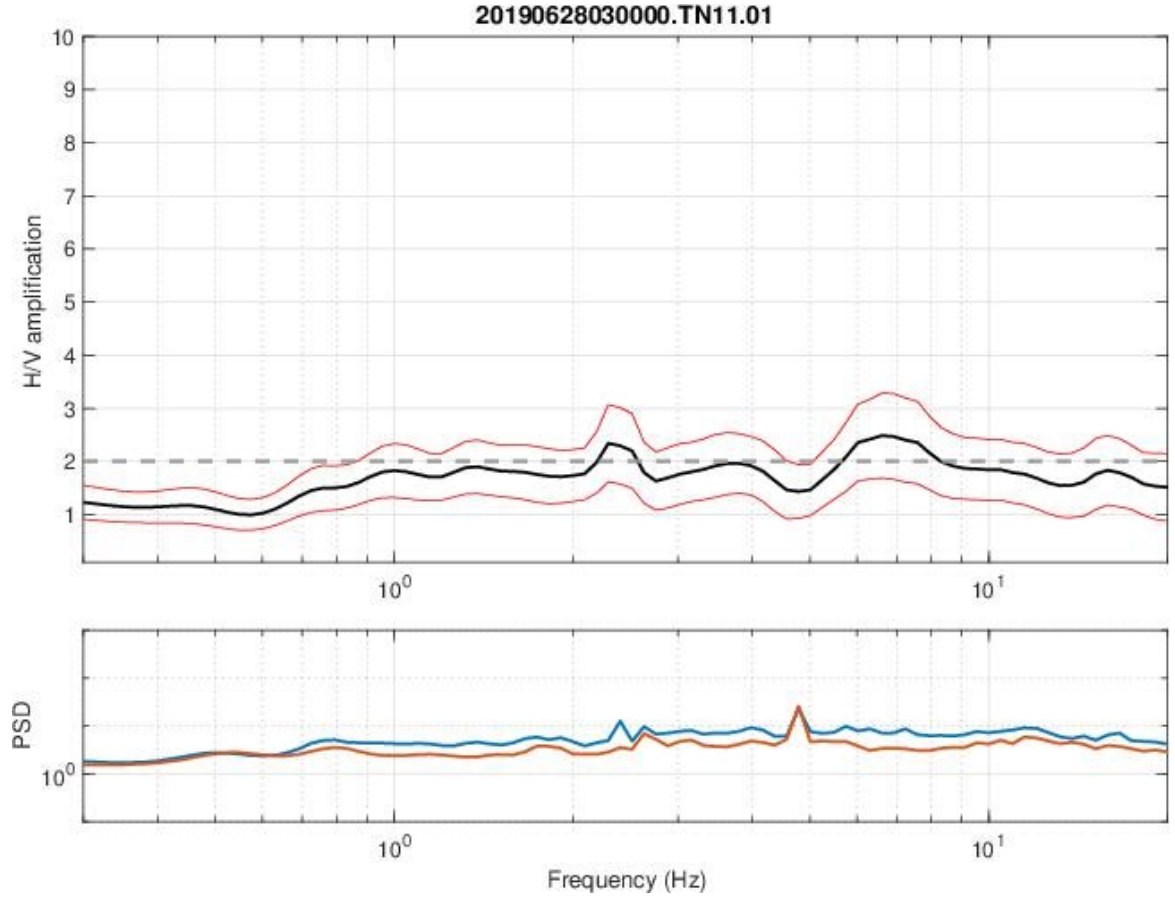

20190628090000.TN06.01
H/V amplification
PSD
Frequency (Hz)

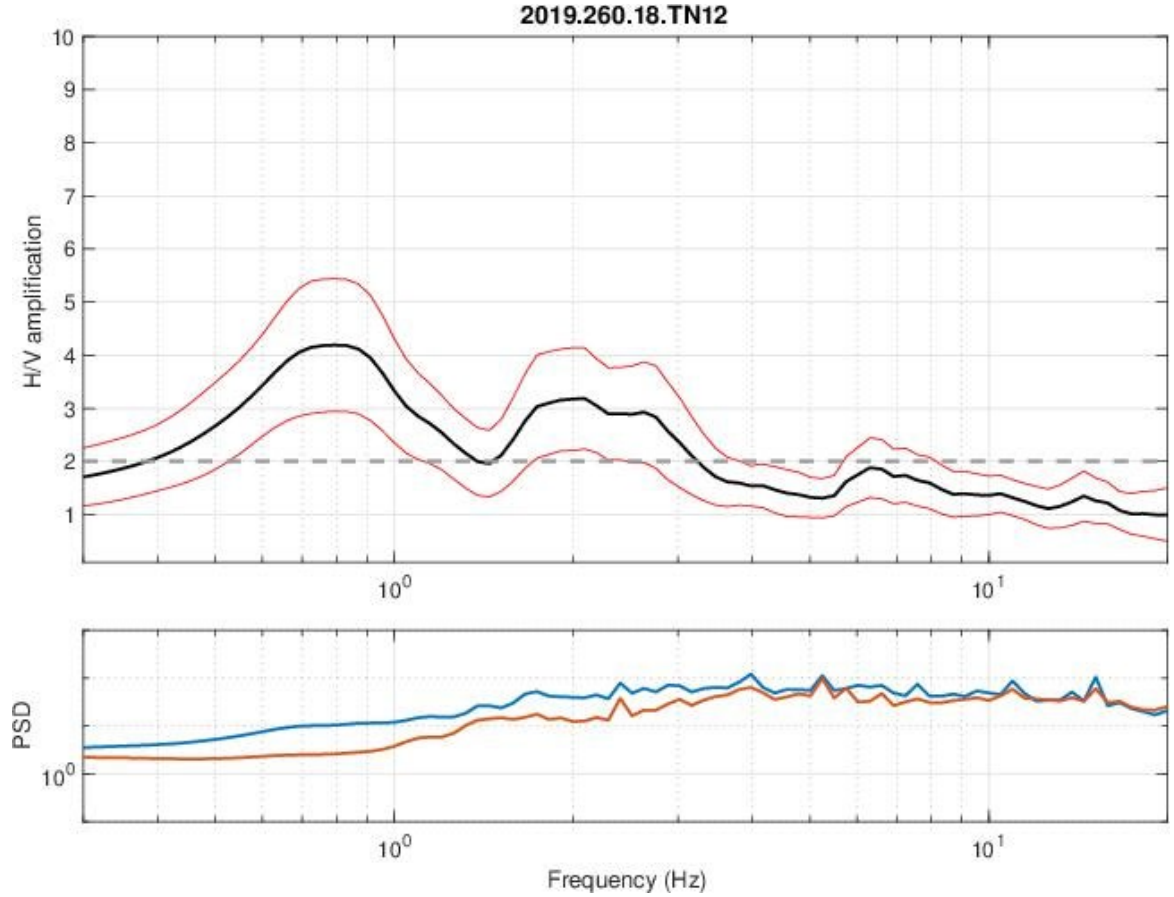

20190628150000.TN07.01
H/V amplification
PSD
Frequency (Hz)

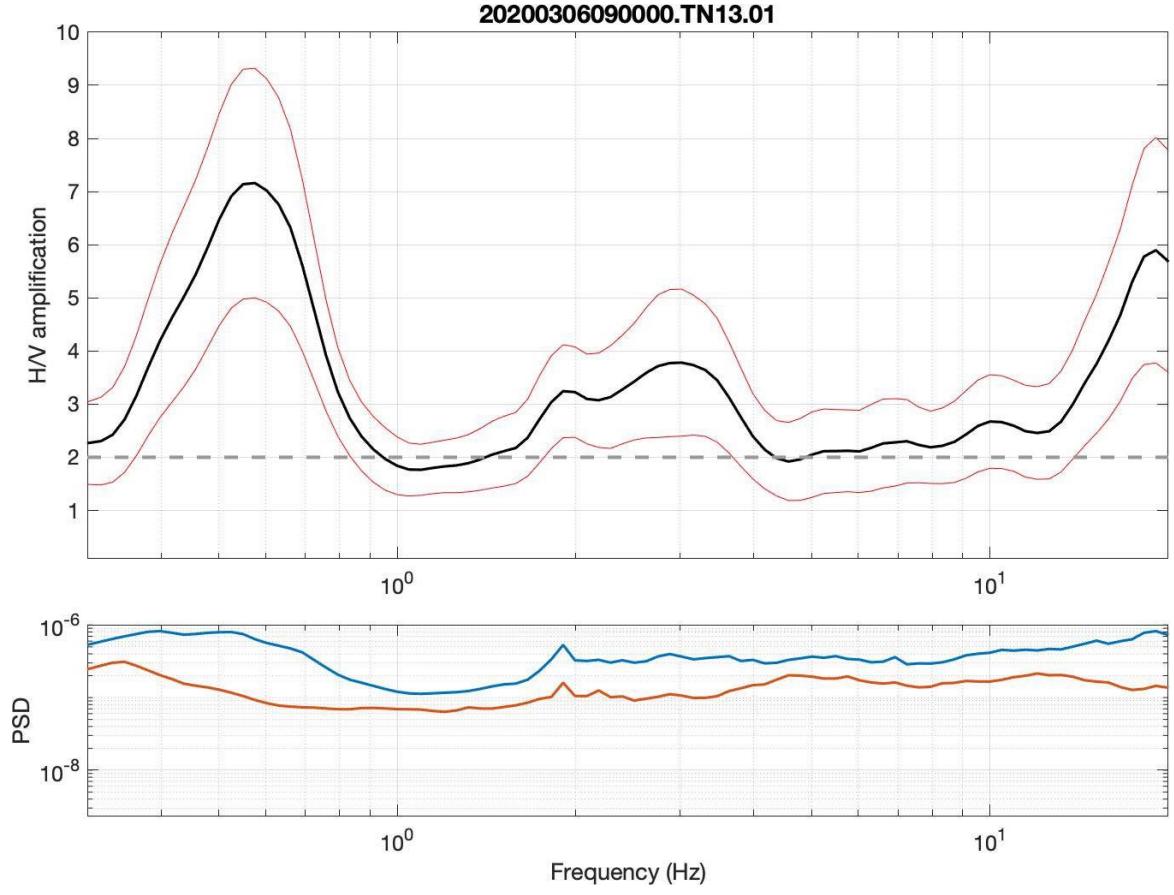

20190628090000.TN08.01
H/V amplification
PSD
Frequency (Hz)

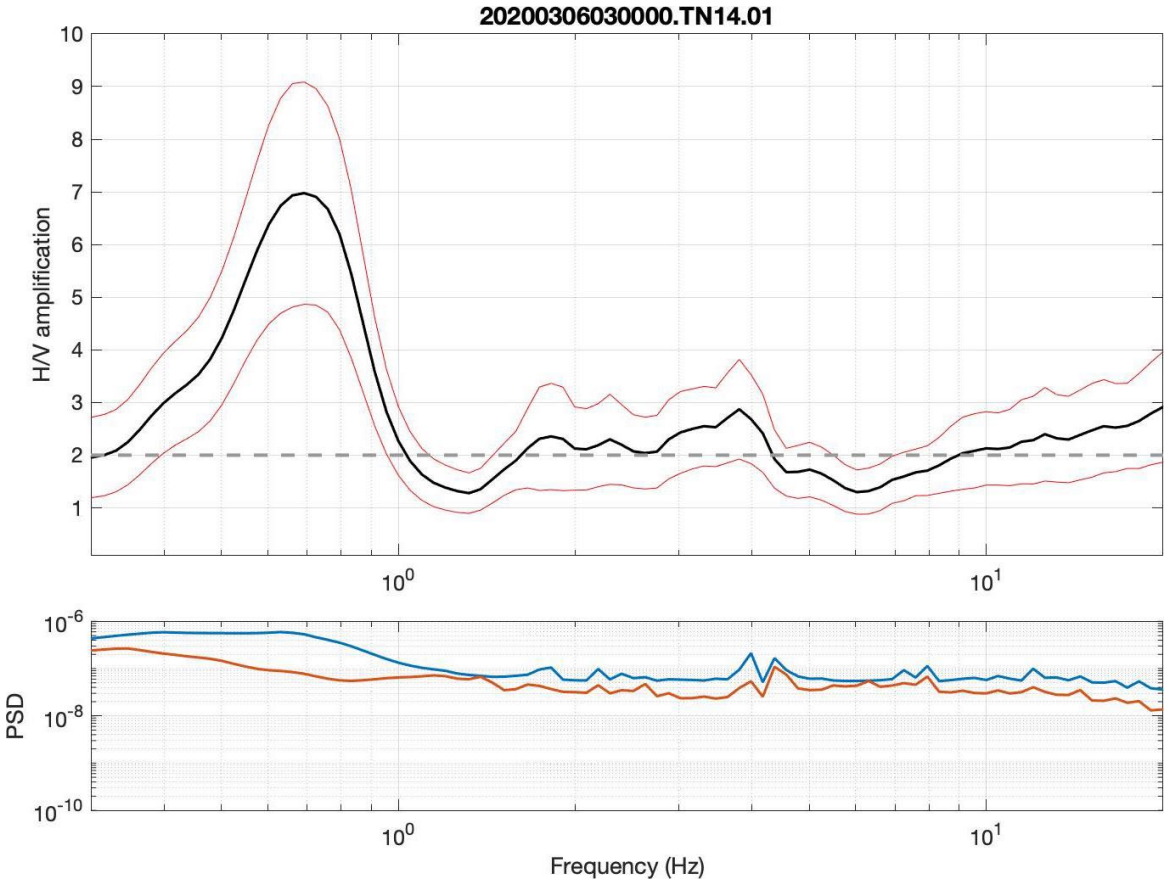

20190628150000.TN09.01
H/V amplification
PSD
Frequency (Hz)

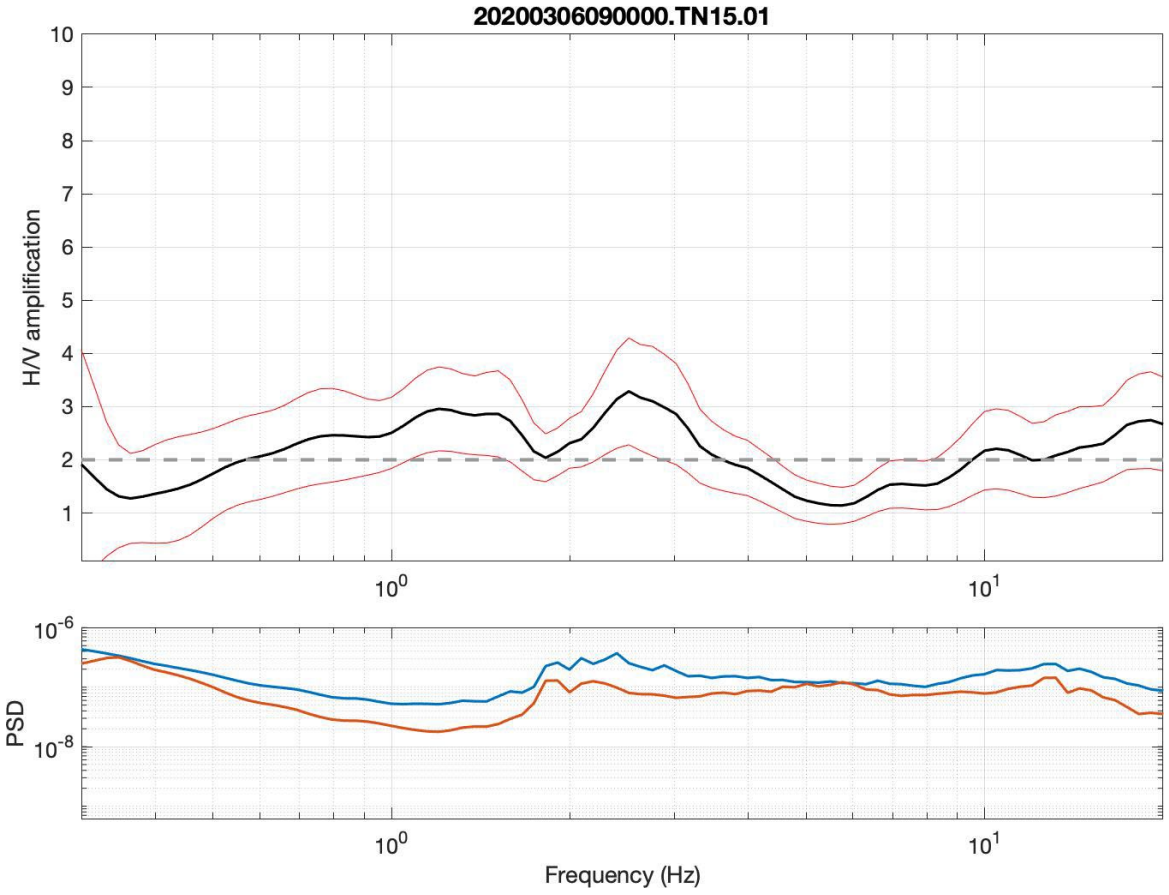

20190630090000.TN10.01
H/V amplification
PSD
Frequency (Hz)

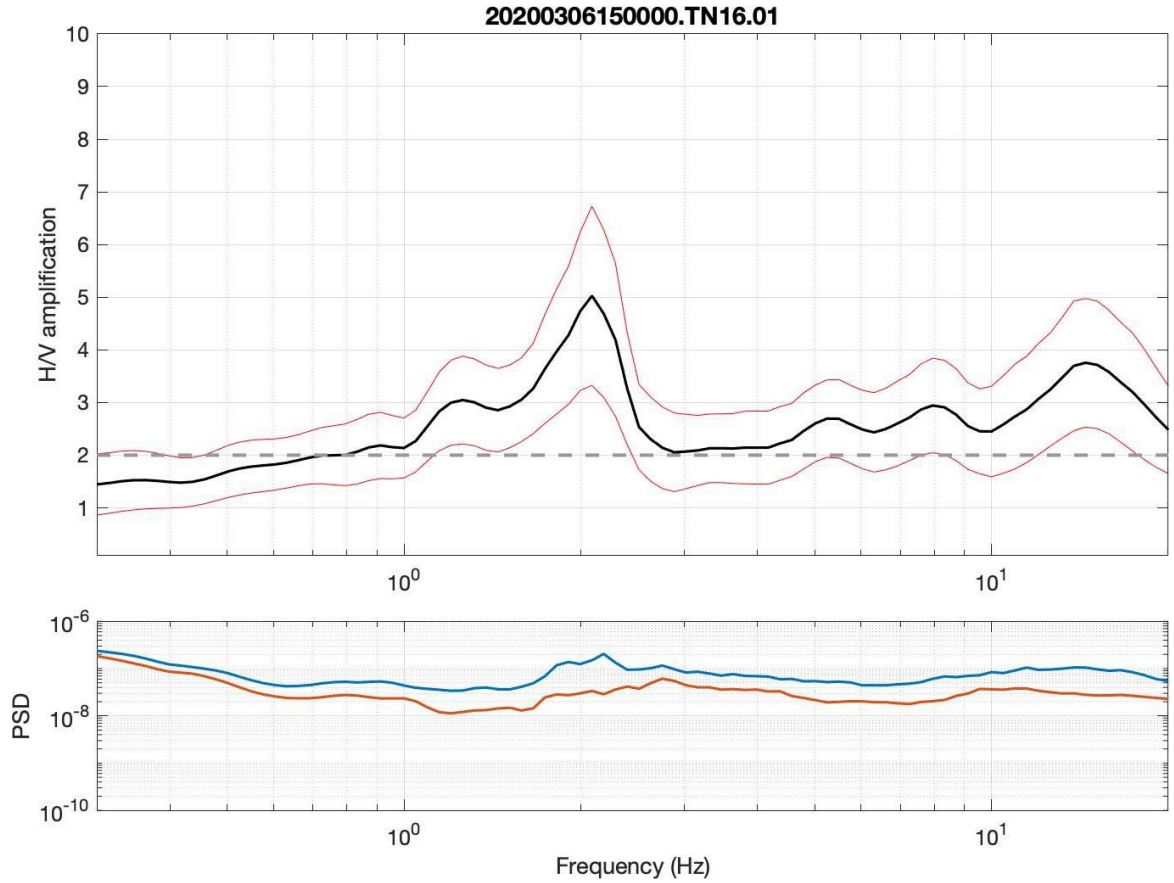

20190628030000.TN11.01
H/V amplification
PSD
Frequency (Hz)

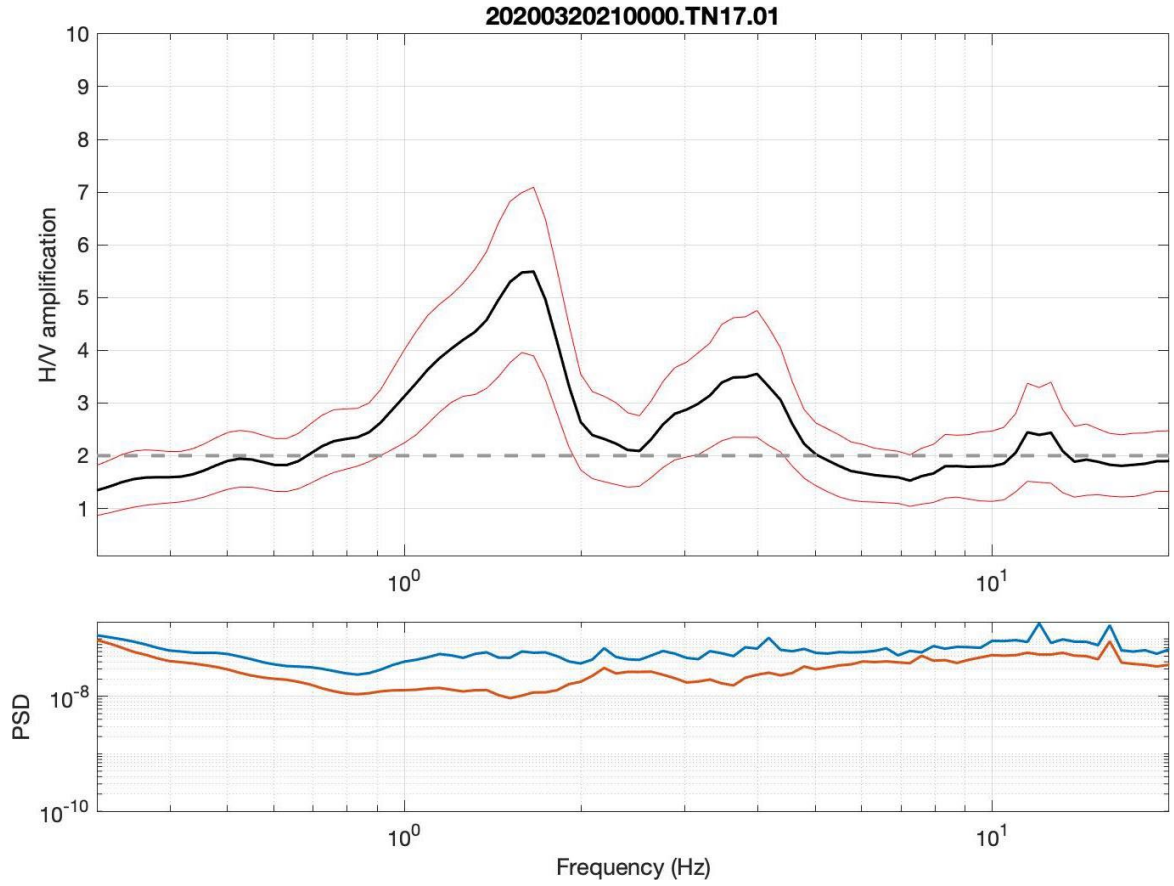

2019.260.18.TN12
H/V amplification
PSD
Frequency (Hz)

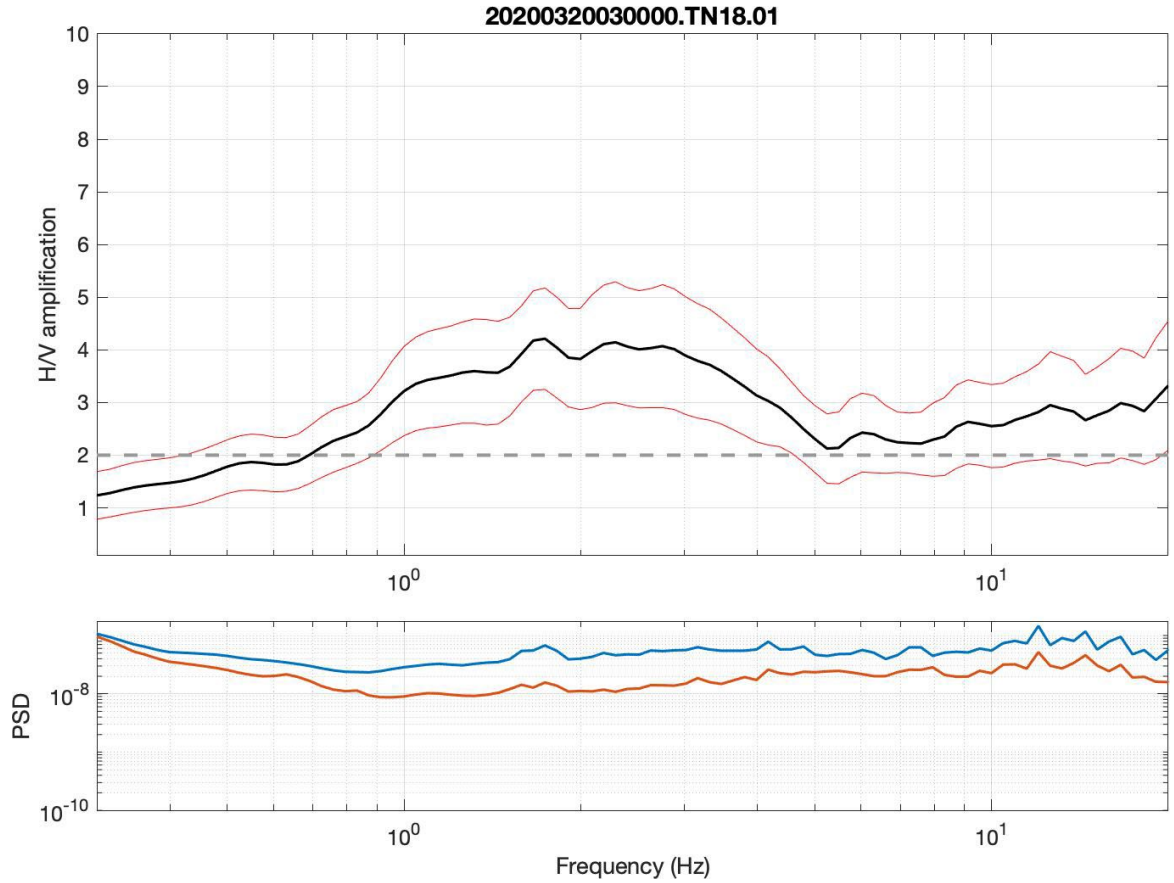

20200306090000.TN13.01
H/V amplification
PSD
Frequency (Hz)

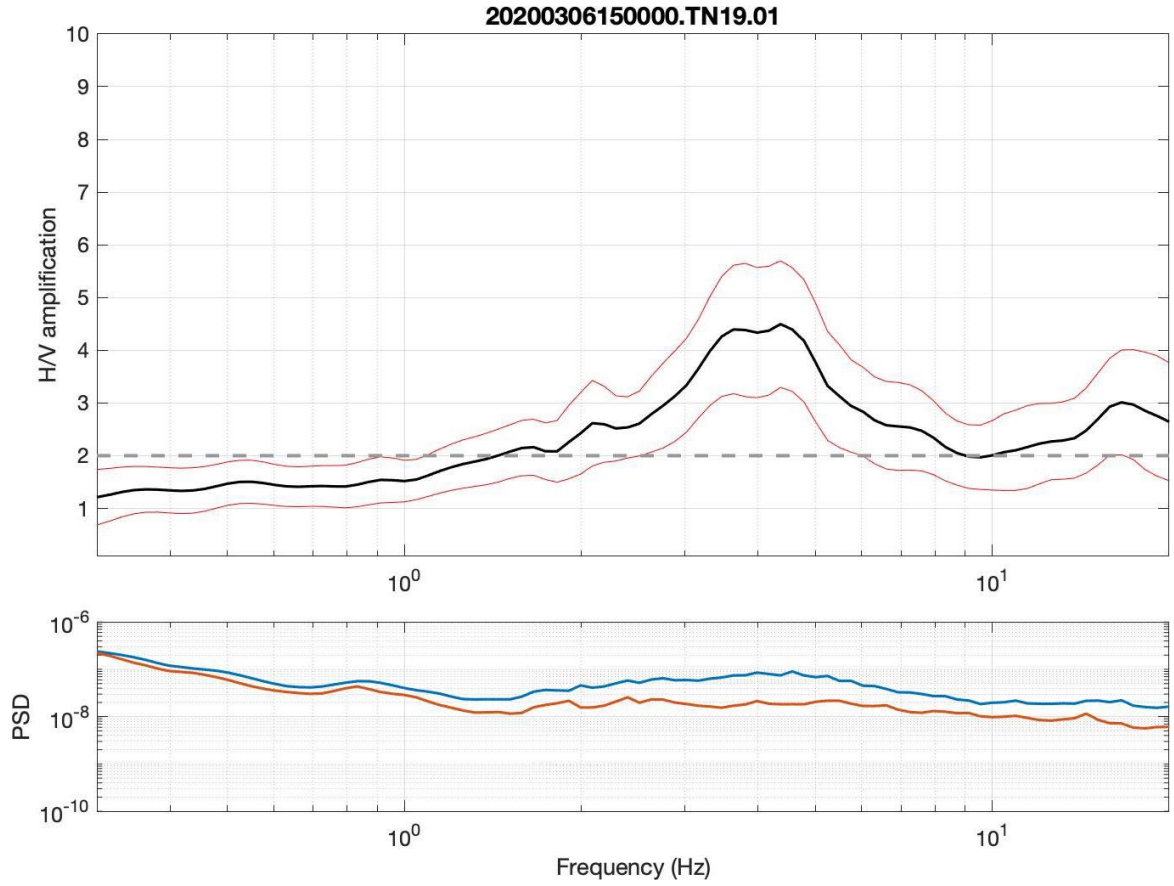

20200306030000.TN14.01
H/V amplification
PSD
Frequency (Hz)

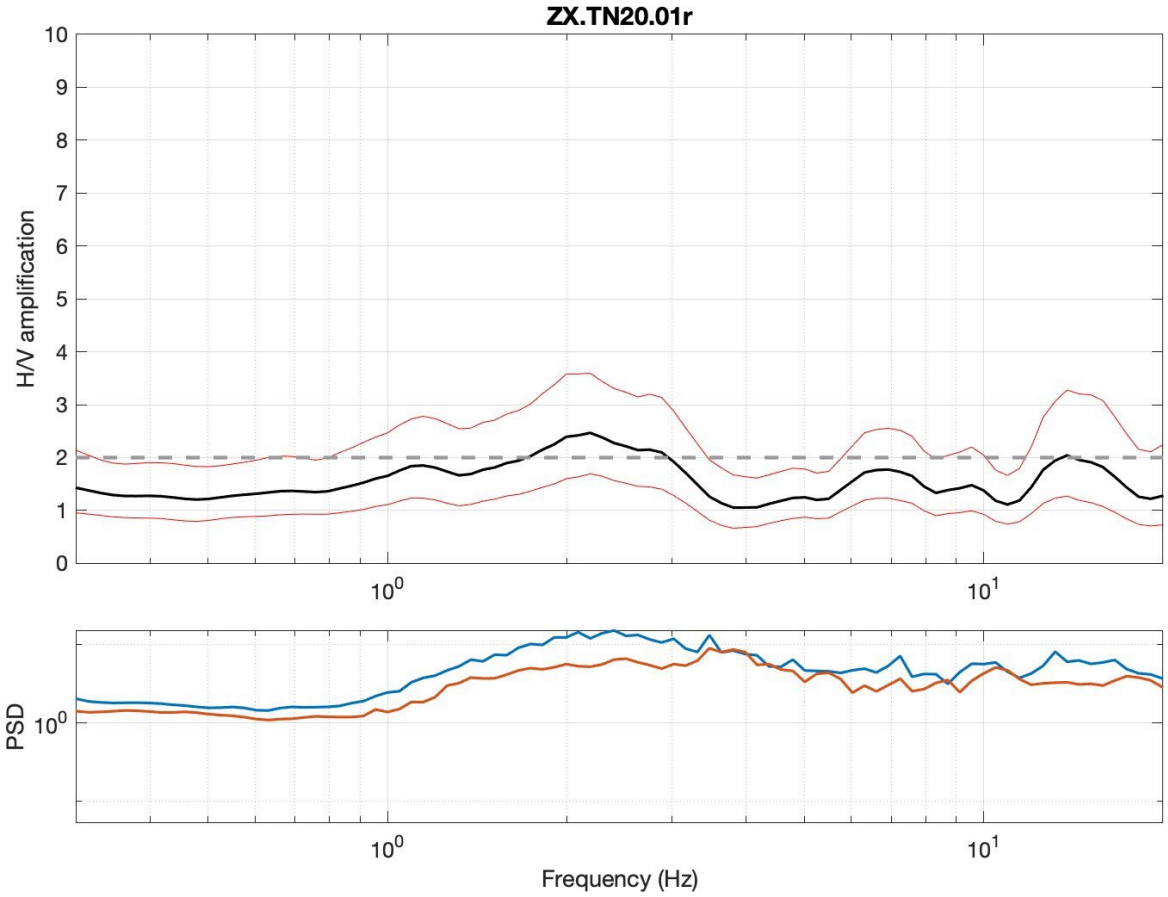

20200306090000.TN15.01
H/V amplification
PSD
Frequency (Hz)


20200306150000.TN16.01
H/V amplification
PSD
Frequency (Hz)


20200320210000.TN17.01
H/V amplification
PSD
Frequency (Hz)


20200320030000.TN18.01
H/V amplification
PSD
Frequency (Hz)


20200306150000.TN19.01
H/V amplification
PSD
Frequency (Hz)


ZX.TN20.01r
H/V amplification
PSD
Frequency (Hz)

REFERENCES

Akcelik, V., Bielak, J., Biros, G., Epanomeritakis, I., Fernandez, A., Ghattas, O., ... & Urbanic, J. (2003, November). High resolution forward and inverse earthquake modeling on terascale computers. In Proceedings of the 2003 ACM/IEEE Conference on Supercomputing (p. 52).

Aki, K. (1988). Local site effect on ground motion. Earthquake Engineering and Soil Dynamics II, 103-155.

Aki, K. (2003). A perspective on the history of strong motion seismology. Physics of the Earth and Planetary Interiors, 137(1-4), 5-11.

Aki, K., & Larner, K. L. (1970). Surface motion of a layered medium having an irregular interface due to incident plane SH waves. Journal of Geophysical Research, 75(5), 933-954.

Amanti, M., Muraro, C., Roma, M., Chiessi, V., Puzzilli, L. M., Catalano, S., ... & Tallini, M. (2020). Geological and geotechnical models definition for 3rd level seismic microzonation studies in Central Italy. Bulletin of Earthquake Engineering, 18, 5441-5473.

Anagnostopoulos, S.A., Kyrkos, M.T., Stathopoulos, K. (2015). Earthquake induced torsion in buildings: critical review and state of the art. Earth Struct. 8 (2), 305–377.

Andrews, D. J. (1986). Objective determination of source parameters and similarity of earthquakes of different sizes. In S. Das, J. Boatwright, & C. H. Scholz (Eds.), Earthquake Source Mechanics (pp. 259–268). American Geophysical Union.

Aoi, S., & Fujiwara, H. (1999). 3D finite-difference method using discontinuous grids. Bulletin of the Seismological Society of America, 89(4), 918-930.

Archuleta, R. J., & Frazier, G. A. (1978). Three-dimensional numerical simulations of dynamic faulting in a half-space. Bulletin of the Seismological Society of America, 68(3), 541-572.

Assimaki, D., Kallivokas, L. F., Kang, J. W., Li, W., & Kucukcoban, S. (2012). Time-domain forward and inverse modeling of lossy soils with frequency-independent Q for near-surface applications. Soil Dynamics and Earthquake Engineering, 43, 139-159.

Bao, H., Bielak, J., Ghattas, O., Kallivokas, L. F., O'Hallaron, D. R., Shewchuk, J. R., & Xu, J. (1998). Large-scale simulation of elastic wave propagation in heterogeneous media on parallel computers. Computer methods in applied mechanics and engineering, 152(1-2), 85-102.

Bard, P. Y. (1982). Diffracted waves and displacement field over two-dimensional elevated topographies. Geophysical Journal International, 71(3), 731-760.

Bard, P. Y., & Bouchon, M. (1985). The two-dimensional resonance of sediment-filled valleys. Bulletin of the Seismological Society of America, 75(2), 519-541.

Bard, P. Y., & Gariel, J. C. (1986). The seismic response of two-dimensional sedimentary deposits with large vertical velocity gradients. Bulletin of the Seismological Society of America, 76(2), 343-366.

Baron, J., Primofiore, I., Klin, P., Vessia, G., & Laurenzano, G. (2022). Investigation of topographic site effects using 3D waveform modelling: amplification, polarization and torsional motions in the case study of Arquata del Tronto (Italy). Bulletin of Earthquake Engineering, 20(2), 677-710.

Basu, U. (2009). Explicit finite element perfectly matched layer for transient three-dimensional elastic waves. International journal for numerical methods in engineering, 77(2), 151-176.

Beskos, D. E. (1987). Boundary element methods in dynamic analysis. Applied Mechanics Reviews, 40(1), 1-23.

Bielak, J., Karaoglu, H., & Taborda, R. (2011). Memory-efficient displacement-based internal friction for wave propagation simulation. Geophysics, 76(6), T131-T145.

Bignardi, S. (2017). The uncertainty of estimating the thickness of soft sediments with the HVSR method: A computational point of view on weak lateral variations. Journal of Applied Geophysics, 145, 28-38.

Bolt, B. A. (1969). Duration of strong motion. In Proceedings of the 4th World Conference on Earthquake Engineering (pp. 1304-1315). Santiago, Chile.

Borcherdt, R. D. (1970). Effects of local geology on ground motion near San Francisco Bay. Bulletin of the Seismological Society of America, 60, 29–61.

Boschi, E., Caserta, A., Conti, C., Di Bona, M., Funiciello, R., Malagnini, L., ... & Salvi, S. (1995). Resonance of subsurface sediments: An unforeseen complication for designers of Roman columns. Bulletin of the Seismological Society of America, 85(1), 320-324.

Boschi, E., Guidoboni, E., Ferrari, G., Mariotti, D., Valensise, G., & Gasperini, P. (2000). Catalogue of Strong Italian Earthquakes from 461 BC to 1997 (Appendix to volume 43 N 4, 2000). Annals of Geophysics, 43(4).

Bouchon, M. (1981). A simple method to calculate Green's functions for elastic layered media. Bulletin of the Seismological Society of America, 71(4), 959-971.

Brambati, A., Faccioli, E., Carulli, G. B., Cucchi, F., Onofri, R., Stefanini, S., & Ulcigrai, F. (1980). Studio di microzonazione sismica dell'area di Tarcento (Friuli). CLUET, Trieste (in Italian).

Brogiolo, G. P. (Ed.). (2013). Paesaggi storici del Sommolago. SAP - Società Archeologica.

Burjánek, J., Edwards, B., & Fäh, D. (2014). Empirical evidence of local seismic effects at sites with pronounced topography: a systematic approach. Geophysical Journal International, 197(1), 608-619.

Calcagno, P., Chilès, J. P., Courrioux, G., & Guillen, A. (2008). Geological modelling from field data and geological knowledge. Part I. Modelling method coupling 3D potential-field interpolation and geological rules. Physics of the Earth and Planetary Interiors, 171(1–4), 147–157.

Casadei, F., Gabellini, E., Fotia, G., Maggio, F., & Quarteroni, A. (2002). A mortar spectral/finite element method for complex 2D and 3D elastodynamic problems. Computer Methods in Applied Mechanics and Engineering, 191(45), 5119-5148.

Castellani, A., Stupazzini, M., & Guidotti, R. (2012). Free field rotations during earthquakes: Relevance on buildings. Earthquake Engineering & Structural Dynamics, 41(5), 875-891.

Castellarin, A., & Cantelli, L. (2000). Neo-Alpine evolution of the Southern Eastern Alps. Journal of Geodynamics, 30, 251–274.

Castellarin, A., Picotti, V., Cantelli, L., Claps, M., Trombetta, L., Selli, L., Carton, A., Borsato, A., Daminato, F., Nardin, M., Santuliana, E., Veronesi, L., & Bollettinari, G. (2005). Note illustrative della carta geologica d'Italia, Foglio n. 80, Riva del Garda.

Castellarin, A., Vai, G. B., & Cantelli, L. (2006). The Alpine evolution of the Southern Alps around the Giudicarie faults: A Late Cretaceous to Early Eocene transfer zone. Tectonophysics, 414, 203–223.

Castro, R. R., Anderson, J. G., & Singh, S. K. (1990). Site response, attenuation and source spectra of S waves along the Guerrero, Mexico, subduction zone. Bulletin of the Seismological Society of America, 80 (6A), 1481-1503.

Celebi, M. (1996). Successful performance of a base-isolated hospital building during the 17 January 1994 Northridge earthquake. The Structural Design of Tall Buildings, 5(2), 95-109.

Celebi, M., Prince, J., Dietel, C., Onate, M., & Chavez, G. (1987). The culprit in Mexico City—amplification of motions. Earthquake Spectra, 3(2), 315-328.

Centamore, E., Adamoli, L., Berti, D., Bigi, G., Bigi, S., Casnedi, R., ... & Salvucci, R. (1992). Carta geologica dei bacini della Laga e del Cellino e dei rilievi carbonatici circostanti (Marche meridionali, Lazio nord-orientale, Abruzzo settentrionale). Studi Geologici Camerti, Vol. Spec. 1991/2

Corubolo, P., Poletto, F., Farina, B., Meneghini, F., Petronio, L., Maffione, S., Barbagallo A. (2013). Rilevo VSP Pozzo Arco 1 Rapporto finale. Delibera della Giunta Provinciale n. 2822 del 23 dicembre 2011. Rel. OGS no. 2013/13 Sez. GEO 3

Crespellani, T., & Facciorusso, J. (2010). Dinamica dei terreni per le applicazioni sismiche. Dario Flaccovio Editore.

Cundall, P. A. (2006). A simple hysteretic damping formulation for dynamic continuum simulations. In P. Varona & R. Hart (Eds.), FLAC and Numerical Modeling in Geomechanics—2006, Proceedings of the 4th International FLAC Symposium (pp. 355–362). Itasca.

D'Amico V, Picozzi M, Baliva F, Albarello D (2008) Ambient noise measurements for preliminary site-effects characterisation in the urban area of Florence. Bull Seismol Soc Am 98(3):1373–1388.

Delgado J, López CasadoC,Estévez A,Giner J, Cuenca A, Molina S (2000a) Mapping soft soils in the Segura river walley (SE Spain): a case study of microtremors as an exploration tool. J Appl Geophys 45:19–32.

Diagourtas, D., Tzanis, A., & Makropoulos, K. (2002). Comparative study of microtremor analysis methods. Earthquake Microzoning, 2463-2479.

DISS Working Group (2021). Database of Individual Seismogenic Sources (DISS), Version 3.3.0: A compilation of potential sources for earthquakes larger than M 5.5 in Italy and surrounding areas. Istituto Nazionale di Geofisica e Vulcanologia (INGV). https://doi.org/10.13127/diss3.3.0

Dobry, R., Oweis, I., & Urzua, A. (1976). Simplified procedures for estimating the fundamental period of a soil profile. Bulletin of the Seismological Society of America, 66(4), 1293-1321.

Evans, J. R., & International Working Group on Rotational Seismology. (2009). Suggested notation conventions for rotational seismology. Bulletin of the Seismological Society of America, 99(2), 1073-1075.

Faccioli, E., & Vanini, M. (2003). Complex seismic site effects in sediment-filled valleys and implications on design spectra. Progress in Structural Engineering and Materials, 5(4), 223-238.

Faccioli, E., Maggio, F., Paolucci, R., & Quarteroni, A. (1997). 2D and 3D elastic wave propagation by a pseudo-spectral domain decomposition method. Journal of Seismology, 1(3), 237-251.

Fairchild, G.M., Lane, J.W., Voytek, E.B., & LeBlanc, D.R. (2013). Bedrock topography of western Cape Cod, Massachusetts, based on bedrock altitudes from geologic borings and analysis of ambient seismic noise by the horizontal-to-vertical spectral-ratio method, U.S. Geological Survey Scientific Investigations Map 3233, 1 sheet, maps variously scaled, p 17. Pamphlet, on one CD–ROM

Felber, M., Veronese, L., Cocco, S., Frei, W., Nardin, M., Oppizzi, P., Santuliana, E., & Violanti, D. (1998). Indagini sismiche e geognostiche nelle valli del Trentino meridionale (Val d'Adige, Valsugana, Valle del Sarca, Valle del Chiese), Italia. Studi Trentini di Scienze Naturali - Acta Geologica, 75, 3–52.

Feldman, L., & Shapira, A. (1994). Analysis of seismic intensities observed in Israel. Natural Hazards, 9(3), 287-301.

Ferrari, G. (2006). Note on the historical rotation seismographs. In Teisseyre, R., Majewski, E., & Takeo, M. (Eds.), Earthquake Source Asymmetry, Structural Media and Rotation Effects (pp. 545-554). Springer, Berlin, Heidelberg.

Fishman, K. L., & Ahmad, S. (1995). Seismic response for alluvial valleys subjected to SH, P, and SV waves. Soil Dynamics and Earthquake Engineering, 14(4), 249-258.

Frankel, A., & Vidale, J. (1992). A three-dimensional simulation of seismic waves in the Santa Clara Valley, California, from a Loma Prieta aftershock. Bulletin of the Seismological Society of America, 82(5), 2045-2074.

Fuganti, A. (2008). Valutazioni geologiche ed idrogeologiche sulle caratteristiche e sull'origine dell'acqua minerale naturale fonte Linfano. Permesso di ricerca per

acqua minerale denominato “Linfano” nel comune di Arco (Trento). Provincia Autonoma di Trento.

Furumura, T., & Koketsu, K. (2000). Parallel 3-D simulation of ground motion for the 1995 Kobe earthquake: The component decomposition approach. Pure and Applied Geophysics, 157(11-12), 2047-2062.

Galli, P., Peronace, E., & Tertulliani, A. (2016). Rapporto sugli effetti macrosismici del terremoto del 24 Agosto 2016 di Amatrice in scala MCS.

Garbin, M., Priolo, E., Bragato, P. L., Fabris, P., Zuliani, D., Rossi, G., & Urban, S. (2018, April 5). Accordo di programma per la realizzazione del progetto “Studio riguardante il monitoraggio sismico e l’elaborazione di dati GPS”. Relazione 2018/23 Sez. CRS 8. Istituto Nazionale di Oceanografia e di Geofisica Sperimentale – OGS, Udine.

Garcia-Jerez A, Luzon F, Navarro M, Perez-Ruiz A (2006) Characterization of the sedimentary cover of the Zafarraya basin, southern Spain, by means of ambient noise. Bull Seismol Soc Am 96(3):957–967.

Gazdag, J. (1981). Modeling of the acoustic wave equation with transform methods. Geophysics, 46(6), 854-859.

Geli, L., Bard, P. Y., & Jullien, B. (1988). The effect of topography on earthquake ground motion: a review and new results. Bulletin of the Seismological Society of America, 78(1), 42-63.

Ghayamghamian, M. R., & Motosaka, M. (2003). The effects of torsion and motion coupling in site response estimation. Earthquake Engineering & Structural Dynamics, 32(5), 691-709.

Ghofrani, H., & Atkinson, G. M. (2015). Duration of the 2011 Tohoku earthquake ground motions. Journal of Seismology, 19, 9-25.

Gosar, A., & Lenart, A. (2010). Mapping the thickness of sediments in the Ljubljana Moor basin (Slovenia) using microtremors. Bulletin of Earthquake Engineering, 8(3), 501-518.

Graziani, L., Del Mese, S., Tertulliani, A., Arcoraci, L., Maramai, A., & Rossi, A. (2019). Investigation on damage progression during the 2016–2017 seismic sequence in Central Italy using the European Macroseismic Scale (EMS-98). Bulletin of Earthquake Engineering, 17, 5535-5558.

Guidoboni, E., & Comastri, A. (2005). Catalogue of Earthquakes and Tsunamis in the Mediterranean Area from the 11th to the 15th Century, Istituto Nazionale di Geofisica e Vulcanologia—Storia Geofisica Ambiente (INGV-SGA), Bologna, 1037 pp.

Guidoboni, E., Ferrari, G., Mariotti, D., Comastri, A., Tarabusi, G., Sgattoni, G., & Valensise, G. (2018). CFTI5Med, Catalogo dei Forti Terremoti in Italia (461 a.C.-1997) e nell'area Mediterranea (760 a.C.-1500). Istituto Nazionale di Geofisica e Vulcanologia (INGV). https://doi.org/10.6092/ingv.it-cfti5

Guidotti, R., Castellani, A., & Stupazzini, M. (2018). Near-field earthquake strong ground motion rotations and their relevance on tall buildings. Bulletin of the Seismological Society of America, 108, 1171-1184.

Guillen, A., Lane, R., Courrioux, G., Lees, T., Calcagno, P., & McInerney, P. (2004). Constrained gravity 3D litho-inversion applied to Broken Hill. ASEG Extended Abstracts.

Gutenberg, B. (1927). Grundlagen der Erdlebenkunde, Berlin.

Haghshenas, E., Bard, P. Y., Theodulidis, N., & Sesame WP04 Team. (2008). Empirical evaluation of microtremor H/V spectral ratio. Bulletin of Earthquake Engineering, 6(1), 75–108.

Hardin, B. O., & Drnevich, V. P. (1972). Shear modulus and damping in soils: Measurement and parameter effects. Journal of Soil Mechanics and Foundations Divisions, 9(2), 603-624.

He, J., Qi, S., Wang, Y., & Saroglou, C. (2020). Seismic response of the Lengzhuguan slope caused by topographic and geological effects. Engineering Geology, 265, 105431.

Hinzen KG, Scherbaum F, Weber B (2004) On the resolution of H/V measurements to determine sediment thickness, a case study across a normal fault in the lower Rhine embayment, Germany. J Earthq Eng 8(6):909–926.

Hisada, Y., Bao, H., Bielak, J., Ghattas, O., & O'Hallaron, D. (1998). Simulations of long-period ground motions during the 1995 Hyogoken-Nanbu (Kobe) earthquake using 3D finite element method. In 2nd International Symposium on Effect of Surface Geology on Seismic Motion, Special Volume on Simultaneous Simulation for Kobe (pp. 59-66).

Housner, G. W. (1952). Spectrum intensities of strong motion earthquakes. In Proceedings of the symposium on earthquake and blast effects on structures (pp. 20-36). Oakland California: EERI.

Housner, G. W. (1959). Behavior of structures during earthquakes. Journal of the Engineering Mechanics Division, ASCE, 85(EM14), 109-129.

Huang, D., Sun, P., Jin, F., & Du, C. (2021). Topographic amplification of ground motions incorporating uncertainty in subsurface soils with extensive geological borehole data. Soil Dynamics and Earthquake Engineering, 141, 106441.

Ibs-von Seht, M., & Wohlenberg, J. (1999). Microtremor measurements used to map thickness of soft sediments. Bulletin of the Seismological Society of America, 89(1), 250-259.

Idriss, I. M., & Seed, H. B. (1968). An analysis of ground motions during the 1957 San Francisco earthquake. Bulletin of the Seismological Society of America, 58(6), 2013-2032.

Igel, H., Bernauer, F., & Schreiber, U. (2015). Rotational seismology: Theory, instrumentation, observations, and applications. In: Schubert, G. (Ed.), Treatise on Geophysics, Vol. 1 (pp. 593-613), Elsevier.

Irikura, K., Kameda, H., & Kudo, K. (1997). Preface: Special issue on the Hyogoken-nanbu earthquake of 1995. Earthquake Engineering & Structural Dynamics, 26(6), 567-570.

ISPRA. (2017). Relazione illustrativa dello studio di microzonazione sismica propedeutico al livello 3 della Macroarea 1 Arquata del Tronto e Montegallo (AP) e allegati. Rapporto inedito per il Dipartimento della Protezione Civile, Roma.

ITHACA Working Group (2019). ITHACA (ITaly HAzards from CApable faults) - Catalogue of capable faults in Italy. http://sgi.isprambiente.it/ithacaweb/viewer/, Istituto Superiore per la Protezione e la Ricerca Ambientale.

Ivanović, S. S., Neilson, R. D., & O'Connor, A. J. (2000). Rotational spectrum technique in site amplification estimation. Bulletin of the Seismological Society of America, 90(4), 964-976.

Jiang, Q., Wei, W., Xu, H., & Dong, T. (2023). A novel seismic topographic effect prediction method based on neural network models. The European Physical Journal Plus, 138(11), 1032.

Johnson, C., & Lane, J. (2016, March). Statistical comparison of methods for estimating sediment thickness from horizontal-to-vertical spectral ratio (HVSR) seismic methods: An example from Tylerville, Connecticut, USA. In Symposium on the Application of Geophysics to Engineering and Environmental Problems 2015 (pp. 317-323). Society of Exploration Geophysicists and Environment and Engineering Geophysical Society.

Kallivokas, L. F., & Assimaki, D. (2006). A robust multiscale domain reduction approach for scalar wave equations. Soil Dynamics and Earthquake Engineering, 26(1), 39-55.

Käser, M., & Dumbser, M. (2006). An arbitrary high-order discontinuous Galerkin method for elastic waves on unstructured meshes—I. The two-dimensional isotropic case with external source terms. Geophysical Journal International, 166(2), 855-877.

Kausel, E. (1974). Forced vibrations of circular foundations on layered media. Research Report R74-11, Massachusetts Institute of Technology, Cambridge, Massachusetts.

Kawase, H., and K. Aki (1990), Topography effect at the critical SV-wave incidence: Possible explanation of damage pattern by the Whittier Narrows, California, earthquake of 1 October 1987. Bull. Seismol. Soc. Am. 80, 1, 1-22.

Kjartansson, E. (1979). Constant Q-wave propagation and attenuation. Journal of Geophysical Research: Solid Earth, 84(B9), 4737-4748.

Komatitsch, D., & Tromp, J. (1999). Introduction to the spectral element method for three-dimensional seismic wave propagation. Geophysical Journal International, 136(3), 536–556.

Komatitsch, D., & Tromp, J. (2002). Spectral-element simulations of global seismic wave propagation – I. Validation. Geophysical Journal International, 149(2), 390–412. https://doi.org/10.1046/j.1365-246X.2002.01653.x

Komatitsch, D., & Vilotte, J. P. (1998). The spectral element method: An efficient tool to simulate the seismic response of 2D and 3D geological structures. Bulletin of the Seismological Society of America, 88(2), 368-392.

Kosloff, D. D., & Baysal, E. (1982). Forward modeling by a Fourier method. Geophysics, 47(10), 1402-1412.

Kramer, S. L. (1996). Geotechnical earthquake engineering. Pearson Education India.

Kuo, J. Y., Kausel, E., & Roësset, J. M. (1998). Local site effects and basin-edge induced waves in Mexico City and the valley of Santiago. Soil Dynamics and Earthquake Engineering, 17(4), 279-295.

Lanzo, G., Tommasi, P., Ausilio, E., Aversa, S., Bozzoni, F., Cairo, R., ... & Zimmaro, P. (2019). Reconnaissance of geotechnical aspects of the 2016 Central Italy earthquakes. Bulletin of earthquake engineering, 17, 5495-5532.

Laurenzano, G., Barnaba, C., Romano, M. A., Priolo, E., Bertoni, M., Bragato, P. L., ... & Garbin, M. (2019). The Central Italy 2016–2017 seismic sequence: site response analysis based on seismological data in the Arquata del Tronto–Montegallo municipalities. Bulletin of Earthquake Engineering, 17, 5449-5469.

Laurenzano, G., Garbin, M., Parolai, S., Barnaba, C., Romanelli, M., & Froner, L. (2023). High-resolution local seismic zonation by cluster and correlation analysis. Soil Dynamics and Earthquake Engineering, 173, 108122.

Lee, S. J., Chan, Y. C., Komatitsch, D., Huang, B. S., & Tromp, J. (2009a). Effects of realistic surface topography on seismic ground motion in the Yangminshan region of Taiwan based upon the spectral-element method and LiDAR DTM. Bulletin of the Seismological Society of America, 99(2A), 681-693.

Lee, V. W., & Trifunac, M. D. (1985). Torsional accelerograms. International Journal of Soil Dynamics and Earthquake Engineering, 4(3), 132-139.

Lee, S. J., Komatitsch, D., Huang, B. S., & Tromp, J. (2009b). Effects of topography on seismic-wave propagation: An example from northern Taiwan. Bulletin of the Seismological Society of America, 99(1), 314-325.

Lermo, J. F., & Chavez-Garcia, F. J. (1993). Site effect evaluation using spectral ratios with only one station. Bulletin of the Seismological Society of America, 83(6), 1574–1594.

Liu, Z., Qiao, Y., Cheng, X., & El Naggar, M. H. (2022). Nonlinear seismic response and amplification effect of 3D sedimentary basin based on bounding surface constitutive model. Soil Dynamics and Earthquake Engineering, 158, 107292.

Livani, M., Scrocca, D., Gaudiosi, I., Mancini, M., Cavinato, G. P., de Franco, R., ... & Moscatelli, M. (2022). A geology-based 3D velocity model of the Amatrice Basin (Central Italy). Engineering Geology, 306, 106741.

Locati M., Camassi R., Rovida A., Ercolani E., Bernardini F., Castelli V., Caracciolo C.H., Tertulliani A., Rossi A., Azzaro R., D'Amico S., Antonucci A. (2022). Database

Macrosismico Italiano (DBMI15), versione 4.0 [Data set]. Istituto Nazionale di Geofisica e Vulcanologia (INGV).

Luo, Y., Cui, L., Wang, R., Cao, Z., & Hao, H. (2018). Effects of canyon topography on seismic ground motions with nonlinear numerical modeling. Soil Dynamics and Earthquake Engineering, 115, 534-546.

Luzi, L., Pacor, F., Lanzano, G., Felicetta, C., Puglia, R., & D'Amico, M. (2019). 2016–2017 Central Italy seismic sequence: Strong-motion data analysis and design earthquake selection for seismic microzonation purposes. Bulletin of Earthquake Engineering, 17(1), 1–19.

Luzi, L., R. Puglia, F. Pacor, M. R. Gallipoli, D. Bindi e M. Mucciarelli (2011). «Proposal for a soil classification based on parameters alternative or complementary to Vs,30». In: Bulletin of Earthquake Engineering 9.6, pp. 1877–1898. issn: 1573- 1456.

Lysmer, J., & Drake, L. A. (1972). A finite element method for seismology. In: Herrmann, R. B. (Ed.), Seismological Algorithms: Computational Methods and Computer Programs (pp. 123-132), Academic Press.

Lysmer, J., & Kuhlemeyer, R. L. (1969). Finite dynamic model for infinite media. Journal of the Engineering Mechanics Division, 95(4), 859–877.

Macmurdo, J. (1824) XXI. Papers relating to the earthquake which occurred in India in 1819. Philosophical Magazine Series 1, 63:310, 105-119

Magri, G., & Molin, D. (1986). I terremoti del 3 Gennaio 1117 e del 25 Dicembre 1222. Rapporto ENEA. RTI-PAS-ISP-GEOL LO (86) 2, 9pp.Marcellini, A., Massa, M., Moscatelli, M., & Stucchi, M. (2007). S4 Project. INGV Seismological Projects, Italy.

Mallet, R. (1862). Great Neapolitan Earthquake of I857, London, 2 vols.

Manolis, G. D., & Beskos, D. E. (1988). Boundary element methods in elastodynamics. (No Title).

Martin, S. (2006). Investigation of ground motion and topographic effects at archaeological sites in Greece. Seismological Research Letters, 77(2), 281-293.

Massa, M., Barani, S., Lovati, S., & Ferretti, G. (2014). Site response analysis at the basin-edge of Aulla (Northern Apennines, Italy): results from 2D numerical simulations. Bulletin of Earthquake Engineering, 12(2), 757-778.

Maufroy, E., Cruz-Atienza, V. M., Cotton, F., & Gaffet, S. (2014). Frequency-scaled curvature as a proxy for topographic site-effect amplification and ground-motion variability. Bulletin of the seismological society of America, 105(1), 354-367.

Mavko, G. (2018). Introduction to rock physics. Stanford Rock Physics Laboratory.

McCallen, D. B., Larsen, S. C., & Carr, D. M. (2005). Parallel simulation of 3D site response. Computers & Structures, 83(14), 1031-1045.

Meletti, C., Montaldo, V., Stucchi, M., & Martinelli, F. (2006). Database della pericolosità sismica MPS04. Istituto Nazionale di Geofisica e Vulcanologia (INGV).

Mendoza, C., & Hartzell, S. (1999). Fault-slip distribution of the 1995 Colima-Jalisco, Mexico, earthquake. Bulletin of the Seismological Society of America, 89(5), 1338-1344.

Mendoza, C., & Hartzell, S. (2000). Slip distribution of the 1995 Colima-Jalisco, Mexico, earthquake: Implications for rupture dynamics and faulting segmentation. Bulletin of the Seismological Society of America, 90(5), 1213-1224.

Milne, J. (1893). A Note on the Great Earthquake of October 28th, 1891. Seismological journal of Japan, 17, 127-151. https://repository.dl.itc.u-tokyo.ac.jp/records/235

Ministero delle Infrastrutture e dei Trasporti. (2018). Aggiornamento delle “Norme Tecniche per le Costruzioni”. Supplemento ordinario alla Gazzetta Ufficiale, n. 42 del 20 febbraio 2018 – serie generale.

Moczo, P., Kristek, J., & Gális, M. (2014). The finite-difference modelling of earthquake motions: Waves and ruptures. Springer Science & Business Media.

Molnar, S., Cassidy, J. F., Castellaro, S., Cornou, C., Crow, H., Hunter, J. A., ... & Yong, A. (2018). Application of microtremor horizontal-to-vertical spectral ratio (MHVSR) analysis for site characterization: State of the art. Surveys in Geophysics, 39, 613-631.

Motamed R, Ghalandarzadeh A, Tawhata I, Tabatabaei SH (2007) Seismic microzonation and damage assessment of Bam city, Southeastern Iran. J Earthq Eng 11(1):110–132

MPS Working Group (2004). Redazione della mappa di pericolosità sismica prevista dall'Ordinanza PCM 3274 del 20 marzo 2003. Rapporto conclusivo per il Dipartimento della Protezione Civile, INGV, Milano-Roma, aprile 2004, 65 pp. + 5 appendici.

Nakamura, Y. (1989). A method for dynamic characteristics estimation of subsurface using microtremor on the ground surface. Quarterly Report of the Railway Technical Research Institute, 30, 25–33.

Newmark, N. (1969). Torsion in symmetrical buildings. In Proceedings of the 4th World Conference on Earthquake Engineering. ASCE.

Nogoshi, M., & Igarashi, T. (1970). On the propagation characteristics of microtremors. Journal of the Seismological Society of Japan, 23, 264–280 (in Japanese with English abstract).

Orszag, S. A. (1980). Spectral methods for problems in complex geometries. Journal of Computational Physics, 37(1), 70-92.

Panzera, F., Alber, J., Imperatori, W., Bergamo, P., & Fäh, D. (2022). Reconstructing a 3D model from geophysical data for local amplification modelling: The study case of the upper Rhone valley, Switzerland. Soil Dynamics and Earthquake Engineering, 155, 107163.

Paolucci, R. (1999a). Numerical evaluation of the effect of cross-coupling of different components of ground motion in site response analyses. Bulletin of the Seismological Society of America, 89(4), 877-887.

Paolucci, R. (1999b). Shear resonance frequencies of alluvial valleys by Rayleigh's method. Earthquake Spectra, 15, 503-522.

Paolucci, R. (2002). Amplification of earthquake ground motion by steep topographic irregularities. Earthquake engineering & structural dynamics, 31(10), 1831-1853.

Parolai S, Bormann P, Milkereit C (2002) New relationship between Vs, thickness of sediments, and resonance frequency calculated by the H/V ratio of seismic noise for the Cologne area (Germany). Bull Seismol Soc Am92(6):2521–2527.

Parolai, S. (2012). Investigation of site response in urban areas by using earthquake data and seismic noise. In P. Bormann (Ed.), New manual of seismological observatory practice 2 (NMSOP-2) (Chap. 14, pp. 1-38). Potsdam, Germany.

Papazachos, C., Pavlides, S., Chatzipetros, A., Papathanassiou, G., Valkaniotis, S., Pitilakis, D., ... & Rouchotas, L. (2014). GEER/EERI/ATC earthquake reconnaissance, January 26th/February 2nd, 2014 Cephalonia, Greece events. Geotechnical Extreme Events Reconnaissance Association. Version 1: June 6, 2014.

Patera, A. T. (1984). A spectral element method for fluid dynamics: Laminar flow in a channel expansion. Journal of Computational Physics, 54(3), 468-488.

Penna, A., Calderini, C., Sorrentino, L., Carocci, C. F., Cescatti, E., Sisti, R., ... & Prota, A. (2019). Damage to churches in the 2016 central Italy earthquakes. Bulletin of Earthquake Engineering, 17, 5763-5790.

Peter, D., Komatitsch, D., Luo, Y., Martin, R., Le Goff, N., Casarotti, E., Le Loher, P., Magnoni, F., Liu, Q., Blitz, C., Nissen-Meyer, T., Basini, P., & Tromp, J. (2011). Forward and adjoint simulations of seismic wave propagation on fully unstructured hexahedral meshes. Geophysical Journal International, 186(2), 721-739.

Picotti, V., Prosser, G., & Castellarin, A. (1995). Structures and kinematics of the Giudicarie - Val Trompia fold and thrust belt (Central Southern Alps, Northern Italy). Memorie della Società Geologica Italiana, 47, 95–109.

Pischiutta, M., Cultrera, G., Caserta, A., Luzi, L., & Rovelli, A. (2010). Topographic effects on the hill of Nocera Umbra, central Italy. Geophysical Journal International, 182(2), 977-987.

Pischiutta, M., Fondriest, M., Demurtas, M., Magnoni, F., Di Toro, G., & Rovelli, A. (2017). Structural control on the directional amplification of seismic noise (Campo Imperatore, central Italy). Earth and Planetary Science Letters, 471, 10–18.

Pischiutta, M., M. Pastori, L. Improta, F. Salvini, and A. Rovelli (2014), Orthogonal relation between wavefield polarization and fast S wave direction in the Val d'Agri region: An integrating method to investigate rock anisotropy, J. Geophys. Res. Solid Earth, 119, 396–408, doi:10.1002/2013JB010077

Pischiutta, Petrosino, S., & Nappi, R. (2022). Directional amplification and ground motion polarization in Casamicciola area (Ischia volcanic island) after the 21 August 2017 Md 4.0 earthquake. Frontiers in Earth Science, 10, 999222.

Pischiutta, M., Rovelli, A., Caserta, A., Luzi, L., & Bindi, D. (2009). Reciprocal interaction of local morphology and seismic motion: An example from Central Italy. Bulletin of the Seismological Society of America, 99(5), 2520-2531.

Pitarka, A., Irikura, K., Iwata, T., & Kagawa, T. (1996). Basin structure effects in the Kobe area inferred from the modeling of ground motions from two aftershocks of the January 17, 1995, Hyogo-ken Nanbu earthquake. Journal of Physics of the Earth, 44(5), 563-576.

Poggi, V., Drouet, S., & Fäh, D. (2013). The amplitude and variability of ground-motion at the base and top of soft sedimentary layers. Geophysical Journal International, 192(2), 962-975.

Poggi, V., Fäh, D., Burjánek, J., Giardini, D., & Michel, C. (2012). The use of Rayleigh wave ellipticity for site-specific hazard assessment and microzonation: Application to the Basel area (Switzerland). Geophysical Journal International, 188(3), 1151-1173.

Pondrelli, S., Salimbeni, S., Ekström, G., Morelli, A., Gasperini, P., & Vannucci, G. (2006). The Italian CMT dataset from 1977 to the present. Physics of the Earth and Planetary Interiors, 159(3-4), 286-303.

Poursartip, B., Fathi, A., & Tassoulas, J. L. (2020). Large-scale simulation of seismic wave motion: A review. Soil Dynamics and Earthquake Engineering, 129, 105909.

Primofiore, I., Baron, J., Klin, P., Laurenzano, G., Muraro, C., Capotorti, F., ... & Vessia, G. (2020). 3D numerical modelling for interpreting topographic effects in rocky hills for Seismic Microzonation: The case study of Arquata del Tronto hamlet. Engineering Geology, 279, 105868.

Puglia, R., Ditommaso, R., Pacor, F., Mucciarelli, M., Luzi, L., & Bianca, M. (2011). Frequency variation in site response as observed from strong motion data of the L'Aquila (2009) seismic sequence. Bulletin of Earthquake Engineering, 9, 869-892.

Raptakis, D., Chávez-Garcıa, F. J., Makra, K., & Pitilakis, K. (2000). Site effects at Euroseistest—I. Determination of the valley structure and confrontation of observations with 1D analysis. Soil Dynamics and Earthquake Engineering, 19(1), 1-22.

Ravazzi, C., Pini, R., Badino, F., de Amicis, M., Londeix, L., & Reimer, P. J. (2014). The latest LGM culmination of the Garda Glacier (Italian Alps) and the onset of glacial termination: Age of glacial collapse and vegetation chronosequence. Quaternary Science Reviews, 105, 26–47.

Reiter, L. (1990). Earthquake Hazard. Analysis: Issues and Insights. Columbia University Press.

Reinoso, E., Wrobel, L. C., & Power, H. (1997). Three-dimensional scattering of seismic waves from topographical structures. Soil Dynamics and Earthquake Engineering, 16(1), 41-61.

Revenaugh, J. S. (1984). The contribution of Rayleigh and Love waves to ground motions at southern California stations. Journal of Geophysical Research, 89(B2), 937-948.

Rollins, K. M., Evans, M. D., Diehl, N. B., & III, W. D. D. (1998). Shear modulus and damping relationships for gravels. Journal of geotechnical and Geoenvironmental Engineering, 124(5), 396-405.

Romero, A., Galvín, P., & Domínguez, J. (2013). 3D non-linear time domain FEM–BEM approach to soil–structure interaction problems. Engineering Analysis with Boundary Elements, 37(3), 501-512.

Rovida, A., Locati, M., Camassi, R., Lolli, B., & Gasperini, P. (2016). Catalogo Parametrico dei Terremoti Italiani, versione CPTI15. Istituto Nazionale di Geofisica e Vulcanologia. doi: http://doi. org/10.6092/INGV. IT-CPTI15.

Sánchez-Sesma, F. J. (1990). Elementary solutions for response of a wedge-shaped medium to incident SH and SV waves. Bulletin of the Seismological Society of America, 80(3), 737-742.

Sanchez-Sesma, F. J., & Campillo, M. (1991). Diffraction of P, SV, and Rayleigh waves by topographic features: A boundary integral formulation. Bulletin of the Seismological Society of America, 81(6), 2234-2253.

Savage, M. K., & Helmberger, D. V. (1991). Wave propagation in 2-D media containing cracks. Journal of Geophysical Research, 96(B3), 1815-1826.

Schwab, F. A., & Knopoff, L. (1970). Surface-wave dispersion computations. Bulletin of the Seismological Society of America, 60(1), 321-344.

Semblat, J. F., Kham, M., Parara, E., Bard, P. Y., Pitilakis, K., Makra, K., et al. (2005). Seismic wave amplification: Basin geometry vs soil layering. Soil Dynamics and Earthquake Engineering, 25(7-10), 529-538.

Seriani, G., & Priolo, E. (1994). Spectral element method for acoustic wave simulation in heterogeneous media. Finite Element Analysis and Design, 16(1), 25–46.

SESAME working group (2004). Guidelines for the implementation of the H/V spectral ratio technique on ambient vibrations measurements, processing and interpretation. European Commission–EVG1-CT-2000-00026 SESAME.

Sextos, A., De Risi, R., Pagliaroli, A., Foti, S., Passeri, F., Ausilio, E., ... & Zimmaro, P. (2018). Local site effects and incremental damage of buildings during the 2016 Central Italy earthquake sequence. Earthquake Spectra, 34(4), 1639-1669.

Seylabi, E. E., Jeong, C., Dashti, S., Hushmand, A., & Taciroglu, E. (2018). Seismic response of buried reservoir structures: A comparison of numerical simulations with centrifuge experiments. Soil Dynamics and Earthquake Engineering, 109, 89-101.

Sgobba, S., Puglia, R., Pacor, F., Luzi, L., Russo, E., Felicetta, C., Lanzano, G., D'Amico, M., Baraschino, R., Baltzopoulos, G., & Iervolino, I. (2019). REXELweb: A tool for selection of ground-motion records from the Engineering Strong Motion database. Seismological Research Letters, 90(3), 999–1006.

Siebert, W. M. (1986). Circuits, signals, and systems. MIT Press.

Silvestri, F. (2005). Comportamento meccanico dei terreni sotto azioni sismiche. In Aspetti geotecnici della progettazione in zona sismica: Linee guida AGI (Capitolo 2). AGI.

Simoni, C., Turri, E., Varanini, G. M., & Sauro, U. (2001). Il lago di Garda (p. 450). Cierre Edizioni. ISBN: 8883141016.

Singh, S. K., Anderson, J. G., & Quaas, R. (1992). Correction for local site effects in hazard analysis of Mexico City. Earthquake Spectra, 8(2), 201-218.

Siro, S., & Goffin, E. (1985). Numerical techniques for seismic site response studies. Earthquake Engineering & Structural Dynamics, 13(2), 119-132.

Sirovich, L. (1982). Southern Italy November 23, 1980 earthquake. Proceedings of the Seventh European Conference on Earthquake Engineering, Vol. 7, Athens, Greece, 1982: 419–429

SM Working Group. (2015). Guidelines for seismic microzonation. Conference of Regions and Autonomous Provinces of Italy—Civil Protection Department, Rome. (Original Italian Edition: Gruppo di lavoro MS, Indirizzi e criteri per la microzonazione sismica, Conferenza delle Regioni e delle Province autonome—Dipartimento della protezione civile, Roma, 2008, 3 vol. e Dvd).

Smerzini, C., Paolucci, R., & Stupazzini, M. (2009). Experimental and numerical results on earthquake-induced rotational ground motions. Journal of Earthquake Engineering, 13(S1), 66-82.

Somerville, P. G., & Yoshimura, C. (2001). The influence of critical structures on the damage distribution of the 1995 Hyogo-ken Nanbu earthquake. Earthquake Spectra, 17(3), 409-426.

Spudich P, Fletcher JB (2008) Observation and prediction of dynamic ground strains, tilts, and torsions caused by the Mw 6.0 2004 Parkfield, California, earthquake and aftershocks, derived from UPSAR array observations. Bull Seismol Soc Am 98:1898–1914.

Spudich, P., Hellweg, M., & Lee, W. H. K. (1996). Directional topographic site response at Tarzana observed in aftershocks of the 1994 Northridge, California, earthquake: implications for mainshock motions. Bulletin of the Seismological Society of America, 86(1B), S193-S208.

Steidl, J. H., Tumarkin, A. G., & Archuleta, R. (1996). What is a reference site? Bulletin of the Seismological Society of America, 86(6), 1733–1748.

Stewart, J. P., Chiou, S. J., Bray, J. D., Graves, R. W., Somerville, P. G., & Abrahamson, N. A. (2002). Ground motion evaluation procedures for performance-based design. Soil dynamics and earthquake engineering, 22(9-12), 765-772.

Stokoe, K. H., Wright, S. G., James, A., & Jose, M. (1994). Characterization of geotechnical sites by SASW method. In Woods, R. D. (Ed.), Geophysical Characterization of Sites (pp. 15-25), Oxford Publishers.

Stupazzini, M., de la Puente, J., Smerzini, C., Käser, M., Igel, H., & Castellani, A. (2009). Study of rotational ground motion in the near-field region. Bulletin of the Seismological Society of America, 99(2B), 1271-1286.

Sun, R., & McMechan, G. A. (2008). Amplitude effect of the free surface in elastic reverse-time extrapolation. Geophysics, 73(5), S177-S184.

Taborda, R., & Bielak, J. (2009). Three-dimensional modeling of earthquake ground motion including nonlinear wave propagation in soils. Seismological Research Letters, 80(2), 320. SSA Annual Meeting, Monterey, CA, USA, April 8-10.

Takemura, M., & Miyake, H. (2001). Strong ground motion estimation in the 2000 western Tottori prefecture earthquake. Journal of Seismology, 5(3), 395-403.

Tarquini, S., Isola, I., Favalli, M., Battistini, A., & Dotta, G. (2023). TINITALY, a digital elevation model of Italy with a 10 meters cell size (Version 1.1). Istituto Nazionale di Geofisica e Vulcanologia (INGV).

Tarquini, S., Isola, I., Favalli, M., Mazzarini, F., Bisson, M., Pareschi, M. T., & Boschi, E. (2007). TINITALY/01: a new triangular irregular network of Italy. Annals of Geophysics.

Thabet, M. (2019). Site-specific relationships between bedrock depth and HVSR fundamental resonance frequency using KiK-NET data from Japan. Pure and Applied Geophysics, 176(11), 4809-4831.

Tokimatsu, K., & Seed, H. B. (1987). Evaluation of settlements in sands due to earthquake shaking. Journal of Geotechnical Engineering, 113(8), 861-878.

Trifunac, M. D. (2009). Rotations in structural response. Bulletin of the Seismological Society of America, 99(2B), 968-979.

Trifunac, M. D. (1971). Surface motion of a semi-cylindrical alluvial valley for incident plane SH waves. Bulletin of the Seismological Society of America, 61(6), 1765-1779.

Trifunac, M. D., & Brady, A. G. (1975). A study on the duration of strong earthquake ground motion. Bulletin of the Seismological Society of America, 65(3), 581-626.

Trifunac, M. D., & Todorovska, M. I. (2001). A note on the useable dynamic range of accelerographs recording translation. Soil Dynamics and Earthquake Engineering, 21, 275-286.

Tumarkin, A. G. (1998). Site response analysis in 3D. In Proceedings of the International Symposium on the Effects of Surface Geology on Seismic Motion (pp. 365-370), Yokohama, Japan, December 1998.

Tun, M., Pekkan, E., O¨ zel, O., & Guney, Y. (2016). An investigation into the bedrock depth in the Eskisehir Quaternary Basin (Turkey) using the microtremor method. Geophysical Journal International, 207(1), 589–607.

Venzo, G. A., Finetti, I., & Armani, V. (1977). Schema geo-tettonico e sismicità dell'area basso Sarca-Valle di Ledro e zone limitrofe. Effetti macrosismici del terremoto del 13-14 dicembre 1976 a Riva, basso Sarca e Val di Ledro. Relazione, Provincia Autonoma di Trento.

Vessia, G., Russo, S., & Lo Presti, D. (2011). A new proposal for the evaluation of the amplification coefficient due to valley effects in the simplified local seismic response analyses. Ital Geotech J, 4, 51-77

Viganò, A., Bressan, G., Ranalli, G., & Martin, S. (2008). Focal mechanism inversion in the Giudicarie–Lessini seismotectonic region (Southern Alps, Italy): Insights on tectonic stress and strain. Tectonophysics, 460, 106–115.

Viganò, A., Scafidi, D., & Ferretti, G. (2021). A new approach for a fully automated earthquake monitoring: The local seismic network of the Trentino region (NE Italy). Journal of Seismology, 25, 419–432.

Viganò, A., Scafidi, D., Martin, S., & Spallarossa, D. (2013). Structure and properties of the Adriatic crust in the central-eastern Southern Alps (Italy) from local earthquake tomography. Terra Nova, 25, 504–512.

Viganò, A., Scafidi, D., Ranalli, G., Martin, S., Della Vedova, B., & Spallarossa, D. (2015). Earthquake relocations, crustal rheology, and active deformation in the central-eastern Alps (N Italy). Tectonophysics, 661, 81–98.

Villenave, J., Bonilla, L. F., Haghshenas, E., Gueguen, P., & Hollender, F. (2020). Spatial variability of linear seismic site response: Analysis from high-density single-station ambient vibration measurements. Geophysical Journal International, 221(1), 125-144.

Wald, D. J., & Mori, J. (2000). Evaluation of methods for estimating linear site-response amplifications in the Los Angeles region. Bulletin of the Seismological Society of America, 90(6), S32-S42.

Wang, G., Du, C., Huang, D., Jin, F., Koo, R. C., & Kwan, J. S. (2018). Parametric models for ground motion amplification considering 3D topography and subsurface soils. Soil Dyn. Earthq. Eng, 115, 41-54.

Wang, G., Huang, J., & Lou, M. (2006). Three-dimensional site response for the Shanghai region. Soil Dynamics and Earthquake Engineering, 26(11), 1021-1036.

Wang, S., & Petersson, N. A. (2019). Fourth order finite difference methods for the wave equation with mesh refinement interfaces. SIAM Journal on Scientific Computing, 41(5), A3246-A3275.

Wang, Y., Liang, J., & Ba, Z. (2023). Weak nonlinear seismic response of 3D sedimentary basin using a new masing soil nonlinear model. Soil Dynamics and Earthquake Engineering, 171, 107982.

Wilcox, L. C., Stadler, G., Burstedde, C., & Ghattas, O. (2010). A high-order discontinuous Galerkin method for wave propagation through coupled elastic–acoustic media. Journal of Computational Physics, 229(24), 9373-9396.

Wood, H.O. (1908). "Distribution of apparent intensity in San Francisco, in the California earthquake of April 18, 1906," Report of the State Earthquake Investigation Commission, Carnegie Institute of Washington, Washington, D.C., Vol. 1, pp. 220-245.

Xie, Z., Komatitsch, D., Martin, R., & Matzen, R. (2014). Improved forward wave propagation and adjoint-based sensitivity kernel calculations using a numerically stable finite-element PML. Geophysical Journal International, 197(3), 1632–1647.

Xu, J., Bielak, J., Ghattas, O., & Wang, J. (2003). Three-dimensional nonlinear seismic ground motion modeling in basins. Physics of the earth and planetary interiors, 137(1-4), 81-95.

Yang, J., Zheng, J., & Liu, J. (2006). Numerical modeling of local site effects on strong ground motion. Soil Dynamics and Earthquake Engineering, 26(1), 18-32.

Yomogida, K., & Etgen, J. T. (1993). 3-D wave propagation in the Los Angeles basin for the Whittier-Narrows earthquake. Bulletin of the Seismological Society of America, 83(5), 1325-1344.

Yoshimoto, M., Kumagai, T., & Ogiso, M. (2013). Estimation of subsurface S-wave velocity structures using array observations of microtremors. Seismological Research Letters, 84(3), 421-429.

Yoshimura, C., & Kataoka, S. (2013). Large-scale 3D nonlinear simulations for site-specific ground motion prediction. Earthquake Engineering & Structural Dynamics, 42(1), 1-16.

Zhao, J. X., Irikura, K., Zhang, J., Fukushima, Y., Somerville, P. G., Asano, A., ... & Ogawa, H. (2006). An empirical site-classification method for strong-motion stations in Japan using H/V response spectral ratio. Bulletin of the Seismological Society of America, 96(3), 914-925.

Zhou, H. (2018). Review on the study of topographic effect on seismic ground motion. Earthquake Science, 31(2), 110-116.

Zhu, C., Thambiratnam, D., & Gallage, C. (2018). Statistical analysis of the additional amplification in deep basins relative to the 1D approach. Soil Dynamics and Earthquake Engineering, 104, 296-306.

ACKNOWLEDGMENT

I would like to express my sincere gratitude to my PhD supervisors, Prof. Vessia Giovanna and Dr. Laurenzano Giovanna, for their tireless support, guidance and invaluable feedback throughout the course of my research.

I am also very grateful to Dr. Klin Peter and Prof. Calista Monia for their essential contribution in performing the three-dimensional simulation analyses of seismic wave propagation.